A modelling of microstructure evolution and crack opening in FCC materials under tension

Nam Nhat Huynh
University of Wollongong

School of Mechanical, Materials and Mechatronics Engineering

Faculty of Engineering

A Modelling of Microstructure Evolution and Crack Opening in FCC Materials under Tension

Nam Nhat Huynh, BE, MEngPrac

"This thesis is presented as part of the requirements for the award of the Degree of Doctor of Philosophy of the University of Wollongong"

August, 2009

Certification

I, Nam N. Huynh, declare that this theis is wholly my own work unless otherwise referenced and acknowledged. The document has not been submitted for qualifications at any other academic institution.

Nam Nhat Huynh
August 2009

Abstract

The field of fracture mechanics can generally be divided into two groups: (i) the study of material behaviour prior to crack and (ii) the developing of crack opening criteria. Even though various studies have been done in both subjects there are still gaps that need to be bridged. This thesis aims at combining both groups of the modelling of dynamic fracture in crystalline materials at a reasonable cost of computational time.

A model of crystal plasticity finite element method has been formulated to account for the effects of lattice structure in the crystalline materials. The model has been applied to simulate tensile deformation around a notch tip in both single crystals and polycrystalline aggregates. By comparing with observations from various experiments, the model has been proved to be able to accurately capture the material's behaviours around a notch tip undergoing tensile load. Particularly, this model is among the very few, if not the first, that accurately predicts various experimental observations of two notch tip orientations (010)[101] and (010)[100] that are widely found in the literature.

This study has also developed a crack opening criterion that is dependent upon the evolution of the lattice structure. The core of this new criterion is an atomic interaction model that estimates energies of the interface of an fcc bicrystal. Results of grain boundary energy of <100> and <110> symmetrical tilt boundaries of an aluminum bicrystal obtained from the atomic interaction model agree very well with those from molecular dynamics simulations.

The newly developed criterion has been applied to the modelling of crack opening and crack growth in a region around the notch tip in single crystals. Elements in the finite element mesh satisfying the criterion are removed from the mesh by using the element removal technique in Abaqus/Standard. Missing elements effectively act as voids in the material. Thus crack opening (in terms of void nucleation) and the

subsequent crack growth (in terms of coalescence of new and existing voids) are captured naturally. The newly developed methodology to model crack opening has been applied to predict mode I crack growth around a notch tip in Cube and Brass oriented fcc single crystals. The obtained results show similar behaviours of crack growth with those from molecular dynamics simulations of single crystals having the same lattice orientations.

The methodology to model crack opening that has been proposed in this thesis is original. It enables the explicit modelling of crack growth without presuming a crack path. Also, a predefined crack opening criterion, which could be erroneous, that has been used in many finite element simulations of fracture is avoided. To the best of the author's knowledge, the criterion of crack opening that depends on the structure of the interface of two misoriented lattices is presented in this study for the first time.

The current thesis focuses into modelling tensile deformation and the subsequent fracture in fcc crystals. The methodology that has been proposed however can be readily applied to crystalline materials of various lattice structures with minor modifications.

Publications

1. N.N. Huynh, C. Lu, G. Michal, K. Tieu, “A Modelling of Tensile Deformation Around the Notch Tip in Single Crystal Aluminium”, *Computational Materials Science*, vol. 48, pp. 179-186, 2010.

2. C. Lu, Y. Gao, G. Michal, G. Deng, N.N. Huynh, H.T. Zhu, X. Liu, A.K. Tieu, “Experiment and Molecular Dynamics Simulation of Nanoindentation of Body Centered Cubic Iron”, *Journal of Nanoscience and Nanotechnology*, vol. 9, pp. 7307-7313, 2009.

3. L.Y. Si, C. Lu, N.N. Huynh, A.K. Tieu, X.H. Liu, “Simulation of rolling behaviour of cubic oriented al single crystal with crystal plasticity FEM”, *Journal of Materials Processing Technology*, vol. 201, pp. 79–84, 2008.

4. C. Lu, Y. Gao, G.Y. Deng, G. Michal, N.N. Huynh, X.H. Liu, A.K. Tieu, “Atomic-scale anisotropy of nanoscratch behavior of single crystal iron”, *Wear*, vol. 267, pp. 1961-1966, 2009.

5. Y. Gao, C. Lu, N.N. Huynh, G. Michal, H.T. Zhu, A.K. Tieu, “Molecular dynamics simulation of effect of indenter shape on nanoscratch of Ni”, *Wear*, vol. 267, pp. 1998-2002, 2009.

6. C. Lu, Y. Gao, G. Michal, N.N. Huynh, H.T. Zhu, A.K. Tieu, “Atomistic simulation of nanoindentation of iron with different indenter shapes”, *Proceedings of the Institution of Mechanical Engineers Part J Journal of Engineering Tribology*, vol. 223, pp. 977-984, 2009.

7. N.N. Huynh, C. Lu, L. Si, K. Tieu, “A study of microstructural evolution around crack tip using crystal plasticity finite-element method”, *Proceedings of the Institution of Mechanical Engineers Part J Journal of Engineering Tribology*, vol. 222, pp. 183-192, 2008.

8. N.N. Huynh, C. Lu, L. Si, K. Tieu, “An orientation-dependent failure criterion for fcc crystals”, *Key Engineering Materials*, vol. 385-387, pp. 801-804, 2008.

Acknowledgements

I would like to thank my supervisors, Prof. Kiet Tieu and Dr. Cheng Lu, for getting me started on this thesis, their helpful advice and constant support throughout the period of my study.

My special thanks go to Guillaume Michal for his help in setting up and administrating the supercomputing cluster (Eukles) without which simulations carried out in this study would be a tedious task. I also appreciate fruitful discussions with my groupmates, Liangying Si, Guillaume Michal, and Yuan Gao, regarding aspects of the theory of crystal plasticity, the Voronoi diagram and some fundamentals of molecular dynamics.

Finally I deeply thank my family for their relentless understanding, devotion and encouragements even at their most difficult times.

Table of Contents

Notations

$\otimes$	Tensor product
α^{tilt}, β^{tilt}	Angles defining orientation of tilt axis in the global coordinate system
$\mathbf{\Omega}$	Spin tensor
$\mathbf{\Omega}^{*}$	Lattice rotation of spin tensor
$\mathbf{\Omega}^{p}$	Plastic parts of spin tensor
α^{th}	A slip system α
α^{hkl}	Angle of rotation about a global [*hkl*] axis
Γ_0	Work of separation
γ	Shear strain of a slip system
γ_0	Reference value of slip
$\dot{\gamma}^{(\alpha)}$	Shear strain-rate caused by the plastic slip in the α^{th} slip system
$\dot{\gamma}_0^{(\alpha)}$	Reference value of shear strain rate
$\delta\mathbf{D}$	Virtual form of the rate of deformation
Δt	Time increment
$\Delta\mathbf{d}_A^i$, $\Delta\mathbf{d}_B^i$	Displacement vectors from time i-1 to time i at points A and B
φ_1, Φ, φ_2	Three Euler angles
δ_n	Corresponding crack opening
$\delta\mathbf{v}$	Kinematically admissible virtual velocity field
$\delta\mathbf{v}^{\mathbf{n}}$	Virtual nodal velocity field
$\boldsymbol{\sigma}$	Cauchy stress
σ_{max}	Peak separation stress
$\dot{\boldsymbol{\sigma}}$	Time derivative of Cauchy stress
$\overset{\nabla}{\boldsymbol{\sigma}}$	Jaumann rate of Cauchy stress on axes rotating with the material
$\boldsymbol{\sigma}_A$, $\boldsymbol{\sigma}_B$	Cauchy stress tensor at points A and B

τ_0	Initial critical resolved shear stress
τ_1	Breakthrough stress where large plastic flow initiates
$\tau^{(\alpha)}$	Resolved shear stress on slip system α.
$\tau_c^{(\alpha)}$	Critical resolved shear stress of slip system α.
a_1	Constants for $f_{\alpha\beta}$ (no junction)
a_2	Constants for $f_{\alpha\beta}$ (Hirth lock)
a_3	Constants for $f_{\alpha\beta}$ (coplanar junction)
a_4	Constants for $f_{\alpha\beta}$ (glissile junction)
a_5	Constants for $f_{\alpha\beta}$ (sessile junction)
$\mathbf{C}_0$	Tensor of elastic moduli
$\mathbf{d}_A^i$, $\mathbf{d}_B^i$	Coordinates of points A and B at time i
$\mathbf{D}$	Stretching tensor
$\mathbf{D}^*$	Elastic part of stretching tensor
$\mathbf{D}^p$	Plastic part of stretching tensor
$\mathbf{D}_L$	Rate of the elastic stretching in the lattice coordinate system
$\mathbf{D}_{gi}$	Matrix transforming a vector in the global coordinate system to the coordinate system of crystal i
D^{damage}	Damage variable
$\mathbf{E}$	Green strain tensor
E_{crit}	Interface fracture energy of a bicrystal
$\dot{\mathbf{E}}$	Rate of Green strain tensor
$\mathbf{f}$	Surface traction per unit of the current area
$\mathbf{F}$	Total deformation gradient
$\dot{\mathbf{F}}$	Time derivative of the total deformation gradient
$\mathbf{F}^*$	Elastic deformation gradient
$\mathbf{F}^p$	Crystallographic slip on the slip system (plastic deformation gradient)
$f_{\alpha\beta}$	Strength of a particular slip interaction between two slip systems α and β
$\mathbf{F}^{(\alpha)P}$	Contribution of α^{th} slip system to $\mathbf{F}^p$
g	Relaxation factor, which varies from 0 to 1
g^{iso}, h^{iso}, r^{iso}	Isoparametric element coordinates

$\mathbf{H}$	Fourth-order hardening parameter tensor
h_0	Hardening modulus just after initial yield
h_s	Hardening modulus during easy glide
$h_{\alpha\alpha}$	Self hardening moduli
$h_{\alpha\beta}$	Instantaneous hardening moduli including self hardening of each system
$\mathbf{I}$	A second-order unit tensor
$\mathbf{K}$	Jacobian matrix
$\mathbf{L}$	Velocity gradient
$\mathbf{L}^*$	Component of velocity gradient due to elastic stretching and lattice rotation
$\mathbf{L}^p$	Plastic contribution of velocity gradient $\mathbf{L}$
$\mathbf{m}^{(\alpha)}$	Normal vector of slip plane of slip system α^{th} in the current configuration
$\mathbf{m}_0^{(\alpha)}$	Normal vector of slip plane of slip system α^{th} in the reference configuration
$\dot{\mathbf{m}}^{(\alpha)}$	Time derivative of the normal vector of a slip system α^{th} in the current configuration
$\mathbf{n}^{\mathbf{intf}}$	Normal vector of the interface of a bicrystal in the global coordinate system
N	Number of slip systems
$\mathbf{N}_\mathbf{i}^\mathbf{0}$	Initial normal vectors {111} in the global coordinate system
$\mathbf{N}_\mathbf{i}^\mathbf{k}$	Normal vectors {111} in the global coordinate system at state k
$\mathbf{N}^{(1)}$, $\mathbf{N}^{(2)}$, $\mathbf{N}^{(3)}$	Normal vectors of slip traces from Rice's solutions for fcc crystal
$\hat{\boldsymbol{\rho}}_\mathbf{l}$	Tilt axis with respect to the coordinate system of the fixed lattice
$\hat{\boldsymbol{\rho}}_\mathbf{g}$	Tilt axis in the global coordinate system
$\mathbf{P}^{(\alpha)}$	Symmetric part of Schmid factor
q	Latent hardening parameter
$\mathbf{R}$	Orthogonal rotation tensor
$\dot{\mathbf{R}}$	Time derivative of the orthogonal rotation tensor
$\mathbf{R}_\mathbf{i}^\mathbf{k}$	Orientation matrix of crystal i at state k

$\mathbf{R}_j^k$	Orientation matrix of crystal j at state k
$\mathbf{R}_{ij}^k$	Misorientation matrix between point i and point j
$\mathbf{R}_L$	Rotation tensor between the lattice coordinate system and the current configuration
$\mathbf{S^{(1)}, S^{(2)}, S^{(3)}}$	Directions of slip traces from Rice's solutions for fcc crystal
$\mathbf{s}^{(\alpha)}$	Slip direction vector of a slip system α^{th} in the current configuration.
$\mathbf{s}_0^{(\alpha)}$	Slip direction vector of a slip system α^{th} in the reference configuration.
$\dot{\mathbf{s}}^{(\alpha)}$	Time derivative of slip direction vector of slip system α^{th} in the current configuration
$\mathbf{s}^{(\alpha)} \otimes \mathbf{m}^{(\alpha)}$	Schmid factor
$\mathbf{t_0}$	Kirchhoff stress in the current configuration at the time t
t_n	Normal stress ahead of crack tip for mode I crack
$\dot{\mathbf{t}}$	Material rate of Kirchhoff stress
$\dot{\mathbf{t}}_0$	Stress rate in the reference configuration
$\dot{\mathbf{t}}_1^*$	Rate of the Kirchhoff stress in the intermediate configuration
$\dot{\mathbf{t}}_L$	Material rate of the Kirchhoff stress in the lattice coordinate system
$\overset{\nabla}{\mathbf{t}}$	Jaumann rate of Kirchhoff stress on axes that rotate with the material
$\overset{\nabla}{\mathbf{t}}^*$	Jaumann rate of Kirchhoff stress on axes that rotate with the lattice
$\mathbf{U}$	Right stretch tensor
$\mathbf{v}$	Velocity in the current configuration
V	Volume of the solid body in the current configuration
$\mathbf{v^n}$	Nodal velocities
$\mathbf{v}_i^n$	Nodal velocities at iteration step i
$\mathbf{W}^{(\alpha)}$	Asymmetric part of Schmid factor
W_{intf}	Net strain energy on the interface under the effects of external loading
$\mathbf{X}$	Position of material points in the current configuration

List of Figures

List of Tables

1. Introduction

Fracture of a solid body is generally defined as the loss of contacts between parts of the body, which leads to significant decrement of its ability to undergo external load. Under the effects of various sources, e.g. mixed-mode loading, environment, defects in the materials, inadequate design and construction, fracture could occur with very little warning, either in brittle or ductile materials. Even though the cost of failure of components due to fracture in monetary terms is tremendous, the loss of human life and injuries is immeasurable. These factors have been the strong motivation for studies carried out in the last few decades toward a comprehensive understanding of the mechanisms of fracture, as well as the ability to accurately predict the material's behaviours prior to and during cracking under various conditions. [1, 2]

A starting assumption in many studies of fracture is that there are existing defects in the forms of voids or notches in the samples being considered. The investigations are then carried out to determine how likely further cracks occur at these sites and under which conditions. This chapter reviews works that have been conducted so far regarding (i) the strength of materials around a crack tip, (ii) techniques employed to model crack initiation and propagation, and (iii) criteria to determine crack opening. A brief review of some classical approaches to predict strength of a crack will be given first. With regard to techniques used in crack modelling, the current chapter will present works using continuous damage mechanics, models of fatigue crack initiation, and cohesive zone technique. Other modelling methods found in the literature are summarized in Section 1.5. Results of deformation around a crack tip in single crystals will be examined in more details because they will be used to verify the modelling results that will be presented in later chapters. Section 1.6 reviews simulations of the deformation of fcc polycrystalline aggregates under tensile loading. A review of works developing crack opening criteria, e.g. surface energy and fracture interface energy, is presented in Section 1.7. At the end of the chapter, the scope of the current study and structure of the thesis will be presented.

1.1 Classical theory of fracture mechanics

1.1.1 Energy-balance approach

Griffith's formulation of an energy criterion that determined the conditions under which an existing crack becomes unstable and propagates has become one of the most well known developments in the field of materials science. Based on the assumption that the material was linear (elastic), Griffith [3] could determine the energy released from a small region around a crack tip when the crack had grown into the material a particular distance. The total energy involved in the process of crack opening was the sum of the positive broken bond energy and the negative strain energy released from the material. When crack grew beyond a critical crack length, the catastrophic fracture occurred. [3]

Griffith's original work applied only to brittle materials. For ductile materials, Irwin [4] and Orowan [5] independently developed models which suggested that a considerable amount of the released strain energy was transferred into plastic flow in the region around the crack tip, and only a small amount was observed to create new surfaces. It was also stated that the catastrophic crack happens only if the energy strain rate reached a critical value that overcame the energy dissipated into plastic deformation around the crack tip and the energy creating new surfaces.

These energy-based formulations of crack opening have formed the basic framework to develop crack criteria in numerous theoretical analyses as well as numerical simulations, e.g. the cohesive zone technique [6-22], and the models of fatigue crack initiation by Mura and co-workers. [23-35]

1.1.2 Stress intensity approach

An alternative approach to the energy-based formulations is directly examining the stress states around a sharp crack tip. There are three types of fracture mode designating the separation of materials geometrically. Sketches of the modes are shown in Figure 1.1. Mode I denotes a symmetrical opening of the two parts of a body where the crack plane is perpendicular to the displacement direction (Figure

1.1a). Mode II and mode III denote anti-symmetrical deformation of the two parts of the sample where the displacement directions are in-plane with the crack plane (Figures 1.1b and 1.1c).

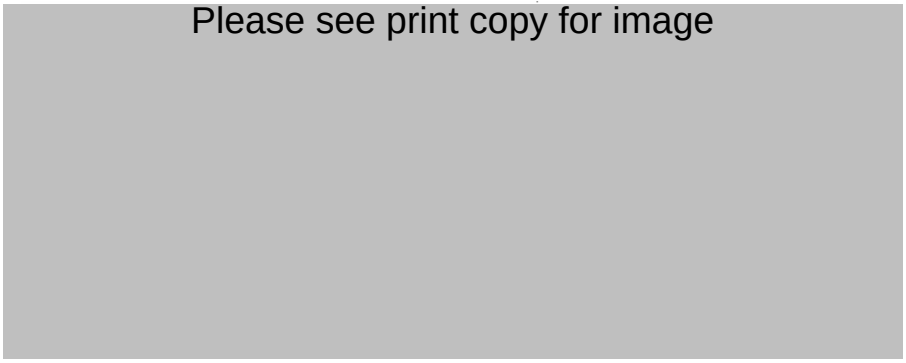

Figure 1.1 Three modes of cracking. [2]

The stresses in a small region around a crack tip undergoing a particular fracture mode could be expressed in terms of a stress intensity factor and the coordinates of the point being considered. Each fracture mode has a corresponding stress intensity factor, which is a function of the applied stress and the crack length. The stress intensity factors can be used to measure the strength of an existing crack by stating that the sample can withstand stresses around the crack tip up to a critical value of stress intensity. Beyond this critical value, crack propagates rapidly. [1]

1.1.3 Continuous damage mechanics

The model of creep rupture developed by Kachanov [36] was the first to introduce the concept of effective stress acting on an effectively resisting area. In a damaged body, the effectively resisting area represented the part of an original section area that remained after voids and cavities were formed. Since then, a series of work based on this effective stress concept has been conducted to develop the continuous damage mechanics, particularly those done by Lemaitre and co-workers [37-39] and those by Chow and co-workers [40-45]. Both groups defined a damage variable D^{damage} ($0 \leq D^{damage} \leq 1$) which characterized the deterioration of the strength of the material during fracture. At $D^{damage} = 0$, the material was undamaged, while $D^{damage} = 1$ indicated the complete fracture of the body into two parts. The major difference between the two groups was the hypothesis used to derive constitutive equations.

Lemaitre and co-workers assumed that the strain behaviour of the damaged material was only characterized through the effective stress (based on the hypothesis of strain equivalence). Meanwhile, Chow and co-workers assumed that the elastic energies of the damaged and undamaged material were equal when the stress tensor in the damaged material was replaced by the effective stress tensor (based on the hypothesis of elastic energy equivalence).

Jiang and Sehitoglu [46] proposed a fatigue damage parameter that incorporated the effects of local mixed mode loading at a point. By applying this parameter to the predictive life of the materials, under pure rolling conditions, particularly Hadfield steel and Bainitic alloy, a new combined rachetting-multiaxial fatigue damage model was also developed. In a later study, Jiang and Feng [47] transferred the fatigue damage parameter into FEM simulations to investigate crack initiation and rate of crack growth under mode I fatigue loading. The effects of material microstructures, e.g. lattice orientation, were not accounted for.

Later, Feng et al. [48] combined continuous damage mechanics with the theory of crystal plasticity to consider the anisotropic nature of crystalline materials and damage. The combined model was transferred into a user subroutine in Abaqus FEM software and an analysis was carried out to investigate how lattice orientations and hardening rates in slip systems would affect creep and damage development. However, a crack opening criteria was not proposed in this work and crack dynamics was not investigated.

More recently, Xue [49] developed a damage plasticity model of ductile fracture, also based on the theory of continuous damage mechanics, in which the nonlinearities of damage was accounted for by applying a power function to dictate the evolution of damage variable. Material anisotropy, in terms of crystalline structure dependent behaviours, was not accounted for. The model was implemented into LS-DYNA in which simulations were carried out to emphasize the model's ability to predict the crack path. The criterion of material fracture at a calculated point was assumed when the accumulated damage variable reaches unity.

However, our experience from finite element simulations of fracture dynamics, which combined the model of continuous damage mechanics and the theory of crystal plasticity, revealed that such fracture criterion ($D^{damage} = 1$) may result in bad convergence. The decrease in material stiffness from the evolution of damage variable causes numerical problems, which become more severe when damage variable approaches unity. We presume that it is because of such bad convergence that not many papers can be found that include both continuous damage mechanics and the theory of crystal plasticity when modelling dynamic fracture.

1.2 Cohesive zone technique

A modelling technique that handles effectly crack opening and has been widely used in FEM simulations is the cohesive zone technique, even though it also does not account for the effects of crystal orientations around crack tip. The technique was originally developed to model problems in which strength of an interface, which is approximated by a cohesive zone, is of interest, e.g. the behaviours of adhesive joints, and interfaces in composites.

Needleman [6] developed a cohesive zone interface model which unified the description of void nucleation from the initial debonding to the complete decohesion and subsequent void growth. Since then, alongside other techniques or theory, e.g. crystal plasticity [7-9], representative volume element (RVE) [10], and discrete dislocation model [11-13], numerous numerical works have taken advantages of cohesive techniques in their models to simulate crack opening or crack tip behaviour.

By setting up a cohesive zone in crack-tip front region, Tang et al. [7] modelled the propagation of the crack tip in $(010)[10\bar{1}]$ orientation in an fcc single crystal under plane strain tensile loading. This was a step forward compared to previous studies by Rice [50], Saeedvafa and Rice [51], Shield et al. [52-54], Cuitino et al. [55-56] in which crack tip was assumed to be either static or quasi-static. This work was also claimed to be the first to include essential nonlinearities such as distortion gradients, crystalline orientations, and finite deformation when studying fractures in ductile single crystals. Tang et al. [7] specified a traction-separation constitutive law for any

cohesive elements used, in which normal stress ahead of the crack tip t_n for mode I crack was related to crack tip opening δ by the exponential universal binding law specified by Rose et al. [14-15]. A schematic representation of the traction-separation relation is shown in Figure 1.2. Although various traction-separation relations, or cohesive laws, have been developed to satisfy various modelling purposes, their shapes are generally similar to that shown in Figure 1.2b. Γ_0 is the work of separation. σ_{max} and δ_n are the peak separation stress and corresponding crack opening, respectively.

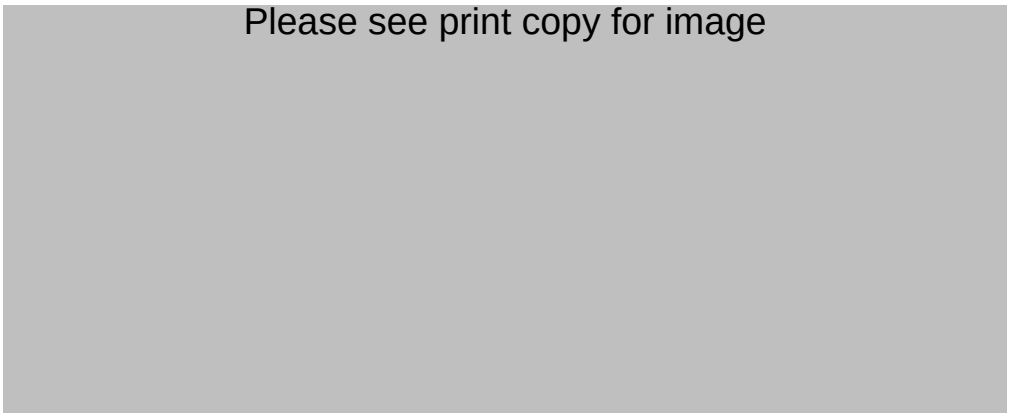

Figure 1.2 Sketch of the traction-separation law used by Tang et al. [7]

Grujicic and co-workers [16-19] modelled cracking along the grain boundaries of polycrystalline lamellar $\gamma+\alpha_2$ titanium aluminide, as well as cracking along the interfaces of the titanium aluminide matrix and bcc β-phase precipitates. Traction-separation relationships were developed for the particular grain boundaries and matrix-precipitate interface as a function of grain misorientation and orientation of the boundary-interface. These decohesion potential functions were then implemented into the user element subroutine UEL of the Abaqus FEM software so that the stiffness matrix of the boundary-interfacial elements could be derived.

In a study where discrete dislocation was used to model the interface fracture of a bi-material sample under mixed mode loading, O'Day and Curtin [12] briefly discussed the effects of the XN cohesive law (developed by Xu and Needleman [20]) and TH cohesive law (developed by Tvergaard and Hutchinson [21]), upon the modelling results of fracture under mixed mode loading. They stated that the XN cohesive law, which is compatible with mixed-mode loading and allows the normal and shear work

of separation to be varied independently, may result in instabilities under moderately to highly mixed mode loading. These instabilities could manifest themselves in the form of brittle crack growth at very small loads, usually before the materials begin to harden. Because the TH cohesive law seemed to avoid such issues, it was the preferred choice of O'Day and Curtin for their simulations.

Zavattieri and Espinosa [22] investigated the accuracy of cohesive models in capturing the dynamic microcrack growth of ceramic observed in experiments of plate impact recovery. A cohesive law was implemented into a 2D micro-mechanical stochastic finite element analysis to characterize microcrack initiation, propagation and coalescence, as well as microcrack interaction and branching. Experimental data such as the history of normal plate impact velocity was used to determine the parameters and conditions under which the models agreed with experiments. The authors concluded that simulated microcrack patterns and velocity histories match experimental observations only when the true geometry of the grain boundary and a particular set of cohesive model parameters was used.

In an FEM analysis, special cohesive elements must be used in regions where the cohesive constitutive law is applied. Because the cohesive constitutive law is different to the constitutive law applied to the bulk material, obviously one cannot mesh the whole simulated region with such special elements so that completely explicit crack growth can be captured. This limits the application of cohesive models to simulating crack opening and propagation in brittle materials where crack is assumed to occur only in grain boundaries or in small regions around the crack tip. Zavattieri and Espinosa [22] assumed the crack initiation and subsequent growth were along the grain boundaries. This could partly explain their conclusions that true grain boundary morphology used in the model is crucial to achieve reasonable agreement between simulated and tested microcrack patterns.

Zavattieri and Espinosa also pointed out another limitation of cohesive models. They are scale-dependent. Simulations taking place at different scales require different sets of cohesive interface parameters and different cohesive models.

1.3 Orientation-dependent behaviours of crack tip fields in single crystals

The works that have been reviewed so far, either theoretical analyses or numerical modelling, neglected the effects of crystal orientation, particularly in the region around a notch tip. This points to the need to investigate and develop models characterizing fracture behaviours that incorporate the influences of lattice orientations of the sample.

The fracture of polycrystalline materials involves firstly the initiation and propagation of microcracks, which dictate any subsequent growth of cracks either in a trans-granular or inter-granular manner. These microcracks mostly occur within a single grain. [57] Therefore an accurate understanding of fractures, particularly plastic deformation around the tip of the crack, in single crystals is mandatory.

This area of study has attracted considerable amount of analytical, experimental, and numerical work. Rice [50] developed an analytical model of crack tip stress and deformation fields in perfectly plastic single crystals under tensile load. An asymptotic analysis was carried out for stationary and quasi-static growing cracks, assuming negligible lattice rotation. Two cases, [101] crack tip on (010) crack plane and [010] crack tip on (101) crack plane, were considered for both fcc and bcc crystals.

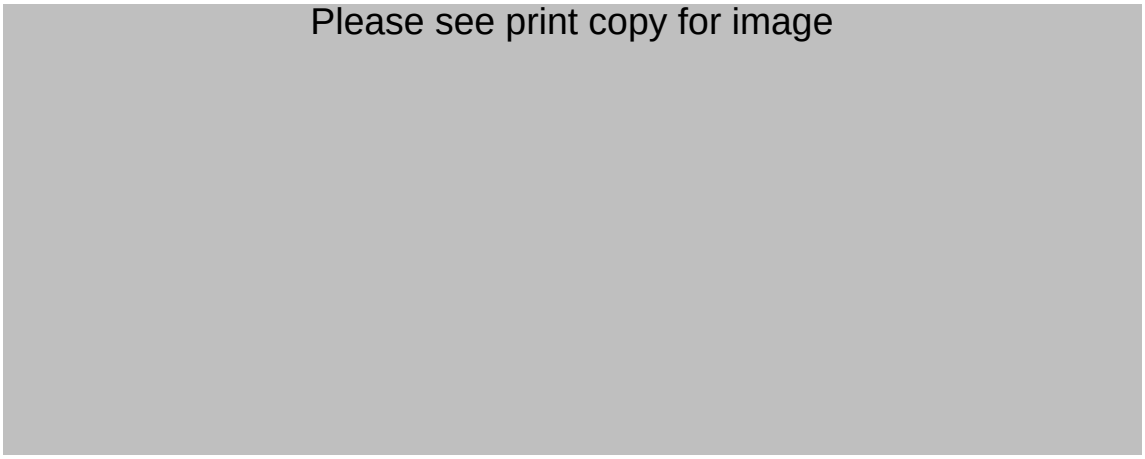

Figure 1.3 Rice's solutions for crack tip in (010)[101] orientation in an fcc single crystal. [50]

Consider the case of a stationary crack in an fcc crystal where the crack tip is in $(010)[101]$ orientation, as shown in Figure 1.3. Assuming a plane strain deformation, which is approximately the case on the mid-thickness plane of the sample, a large plastic strain at the crack tip can only occur in three combinations of slip systems. The first comprises equal slips in $(1\bar{1}1)[110]$ and $(1\bar{1}1)[011]$ directions, which results in a total effective slip in $[121]$. The second and third combinations are of slip systems $(11\bar{1})[101]$ and $(\bar{1}11)[101]$ resulting in a total slip in [101] direction, and of slip systems $(111)[1\bar{1}0]$ and $(111)[0\bar{1}1]$ resulting in a total slip in $[1\bar{2}1]$ direction. The intersections of these three combined slip systems with the sample surface, i.e. plane $(\bar{1}01)$, results in three slip traces inclined at 54.7^o, 0^o, and 125.3^o with notch tip orientation, respectively, as shown in Figure 1.3a. Let ($\mathbf{S}^{(1)}$, $\mathbf{N}^{(1)}$), ($\mathbf{S}^{(2)}$, $\mathbf{N}^{(2)}$), and ($\mathbf{S}^{(3)}$, $\mathbf{N}^{(3)}$), respectively denote the direction and normal vectors of the three slip traces obtained from Rice's solutions. According to Rice's analytical model, these vectors define boundaries of four angular sectors around crack tip in the half plane bounded by the line of the notch tip direction (Figure 1.3b). Stress states are constants in these sectors and change discontinuously from one sector to another. Even though the displacement (strain) fields were not uniquely determined, Rice's solutions revealed that rays inclining 54.74^o and 125.26^o with crack tip direction are bands of displacement discontinuities formed by slip on octahedral slip planes. Because the ray inclined at 90^o with notch tip is perpendicular to slip trace [101], it is the band of displacement discontinuity formed by concentrated kinks on the octahedral slip plane. In the theory of dislocation, a kink is defined as a displacement step of a dislocation on the same slip plane. A kink is hence perpendicular to a slip system.

Saeedvafa and Rice [51] extended Rice's model by allowing the crystal to undergo Taylor hardening with a power law relationship between stress and strain where the strain was large enough. The extended model resulted in fourteen angular sectors of constant-stress in the near-tip region, compared to seven constant-stress sectors by Rice's model [50] where there was no hardening.

Mohan et al. [58] reported that their work extended Rice's analysis of crack tip deformation and stress fields in a single crystal under mode I loading. This analysis accounted for three dimensional effects, and finite deformation and finite lattice rotations which had been assumed negligible in Rice's solutions. These new results partially agreed with the previous analytical and numerical results, and matched with experimental observations quite well, particularly those reported by Shield and Kim [52]. From their analysis, Mohan et al. agreed with Shield and Kim [52] that deformation, lattice rotations, and lattice hardening strongly influence the structure of crack tip fields.

Later, Drugan [57], while agreeing that the asymptotic solutions from Rice's analysis [50] could predict important features of stationary and quasi-static crack tips fields, also argued that they still had significant deviations from the experimental observations and simulations. Drugan especially pointed out that the reported experimental observations, and the results from the discrete dislocation simulations, for the symmetric crack tip orientations did not reveal concentrations of kink-type shear predicted in Rice's solutions. Drugan then reconsidered the analysis of crack tip fields for crack tip in $(010)[101]$ and $(101)[010]$ orientations, in both fcc and bcc crystals, i.e. similar to cases studied by Rice, and seeked for solutions for crack tip fields that were free of kink-type displacement discontinuities. The resulting solutions differed from Rice's at some points. The major difference was that for the same crack tip orientations in fcc and bcc crystals, Rice's analysis ended up with the same structure of angular constant-stress fields around the crack tip, while Drugan's results revealed that these angular constant-stress fields are different for fcc and bcc crystals. Moreover, in an fcc crystal, Rice's solutions of crack tip fields for two different crack tip orientations were the same but were different in Drugan's solutions.

A sketch of Drugan's new asymptotic solutions for fcc crystals are shown in Figure 1.4. Even though Drugan's solutions for crack tip fields no longer contain the concentrated shear of kinking mode seen in Rice's solutions, i.e. the 90^o discontinuity line in Figure 1.3b, both solutions agree with each other at one point. They both have rays of displacement discontinuity at 54.7^o and 125.3^o with notch tip, which are traces of activated slips on crystal slip planes.

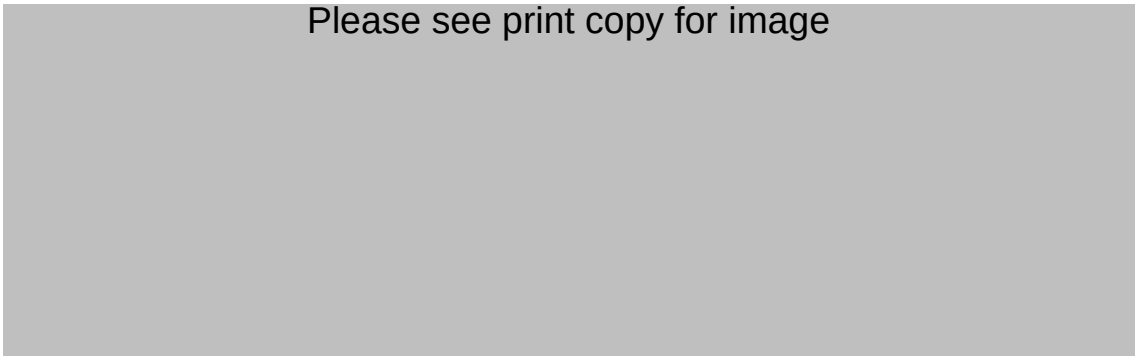

Figure 1.4 Drugan's solutions for a stationary crack tip in $(010)[101]$ orientation in an fcc single crystal. [57]

Figure 1.5 Solutions for crack tip in $(001)[100]$ orientation in fcc single crystal by Flouriot et al. [59]

Also following on the analytical framework set out by Rice [50], Flouriot et al. [59] developed an asymptotic solution for the deformation field around the crack tip in fcc crystal with the crack tip in $(001)[100]$ orientation. A basic form of the solutions had four independent constant-stress angular sectors around the crack tip. A sketch of these sector boundaries taken from [59] is shown in Figure 1.5.

The analytical results, particularly the asymptotic solutions by Rice [50], have attracted a considerable amount of numerical and experimental work. The objectives have been either to capture the basic features of the crack tip fields predicted in the analytical solutions or to investigate the effects of various hardening laws and sample thickness, and then evaluate the validity range of the plane-strain and plane-stress solutions.

Rice et al. [60] summarised the analytical asymptotic results and then compared them with those from the numerical finite element simulations. By observing the distribution of the sum of the cumulative slip on all slip systems, it was concluded that finite element simulations predicted the important features of asymptotic solutions quite well, i.e. the existence and orientations of concentrated slip around the crack tip.

Narasimhan et al. [61] reported on a numerical investigation using FEM simulations of the three dimensional effects in regions around a crack tip of a single crystal

during three-point bending. In particular, the authors assessed the extent to which plane-strain and plane-stress solutions could be applied in actual 3D crack tip fields. The material was 4340 carbon steel, which was assumed to be homogenous, isotropic and obey Huber-Von Mises yield criterion. The effects of crack tip orientation were not clearly specified. The results revealed that plane-strain analytical solutions dominate the region very close to the crack tip inside the specimen. When the distance from crack tip is longer than about half of the thickness of the sample, then plane-stress conditions prevail.

Subramanya et al. [62] also aimed at evaluating the validity range of plane-strain and plane-stress asymptotic solutions, but by using 3D and 2D finite element simulations of a ductile material under small strain mixed mode (mode I and mode II) loading. The 3D results of plastic zones and radial, angular and thickness dependence of stress fields around the crack tip were compared with the 2D simulations and analytical solutions to address the suitability of 2D (either plane stress or plane strain condition) approximations in other studies. Even though neither the effects of crack tip orientation nor the crystal structures (e.g. fcc or bcc) were clearly specified, the study concluded that at small loads and in a small region around the crack tip, the 2D results matched those from 3D simulations on the interior planes. On planes closer to the sample surface, the plastic zones were higher than the plane strain plastic zone.

Cuitino et al. [55] developed a model that fully described the hardening of crystals under monotonic loading. They did this by formulating a statistical mechanical model of dislocation motion through forest dislocations combined with equations of evolution of dislocation densities. Forest dislocations are defined as dislocations crossing a slip plane and intersecting with dislocation(s) on that plane. The predictive capabilities of the hardening model were demonstrated by finite element simulation of stationary crack tip fields in single crystal copper and then comparing the numerical results with experimental observations and the analytical results of Rice et al. [50-51]. These simulations yielded results that closely matched Rice's solutions in regions outside the plastic zone where strains and lattice rotations are small. The behaviour of the crystal could be approximated as perfectly plastic as assumed in Rice's solutions [50]. The crystal entered stage II hardening, which was characterized by strong interactions between slip systems and the dramatic increase

of hardening in slip systems, near the crack tip. Therefore isotropic hardening models such as those considered by Rice [50] and Saeedvafa and Rice [51] are no longer accurate, which resulted in considerable differences between the numerical and analytical solutions.

In a later study, Cuitino and Ortiz [56] simulated a single crystal undergoing four-point bending to investigate (i) the dependence of crack tip fields upon various hardening laws, (ii) the reciprocal relationship between the crack tip fields on a free surface and those on interior surfaces, and (iii) the degree of relevance of plane strain and three dimensional fields. It was concluded that the slip patterns on the sample surface differ significantly from those on interior planes. Thus the ability of certain experimental techniques, e.g. Moiré interferometry [52-54], to predict the true responses of materials under load, as well as the applicability of the plane-strain asymptotic solutions proposed by Rice and co-workers [50-51] were not viable.

Among the most extensive experiments studying crack tip fields were those conducted by Shield and co-workers [52-54]. Shield and Kim [52] reported on the experimental results of plastic deformation near the crack-tip in an iron -3% silicon (bcc) single crystal, with crack tip being in $[01\bar{1}]$ direction, and the crack plane being (011). The sample was extensively deformed by four-point bending and then unloaded. Measurements of the surface strain were then carried out by microscopic Moiré interferometry. The in-plane Almansi strain components obtained by digitally processing Moiré fringes revealed asymptotic fields well-structured into angular sectors approximately 350-500 μm from the notch tips, where plastic strains reached 9%. Three of these sectors had reasonably constant strain fields, while the fourth one had surface strains approximately inversely proportional to the distance from the notch tip. The borders of these sectors were narrow regions in which the strain changed drastically. The constant-strain sectors were analyzed and compared with analytical solutions found in the literature. It was concluded that there were two major deviations between the experimental and analytical results. Firstly, unloading regions existed near the crack tip in the constant-strain sectors where proportional loading in the analytical models was assumed. Secondly stress state ahead of the crack initiating plastic flow obtained from experiments differed from the theoretical

predictions. Shield and Kim commented that these differences were evidence that the extensive effects of lattice hardening and lattice rotations upon the crystal structure at large strains were not properly accounted for in the analytical models by Rice et al. [50-51].

Shield and co-workers [53-54] conducted further experimental observations of strain fields during four-point bending around the crack tip in single crystal copper (fcc) with crack tip orientation being $(101)[10\bar{1}]$, and in single crystals of copper and copper-beryllium with crack tip orientation being $(010)[\bar{1}01]$. These observations complemented the conclusions regarding the strain field around the crack tip previously made on iron -3% silicon (bcc) single crystal. Similar constant-strain angular sectors were also observed around the crack tips, the boundaries of which did not rotate during loading. However the angles between boundaries of the sector and the notch tip differed from those predicted in Rice's model [50]. Although Rice [50] pointed out that the sector boundaries comprised kink or slip type deformation, for the experimental crystallographic orientations, the boundary angles did not match the angles where kink and slip bands could occur.

Even so the strain observed at smaller loads agreed with the analytical results to some extent, which led to the conclusion that assumptions of negligible crystal rotation and perfect plastic crystal in Rice's models do not apply at higher loads. Shield also suggested that a comprehensive understanding of plastic deformation around the crack tip in single crystals meant that factors such as crystal structures, orientation of the crack tip, and types of loading should be accounted for.

It was later argued that the Moiré interferometry technique employed by Shield et al. could only provide a precise in-plane normal and shear strain on surfaces of the sample [63]. These results are neither in plane strain or plane stress conditions and therefore could not be compared with those from the analytical or numerical analyses where plane strain conditions were assumed. Kysar and Briant [63] reported that measurements of the in-plane rotation field accompanied the displacement field at a crack tip on the interface of a pure aluminum bi-crystal. EBSD technique was used to capture the lattice orientations around the crack tip on the centre line of a sectioned

specimen after deformation occurs. With the orientation of single crystals serving as a reference, a spatial mapping of in-plane lattice rotation around the crack tip in true plane strain conditions could be obtained. Because lattice rotation is associated with plastic deformation it was expected that the orientation of the crystal around the crack tip would also exhibit a discontinuity at the sector boundaries, similar to those in the analytical models. Kysar and Briant concluded that their experimental techniques helped observe a kink shear sector boundary which corresponds closely with those predicted by Rice's models.

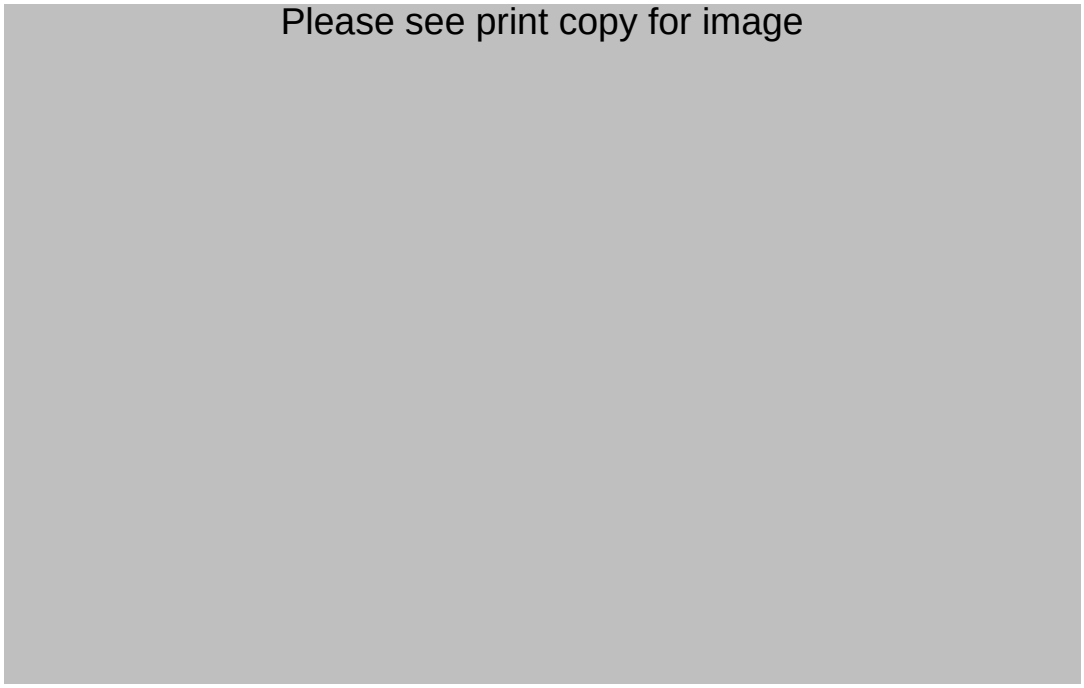

Figure 1.6 Simulation and experimental results for (110)[001] crack tip [64] (a) Equivalent plastic slip around crack tip on sample surface from FEM modelling, (b) experimental view of slip traces around crack tip and discontinuity lines according to Rice's analytical solutions.

Later, the EBSD results of the compact tension experiments on pre-cracked single crystal nickel-based fcc alloy conducted by Flouriot et al. [64] also revealed the existence of a kink band near the crack tip that inclined 90^{o} to the crack tip, as shown in Figure 1.6b. The same authors used crystal plasticity FEM (CPFEM) to simulate two cases of notch tip in (110)[001] and (001)[100] orientations. The lattice orientations near the crack tip were generally in good agreement with the EBSD results. The best match was the notch tip in (110)[001] orientation where the equivalent plastic slip field predicted from the FEM modelling was in bands that

inclined about 54^o and 90^o to the notch tip, as seen on the surface of the sample. The shape of the deformation zone and set of active slip systems also agreed with the experiments. Both the simulation and experimental results for this case are shown in Figure 1.6. The agreement between the simulated and experimental results for the $(001)[100]$ notch tip was not good, as shown in Figure 1.7. The vertical band and plastic zone behind the crack tip could not be seen on the tested sample but the slip traces emanating from the crack tip on surface of the sample inclined by $\pm 45^o$ to notch tip. The secondary set of slip traces also inclined by $\pm 90^o$ with the first set in the area in front of the notch tip. These observations well matched the discontinuity lines predicted from the analytical model derived earlier [59] for this case of notch tip, as shown in Figure 1.7b.

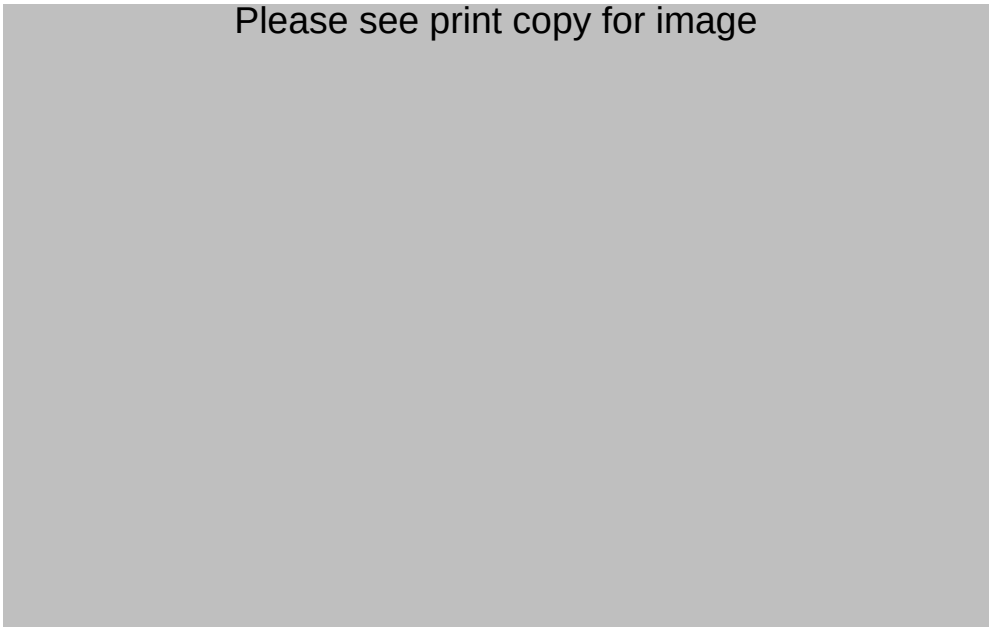

Figure 1.7 Simulation and experimental results for the $(001)[100]$ crack tip. [64] (a) Equivalent plastic slip around crack tip on sample surface from FEM modelling, (b) experimental view of slip traces around crack tip and discontinuity lines according to Flouriot's analytical solutions.

Patil et al. [65] conducted a combined experimental and computational study of crack tip fields on single crystal aluminum under small constraint mode I loading. The crack tip was effectively replaced by a narrow notch oriented to $(010)[101]$ on a tensile specimen, for both experimental and simulation purposes. Scanning electron micrographs of the proximity of the crack tip at various loading stages are shown in

Figure 1.8. Slip traces appeared around the crack tip on the surface of the sample at a very early stage of loading (0.1 mm extension or 0.5% nominal strain), and inclined by ± 55^{o} to the notch tip. As the load increased the slip traces increased in number and the degree of severity. With reference to Rice's asymptotic solutions [50], these slip traces were denoted by ($\mathbf{S}^{(1)}$, $\mathbf{N}^{(1)}$) in Figure 1.3. Interestingly, at an extension of 0.2 mm or a nominal strain of 1%, although not explicitly described in the text, there were slip traces oriented at 0^{o} with the notch tip, which with respect to Rice's solutions were denoted by ($\mathbf{S}^{(2)}$, $\mathbf{N}^{(2)}$) in Figure 1.3.

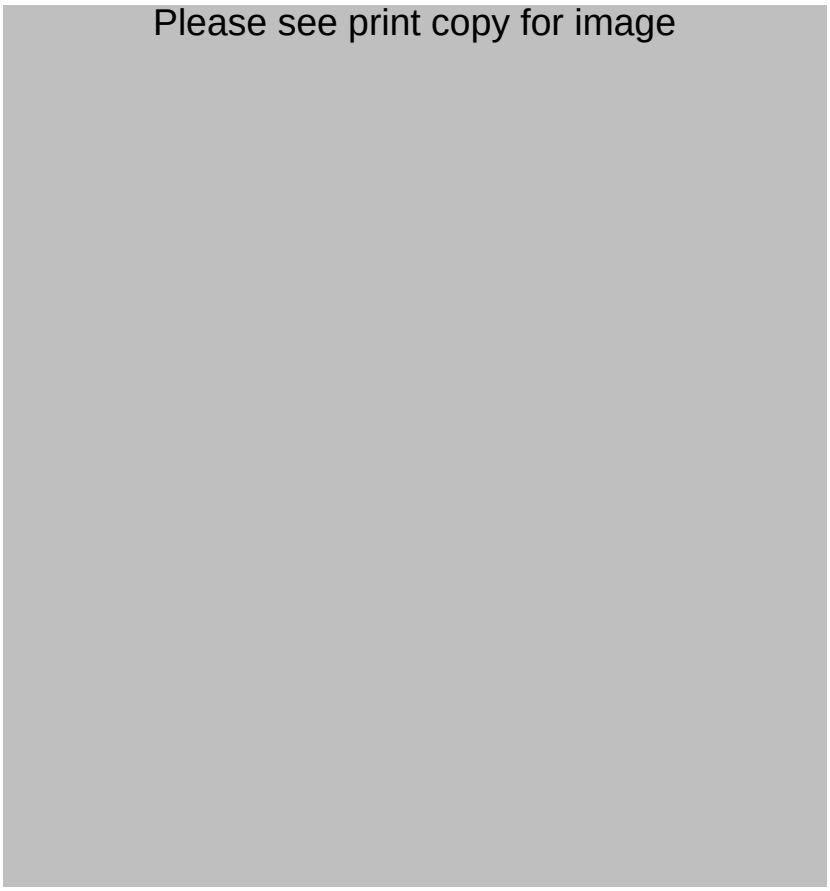

Figure 1.8 SEM results of the sample surface around the $(010)[10\bar{1}]$ crack tip at various extensions (a) 0 mm, (b) 0.1 mm, (c) 0.15 mm, (d) 0.2 mm [65].

One can already see traces around the notch tip for 0 mm extension, which were not not explain nor mention by Patil et al. [65] in their paper. My interpretations of their existence are as follows

- The mechanical preparation of the notch might cause crystals around the notch tip deform as if it was done by a tensile load; or

- More likely, the sample was slightly stretched when it was clamped to the tensile module inside the SEM chamber.

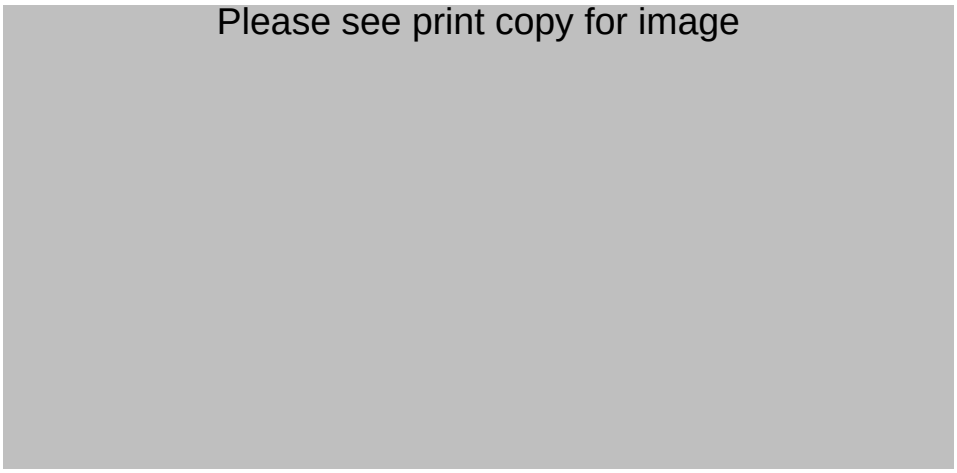

Figure 1.9 (a) Inverse pole figure obtained from EBSD for sample surface around the $(010)[101]$ crack tip and (b) the color code used [65].

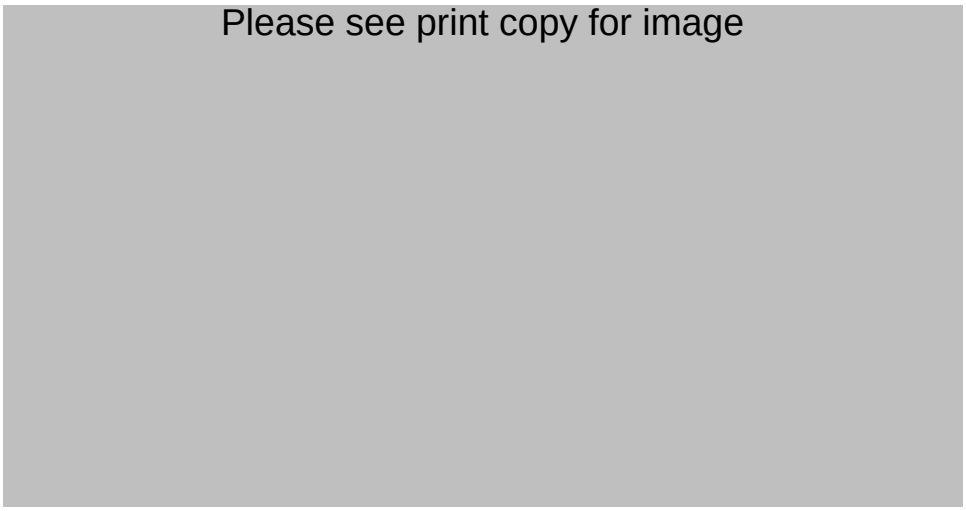

Figure 1.10 (a) Simulation results of plastic slip around the $(010)[101]$ crack tip superposed on the experimental scanning electron micrograph, (b) Contour of misorientation angle. [65]

A map of the inverse pole figure obtained from the EBSD for surface sample around the crack tip is shown in Figure 1.9a. The crystal orientation at one point is denoted by colour. The colour code used in the inverse pole figure in Figure 1.9a is shown in Figure 1.9b. The homogeneity of crystal around the crack tip represented by the colour green is divided into two misorientation bands which began from the crack tip. One band inclines 45^{o} with the notch tip direction, and the other $90^{o.}$. Patil et al.

[65] argued that these misorientation bands proved the existence of concentrated kink type shear similar to those predicted in Rice's solutions.

Simulated tensile tests were carried out by crystal plasticity theory transferred into the finite element analysis software Abaqus. Hardening of the slip systems was assumed to be isotropic. The results from the simulation work were then compared with the experimental observations at an extension of 2 mm (1% nominal strain), as shown in Figure 1.10. As with many other simulations of crack tip fields, the slip traces represented the sum of the slip accumulated on all the slip systems (Figure 1.10a). The simulation results of plastic slip were superposed on the experimental scanning electron micrograph so that the deformed notch profile from the simulation matched that from the experiments. The distributed misorientation (Figure 1.10b) was determined with respect to the initial orientation of the crystal.

1.4 Models of fatigue crack initiation

The model of fatigue crack initiation based on dislocation pile-ups, which was first proposed by Tanaka and Mura [23], has been among the most widely used theoretical models that incorporate the effects of the microstructure of crystals. Indeed, works by Smith [66] and Lin and Ito [67] were among the first to formulate the formation of cleavage crack as a result of dislocation pile-up. The analytical model by Lin and Ito [67] described the build-up of large local plastic strains under cyclic loading within a favourably oriented crystal located close to the surface of the sample. The model presumed that a slip band created in fatigue testing comprised of two thin slip slices close together having an initial shear stress of opposite signs that had previously been resolved. These thin slices slide in opposite directions, one in forward loading and the other during reverse loading. The results from this model showed that the local plastic shear strains in each slice increased dramatically after a few hundred tension-compression cycles which created intrusions and extrusions on the surface which started the nucleation of a fatigue crack.

Tanaka and Mura [23] later argued that the initial shear stress resolved within each slice was not always realistic but used the idea of slip bands comprising two opposite

slices sliding to develop a dislocation model for fatigue crack initiation. A grain located close to the surface was considered. The two thin slices that comprised a slip band in Lin and Ito's model were then replaced by two adjacent layers of dislocation. Under fatigue loading, these layers accommodate equal, opposite, and irreversible motions of dislocation. The surface of the sample acted like an obstacle blocking the dislocation lines from moving, i.e. an accumulative dislocation dipoles result. These accumulative dislocation dipoles increase the internal tensile stress, making the slip bands energetically unstable. At a critical point stress is released in the form of a microcrack within the slip bands. This critical point was determined by comparing the magnitude of total strain energy within a slip band with the critical specific fracture energy.

After this initial work, Mura and co-workers further developed a model to account for the effect of inclusions upon the reduction in fatigue strength [24], to produce a stress versus number of cycles (S-N) curve under various loading conditions [25-26], to investigate the early stage of fatigue microcrack propagation [27], and to investigate the effects of the environment and thin film coatings on materials [28]. Tanaka-Mura's model of fatigue crack initiation has been implemented into simulations by various research groups [29-32]. Bruckner-Foit and co-workers [29-30] implement the model into RVE simulations to predict the number of cracks initiated transgranularly. Tryon and Cruse [31-32] developed probability-based models to study statistical distribution in fatigue crack nucleation life.

The same approach to modelling fatigue crack was also used by other researchers [33-35], even though Mura's formulation was not used. For example, Andersson [33] investigated the influence of metal grain sizes upon fatigue lives. The short crack growth model by Navarro-de los Rios was modified and used to calculate the distribution of fatigue cracks during loading. This approach is similar to that used by Bruckner-Foit and co-workers [29-30], who assumed that if slips initiated at a point in a grain then the whole grain slipped. Once started, the crack would spread across the whole grain and would only be blocked by the boundaries. Depres et al. [35] conducted high cycle fatigue test and modelling on single crystal 316L austenitic stainless steels (fcc) using 3D discrete dislocation simulation. Their studies of elastic energies stored in the crystal revealed that a crack may nucleate somewhere close to

the boundary of a grain but then move quickly towards the free surface, i.e. the crack eventually begins at the intrusion after a critical number of cycles. Depres et al also concluded that plastic shear alone could produce fatigue cracks that began at the free surface, similar to those made from a slip-based model of initiation of fatigue cracks by Tanaka and Mura. [23]

The common point of these modelling works was that they assumed that cracks originated along slip bands in a trans-granular manner, but their exact location within a grain was not predicted. It would also be difficult to specify the value of crack energy when using the Tanaka-Mura model, i.e. the energy required to create a new surface, because it must be compared with the total elastic strain energy to determine crack initiation, which is generally not readily available. They not only vary with materials but are also dependent upon the crystalline structures of the material being considered. A review of work determining this factor is presented in Section 1.7.

Another difficulty is the assumption that cracks begin as a result of stress released within a persistent slip band made up of two slips moving in opposite directions. Hence, the basic principle of crack initiation of the model cannot be applied to predict damage of the materials under other types of loading which do not yield persistent slip bands.

1.5 Other methods modelling crack initiation and crack growth

Molecular dynamics (MD) [68-72] has been widely used to simulate crack growth. This approach requires no criteria for crack opening because it occurs “naturally” when two or amore atoms are separated beyond their interactive range. The disadvantages of this method are a limited modelling scale in terms of time and size. MD simulations of a real tensile test would be extremely expensive computationally. Another drawback is that the crack tip morphology could be ambiguous at the early stages of crack growth because the boundaries of the newly created surface formed by most outer atoms are not uniquely determined. Also, the results are sensitive to the applied potential.

An increasing number of research works [73-77] focused on multi-scale FEM combined with MD or molecular statics (MS) simulations, to model dynamic crack growth. By means of MD/MS simulations, this approach accounts for the effects of crystalline orientation and provides a sound physical base of crack tip opening when modelling macro-scale problems, i.e. eliminating the size-scale issues mentioned above in MD simulations. A highly flexible mesh with the ability to avoid re-meshing at moderate loadings is also possible if meshless FEM is used. However, disadvantages, which mainly come from the MD/MS side of this approach, do exist, i.e. long computational time.

Other common approaches to the problem of crack growth are cell models which have been widely used to model porous solids, fatigue crack with micro-defects, and rupture of multi-phase solid [78-80], or by using the extended FEM [81-83]. Even though these approaches could well handle the dynamics of crack growth and crack initiation in terms of void nucleation [78-80] to some extent, they have been restricted to isotropic or layered materials. The influence of the crystalline structures of the sample have not been accounted for.

Watanabe and Yamamoto [84] introduced two types of fracture modes of microcracking, cleavage and shearing applied to FEM modelling. The basic idea was to apply a crack opening criterion to a node, which, if it satisfied such criterion, would be split into two nodes. The criterion was stress-based, i.e. a critical stress was presumed and assigned as a material property. This approach was similar to the cohesive zone model even though the technique used to split a node into two was not clearly specified.

Another technique for modelling crack growth that could be found in the literature was element removal applied in FEM modelling, although only a handful of works have been reported [85-87]. This approach simulates dynamic crack growth without remeshing or pre-specifying some special elements that could be removed. Similar to many other techniques, crack opening criteria are required to determine which are elements to be removed from the original mesh. Other works in the literature that use the element removal technique with timber as the material and assumed to be isotropic.

1.6 Tensile deformation of fcc polycrystalline aggregates

Various studies have used the crystal plasticity theory combined with finite element method to carry out simulations investigating the deformation of polycrystalline sample under tensile loading [88-92]. Some of these studies will be reviewed below. Very often, the polycrystalline aggregate is approximated by a Voronoi diagram, which is a set of convex polygons. The polygons can be in 2D or 3D space. Each of these polygons represents a grain.

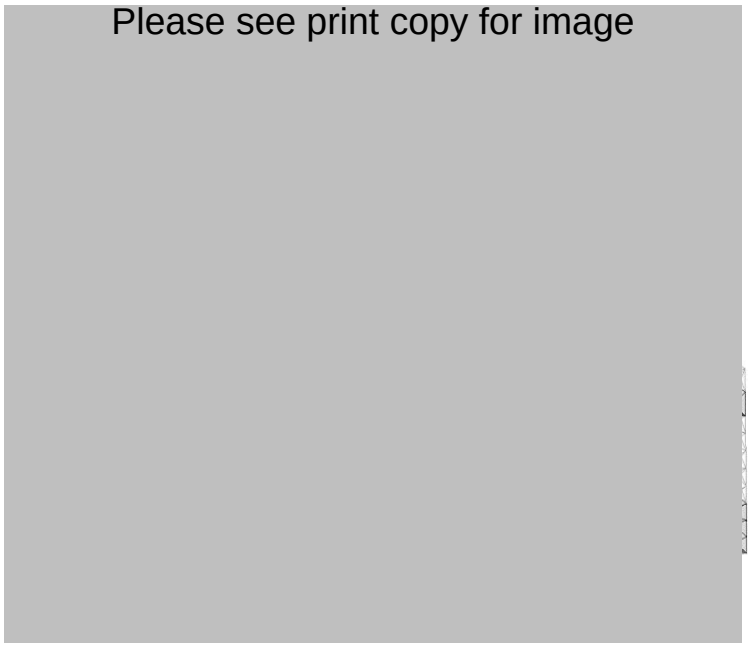

Figure 1.11 (a) Quasi three-dimensional Voronoi diagram and
(b) Full three dimensional Voronoi diagram [88].

You et al. [88] performed 3D simulations of the tensile deformation of a thin 316LVM stainless steel specimen. Quasi three-dimensional and full three dimensional Voronoi diagrams were used to approximate the fcc polycrystalline specimen. Sketches of these two Voronoi digrams are shown in Figure 1.11. The study concluded that both types of Voronoi diagram could predict very well the global stress-strain curve obtained from experiments, although the full 3D Voronoi diagram was slightly better. Simulations using both diagrams also produced the distribution of strain on the sample surface and the evolution of active slip systems at

the grain level that qualitatively agreed with those observed in experiments. You et al. [88] reported that their models failed to predict the reorientation of crystals during deformation. They concluded that the deficiencies were due to the Asaro's hardening law used in their models, and that a more accurate description of the material strain hardening would improve the accuracy of their models.

Fulop et al. [89] studied the effects of initial grain orientations and sample thickness on the deformation of a pure aluminum polycrystalline aggregate. In order to avoid the complexity and time consuming in constructing a full 3D Voronoi diagram, Fulop et al. assumed that the geometry grain boundaries were unchanged along the sample thickness. A 2D Voronoi structure was constructed and extruded along the sample thickness. The effects of grains along the thickness of the sample were obtained by assigning different orientations to Voronoi cells within each layer along the thickness. From simulation results, Fulop et al. [89] concluded that the sample thickness affected the sample deformation in a couple of ways. Particularly, the thinner is the sample, i.e. the smaller number of grain along the sample thickness, the smaller are the initial yield limit and the hardening. They also observed that thinner samples appeared to be more affected by the inhomogeneity of the initial grain orientation. No conclusions were made regarding the lattice revolution in each grain. It is noted that Fulop et al. used a strain hardening law similar to Asaro's formulation, i.e. it does not account for interactions between slip systems in the formulation of self hardening.

Wei and Anand [90] developed a model based on the theory of crystal plasticity to account for the effects of grain boundary in an fcc nano-crystalline aggregate. Similar to Fulop et al. [89], Wei and Anand approximated the polycrystalline structure by a quasi three-dimensional Voronoi diagram. Using this Voronoi diagram and their newly developed constitutive law of grain boundary, Wei and Anand investigated effects of grain size on the tensile deformation of the aggregate, and demonstrated the capability of the new model to capture fracture along grain boundaries. Their simulations showed that the ultimate tensile stress of the aggregate increased with grain size, and then rapidly decreased after the grain size reached a threshold value.

Nakamichi et al. [91] developed a new hardening-softening law to characterize interactions of slip systems in an fcc crystal structure. The law was applied into modelling the deformation of fcc single crystals and polycrystalline aggregates. The single crystal had various initial orientations. The polycrystalline aggregate was approximated by a 2D Voronoi diagram, with various grain sizes. It was concluded from the numerical results that in single crystal, the initial orientation affects very much the initial yield stress, slip band formation and the localized necking. Results for polycrystalline aggregate showed that the larger the grain size (the smaller the number of grain), the higher the localized strain at a specific crystal and the less clearly the localized necking can be observed.

Haldrup et al. [92] conducted simulations of tensile test on a full 3D Voronoi diagram of fcc polycrystalline aggregate. Two cases of boundary conditions, namely free and cyclic boundary conditions, were applied on a cubic polycrystalline sample. In both sets of boundary conditions, one surface was pinned and the opposite surface was stretched out (in the normal direction of the surfaces). For free boundary conditions, nodes on the other surfaces were set to deform freely. For cyclic boundary conditions, on each pair of surface in the other two directions, the displacements of nodes on one surface were equal to those on the opposite surface. Haldrup et al. concluded that cyclic boundary conditions made the sample slightly stiffer than free boundary conditions. Also, grain size did not affect the difference between slip activities on the sample surface and on an interior plane. It appeared that the difference depended only on the distance from the free surface.

1.7 Surface energy and interface fracture energy

Throughout the above discussions fracture energy plays a key role in most studies of fracture, either analytical or simulated. Apart from those that include MD or MS in their models, and those that use damage variables, fracture energy has been given in many studies as a constant material property. This could be erroneous because this parameter depends not only on material types but also on the crystalline structures, e.g. lattice orientation.

Numerous works determining fracture energy experimentally and numerically have been reported. Gilman [93] described the direct measurements of the surface energy of crystals and reported the results of various substances. A reasonably comprehensive summary of the experimental results of surface energy for a wide range of metals was later reported by Kumikov et al. [94]. The considerable uncertainty that accompanied these results makes them acceptable only for general approximations, and inappropriate for an accurate simulation of crack initiation. More precise results of fracture energy could be obtained by analytical atom-based models or molecular dynamic simulations, if an appropriate potential function is used.

Howe [95] described the calculation of surface energy using the nearest-neighbor broken bond model where atoms were considered as hard spheres. The surface energy appears when an atom in a particular plane or surface loses one or some of its neighboring atoms and hence has higher energy than other atoms in the bulk material. The surface energy is then equal to the energy gained from the broken atomic bonds. In other words, if fracture energy is defined as the energy required to break atomic bonds along a plane, it is identical to the surface energy of that plane. Obviously, the surface energy depends on the orientation of the plane being considered and the potential function being used to describe the interaction between atoms. Various potential functions have been reported. Among the most commonly used are the Lennard-Jones potential [95], the Morse potential [96], and the embedded atom method (EAM) potential [97] and its variations [98-102].

The nearest-neighbor broken model has been used by numerous research groups to determine the surface energy of various materials in various planes, and with various potential functions [103-110]. It should be noted however that the concept of surface energy refers to the energy required to cleave a single crystal along a chosen lattice plane. It is therefore generally applicable to contexts where a single crystal is involved (e.g. fatigue crack initiation model by Mura and co-workers [23-35]) or where a change of lattice orientation is irrelevant (e.g. cohesive zone technique, where material properties in the cohesive zone are assumed to be isotropic).

For grain boundaries, or more generally, interfaces created by two lattices of different structures, the determination of fracture energy is more complicated, even though the principles remain unchanged, i.e. calculating the energy required to break the bonds between atoms along the interface. Unfortunately a majority of research work about grain boundaries found in the literature focused on estimating the interface energy rather than the interface fracture energy. In the context of a homophase interface, the interface energy could be interpreted as that required to create an interface from a single crystal. Nevertheless, calculation models in those works could help to develop a new model for determining the interface fracture energy. The results of the boundary energy could then be used to verify the accuracy of any newly developed model.

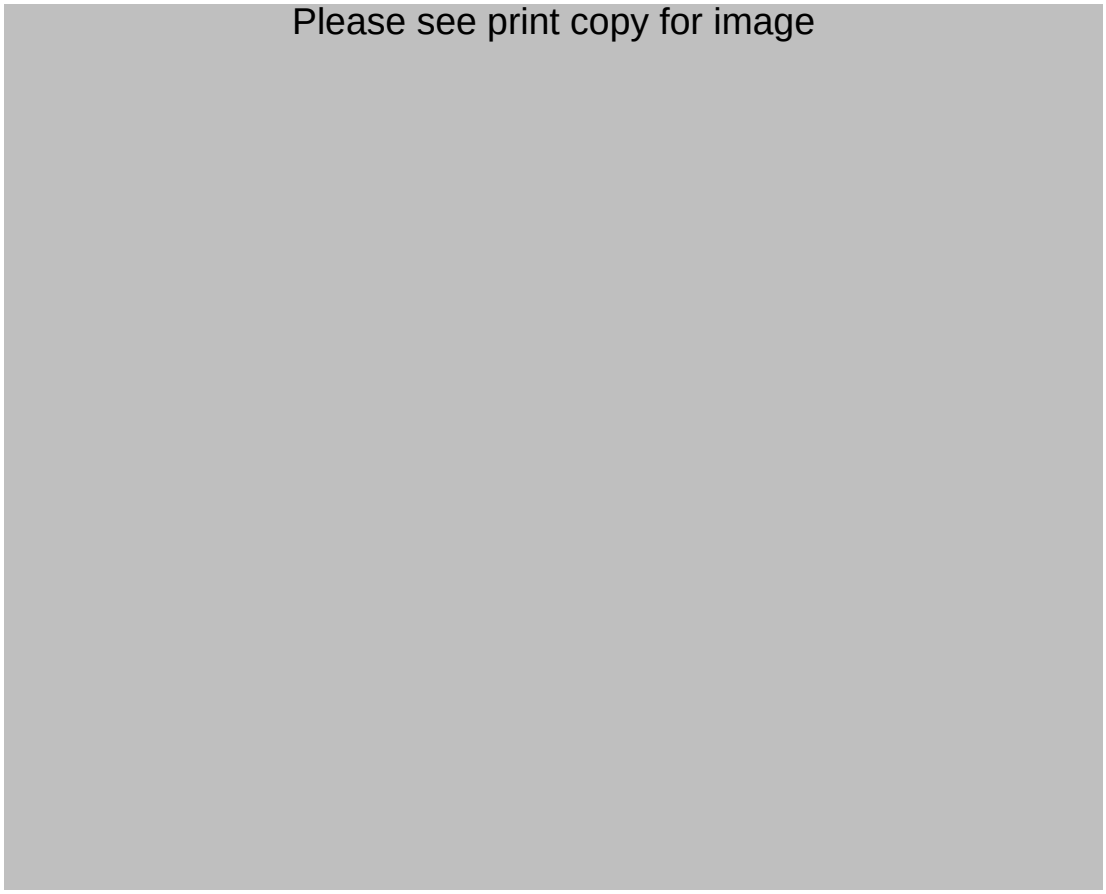

Figure 1.12 Measured relative interface energy in aluminum (a) <001> symmetrical tilt boundary and (b) <011> symmetrical tilt boundary. Corresponding results from MD simulations for (c) <001> symmetrical tilt boundary and (d) <011> symmetrical tilt boundary. [111]

Experimental measurements of the interface energies of aluminum <001> and <011> tilt boundaries reported by Hasson and Goux [111] were used to verify the many simulation models that follow. The same authors also conducted molecular dynamic simulations for the same tilt boundaries using Morse potential for aluminum. These experimental and modelling results are given in Figure 1.12. The term "misorientation" in Figure 1.12 refers to the tilt angle (in degrees).

Wolf [112] determined the symmetrical tilt grain boundary energies of fcc single crystals numerically, particularly for Au and Cu, and compared the results obtained from the Lennard-Jones and EAM potential. Various cases of symmetrical tilt boundary (i.e. the orientation of the tilt axis with respect to the original crystal coordinate system), particularly <011>, <112>, <111> and <001>, were considered. For a comparison with the experimental and numerical results by Hasson and Goux, only the results of <001> and <011> tilt boundary energies by Wolf are given in Figure 1.13. The horizontal and vertical axes in plots, shown in Figure 1.13, refer to the tilt angle in degrees and boundary energy in mJ/m^2, respectively.

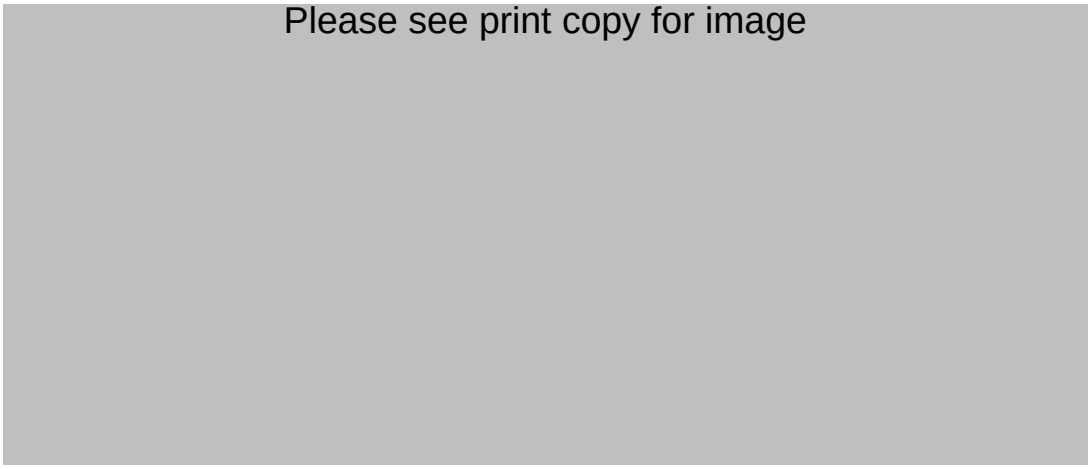

Figure 1.13 Boundary energies of Cu and Au using different potentials [112] (a) <001> symmetrical tilt boundary, (b) <011> symmetrical tilt boundary.

Nishitani et al. [113] repeated the calculation of <011> symmetric tilt boundary in aluminum using their newly developed EAM potential, namely the environmental dependent EAM for Al. Their resulting plot of boundary energy versus tilt angle is given in Figure 1.14.

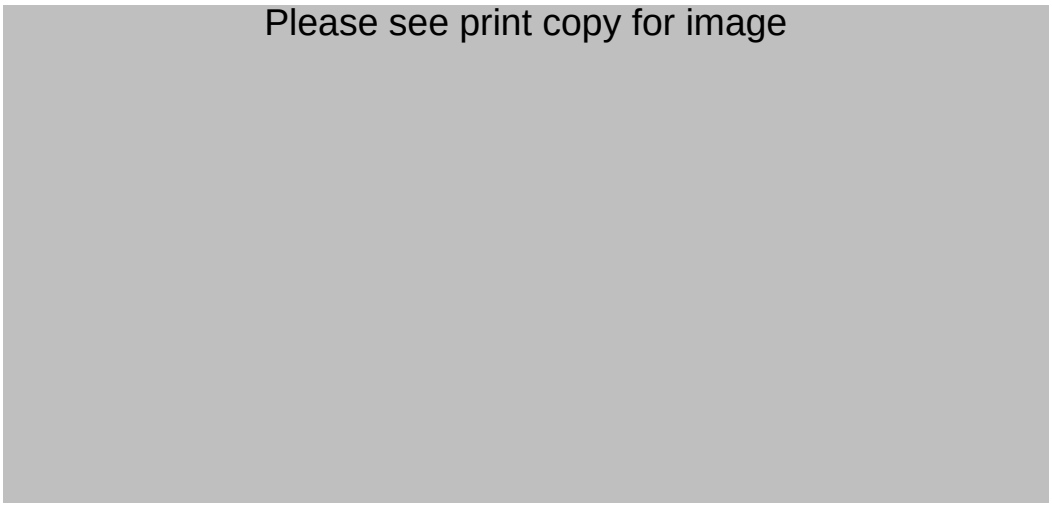

Figure 1.14 Energies of <011> symmetrical tilt grain boundary in Al using environment dependent EAM. [113]

Figure 1.15 Energies of <011> symmetrical tilt grain boundary in Al using second nearest neighbor modified EAM [114]

More recently, Lee and Choi [114] proposed a new method for calculating the grain boundary energy of the arbitrary tilt angle and tilt axis where the five degrees of freedom of an interface are fully accounted for. Their method was demonstrated by calculating the energy of <011> symmetrical tilt boundary in aluminum, using a semi-empirical atomic potential, namely the second nearest neighbor modified EAM. The result is given in Figure 1.15.

Numerical simulations conducted by various groups resulted in quite different values of boundary energy, particularly those of <011> symmetrical tilt boundary in Al. The reasons may lie in the different potential functions used to characterize the atomic interaction or the different modelling methods; while Hasson and Goux, Wolf, and Nishitani et al. used MD, Lee and Choi chose MS simulation.

Even so the results reviewed above possess common points that reveal interesting features of tilt boundary in fcc crystals. Firstly, the maximum energy of <001> symmetrical tilt boundary was generally higher than that of <001> symmetrical tilt boundary. Secondly, small energy cusps occur for <001> tilt boundary at tilt angles between 20^{o} and 70^{o}, but are more severe for the <011> tilt boundary where two large cusps occur at 70^{o} and 129^{o}. Howe [95] stated that such large cusps are

associated with low-energy {111} and {113} twin boundaries that result when tilting two fcc crystals around <011> axis at 70^{o} and 129^{o}, respectively.

1.8 Problem statement and thesis structure

The above review has shown that the field of fracture mechanics could generally be divided into the study of material deformation leading to crack opening and crack opening criteria. Even though both subjects have been studied by various groups for some decades there are still gaps that must be bridged, particularly in the modelling of crack initiation and subsequent growth in crystalline materials.

Most analytical works in this field (e.g. those pioneered by Rice and co-workers [50], models of fatigue crack initiation by Mura and co-workers [23-28], or continuous damage mechanics [37-45]), and the majority of numerical models (e.g. those using the cohesive zone technique) focused into explaining material behaviour that lead to cracks opening. If the strain energy at particular regions in the material reaches a critical value, which is mostly a predefined constant of surface energy, a crack is assumed to occur. The second aspect, determining the crack opening criteria, has been by-passed. Indeed, various studies concluded that crack opening criteria such as surface energy or interface fracture energy, vary with the materials and the crystal structures of the sample being considered.

More recently, molecular dynamic (MD) simulations and multi-scale models that incorporate MD simulations are able to combine both fields. Material deformation before cracking was modelled by inter-action between atoms where the crack opening was predicted “naturally” by the dynamics of the atoms. This approach is better used to study material behaviour qualitatively rather than determine their properties quantitatively because the sizes and time frames are different to real applications. An MD simulation of a real tensile test would be extremely expensive computationally.

This thesis combines both fields of the modelling of dynamic fracture in crystalline materials with a reasonable cost of computational time. Material behaviour before

cracking is modelled by implementing the theory of crystal plasticity into the traditional FEM analysis (CPFEM). The analysis of crack opening criteria is incorporated into the modelling procedure to account for changes in the crystal structures to the critical fracture energy. Elements in the FEM mesh satisfying the crack opening criteria are removed by the element removal technique. This combined approach allows the modelling of explicit dynamic crack growth without presuming a path or energy criterion. To the best of the author's knowledge, this combined approach is original and such modelling capability have not been available anywhere.

The current study is limited to the modelling of crack initiation and crack growth in a single-edge notched (SEN) aluminum single crystal under tensile test. The notch effectively acts as a defect in the material where concentrated deformations take place and cracks are likely to initiate. The numerical models and methodology proposed could, with minor modifications, also be used to predict crack nucleation and growth in crystals of various types under various loadings.

Section 1.6 showed that numerous studies have used CPFEM simulations to investigate the effects of various factors, e.g. sample thickness, grain size and initial orientations, to the deformation of an fcc polycrystalline aggregate. In many of these studies the strain hardening of the crystal lattice was described by a constant hardening modulus or a simple function that monotonically decreased with shear strain [88-92]. These descriptions of strain hardening might cause inaccuracies in predicting the reorientation of crystals in a polycrystalline aggregate [88]. A more accurate hardening law, which accounts for the influence of other slip systems in the lattice structure on the self hardening of a slip system [115], is used in this thesis. Using this hardening law, this thesis reports an initial investigation of the effects of initial orientation and notch shape to the evolution of crystals in the region around the notch tip in an SEN aluminum polycrystalline sample.

The subsequent chapters are structured as follows.

Chapter 2 presents the formulation of the theory of crystal plasticity and its implementation into an FEM analysis in Abaqus/Standard. The hardening law formulated by Bassani and Wu [115] will be used.

Chapter 3 presents the analyses of FEM results around the notch tip in a single crystal to verify the CPFEM model developed in Chapter 2. Particularly, the modelling results and analyses carried out in Chapter 3 are compared with the experimental observations found in the literature.

Chapter 4 presents the analyses of FEM results investigating the deformation in the region close to notch tip in single crystals with Cube and Brass initial orientations. The results for single crystals in this chapter form a basis for the crack opening modelling carried out in Chapter 6.

Chapter 5 investigates the effects of the geometry of the notch and initial orientation on the plastic deformation, particularly the evolution of microstructure, at the notch tip in a polycrystalline aggregate, using the hardening law formulated by Bassani and Wu [115].

Chapter 6 proposes a newly developed misorientation-dependent crack opening criterion, combined with the element removal technique in Abaqus/Standard. The chapter also presents the analyses and discussions of the modelling results of void nucleation and crack growth.

The overall conclusions and suggestions for further developments are presented in Chapter 7.

2. Formulation of CPFEM

This chapter presents a CPFEM model with Bassani and Wu's hardening model [115, 116] that has been developed in this study to investigate the fracture behaviour of pure aluminum. The implementation of the developed CPFEM model into Abaqus/Standard is also discussed.

To simplify the writing, the bold-faced notation represents vectors, tensor and matrices in the subsequent context. The superscript -1 of a matrix denotes the inverse, while the superscript T of a matrix means its transposition.

2.1 Theory of crystal plasticity

2.1.1 Kinematics of crystalline deformation [117]

Crystalline material under load undergoes crystallographic slip due to dislocation on the active slip systems and elastic deformation including stretching and rotating of the crystal lattice. These modes should occur simultaneously during deformation, from a reference to a current configuration. For mathematical convenience it is assumed that there is an intermediate configuration between the reference and current configuration, as shown in Figure 2.1. This crystallographic slip is assumed to occur firstly from the reference to the intermediate configuration, and secondly by an elastic stretching and rotation from the intermediate to current configuration. [117] Therefore, the total deformation gradient (**F**) can be decomposed into two components $\mathbf{F}^{P}$ and $\mathbf{F}^{*}$ as

$$\mathbf{F} = \frac{\partial \mathbf{x}}{\partial \mathbf{X}} = \mathbf{F}^{P}\mathbf{F}^{*} \tag{2.1}$$

where **X** is the position of material points in the reference configuration and **x** is the position of material points in the current configuration. $\mathbf{F}^{p}$ describes crystallographic slip on the slip system, which is also referred to as the plastic deformation gradient. $\mathbf{F}^{*}$ represents the elastic deformation gradient. [117]

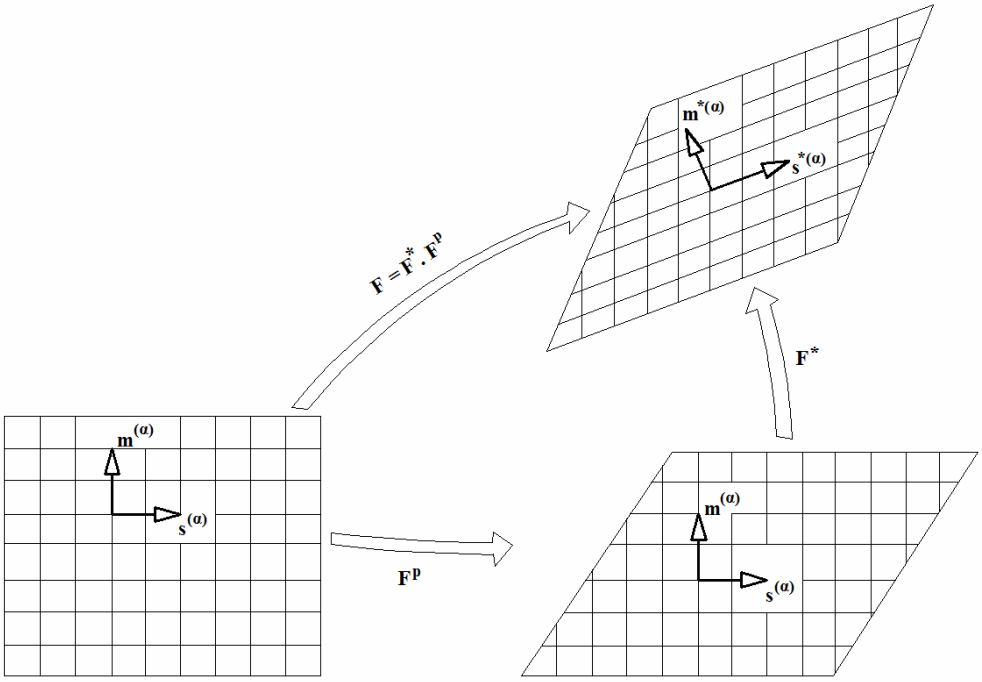

Figure 2.1 Kinematics of deformation in crystalline material.

The Green strain tensor (**E**) can be written as

$$\mathbf{E} = \frac{1}{2}(\mathbf{F}^{\mathrm{T}}\mathbf{F} - \mathbf{I}) \tag{2.2}$$

A slip system α^{th} in the reference configuration is specified by the slip direction vector $\mathbf{s}_0^{(\alpha)}$ and the normal vector to the slip plane $\mathbf{m}_0^{(\alpha)}$. Both $\mathbf{s}_0^{(\alpha)}$ and $\mathbf{m}_0^{(\alpha)}$ are unit vectors. They should satisfy the orthogonal relationship

$$\mathbf{s}_0^{(\alpha)} \cdot \mathbf{m}_0^{(\alpha)} = 0 \tag{2.3}$$

$\mathbf{s}_0^{(\alpha)}$ and $\mathbf{m}_0^{(\alpha)}$ do not change during crystallographic slip from the reference configuration to the intermediate configuration. The plastic deformation gradient ($\mathbf{F}^{\mathrm{p}}$) can be written as [117]

$$\mathbf{F}^{\mathrm{P}} = \sum_{\alpha=1}^{\mathrm{N}} \mathbf{F}^{(\alpha)\mathrm{P}} = \sum_{\alpha=1}^{\mathrm{N}} \mathbf{I} + \gamma^{(\alpha)} \mathbf{s}_0^{(\alpha)} \otimes \mathbf{m}_0^{(\alpha)} \tag{2.4}$$

where $\mathbf{F}^{(\alpha)\mathrm{P}}$ is the contribution of α^{th} slip system to $\mathbf{F}^{\mathrm{p}}$, γ is the shear strain of a slip system, $\otimes$ indicates the tensor product, $\mathbf{I}$ is a second-order unit tensor and N is the number of active slip systems.

The slip direction vector and normal vector to the slip plane convect with the lattice when the lattice is stretched and rotated from the intermediate to the current configuration. They are defined as $\mathbf{s}^{(\alpha)}$ and $\mathbf{m}^{(\alpha)}$ in the current configuration, respectively. Under the total deformation gradient ($\mathbf{F}$) the slip direction is transformed from $\mathbf{s}_0^{(\alpha)}$ to $\mathbf{s}^{(\alpha)}$, such that

$$\mathbf{s}^{(\alpha)} = \mathbf{F}^{(\alpha)} \mathbf{s}_0^{(\alpha)} = \mathbf{F}^{*} \mathbf{F}^{(\alpha)\mathrm{P}} \mathbf{s}_0^{(\alpha)} \tag{2.5}$$

Substituting Equation (2.4) into Equation (2.5) gives

$$\mathbf{s}^{(\alpha)} = \mathbf{F}^{*} (\mathrm{I} + \gamma^{(\alpha)} \mathbf{s}_0^{(\alpha)} \otimes \mathbf{m}_0^{(\alpha)}) \mathbf{s}_0^{(\alpha)} = \mathbf{F}^{*} \mathbf{s}_0^{(\alpha)} \tag{2.6}$$

The above equation indicates that the slip direction vector only varies with the elastic stretching and rotation. Due to the orthogonal relationship between the slip direction vector and normal vector to the slip plane in any configuration, the latter $\mathbf{m}^{(\alpha)}$ in the current configuration is governed by [117]

$$\mathbf{m}^{(\alpha)} = \mathbf{m}_0^{(\alpha)} \mathbf{F}^{*-1} \tag{2.7}$$

The velocity gradient **L** is evaluated from the deformation gradient by

$$\mathbf{L} = \frac{\partial \mathbf{v}}{\partial \mathbf{x}} = \dot{\mathbf{F}}\mathbf{F}^{-1} = \mathbf{L}^{*} + \mathbf{L}^{\mathrm{P}} \tag{2.8}$$

$$\mathbf{L}^{*} = \dot{\mathbf{F}}^{*}\mathbf{F}^{*-1} \tag{2.9}$$

$$\mathbf{L}^{\mathrm{P}} = \mathbf{F}^{*}\dot{\mathbf{F}}^{\mathrm{P}}\mathbf{F}^{\mathrm{P}-1}\mathbf{F}^{*-1} \tag{2.10}$$

where **v** is the velocity in the current configuration, $\dot{\mathbf{F}}$ expresses a time derivative of **F**, $\mathbf{L}^{*}$ is the contribution of the elastic stretching and lattice rotation to **L,** and $\mathbf{L}^{\mathrm{P}}$ is the plastic contribution. Decomposing **L** into a symmetric part **D** (stretching tensor) and an asymmetric part **Ω** (spin tensor) yields

$$\mathbf{L} = \mathbf{D} + \mathbf{\Omega} \tag{2.11}$$

$$\mathbf{D} = \frac{1}{2}(\mathbf{L} + \mathbf{L}^{\mathrm{T}}) \tag{2.12}$$

$$\mathbf{\Omega} = \frac{1}{2}(\mathbf{L} - \mathbf{L}^{\mathrm{T}}) \tag{2.13}$$

D is also commonly called the rate of deformation. Same as **L**, **D** and **Ω** can also be decomposed into the elastic stretching and lattice rotation parts ($\mathbf{D}^{*}$ and $\mathbf{\Omega}^{*}$) and plastic parts ($\mathbf{D}^{\mathrm{p}}$ and $\mathbf{\Omega}^{\mathrm{p}}$), namely

$$\mathbf{D} = \mathbf{D}^{*} + \mathbf{D}^{P},\ \mathbf{\Omega} = \mathbf{\Omega}^{*} + \mathbf{\Omega}^{P} \tag{2.14}$$

Differentiating Equation (2.2) yields the rate of Green strain tensor $\dot{\mathbf{E}}$, which refers to the reference configuration.

$$\dot{\mathbf{E}} = \mathbf{F}^{\mathrm{T}}\mathbf{D}\mathbf{F} \tag{2.15}$$

From Equation (2.4) $\mathbf{L}^{\mathrm{p}}$ can be derived as

$$\mathbf{L}^{\mathrm{P}} = \sum_{\alpha=1}^{\mathrm{N}} \dot{\gamma}^{(\alpha)} \mathbf{s}^{(\alpha)} \otimes \mathbf{m}^{(\alpha)} \tag{2.16}$$

where $\dot{\gamma}^{(\alpha)}$ is the shear strain-rate caused by the plastic slip in the α^{th} slip system.

And then

$$\mathbf{D}^{\mathrm{P}} = \frac{1}{2}(\mathbf{L}^{\mathrm{P}} + \mathbf{L}^{\mathrm{P}^{\mathrm{T}}}) = \sum_{\alpha=1}^{\mathrm{N}} \mathbf{p}^{(\alpha)} \dot{\gamma}^{(\alpha)} \tag{2.17}$$

$$\mathbf{\Omega}^{\mathrm{P}} = \frac{1}{2}(\mathbf{L}^{\mathrm{P}} - \mathbf{L}^{\mathrm{P}^{\mathrm{T}}}) = \sum_{\alpha=1}^{\mathrm{N}} \mathbf{W}^{(\alpha)} \dot{\gamma}^{(\alpha)} \tag{2.18}$$

where $$\mathbf{P}^{(\alpha)} = \frac{1}{2}(\mathbf{s}^{(\alpha)} \otimes \mathbf{m}^{(\alpha)} + \mathbf{m}^{(\alpha)} \otimes \mathbf{s}^{(\alpha)}) \tag{2.19}$$

$$\mathbf{W}^{(\alpha)} = \frac{1}{2}(\mathbf{s}^{(\alpha)} \otimes \mathbf{m}^{(\alpha)} - \mathbf{m}^{(\alpha)} \otimes \mathbf{s}^{(\alpha)}) \tag{2.20}$$

$\mathbf{s}^{(\alpha)} \otimes \mathbf{m}^{(\alpha)}$ is called the Schmid factor. $\mathbf{P}^{(\alpha)}$ and $\mathbf{W}^{(\alpha)}$ are symmetric and asymmetric part of Schmid factor, respectively. [117]

2.1.2 Lattice rotation [117]

If the polar decomposition is performed on the deformation gradient, we have

$$\mathbf{F} = \mathbf{R}\mathbf{U} \tag{2.21}$$

where $\mathbf{R}$ is the orthogonal rotation tensor and $\mathbf{U}$ the right stretch tensor, which is a positively defined symmetric tensor. They have the following properties

$$\mathbf{R}^{\mathrm{T}} = \mathbf{R}^{-1} \tag{2.22}$$

$$\mathbf{U} = \mathbf{U}^{\mathrm{T}} \tag{2.23}$$

Substituting Equation(2.21) into Equation(2.8) yields

$$\mathbf{L} = \dot{\mathbf{R}}\mathbf{R}^{-1} + \mathbf{R}\dot{\mathbf{U}}\mathbf{U}^{-1}\mathbf{R}^{-1} \tag{2.24}$$

$\dot{\mathbf{R}}$ is the time derivative of the orthogonal rotation tensor. Therefore, the asymmetric part $\boldsymbol{\Omega}$ of the velocity gradient can be written as

$$\boldsymbol{\Omega} = \frac{1}{2}((\dot{\mathbf{R}}\mathbf{R}^{-1} - \mathbf{R}\dot{\mathbf{R}}^{-1}) + \mathbf{R}(\dot{\mathbf{U}}\mathbf{U}^{-1} - \mathbf{U}^{-1}\dot{\mathbf{U}})\mathbf{R}^{\mathrm{T}}) \tag{2.25}$$

The derivative of $\mathbf{R}\mathbf{R}^{-1} = \mathbf{I}$ gives

$$\dot{\mathbf{R}}\mathbf{R}^{-1} = -\mathbf{R}\dot{\mathbf{R}}^{-1} \tag{2.26}$$

If $\mathbf{U}$ in the reference configuration is a unit tensor, we can obtain

$$\dot{\mathbf{U}}\mathbf{U}^{-1} = \mathbf{U}^{-1}\dot{\mathbf{U}} \tag{2.27}$$

Therefore, $\boldsymbol{\Omega}$ becomes

$$\boldsymbol{\Omega} = \dot{\mathbf{R}}\mathbf{R}^{-1} \tag{2.28}$$

Accordingly we have

$$\mathbf{R} = (\mathbf{I} + \frac{1}{2}\mathbf{\Omega}\Delta t)(\mathbf{I} - \frac{1}{2}\mathbf{\Omega}\Delta t)^{-1} \tag{2.29}$$

where Δt is the time increment. Equation (2.30) can also be written as

$$\mathbf{\Omega} = \frac{2}{\Delta t}(\mathbf{R} - \mathbf{I})(\mathbf{R} + \mathbf{I})^{-1} \tag{2.30}$$

The derivatives of Equations (2.6) and (2.7) yield

$$\dot{\mathbf{s}}^{(\alpha)} = \mathbf{L}^{*}\mathbf{s}^{(\alpha)} = (\mathbf{D}^{*} + \mathbf{\Omega}^{*})\mathbf{s}^{(\alpha)} \tag{2.31}$$

$$\dot{\mathbf{m}}^{(\alpha)} = -\mathbf{m}^{(\alpha)}\mathbf{L}^{*} = -\mathbf{m}^{(\alpha)}(\mathbf{D}^{*} + \mathbf{\Omega}^{*}) \tag{2.32}$$

2.1.3 Constitutive law [117]

Let $\mathbf{t_0}$ be the Kirchhoff stress in the reference configuration at the time t + Δt, it is also the Kirchhoff stress in the current configuration at the time t. According to the description in Section 2.1.1, deformation occurs first by crystallographic slip from the reference to the intermediate configuration, and then the lattice stretching and rotation from the intermediate configuration to the current configuration. It is assumed that the change in stress caused by the slip and lattice stretching is $\dot{\mathbf{t}}_0\Delta t$, where $\dot{\mathbf{t}}_0$ is the stress rate in the reference configuration. The stress $(\mathbf{t_0} + \dot{\mathbf{t}}_0\Delta t)$ will be rotated to the current configuration. The rotation tensor is **R**. The Kirchhoff stress **t** in the current configuration can be expressed by

$$\mathbf{t} = \mathbf{R}(\mathbf{t}_0 + \dot{\mathbf{t}}_0\Delta t)\mathbf{R}^{\mathrm{T}} \tag{2.33}$$

Taking the time derivative then gives

$$\begin{aligned}\dot{\mathbf{t}} &= \mathbf{R}\dot{\mathbf{t}}_0\mathbf{R}^{\mathbf{T}} + \dot{\mathbf{R}}(\mathbf{t}_0 + \dot{\mathbf{t}}_0\Delta t)\mathbf{R}^{\mathbf{T}} + \mathbf{R}(\mathbf{t}_0 + \dot{\mathbf{t}}_0\Delta t)\dot{\mathbf{R}}^{\mathbf{T}} \\ &= \mathbf{R}\dot{\mathbf{t}}_0\mathbf{R}^{\mathbf{T}} + \boldsymbol{\Omega}\mathbf{t} - \mathbf{t}\boldsymbol{\Omega}\end{aligned} \tag{2.34}$$

where $\dot{\mathbf{t}}$ is the material rate of Kirchhoff stress. $\mathbf{R}\dot{\mathbf{t}}_0\mathbf{R}^{\mathbf{T}}$ is defined as the Jaumann rate of Kirchhoff stress ($\overset{\nabla}{\mathbf{t}}$) on axes that rotate with the material. Therefore, we have

$$\overset{\nabla}{\mathbf{t}} = \dot{\mathbf{t}} - \boldsymbol{\Omega}\mathbf{t} + \mathbf{t}\boldsymbol{\Omega} \tag{2.35}$$

If deformation from the intermediate to the current configuration alone is taken into account then Equation (2.35) can be rewritten as

$$\overset{\nabla}{\mathbf{t}}^{*} = \dot{\mathbf{t}} - \boldsymbol{\Omega}^{*}\mathbf{t} + \mathbf{t}\boldsymbol{\Omega}^{*} \tag{2.36}$$

$$\overset{\nabla}{\mathbf{t}}^{*} = \mathbf{R}\dot{\mathbf{t}}_1^{*}\mathbf{R}^{\mathbf{T}} \tag{2.37}$$

where $\overset{\nabla}{\mathbf{t}}^{*}$ is the Jaumann rate of Kirchhoff stress on axes that rotate with the lattice and $\dot{\mathbf{t}}_1^{*}$ is the rate of the Kirchhoff stress in the intermediate configuration.

The difference between Equation (2.35) and Equation (2.36) is

$$\overset{\nabla}{\mathbf{t}}^{*} - \overset{\nabla}{\mathbf{t}} = \sum_{\alpha=1}^{N} \boldsymbol{\beta}^{(\alpha)}\dot{\gamma}^{(\alpha)} \tag{2.38}$$

where $$\boldsymbol{\beta}^{(\alpha)} = \mathbf{W}^{(\alpha)}\mathbf{t} - \mathbf{t}\mathbf{W}^{(\alpha)} \tag{2.39}$$

The lattice is elastically stretched along the lattice axis. The lattice stretching can be described in the lattice coordinate system by

$$\dot{\mathbf{t}}_{\mathrm{L}} = \mathbf{C}_0 : \mathbf{D}_{\mathrm{L}} \tag{2.40}$$

where $\dot{\mathbf{t}}_L$ is the material rate of the Kirchhoff stress in the lattice coordinate system, $\mathbf{D}_L$ is the rate of the elastic stretching in the lattice coordinate system, $\mathbf{C}_0$ is the tensor of elastic moduli.

Provided the rotation tensor between the lattice coordinate system and the current configuration is $\mathbf{R}_L$, the elastic deformation rate $\mathbf{D}^*$ in the current configuration can be linked to $\mathbf{D}_L$ by the following equation

$$\mathbf{D}^* = \mathbf{R}_L \mathbf{D}_L \mathbf{R}_L^T \tag{2.41}$$

The rate of Kirchhoff stress $\dot{\mathbf{t}}_1^*$ in the intermediate configuration can be given by

$$\dot{\mathbf{t}}_1^* = \mathbf{R}^T \mathbf{R}_L \dot{\mathbf{t}}_L \mathbf{R}_L^T \mathbf{R} \tag{2.42}$$

Therefore, the Jaumann rate $\overset{\nabla}{\mathbf{t}}^*$ can be expressed by

$$\overset{\nabla}{\mathbf{t}}^* = \mathbf{R}_L \dot{\mathbf{t}}_L \mathbf{R}_L^T \tag{2.43}$$

Equations (2.41) and (2.43) can be rewritten as

$$\mathbf{D}_L = (\mathbf{R}_L^T \otimes \mathbf{R}_L^T) : \mathbf{D}^* \tag{2.44}$$

$$\dot{\mathbf{t}}_L = (\mathbf{R}_L^T \otimes \mathbf{R}_L^T) : \overset{\nabla}{\mathbf{t}}^* \tag{2.45}$$

Substituting Equations (2.44) and (2.45) into Equation (2.40) yields

$$\overset{\nabla}{\mathbf{t}}^* = \mathbf{C} : \mathbf{D}^* \tag{2.46}$$

$$\mathbf{C} = (\mathbf{R}_L \otimes \mathbf{R}_L) \cdot \mathbf{C}_0 \cdot (\mathbf{R}_L^T \otimes \mathbf{R}_L^T) \tag{2.47}$$

Substituting Equation (2.46) into Equation (2.36) gives

$$\overset{\nabla}{\mathbf{t}} = \mathbf{C} : \mathbf{D} - \sum_{\alpha=1}^{N} (\mathbf{C} : \mathbf{P}^{(\alpha)} + \boldsymbol{\beta}^{(\alpha)}) \dot{\gamma}^{(\alpha)} \tag{2.48}$$

It was assumed that slip is the plastic deformation mechanism. The resolved shear stress on each slip system can be used as the vital variable to evaluate plastic flow. The resolved shear stress $\tau^{(\alpha)}$ can be calculated from

$$\tau^{(\alpha)} = \mathbf{P}^{(\alpha)} : \mathbf{t} \tag{2.49}$$

Taking the time derivative gives

$$\dot{\tau}^{(\alpha)} = \dot{\mathbf{P}}^{(\alpha)} : \mathbf{t} + \mathbf{P}^{(\alpha)} : \dot{\mathbf{t}} \tag{2.50}$$

Equation (2.50) can also be written as

$$\dot{\tau}^{(\alpha)} = (\mathbf{C} : \mathbf{P}^{(\alpha)} + \boldsymbol{\beta}^{(\alpha)}) : (\mathbf{D} - \sum_{\beta=1}^{N} \mathbf{p}^{(\beta)} \dot{\gamma}^{(\beta)}) \tag{2.51}$$

The relationship of the Cauchy stress $\boldsymbol{\sigma}$ and the Kirchhoff stress can be expressed by

$$\mathbf{t} = J\boldsymbol{\sigma} \tag{2.52}$$

$$J = \frac{1}{|\mathbf{F}|} \tag{2.53}$$

The derivative of Equation (2.52) with time can be written as

$$\begin{aligned}\dot{\mathbf{t}} &= J\dot{\boldsymbol{\sigma}} + \dot{J}\boldsymbol{\sigma} \\ &= J\dot{\boldsymbol{\sigma}} + Jtr(\mathbf{D})\boldsymbol{\sigma}\end{aligned} \tag{2.54}$$

$\dot{\boldsymbol{\sigma}}$ is the time derivative of Cauchy stress. Substituting Equations (2.52) and (2.54) into Equations (2.33), (2.35), (2.48), (2.51) gives the constitutive law based on Cauchy stress

$$\boldsymbol{\sigma} = \mathbf{R}(\boldsymbol{\sigma}_0(1+\mathrm{tr}(\mathbf{D})))\mathbf{R}^{\mathbf{T}} + \overset{\nabla}{\boldsymbol{\sigma}}_0 \Delta t \tag{2.55}$$

$$\overset{\nabla}{\boldsymbol{\sigma}} = \dot{\boldsymbol{\sigma}} - \boldsymbol{\Omega}\boldsymbol{\sigma} + \boldsymbol{\sigma}\boldsymbol{\Omega} \tag{2.56}$$

$$\overset{\nabla}{\boldsymbol{\sigma}} = \mathbf{C} : \mathbf{D} - \mathrm{tr}(\mathbf{D})\boldsymbol{\sigma} - \sum_{\alpha=1}^{N}(\mathbf{C} : \mathbf{P}^{(\alpha)} + \boldsymbol{\beta}_1^{(\alpha)})\dot{\gamma}^{(\alpha)} \tag{2.57}$$

$$\dot{\tau}^{(\alpha)} = (\mathbf{C} : \mathbf{P}^{(\alpha)} + \boldsymbol{\beta}_1^{(\alpha)}) : (\mathbf{D} - \sum_{\beta=1}^{N}\mathbf{p}^{(\beta)}\dot{\gamma}^{(\beta)}) \tag{2.58}$$

Where $$\boldsymbol{\beta}_1^{(\alpha)} = \mathbf{W}^{(\alpha)}\boldsymbol{\sigma} - \boldsymbol{\sigma}\mathbf{W}^{(\alpha)} \tag{2.59}$$

$\overset{\nabla}{\boldsymbol{\sigma}}$ is the Jaumann rate of Cauchy stress on axes rotating with the material.

2.1.4 Rate-dependent hardening model

In this study, the rate-dependent hardening model with a power law, which dictates the relationship of the resolved shear stress ($\tau^{(\alpha)}$) and the shear strain rate $\dot{\gamma}^{(\alpha)}$ on a slip system α, is used. Slip on a slip system also obeys Schmid's law, which states that slip begins when the resolved shear stress reaches a critical value. [117]

$$\dot{\gamma}^{(\alpha)} = \dot{\gamma}_0^{(\alpha)}\,\mathrm{sgn}(\tau^{(\alpha)})\left|\frac{\tau^{(\alpha)}}{\tau_c^{(\alpha)}}\right|^n, \text{ for } \tau^{(\alpha)} \geq \tau_c^{(\alpha)} \tag{2.60a}$$

$$\dot{\gamma}^{(\alpha)} = 0, \text{ for } \tau^{(\alpha)} < \tau_c^{(\alpha)} \tag{2.60b}$$

and $$\text{sgn}(x) = \begin{cases} 1 & \text{for } x \geq 1 \\ -1 & \text{for } x < 1 \end{cases}$$

where $\dot{\gamma}_0^{(\alpha)}$ is the reference value of shear strain rate which is a constant for all slip systems, n is the rate sensitive exponent. Both $\dot{\gamma}_0^{(\alpha)}$ and n are material parameters. $\tau_c^{(\alpha)}$ is the critical resolved shear stress of slip system α.

A linear hardening is assumed and the rate of change of the critical resolved shear stress is expressed as [117]

$$\dot{\tau}_c^{(\alpha)} = \sum_{\beta=1}^{N} h_{\alpha\beta} \dot{\gamma}^{(\beta)} \tag{2.61}$$

After reviewing various experimental results of fcc single crystals undergoing uniaxial stressing, Wu et al. [116] described the revolution of the resolved shear stress in a slip system with respect to the shear strain as a three-stage process, as shown in Figure 2.2. In stage I, the hardening rate is low and is almost a constant. In stage II, rapid hardening occurs. The hardening rate in this stage is also almost constant and is about an order of magnitude larger than the hardening rate in stage I. In stage III (parabolic hardening), the hardening rate decreases continuously until fracture occurs.

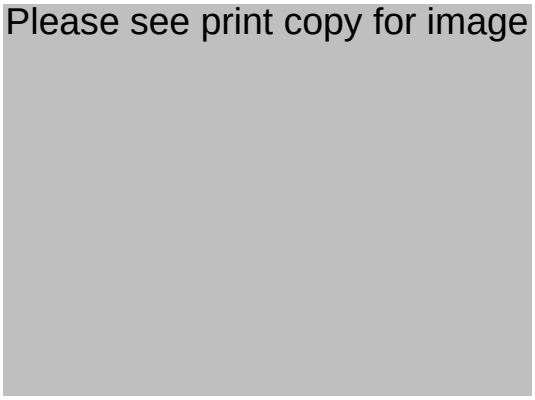

Figure 2.2 A typical curve of resolved shear stress versus shear strain in a slip system with three-stage hardening. [115]

In various hardening laws, e.g. those proposed by Taylor [118], Budiansky and Wu [119], Hutchinson [120], Asaro [117], Havner and Shalaby [121], it was assumed that the self hardening modulus was either a constant or a simple function that monotonically decreased with shear strain. These assumptions obviously could not capture the shear stress – shear strain curve in Figure 2.2. Bassani and Wu [115] incorporated the history of slip into the development of a new hardening law. As a result, the new hardening modulus was able to capture the transition of stages of hardening (see Figure 2.2) and the orientation dependence of hardening. The self-hardening and latent hardening moduli are shown in Equation (2.62)

$$h_{\alpha\alpha} = \left[(h_0 - h_s)\,\mathrm{sech}^2\left(\frac{(h_0 - h_s)\gamma^{(\alpha)}}{\tau_1 - \tau_0} \right) + h_s \right] \left[1 + \sum_{\substack{\beta=1 \\ \beta \neq \alpha}}^{N} f_{\alpha\beta} \tanh\left(\frac{\gamma^{(\beta)}}{\gamma_0}\right) \right] \tag{2.62a}$$

$$h_{\alpha\beta} = q h_{\alpha\alpha}, \ \alpha \neq \beta \tag{2.62b}$$

where $h_{\alpha\beta}$ are instantaneous hardening moduli including the self hardening of each system ($\alpha=\beta$) and latent hardening ($\alpha\neq\beta$); $h_{\alpha\alpha}$ is the self hardening moduli; q is a latent hardening parameter; γ_0 is the reference value of slip; γ is the shear strain; τ_0 is the initial critical resolved shear stress; τ_1 is the breakthrough stress where large plastic flow initiates; h_0 is the hardening modulus just after initial yield, h_s is the hardening modulus during easy glide and $f_{\alpha\beta}$ represents the magnitude of the strength of a particular slip interaction between two slip systems α and β. The factors $f_{\alpha\beta}$ depend on the geometric relation between two slip systems. There are five constants for $f_{\alpha\beta}$, namely a_1 (no junction), a_2 (Hirth lock), a_3 (coplanar junction), a_4 (glissile junction) and a_5 (sessile junction). [115]

The nature of the function $G\left(\gamma^{(\beta)}\right) = \left[1 + \sum_{\substack{\beta=1 \\ \beta \neq \alpha}}^{N} f_{\alpha\beta} \tanh\left(\frac{\gamma^{(\beta)}}{\gamma_0}\right) \right]$ and the scalar value q are different and they serve different purposes. The function $G\left(\gamma^{(\beta)}\right)$ is used to account for the effects of shear strain on other slip systems in the calculation of the self hardening

modulus of a system α (Equation 2.62a). Meanwhile, the scalar value q is used to determine latent hardening moduli of a slip system α based on its self hardening modulus (Equation 2.62b).

2.2 CPFEM formulation

2.2.1 Basic theory of the displacement-based FEM

The equilibrium for problems neglecting the body forces can be expressed by the virtual work principle in rate form

$$\int_V \boldsymbol{\sigma} : \delta\mathbf{D} dV = \int_S \mathbf{f} \cdot \delta\mathbf{v} dS \tag{2.63}$$

where V is the volume of the solid body in the current configuration; S is the bounding surface of the volume V; $\boldsymbol{\sigma}$ is the Cauchy stress; $\mathbf{f}$ is the surface traction per unit of the current area; $\delta\mathbf{v}$ is the kinematically admissible virtual velocity field, which is infinitesimal and completely arbitrary except that it must obey the boundary conditions on displacement; $\delta\mathbf{D}$ is the virtual form of the rate of deformation

In FEM, the solid body is divided into n elements, where each element is associated with m nodal points. The velocity field in each element is interpolated by interpolation functions $\mathbf{N}$ (shape functions), which link the velocity field ($\mathbf{v}$) to the nodal velocities ($\mathbf{v}^n$) as follows

$$\mathbf{v} = \mathbf{N}\mathbf{v}^n \tag{2.64}$$

Based on Equation (2.64), the interpolation for the rate of the deformation $\mathbf{D}$ and the spin tensor $\boldsymbol{\Omega}$ can be expressed as:

$$\mathbf{D} = \mathbf{B}\mathbf{v}^{\mathbf{n}} \tag{2.65}$$

$$\mathbf{\Omega} = \mathbf{G}\mathbf{v}^{\mathbf{n}} \tag{2.66}$$

where **B** and **G** are respectively the symmetric part and the skew part of the coefficient matrix of velocity gradient.

Normally surface tractions **f** in Equation (2.63) are the force (or stress) boundary conditions. If **f** is the function of nodal velocities, it can be written as

$$\mathbf{f}=\mathbf{T}\mathbf{v}^{n} \tag{2.67}$$

where **T** is the coefficient matrix between stress boundary conditions and nodal velocity.

Corresponding to Equations (2.64) and (2.65), the virtual velocity field $\delta\mathbf{v}$ and the virtual rate of deformation $\delta\mathbf{D}$ can be written as

$$\delta\mathbf{v} = \mathbf{N}\delta\mathbf{v}^{\mathbf{n}} \tag{2.68}$$

$$\delta\mathbf{D} = \mathbf{B}\delta\mathbf{v}^{\mathbf{n}} \tag{2.69}$$

The equilibrium equation (Equation (2.63)) is discretized by substituting Equations (2.68) and (2.69) into Equation (2.63)

$$\int_V \mathbf{B}^{\mathbf{T}}\boldsymbol{\sigma}\mathrm{d}V : \delta\mathbf{v}^{\mathbf{n}} = \int_S \mathbf{N}^{\mathbf{T}}\mathbf{f}\mathrm{d}S : \delta\mathbf{v}^{\mathbf{n}} \tag{2.70}$$

Since $\delta\mathbf{v}^{\mathbf{n}}$ is arbitrary, one obtains

$$\int_V \mathbf{B}^{\mathbf{T}}\boldsymbol{\sigma}\mathrm{d}V = \int_S \mathbf{N}^{\mathbf{T}}\mathbf{f}\mathrm{d}S \tag{2.71}$$

The above non-linear equations are functions of the nodal velocities $\mathbf{v}^{\mathbf{n}}$. They form the basis of the displacement-based FEM. Equation (2.71) can be rewritten as

$$\mathbf{F}(\mathbf{v}^{\mathbf{n}}) = \int_V \mathbf{B}^{\mathbf{T}}\boldsymbol{\sigma} dV - \int_S \mathbf{N}^{\mathbf{T}}\mathbf{f} dS = \mathbf{0} \tag{2.72}$$

The Newton algorithm is generally used to solve non-linear equations (Equation (2.72)). An iteration process is performed. In the $(i+1)^{th}$ iteration step the nodal velocities are updated by

$$\mathbf{v}_{i+1}^{n} = \mathbf{v}_{i}^{n} - \mathbf{K}^{-1}\mathbf{F}(\mathbf{v}_{i}^{n}) \tag{2.73}$$

$$\mathbf{K} = \mathbf{F}'(\mathbf{v}_{i}^{n}) \tag{2.74}$$

where $\mathbf{v}_{i}^{n}$ and $\mathbf{v}_{i+1}^{n}$ are the nodal velocities at iteration steps i^{th} and $(i+1)^{th}$, respectively; $\mathbf{K}$ is the Jacobian matrix, which is the derivative of $\mathbf{F}(\mathbf{v}^{n})$ with respect to $\mathbf{v}^{n}$ at $\mathbf{v}^{n} = \mathbf{v}_{i}^{n}$. To solve Equation (2.72) $\mathbf{K}$ must be developed. It can be expressed by

$$\mathbf{K} = \int_V \mathbf{B}^{\mathbf{T}} \frac{d\boldsymbol{\sigma}}{d\mathbf{v}^{n}} dV - \int_S \mathbf{N}^{\mathbf{T}}\mathbf{T} dS \tag{2.75}$$

For rate-dependent materials, the constitutive relation can be described in incremental form as follows

$$\overset{\nabla}{\boldsymbol{\sigma}} = \mathbf{H} : \mathbf{D} \tag{2.76}$$

where $\mathbf{H}$ is the fourth-order hardening parameter tensor. The derivative of the Cauchy stress with respect to $\mathbf{v}^{n}$ can be calculated by Equation (2.56) as follows

$$\frac{d\boldsymbol{\sigma}}{d\mathbf{v}^{n}} = \frac{d\overset{\nabla}{\boldsymbol{\sigma}}}{d\mathbf{v}^{n}} + \frac{d\boldsymbol{\Omega}}{d\mathbf{v}^{n}}\boldsymbol{\sigma} - \boldsymbol{\sigma}\frac{d\boldsymbol{\Omega}}{d\mathbf{v}^{n}} \tag{2.77}$$

Substituting Equations (2.65), (2.66) and (2.76) into Equation (2.77) yields

$$\frac{\mathrm{d}\boldsymbol{\sigma}}{\mathrm{d}\mathbf{v}^{n}} = \mathbf{H} : \mathbf{B} + \mathbf{G}\boldsymbol{\sigma} - \boldsymbol{\sigma}\mathbf{G} \tag{2.78}$$

Therefore, the Jacobian matrix (**K**) can be expressed as

$$\mathbf{K} = \int_{V} \mathbf{B}^{T}(\mathbf{G}\boldsymbol{\sigma} - \boldsymbol{\sigma}\mathbf{G} + \mathbf{H} : \mathbf{B})\mathrm{d}V - \int_{S} \mathbf{N}^{T}\mathbf{T}\mathrm{d}S \tag{2.79}$$

To determine **K**, the hardening parameter tensor **H** needs to be calculated based on the constitutive law.

2.2.2 Implementing crystal plasticity into the FEM framework

The implementation of the theory of crystal plasticity into FEM framework has attracted work by various research groups [142]. For the rate-independent crystal plasticity, McGinty and McDowell [143] developed a semi-implicit integration scheme to quantify the order of activation of slip systems and then determine their shear strain rates. Zamiri et al. [144] proposed a modified yield function for single crystal that was computationally efficient and flexible. Takahashi et al. [145] proposed a successive integration method to determine shear strain rates. Some other methods implementing the rate independent crystal plasticity into FEM included those proposed by Nemat-Nasser et al. [146], Knockaert et al. [147], and Anand and Kothari [148].

In the rate dependent crystal plasticity model, all slip systems are assumed to be always active. The numerical integration of the model is highly unstable because of the high-order nonlinear flow rule of slip systems [142]. Kalidindi et al. [149] and Delannay et al. [150] used the Newton-Raphson iteration method to overcome such numerical instability to solve the crystal constitutive laws. In order to improve numerical stability, Cuitino and Ortiz [55] later introduced a line search approach into the Newton-Raphson iteration to optimize the obtained convergent solutions. McGinty [151] later improved the

algorithm proposed by Cuitino and Ortiz by repeating the integration in two smaller time increments when the line search approach diverges. Other studies also focusing on numerically solving the constitutive law of the rate dependent crystal plasticity model were those done by Pierce et al. [152], Needleman et al. [153], Raphanel et al. [154], and Li et al. [142]. Some of the above rate dependent CPFEM models were examined by Busso and Cailletaud [155], Ling et al. [156], and Rousselier and Leclercq [157].

The crystal plasticity constitutive model described earlier is implemented into the implicit finite element code ABAQUS/Standard by using the user material subroutine (UMAT) [122]. ABAQUS/Standard is a displacement-based finite element code. In ABAQUS/Standard the loading history is divided into steps where deformation is assumed to be static in each step. The stresses, strains and other state variables are known at the beginning of each step. Equation (2.72) is solved using Newton's method where an iterative algorithm (Equation (2.73)) is conducted until it reaches convergence. After iteration finishes the velocity field solution to Equation (2.72) and other variables can be obtained at the end of the step. All the calculated variables will be transferred to the next step as entries. This step-by-step procedure continues until the deformation is finished.

When Equations (2.73) and (2.79) are implemented ABAQUS/Standard calls UMAT to calculate the hardening parameters and to update the stresses and the solution dependent state variables. In this study we follow the UMAT framework developed by Huang [123] and use the Bassani-Wu's formulations [115] as the hardening model. The procedure in UMAT includes [123]

1. Through ABAQUS/Standard user interface, inputs for UMAT are provided, including stresses ($\boldsymbol{\sigma}$), logarithmic strains ($\int_0^t \mathbf{D}dt$), increments of logarithmic strains ($\mathbf{D}\Delta t$), rotation increments ($\mathbf{R}$), time increment (Δt), constants, solution dependent variables, etc.. The constants include elastic moduli, parameters characterizing slip systems, materials parameters in the hardening model and the forward gradient time integration parameter. All the constant can be modified in

the ABAQUS input file or through ABAQUS/CAE user interface. The solution dependent variables include the slip directions $\mathbf{s}^{(\alpha)}$, normals to slip planes $\mathbf{m}^{(\alpha)}$, shear strain rates $\dot{\gamma}^{(\alpha)}$, resolved shear stresses $\tau^{(\alpha)}$, and critical resolved shear stress τ_c on all slip systems.

2. Determine the slip systems using input parameters characterizing the slip systems when UMAT is called the first time.

3. Calculate the spin tensor ($\mathbf{\Omega}$) by Equation (2.30).

4. Update $\mathbf{s}^{(\alpha)}$ and $\mathbf{m}^{(\alpha)}$ using Equations (2.31) and (2.32).

5. Determine the rotation tensor $\mathbf{R}$ from the local lattice system to the global system using the slip directions $\mathbf{s}^{(\alpha)}$ and normals to the slip plane $\mathbf{m}^{(\alpha)}$.

6. Calculate the elastic moduli $\mathbf{C}$ in the global system by Equation (2.47).

7. Calculate $\mathbf{P}$, $\mathbf{W}$ and $\boldsymbol{\beta}_1$ by Equations (2.19), (2.20) and (2.58).

8. Calculate $\dfrac{d\dot{\gamma}^{(\alpha)}}{d\mathbf{D}}$. The Taylor expansion of Equation (2.59a) at the time step (t+Δt) yields

$$\dot{\gamma}^{(\alpha)}_{t+\Delta t} = \dot{\gamma}^{(\alpha)}_{t} + \left.\frac{\partial\dot{\gamma}^{(\alpha)}}{\partial\tau^{(\alpha)}}\right|_t \Delta\tau^{(\alpha)} + \left.\frac{\partial\dot{\gamma}^{(\alpha)}}{\partial g^{(\alpha)}}\right|_t \Delta g^{(\alpha)} \tag{2.80}$$

A relaxation scheme is used to calculated $\Delta\tau^{(\alpha)}$ and $\Delta g^{(\alpha)}$, namely

$$\Delta\tau^{(\alpha)} = (1-\theta)\dot{\tau}^{(\alpha)}_{t} + \theta\dot{\tau}^{(\alpha)}_{t+\Delta t} \tag{2.81}$$

$$\Delta g^{(\alpha)} = (1-\theta)\dot{g}^{(\alpha)}_{t} + \theta\dot{g}^{(\alpha)}_{t+\Delta t} \tag{2.82}$$

where g is the relaxation factor, which varies from 0 to 1.

Substituting Equations (2.81) and (2.82) into Equation (2.80) gives

$$\dot{\gamma}^{(\alpha)}_{t+\Delta t} = a_1 + \theta a_2 \dot{\tau}^{(\alpha)}_{t+\Delta t} + \theta a_3 \dot{g}^{(\alpha)}_{t+\Delta t} \tag{2.83a}$$

$$a_1 = \dot{\gamma}^{(\alpha)}_t + (1-\theta)\left.\frac{\partial \dot{\gamma}^{(\alpha)}}{\partial \tau^{(\alpha)}}\right|_t \dot{\tau}^{(\alpha)}_t + (1-\theta)\left.\frac{\partial \dot{\gamma}^{(\alpha)}}{\partial g^{(\alpha)}}\right|_t \dot{g}^{(\alpha)}_t \tag{2.83b}$$

$$a_2 = \left.\frac{\partial \dot{\gamma}^{(\alpha)}}{\partial \tau^{(\alpha)}}\right|_t \tag{2.83c}$$

$$a_3 = \left.\frac{\partial \dot{\gamma}^{(\alpha)}}{\partial g^{(\alpha)}}\right|_t \tag{2.83d}$$

Further substituting Equations (2.58) and (2.61) into the Equation(2.83a) yields

$$\dot{\gamma}^{(\alpha)}_{t+\Delta t} = a_1 + \theta a_2 (\mathbf{C} : \mathbf{P}^{(\alpha)} + \boldsymbol{\beta}^{(\alpha)}_1) : (\mathbf{D} - \sum_{\beta=1}^{N} \mathbf{P}^{(\beta)} \dot{\gamma}^{(\beta)}_{t+\Delta t}) + \theta a_3 \sum_{\beta=1}^{N} h_{\alpha\beta} \dot{\gamma}^{(\beta)}_{t+\Delta t} \tag{2.84}$$

Therefore we obtain

$$\left.\frac{d\dot{\gamma}^{(\alpha)}}{d\mathbf{D}}\right|_{t+\Delta t} = \frac{\theta a_2 (\mathbf{C} : \mathbf{P}^{(\alpha)} + \boldsymbol{\beta}^{(\alpha)}_1)}{(1 + \theta a_2 (\mathbf{C} : \mathbf{P}^{(\alpha)} + \boldsymbol{\beta}^{(\alpha)}_1) : \mathbf{P}^{(\alpha)} - \theta a_3 h_{\alpha\alpha})} \tag{2.85}$$

9. Calculate $\frac{d\overset{\nabla}{\boldsymbol{\sigma}}}{d\mathbf{D}}$ by differentiating Equation (2.57) which yields

$$\mathbf{H} = \frac{d\overset{\nabla}{\boldsymbol{\sigma}}}{d\mathbf{D}} = \mathbf{C} - \boldsymbol{\sigma} \otimes \mathbf{I} - \sum_{\alpha=1}^{N} (\mathbf{C} : \mathbf{P}^{(\alpha)} + \boldsymbol{\beta}^{(\alpha)}) \otimes \frac{d\dot{\gamma}^{(\alpha)}}{d\mathbf{D}} \tag{2.86}$$

10. Update stresses and the solution dependent state variables.

2.3 Parameters for CPFEM model and Bassani-Wu hardening law

The parameters used for the hardening model, as described in Equation (2.60) to Equation (2.62) are shown in Table 2.1. They were found by fitting the simulated stress strain curve with the experimental results of single crystal alumnium under plane strain compression [124-126]. Three elastic moduli that form the tensor of elastic moduli $\mathbf{C_0}$ which appears in Equation (2.40) are $[\mathbf{C_0}]_{11}$ = 112,000 MPa, $[\mathbf{C_0}]_{12}$ = 66,000 MPa, and $[\mathbf{C_0}]_{44}$ = 28,000 MPa. Other elements in $\mathbf{C_0}$ are zeros. In the deformed aluminum samples in this study slips occur on {111} planes and in <110> directions. Their combination defines 12 slip systems. Hence the value for N in equations in Sections 2.1 and 2.2 is 12. These parameters characterize the properties of a pure aluminum single crystal and will be used throughout the simulations in this work.

Table 2.1 Parameters used in the Bassani-Wu hardening model

n	$\dot{\gamma}_0$ (1/s)	H_0(MPa)	h_s(MPa)	τ_1(MPa)	T_0(MPa)	q	γ_0
300	0.0001	100	0.01	6.3	6	0	0.001

a1	a2	a3	a4	a5
1.75	1.75	1.75	2	2.25

The value of the latent hardening ratio q, as it appeared in Equation (2.62b), used during this work is 0. Note that the single slip hardening law described by Equation (2.62a) comprises of two parts $F\left(\gamma^{(\alpha)}\right)=\left[(h_0-h_s)\sec h^2\left(\frac{(h_0-h_s)\gamma^{(\alpha)}}{\tau_1-\tau_0}\right)+h_s\right]$, which is the instantaneous hardening modulus under single slip and cross hardening $G\left(\gamma^{(\beta)}\right)=\left[1+\sum_{\substack{\beta=1\\ \beta\neq\alpha}}^{N} f_{\alpha\beta}\tanh(\frac{\gamma^{(\beta)}}{\gamma_0})\right]$, which describes the hardening of system α due to slip on system β. The latent hardening effect is hence naturally adopted [115].

2.4 Conclusions

This chapter has described the basic theory of crystal plasticity and presented the step-by-step implementation of this theory into Abaqus/Standard. The chapter has also discussed aspects of the Bassani-Wu hardening law. The number of parameters required to characterize this hardening law is greater than many other hardening laws, e.g. those proposed by Taylor [118], Budiansky and Wu [119], Hutchinson [120], Asaro [117], Havner and Shalaby [121]. This may be the reason that not many crystal plasticity models found in the literature incorporate the Bassani-Wu hardening law. However, by using the Bassani-Wu hardening law, the CPFEM model developed in this chapter can capture more accurately the three-stage hardening within slip systems. This capability is not available if other hardening laws are used.

A single set of parameters will be used throughout simulations in this thesis to characterize the constitutive law of the crystal plasticity theory and the Bassani-Wu hardening law. These parameters have been determined by the current author and his co-workers from fitting simulated stress strain curves with various experimental results of single crystal aluminum under plane strain compression.

3. Verification of the CPFEM Formulation

The aim of this chapter is validating the CPFEM model developed in Chapter 2. Patil et al. [65] and Flouriot et al. [64] have conducted experiments to investigate behaviours of crack tip fields in fcc single crystal under tensile load. Details of their experimental results have been presented in Section 1.3. In this chapter the CPFEM model has been used to simulate these experiments. Qualitative comparison of the predicted slip trace direction and misorientation angle with the experimental observations clearly indicates that the developed CPFEM can accurately predict the texture evolution during the deformation of SEN single crystals aluminum under tensile test.

3.1 CPFEM model

Two experimental cases have been modelled and compared. They are denoted as Case I for experiments done by Patil et al. [65] and Case II for those done by Flouriot et al [64]. The sample dimensions and initial crystal orientation in the CPFEM model are identical to the experiments. The geometry of the sample, the boundary conditions, and crystal orientations with respect to the sample coordinate system are sketched in Figure 3.1. The sample thickness is 1 mm. The extension was applied at the rate of 0.1 mm/min, until it reached 0.1 mm. The sample was meshed by 114,320 C3D8 elements (8-node linear brick), with ten elements along the sample thickness, and finer mesh in the region around the notch. The mesh is shown in Figure 3.2.

To simulate Case I, the initial crystal orientation was arranged so that the [101] and [010] orientations in the local coordinate system of the crystal were coincident with the X and Y axes in the sample coordinate system (Figure 3.1). For Case II sample, the X and Y global axes are coincident with the [100] and [010] lattice orientations respectively. The mesh, the load and the boundary conditions were not altered.

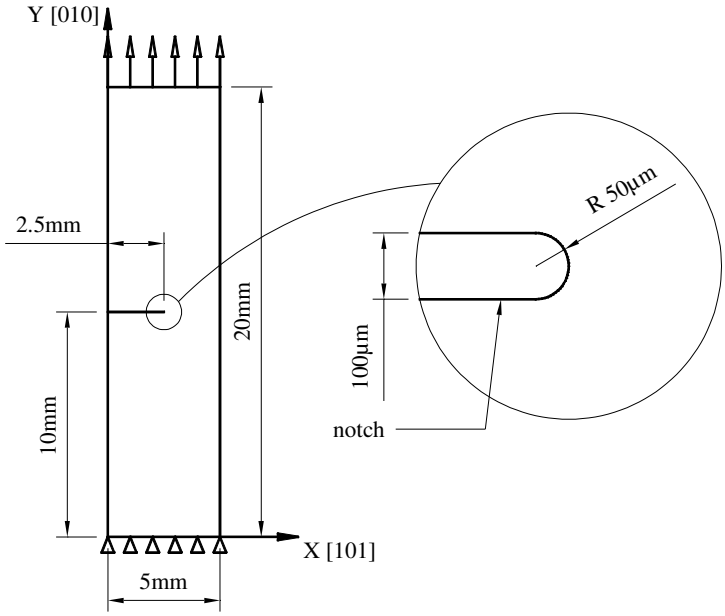

Figure 3.1 Sketch of the FEM model of tensile test sample for verification purposes.

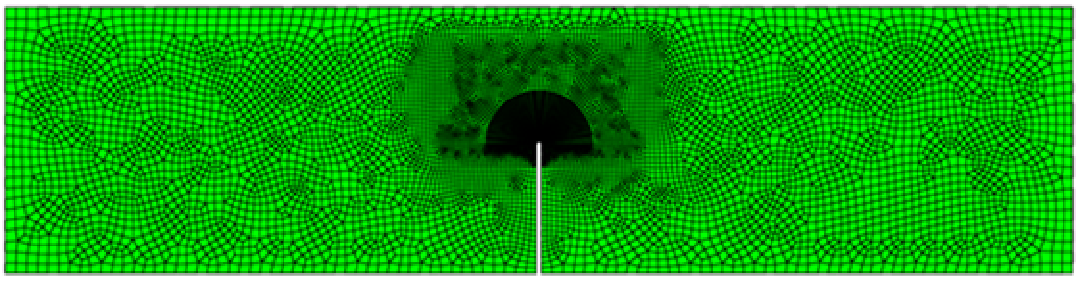

(a) Mesh of the whole sample

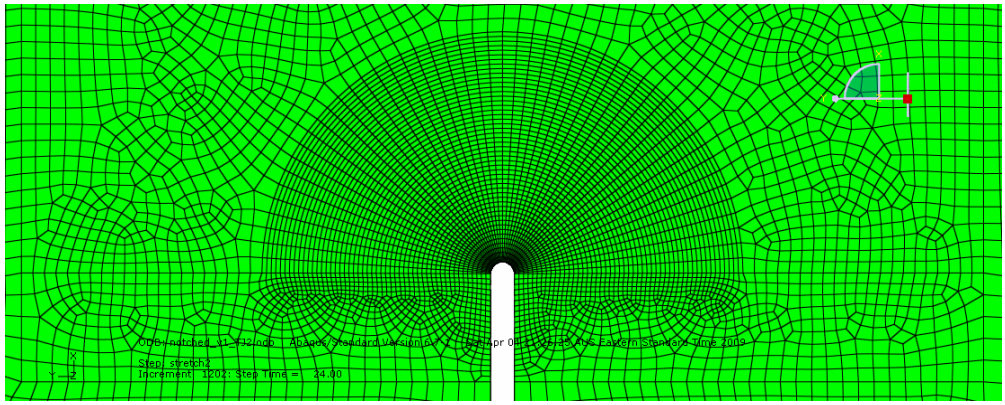

(b) Mesh in region around notch

Figure 3.2 Mesh of the FEM model for verification purposes.

3.2 Analyses and discussions of CPFEM results

3.2.1 Slip traces

Experimental observations of the slip trace reported by Patil et al. [65] are shown in Figure 3.3. It shows that slip traces appear around the notch tip on the sample surface at a very early stage of loading (0.1 mm extension or 0.5% nominal strain), and approximately incline ± 55^{o} to the direction of the notch tip. As the loading increases, slip traces increase both in number and degree of severity. At 0.2 mm extension or 1% nominal strain, another set of slip traces appear, which are parallel to the direction of the notch tip, as shown in Figure 3.3b.

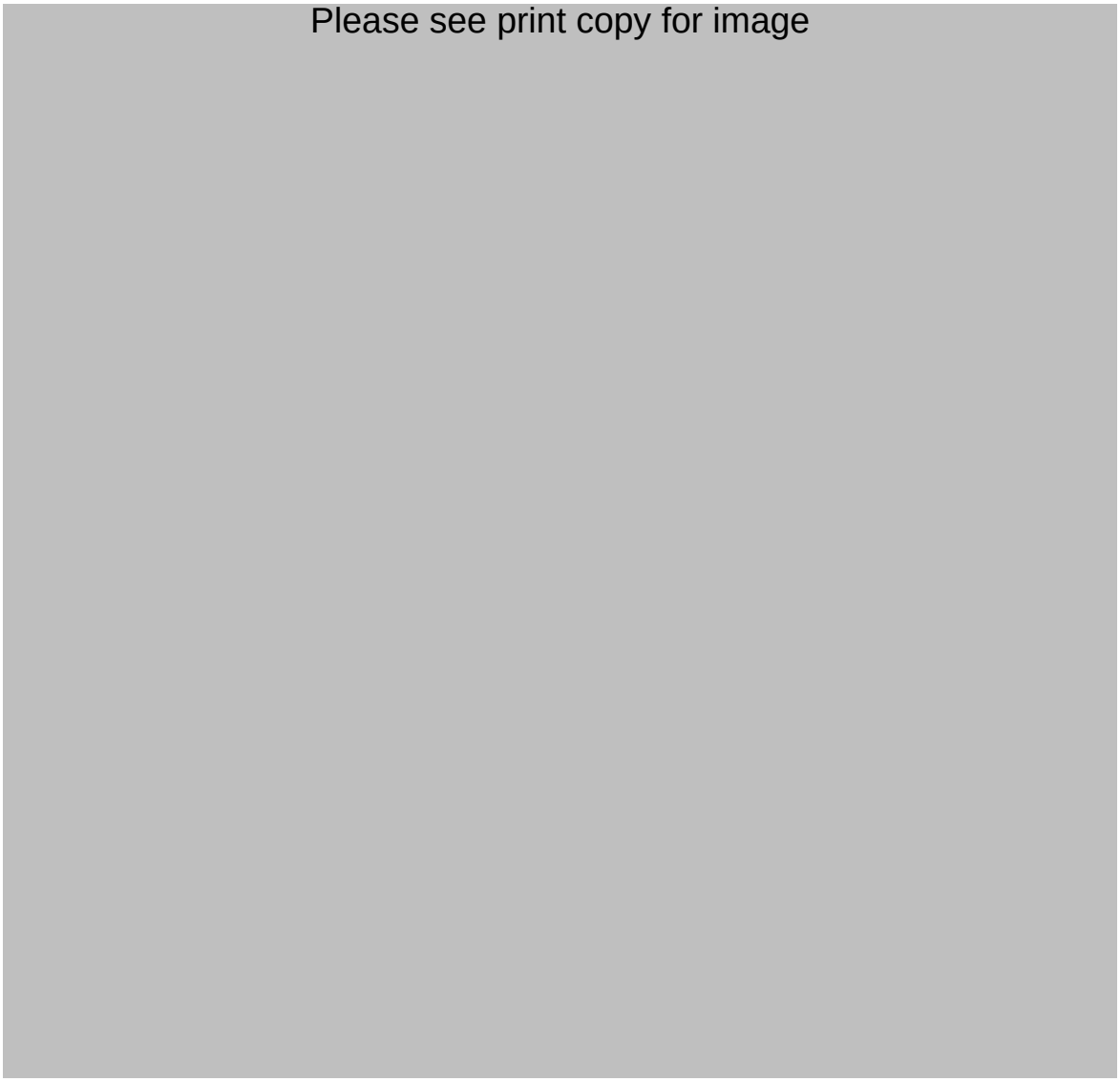

(b) Slip traces at 0.2 mm extension (1% nominal strain)

Figure 3.3 Slip traces observed in tensile experiments [65].

Rice et al. [60] and Patil et al. [65] used contour plots of the sum of magnitude of slips over all the slip systems to represent the constant stress angular zones from Rice's solutions for a stationary crack tip in the $(010)[101]$ orientation [50]. These contour plots are shown in Figure 3.4. In Figure 3.4a, the notch lies along the horizontal axis with its tip at x = 0. The same approach was used by Flouriot et al. [64] to numerically verify their analytical solutions for a stationary crack tip in the $(001)[100]$ orientation. The contour plot of the sum of magnitude of slips in this case is shown in Figure 3.9a. Indeed these approaches do not exactly describe the nature of the slip traces involved in the theoretical analyses and those observed in the experiments. Slip traces are defined as intersections between slip planes on which major plastic slips occur and the plane being considered (in a plane strain analysis), or with the sample surface (in experimental observations where the deformed sample surface remains reasonably parallel with the original one, i.e. in small deformations).

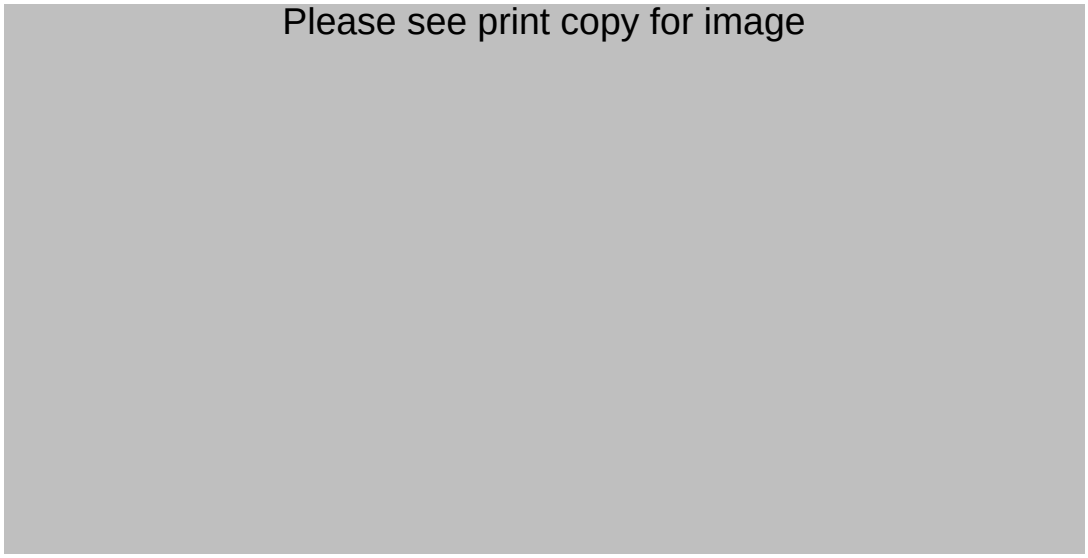

Figure 3.4 Contour plots of the sum of magnitude of slip over all the slip systems around a stationary $(010)[101]$ notch tip by (a) Rice et al. [60] and (b) Patil et al. [65]

Let us assume that the load is small enough so that moderate deformation occurs in the region around the notch tip, but not too close to the boundary where stress concentration may occur. The orientation of slip traces on the sample surface can be predicted based on the original orientation of the crystals. These analyses for slip traces are schematically demonstrated in Figures 3.5 and 3.10 for the notch tip in $(010)[101]$ (Case I) and $(001)[100]$ (Case II) orientations, respectively.

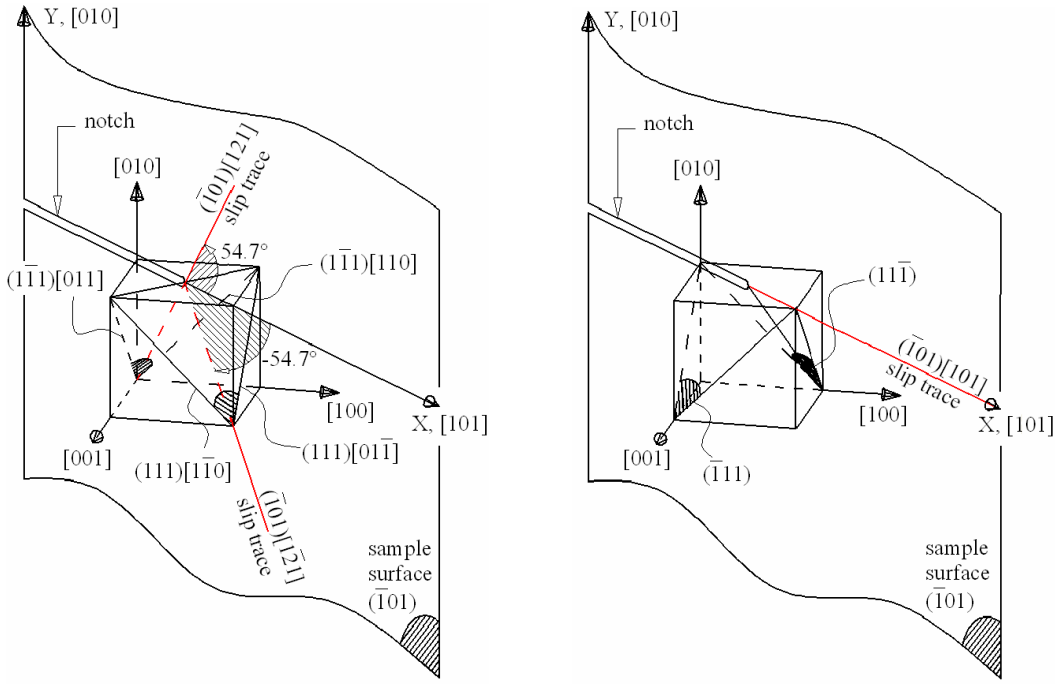

(a) Slip traces $(121)[\bar{1}01]$ and $(1\bar{2}1)[\bar{1}01]$ (b) Slip trace $(101)[\bar{1}01]$

Figure 3.5 Sketch of traces on the sample surface for the $(010)[101]$ notch tip.

Using the normal vectors to slip plane from CPFEM results, the direction of slip traces of active slip systems can be plotted on the sample surface. At each integration point of those elements closest to the sample surface, the slip system with maximum absolute shear strain is picked out. It is also noted that slip value is weighted by a scalar product that reflects the relative orientations of the sample surface and the considered slip system. If this product vanishes (e.g. in the case where the slip system is parallel with the observation surface plane), the trace will not be visible on the surface even if the actual theoretical amount of slip is large. The orientation of the intersection of the corresponding slip plane and the plane of the sample surface is determined. The sample surface plane is determined via three corners of the sample surface. Each intersecting line is represented by a segment of straight line, the direction of which infers the orientation of the slip trace. Segments of straight line corresponding to the integration points in the same element are plotted at the same point, which is the centroid of that element at the current deformed state. Darker lines infer higher shear strains.

Following the above discussions, the plots of slip traces around the notch tip on the sample surface in the final deformed state (extension 0.1 mm or 0.5% nominal strain)

are shown on the left of Figure 3.6. Slip traces in the upper half and lower half of the notch are symmetrical. Two insets (a) and (b), located at the top-right and front of the notch, respectively, are selected and separately shown on the right of the figure. Evidently, inset (a) shows that slip traces appear to incline at 54.5^{o} to the direction of the notch tip, which agree with the experimental results in Figure 3.3a very well. Inset (b) shows traces parallel to the direction of the notch tip while they do not seem to appear on the tested sample surface. It should be noted that these traces on the numerical plot are considerably lighter than others, which could be interpreted in the experimental context that they are not (yet) significant to be seen. Indeed, at a higher applied extension of 0.2 mm (1% nominal strain), the experimental images of the sample surface in Figure 3.3b clearly show the existence of these traces. In a region very close to the notch boundary, as shown in inset (c), concentrated stress exists. The crystal in this region deforms and rotates severely from the original orientation. Thus the direction of slip traces in this area deviates considerably from the three major directions, i.e. ± 54.7^{o} and 0^{o} shown in Figure 3.5. It is also noted that darker slip traces in inset (c) compared to slip traces in other regions indicate the existence of the concentrated deformation in this region around the boundary of the notch.

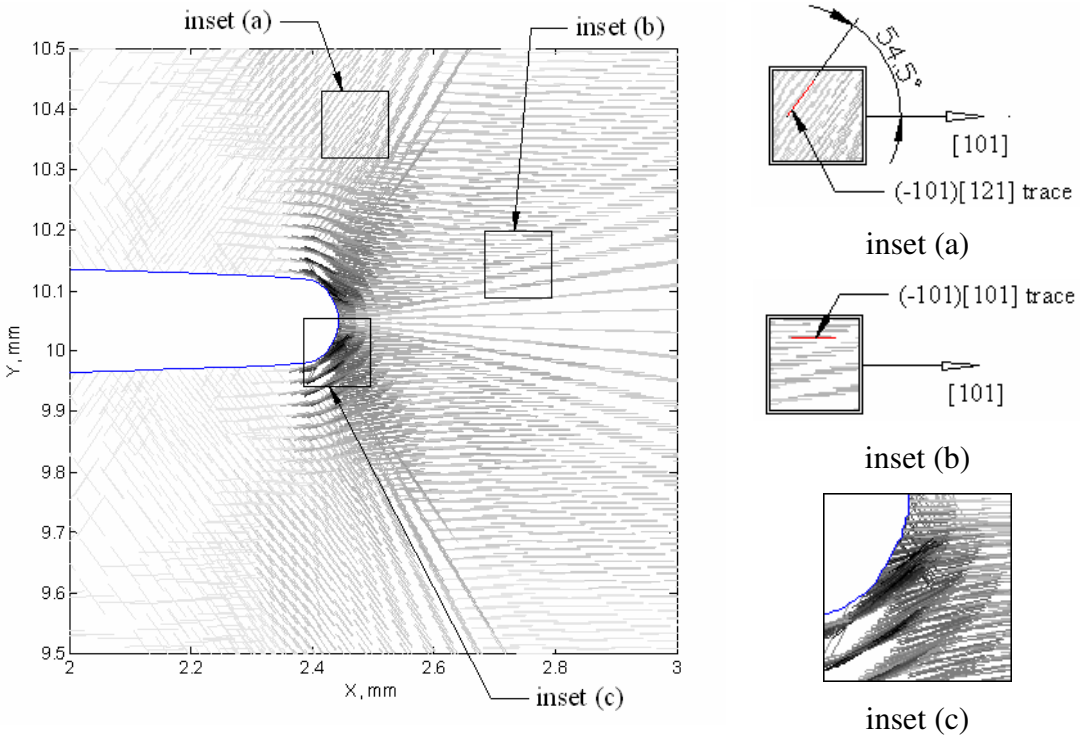

Figure 3.6 Numerical plots of slip traces on the sample surface around the (010)[101] notch tip, at 0.5% nominal strain.

Figure 3.5 shows that traces on the sample surface are in directions [121], $[1\bar{2}1]$ and [101]. Trace [121] is the result of simultaneous and equal slips on the $(1\bar{1}1)[110]$ and $(1\bar{1}1)[011]$ slip systems. Hence if we let $\Gamma^{[121]}$ be the resulting slip in [121] direction we then have

$$\begin{aligned}\Gamma^{[121]} &= \left|\gamma^{(1\bar{1}1)[110]}_{(\bar{1}01)}\right| + \left|\gamma^{(1\bar{1}1)[011]}_{(\bar{1}01)}\right| \\ &= \left|\gamma^{(1\bar{1}1)[110]}\right|\cos(30^o) + \left|\gamma^{(1\bar{1}1)[011]}\right|\cos(30^o)\end{aligned} \tag{3.1}$$

The notation $\left|\gamma^{\alpha}_{(\beta)}\right|$ indicates the absolute value of slip on system α projected to plane (β). Similarly, the resulting slips in the $[1\bar{2}1]$ direction (as a result of combined slips on $(111)[1\bar{1}0]$ and $(111)[0\bar{1}1]$ systems) and in the [101] direction (as a result of combined slips on $(11\bar{1})[101]$ and $(\bar{1}11)[101]$ systems) are expressed respectively as

$$\begin{aligned}\Gamma^{[1\bar{2}1]} &= \left|\gamma^{(111)[1\bar{1}0]}_{(\bar{1}01)}\right| + \left|\gamma^{(111)[0\bar{1}1]}_{(\bar{1}01)}\right| \\ &= \left|\gamma^{(111)[1\bar{1}0]}\right|\cos(30^o) + \left|\gamma^{(111)[0\bar{1}1]}\right|\cos(30^o)\end{aligned} \tag{3.2}$$

$$\Gamma^{[101]} = \left|\gamma^{(11\bar{1})[101]}\right| + \left|\gamma^{(\bar{1}11)[101]}\right| \tag{3.3}$$

Contour plots of $\Gamma^{[121]}$, $\Gamma^{[1\bar{2}1]}$ and $\Gamma^{[101]}$ on the sample surface and on the mid-thickness plane for the $(010)[101]$ notch tip are presented in Figures 3.7 and 3.8, respectively. Compared to the contour plots of the total of magnitude of slip in all slip systems in Figure 3.4, the plots in Figures 3.7 and 3.8 show more clearly the distribution of shear strain of each slip trace. Large values of $\Gamma^{[101]}$ distribute 90^o to the notch tip while the orientation of the distributions of $\Gamma^{[121]}$ and $\Gamma^{[1\bar{2}1]}$ incline about $\pm 61^o$ to the notch tip direction. The shape of contours on the sample surface (Figure 3.7) and on the interior plane (Figure 3.8) is similar at every stage of loading. Superposing Figures 3.7a, 3.7b and 3.7c results in a contour plot that has the general shape similar with those in Figure 3.4.

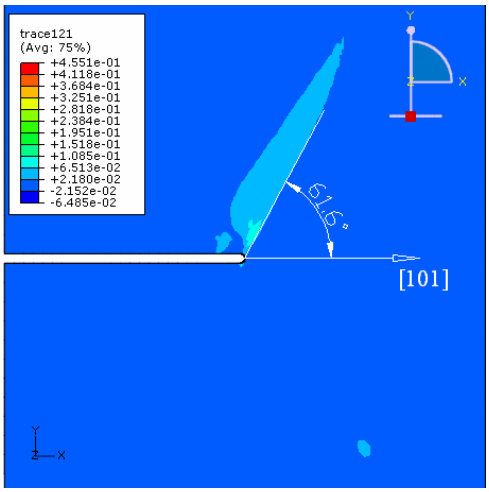

(a) $\Gamma^{[121]}$

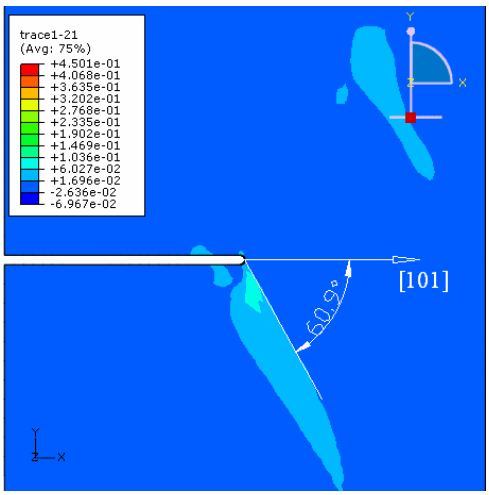

(b) $\Gamma^{[1\bar{2}1]}$

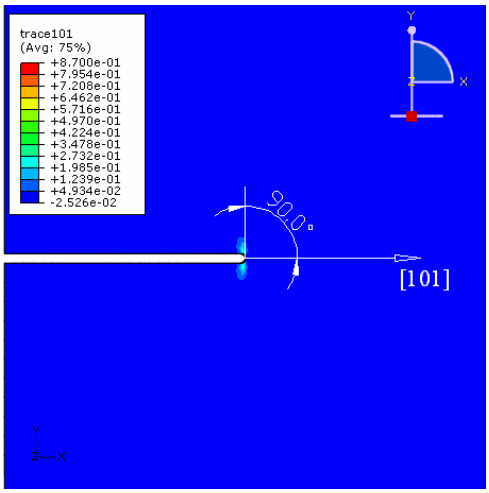

(c) $\Gamma^{[101]}$

Figure 3.7 Contour plots of $\Gamma^{[121]}$, $\Gamma^{[1\bar{2}1]}$ and $\Gamma^{[101]}$ on the sample surface, (010)[101] notch tip, at 0.5% nominal strain.

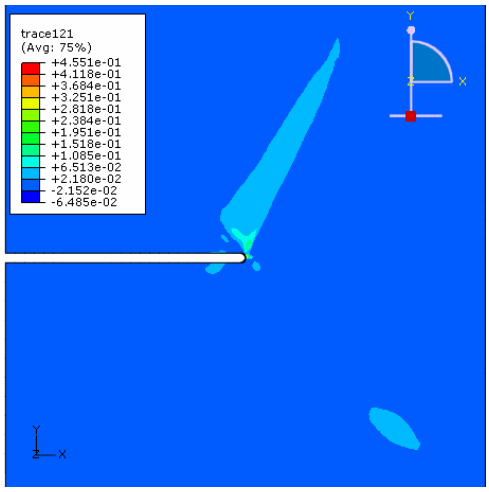

(a) $\Gamma^{[121]}$

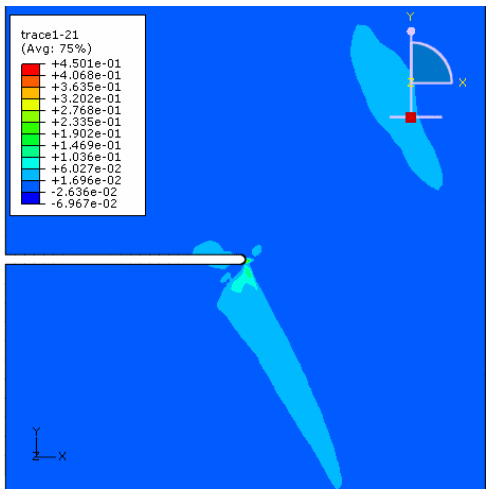

(b) $\Gamma^{[1\bar{2}1]}$

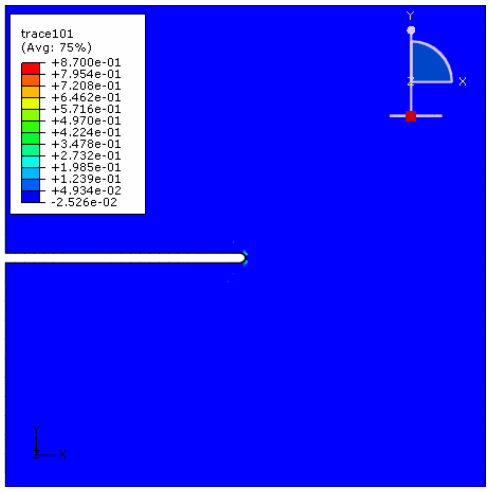

(c) $\Gamma^{[101]}$

Figure 3.8 Contour plots of $\Gamma^{[121]}$, $\Gamma^{[1\bar{2}1]}$ and $\Gamma^{[101]}$ on the mid-thickness plane, (010)[101] notch tip, at 0.5% nominal strain.

For a notch tip in the $(001)[100]$ orientation, the experimental image of slip traces on the sample surface around the notch tip is shown in Figure 3.9b [64]. It is evident that the slip traces symmetrically incline 45^o to the notch tip direction. These traces are intersections of the activated slip plane $(1\bar{1}1)$ and (111) with plane (001), as schematically demonstrated in Figure 3.10.

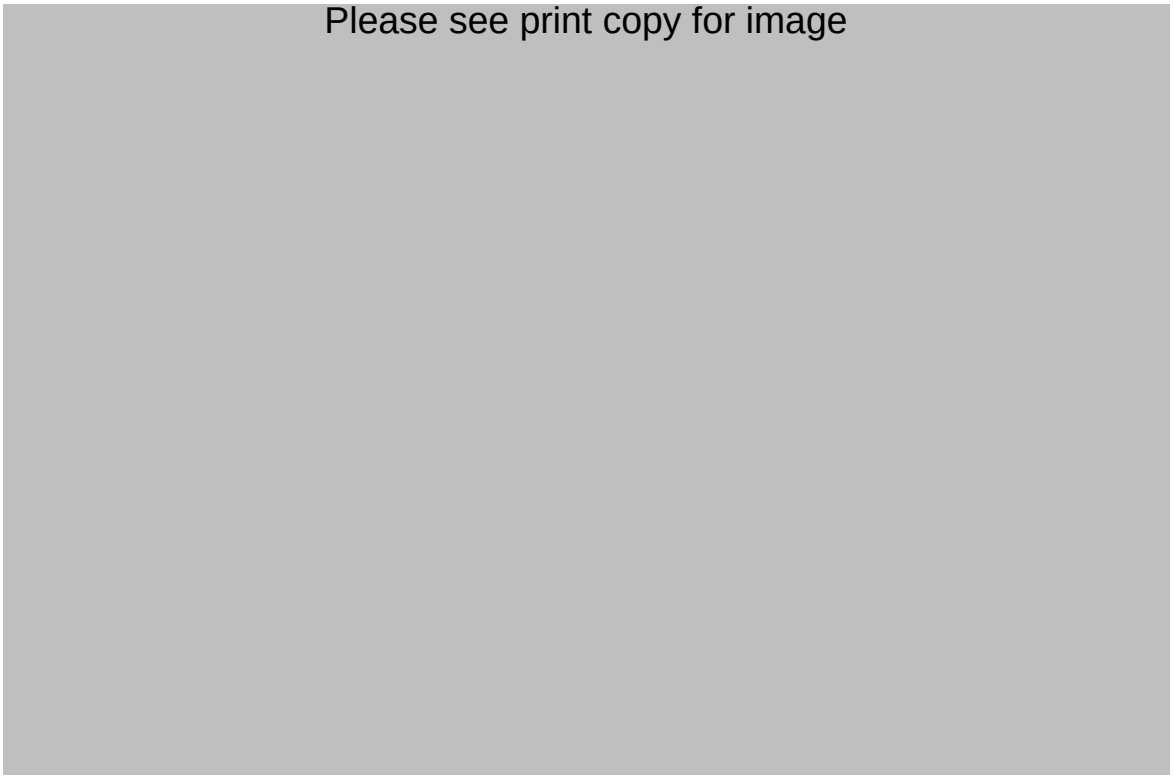

Figure 3.9 Results around the $(001)[100]$ crack tip [64] (a) Contour plot of the total of magnitude of slip on all slip systems, (b) Slip traces observed in experiments.

Following the discussions used to produce Figure 3.6, slip traces on the sample surface for this case of notch tip (in the $(001)[100]$ direction) are plotted in Figure 3.11. Insets (a) and (b) located symmetrically ahead of the notch tip clearly show that traces incline $\pm 45^o$ to the direction of notch tip. These results match very well with the image of slip traces obtained from experiments (see Figure 3.9b). Inset (c) in Figure 3.11 shows slip traces in a region close to the boundary of the notch. It reveals that large deformation occurs in this area, evinced by darker slip traces, compared to other regions, e.g. insets (a) and (b). However, the crystals do not appear to rotate much from the original orientation. This is evidenced by the direction of slip traces in this region, which incline approximately $\pm 45^o$ to the direction of the notch tip.

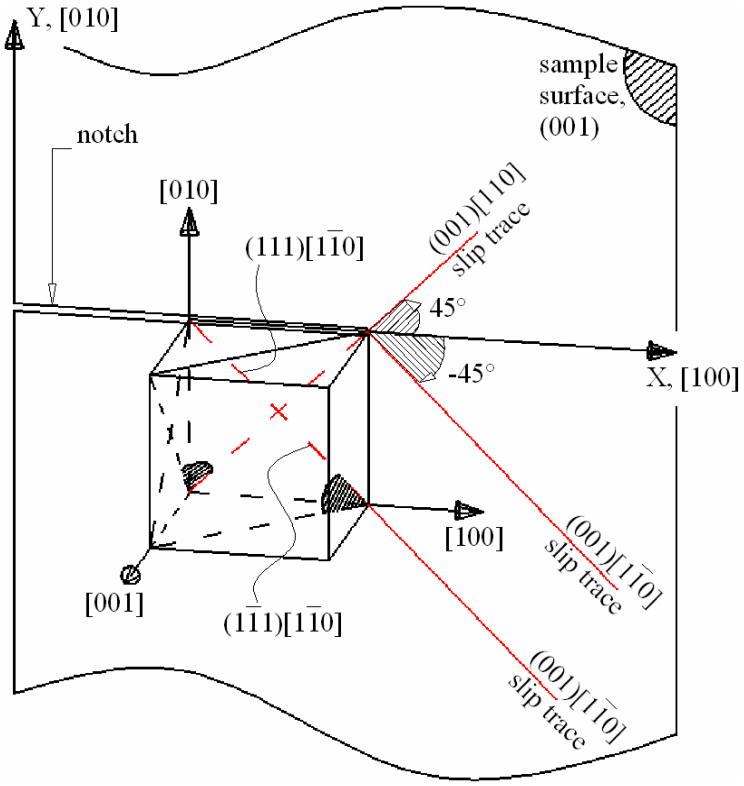

(a) Slip traces (001)[110] and (001)[1 $\bar{1}$ 0]

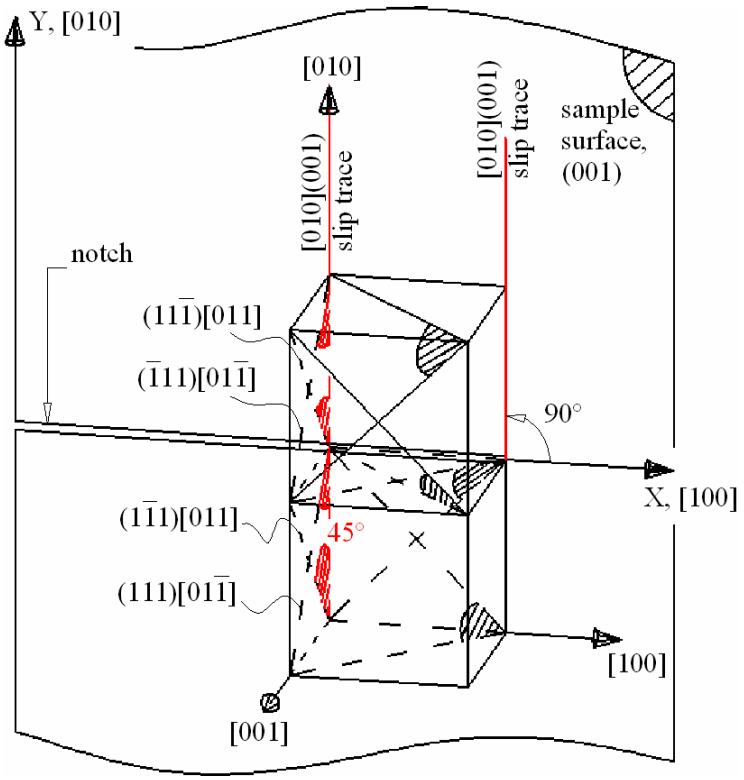

(b) Slip trace (001)[010]

Figure 3.10 Sketch of traces on the sample surface for the (001)[100] notch tip.

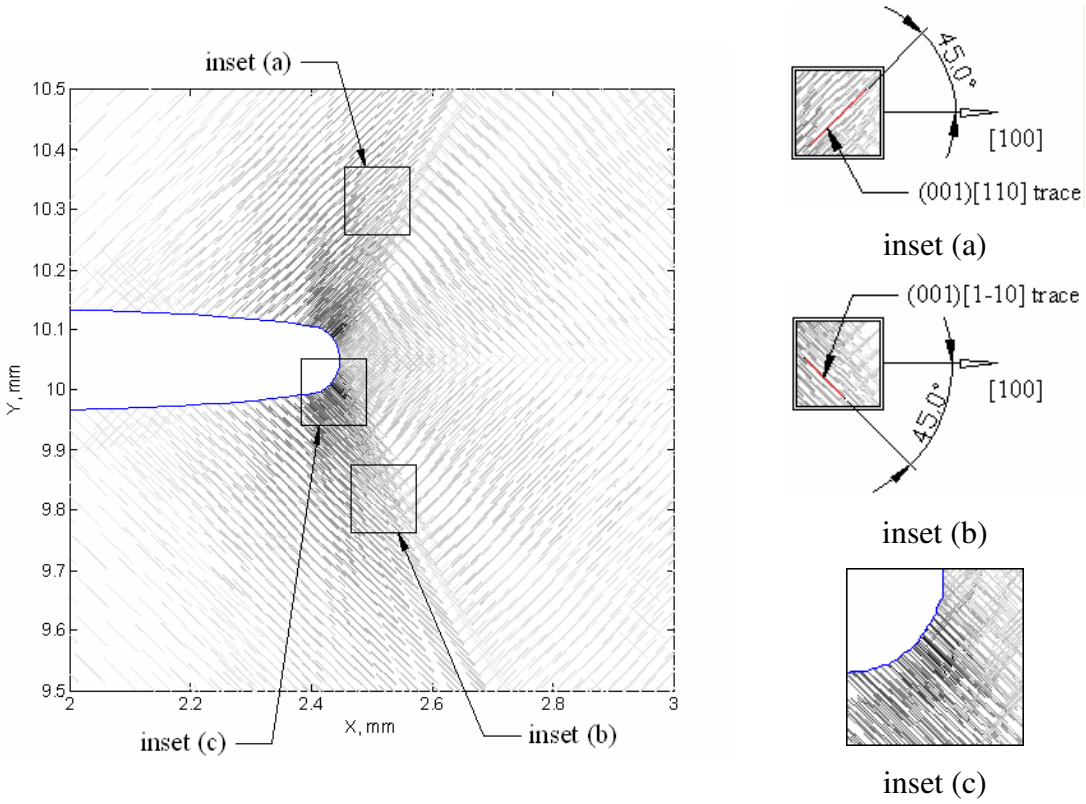

Figure 3.11 Numerical plot of slip traces on the sample surface around the $(001)[100]$ notch tip at 0.5% nominal strain.

As shown in Figure 3.10, traces around the notch tip in this case can be reasonably considered as the superpose of net slips occurring on systems $(\bar{1}11)[110]$ and $(1\bar{1}1)[110]$ (for the 45° ray) and of net slips on systems $(111)[1\bar{1}0]$ and $(11\bar{1})[1\bar{1}0]$ (for the 135° or -45° ray). The vertical ray can be considered as the sum of simultaneous slips occurring on four octahedral systems $(111)[0\bar{1}1]$, $(\bar{1}11)[0\bar{1}1]$, $(1\bar{1}1)[011]$ and $(11\bar{1})[011]$. Similar to the $(010)[101]$ notch tip, the resulting slips of the above combinations are expressed mathematically as

$$\Gamma^{[110]} = \left|\gamma^{(\bar{1}11)[110]}\right| + \left|\gamma^{(1\bar{1}1)[110]}\right| \tag{3.4}$$

$$\Gamma^{[1\bar{1}0]} = \left|\gamma^{(111)[1\bar{1}0]}\right| + \left|\gamma^{(11\bar{1})[1\bar{1}0]}\right| \tag{3.5}$$

$$\begin{aligned}\Gamma^{[010]} &= \left|\gamma^{(111)[0\bar{1}1]}_{(001)}\right| + \left|\gamma^{(\bar{1}11)[0\bar{1}1]}_{(001)}\right| + \left|\gamma^{(1\bar{1}1)[011]}_{(001)}\right| + \left|\gamma^{(11\bar{1})[011]}_{(001)}\right| \\ &= \left(\left|\gamma^{(111)[0\bar{1}1]}\right| + \left|\gamma^{(\bar{1}11)[0\bar{1}1]}\right| + \left|\gamma^{(1\bar{1}1)[011]}\right| + \left|\gamma^{(11\bar{1})[011]}\right|\right)\cos(45^o)\end{aligned} \tag{3.6}$$

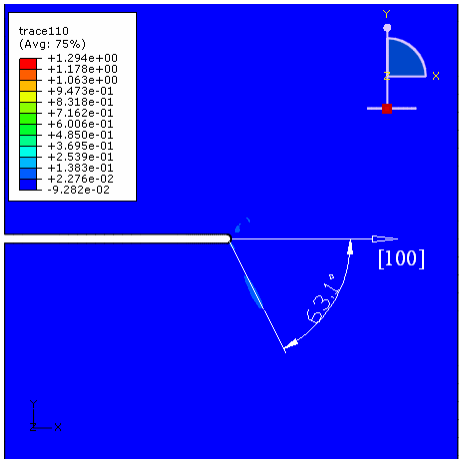

(a) $\Gamma^{[110]}$

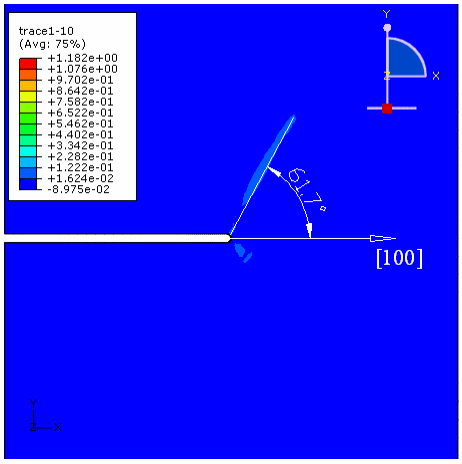

(b) $\Gamma^{[1\bar{1}0]}$

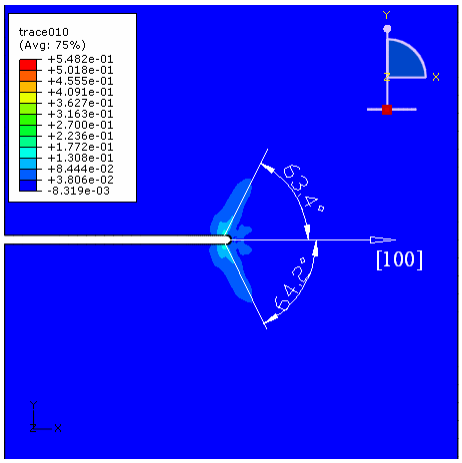

(c) $\Gamma^{[010]}$

Figure 3.12 Contour plots of $\Gamma^{[110]}$, $\Gamma^{[1\bar{1}0]}$, $\Gamma^{[010]}$ on sample surface, (001)[100] notch tip, at 0.5% nominal strain

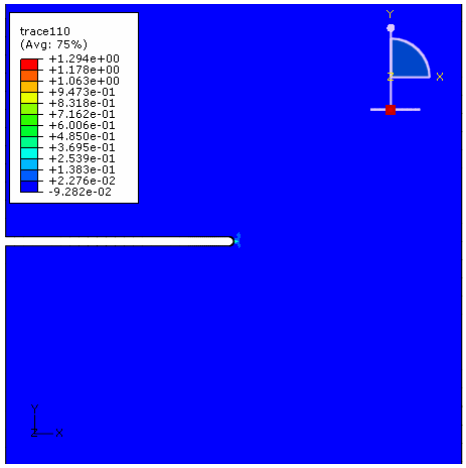

(a) $\Gamma^{[110]}$

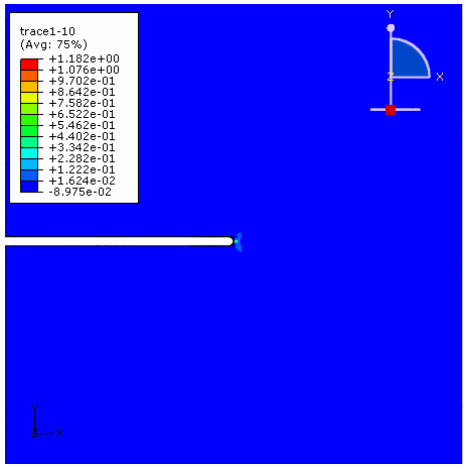

(b) $\Gamma^{[1\bar{1}0]}$

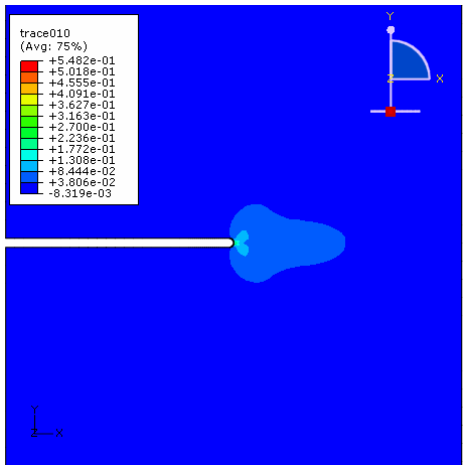

(c) $\Gamma^{[010]}$

Figure 3.13 Contour plots of $\Gamma^{[110]}$, $\Gamma^{[1\bar{1}0]}$, $\Gamma^{[010]}$ on the mid-thickness plane, (001)[100] notch tip, at 0.5% nominal strain

The contour plot of the total of magnitude of slip on all slip systems from FEM simulation by Flouriot et al. [64] is shown in Figure 3.9(a). It shows that bands of concentrated slip incline at about 60^o to the direction of the notch tip. The contour plots of $\Gamma^{[110]}$, $\Gamma^{[1\bar{1}0]}$ and $\Gamma^{[010]}$ on the sample surface and the mid-thickness plane are shown in Figures 3.12 and 3.13, respectively. The use of $\Gamma^{[110]}$, $\Gamma^{[1\bar{1}0]}$ and $\Gamma^{[010]}$ to separately represent slip traces helps showing the distribution of shear strain in each slip trace more clearly. The maximum shear strain in slip trace $(001)[110]$ inclines -63.1^o to the notch tip while that in slip trace $(001)[1\bar{1}0]$ distributes in a band that inclines 61.7^o to the notch tip. Shear strain in slip trace $(001)[010]$ forms two bands approximately symmetric around the notch tip direction. These bands incline 63.4^o and -64.2^o to the notch tip direction. The inclination of bands in contour plots in Figure 3.12 is similar to that in Figure 3.9(a). Also, contour plots in Figures 3.12 and 3.13 have same shape and reveal that more slip activities generally occur on the sample surface (Figure 3.12) than on the interior plane (Figure 3.13).

3.2.2 Crystal rotations

Patil et al. [65] also reported the measuring of the inhomogeneity of crystal orientations around the notch tip in the $(010)[101]$ direction by using an inverse pole figure, which revealed concentrated bands of misorientation that inclined 45^o and 90^o with the notch tip direction (see Figure 3.14).

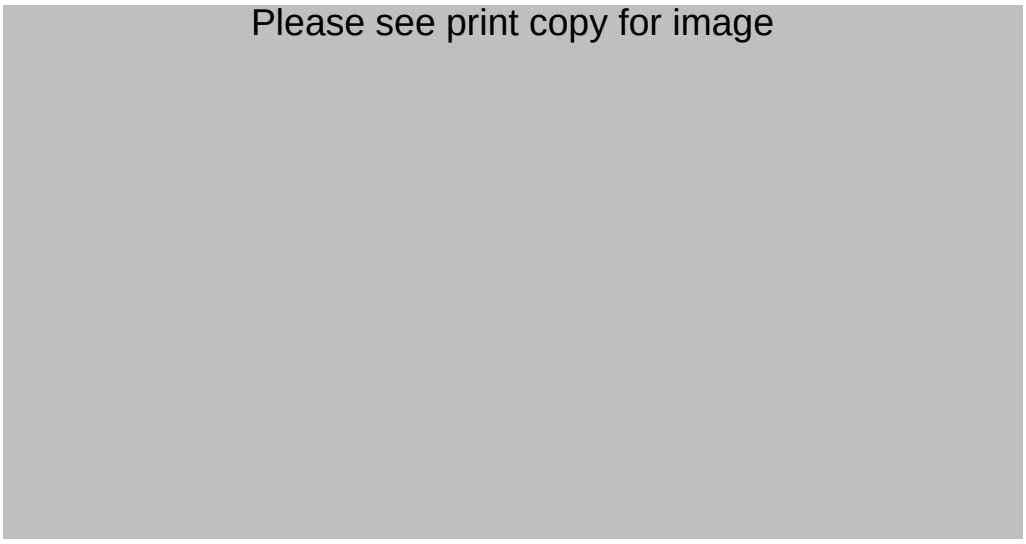

Figure 3.14 (a) Inverse pole figure obtained from EBSD for sample surface around the $(010)[101]$ notch tip and (b) the color code used [65].

Theoretically, such inhomogeneity is the result of different crystal rotations at various points. Numerically, if we characterize the evolution of crystal orientation at a crystal *i* by a matrix $\mathbf{R}_\mathbf{i}^\mathbf{k}$ which transforms the crystal lattice from the original state (no loading applied) to a later state *k* during loading, $\mathbf{R}_\mathbf{i}^\mathbf{k}$ can be expressed as

$$\mathbf{R}_\mathbf{i}^\mathbf{k} = \mathbf{N}_\mathbf{i}^\mathbf{k} \bullet \left(\mathbf{N}_\mathbf{i}^\mathbf{0}\right)^{-1} \tag{3.7}$$

$\mathbf{N}_\mathbf{i}^\mathbf{0}$ representing the initial orientation of the crystal lattice at a crystal *i* comprises any three of the four normal vectors of slip planes {111} in the global coordinate system. $\mathbf{N}_\mathbf{i}^\mathbf{k}$ is a set of the corresponding normal vectors in $\mathbf{N}_\mathbf{i}^\mathbf{0}$ at a state *k*, representing the orientation of crystal *i* in the global coordinate system at this state. It is assumed in CP theory that the crystal structures remain unchanged during loading, i.e. the relative angles between normal vectors of {111} planes are reserved. Hence, if normal vectors in $\mathbf{N}_\mathbf{i}^\mathbf{0}$ and $\mathbf{N}_\mathbf{i}^\mathbf{k}$ are normalized, the matrix $\mathbf{R}_\mathbf{i}^\mathbf{k}$ determined in Equation (3.7) becomes an orthogonal and normalized rotation matrix. This implies that three columns of $\mathbf{R}_\mathbf{i}^\mathbf{k}$ are coordinates of three unit vectors defining the local coordinate system of crystal *i* in the global coordinate system. Hence, $\mathbf{R}_\mathbf{i}^\mathbf{k}$ is called in this work the orientation matrix of crystal *i* at state *k*. The total rotation angle of crystal *i* from the initial orientation to that at state *k* can be determined from $\mathbf{R}_\mathbf{i}^\mathbf{k}$ by

$$2\cos\theta_i + 1 = \left(\mathbf{R}_\mathbf{i}^\mathbf{k}\right)_{11} + \left(\mathbf{R}_\mathbf{i}^\mathbf{k}\right)_{22} + \left(\mathbf{R}_\mathbf{i}^\mathbf{k}\right)_{33} \tag{3.8}$$

A contour plot of θ_i could be used to capture the inhomogeneity in crystal orientation around the notch tip as observed experimentally by Patil et al [65]. For a notch tip in the $(010)[101]$ direction, the initial crystal orientation was specified in Section 3.1. Hence, $\mathbf{N}_\mathbf{i}^\mathbf{0}$ which is the same at all points as single crystal is being considered is determined as

$$\mathbf{N}_\mathbf{i}^\mathbf{0} = \begin{bmatrix} 2/\sqrt{6} & 0 & 2/\sqrt{6} \\ 1/\sqrt{3} & 1/\sqrt{3} & -1/\sqrt{3} \\ 0 & 2/\sqrt{6} & 0 \end{bmatrix} \tag{3.9}$$

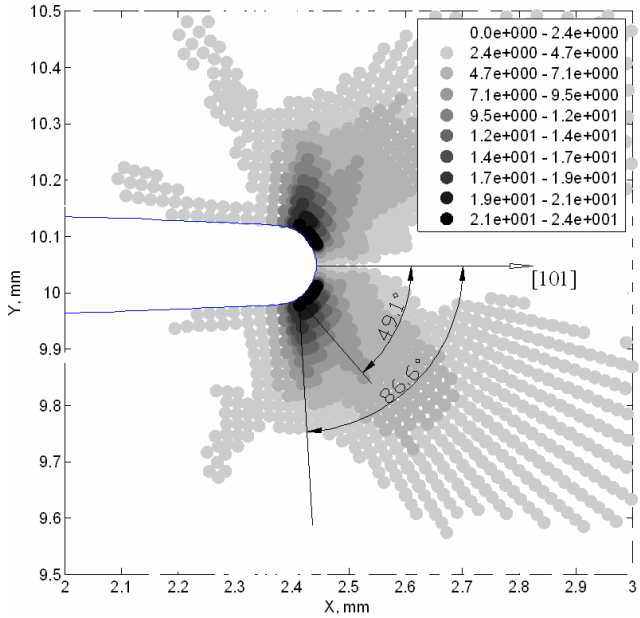

Figure 3.15 Contour plot of the total rotation angle (in degrees) with respect to the initial state, $(010)[101]$ notch tip, at 0.5% nominal strain.

With $\mathbf{N}_i^k$ determined at each integration point from CPFEM modelling, a contour plot of the total rotation angle with respect to the initial state is produced, as shown in Figure 3.15. The same plot is also produced for notch tip in $(001)[100]$ direction as shown in Figure 3.16, with $\mathbf{N}_i^0$ described by Equation 3.10. The unit in these plots is degrees.

$$\mathbf{N}_i^0 = \begin{bmatrix} 1/\sqrt{3} & -1/\sqrt{3} & 1/\sqrt{3} \\ 1/\sqrt{3} & 1/\sqrt{3} & -1/\sqrt{3} \\ 1/\sqrt{3} & 1/\sqrt{3} & 1/\sqrt{3} \end{bmatrix} \tag{3.10}$$

Figure 3.15 reveals the same inhomogeneous features as seen in experimental results in Figure 3.14 with some deviations, i.e. concentration bands inclined at roughly 49^o and 87^o to the notch tip. These predictions reasonably agree with the experimental observations (45^o and 90^o). Even though the above contour plots do not give the orientation of crystals at the current state, as seen in an inverse pole figure, they provide a direct measurement of how intensive the crystal evolutions are in the material. For instance, the maximum rotation angle is about 24^o for the notch tip in $(010)[101]$ direction, while that for the notch tip in the $(001)[100]$ direction is only

about 9°. So it can readily be concluded that crystal evolution is more severe in the first case. It is also noticed that the contour is slightly unsymmetrical around the line of the notch tip direction in Figure 3.16. This may be due to the scale of the contour plot is not fine enough to capture small changes of the rotation in the upper half and lower half of the notch.

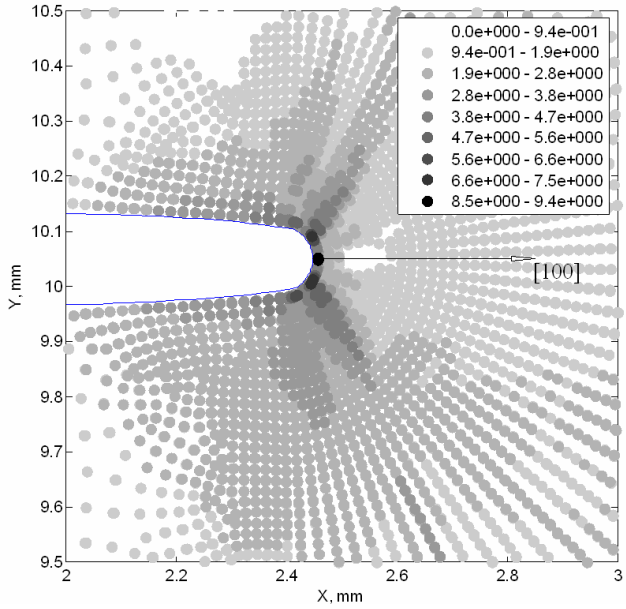

Figure 3.16 Contour plot of the total rotation angle (in degrees) with respect to the initial state, $(001)[100]$ notch tip, at 0.5% nominal strain.

The total rotation angles in Equation (3.8) and in Figures 3.15 and 3.16 can be divided into three components about three axes of the global coordinate system. Such division is carried out following the analysis by Wert et al. [127], which is rewritten in Equation (3.11)

$$\tan\left(\alpha^{hkl}\right)=\frac{A}{B} \tag{3.11}$$

$$A=h\left[\left(\mathbf{R}_{\mathbf{i}}^{\mathbf{k}}\right)_{32}-\left(\mathbf{R}_{\mathbf{i}}^{\mathbf{k}}\right)_{23}\right]+k\left[\left(\mathbf{R}_{\mathbf{i}}^{\mathbf{k}}\right)_{13}-\left(\mathbf{R}_{\mathbf{i}}^{\mathbf{k}}\right)_{31}\right]+h\left[\left(\mathbf{R}_{\mathbf{i}}^{\mathbf{k}}\right)_{21}-\left(\mathbf{R}_{\mathbf{i}}^{\mathbf{k}}\right)_{12}\right]$$

$$\begin{aligned}B=&\left(h^2-1\right)\left(\mathbf{R}_{\mathbf{i}}^{\mathbf{k}}\right)_{11}+\left(k^2-1\right)\left(\mathbf{R}_{\mathbf{i}}^{\mathbf{k}}\right)_{22}+\left(l^2-1\right)\left(\mathbf{R}_{\mathbf{i}}^{\mathbf{k}}\right)_{33}+\\&hk\left[\left(\mathbf{R}_{\mathbf{i}}^{\mathbf{k}}\right)_{12}+\left(\mathbf{R}_{\mathbf{i}}^{\mathbf{k}}\right)_{21}\right]+kl\left[\left(\mathbf{R}_{\mathbf{i}}^{\mathbf{k}}\right)_{23}+\left(\mathbf{R}_{\mathbf{i}}^{\mathbf{k}}\right)_{32}\right]+lh\left[\left(\mathbf{R}_{\mathbf{i}}^{\mathbf{k}}\right)_{31}+\left(\mathbf{R}_{\mathbf{i}}^{\mathbf{k}}\right)_{13}\right]\end{aligned}$$

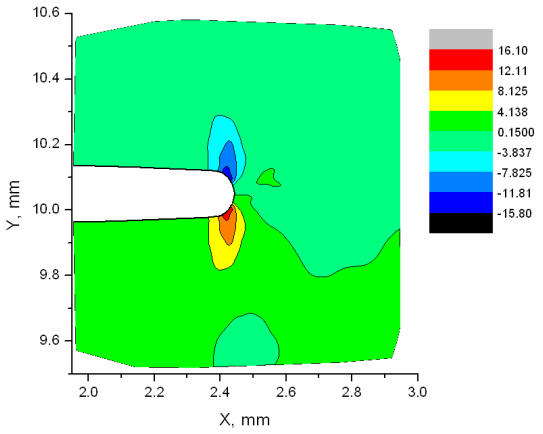

(a) Rotation about global [001] axis

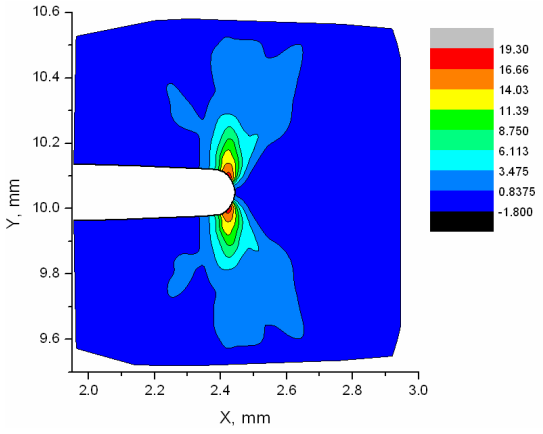

(b) Rotation about global [010] axis

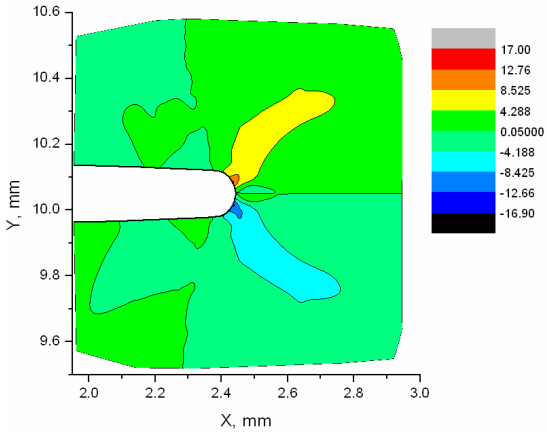

(c) Rotation about global [100] axis

Figure 3.17 Contour plots of component rotations (in degrees) on the sample surface for (010)[101] notch tip, at 0.5% nominal strain.

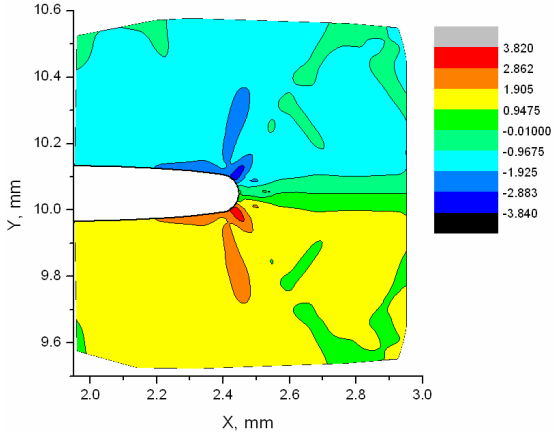

(a) Rotation about global [001] axis

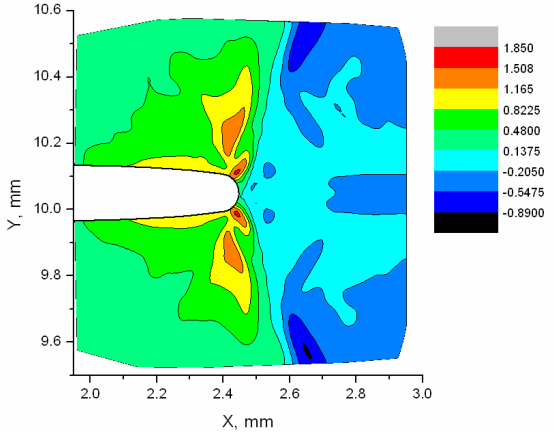

(b) Rotation about global [010] axis

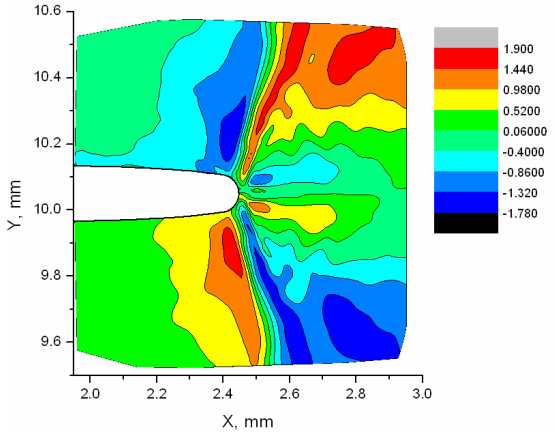

(c) Rotation about global [100] axis

Figure 3.18 Contour plots of component rotations (in degrees) on the sample surface for (001)[100] notch tip, at 0.5% nominal strain.

α^{hkl} is the angle of rotation about a [*hkl*] axis which is in the global coordinate system. To determine the rotation angles about the X, Y and Z axes, [*hkl*] takes the

value of [100], [010], and [001], respectively. The contour plots of these rotation angles on sample surface for the notch tip in the (010)[101] and (001)[100] directions are shown in Figures 3.17 and 3.18. The unit in these plots is degrees.

The larger rotation of crystals in the regions around (010)[101] notch tip compared to the (001)[100] notch tip is also reflected in the component rotations. Figure 3.17 reveals that the upper half and lower half of the regions in front of the notch tip rotate equally in opposite directions around the global [001] and [100] axes. The maximum magnitudes of rotation, which occur at the boundary of the notch, are approximately 16^{o} about the [001] axis (Figure 3.17a) and 17^{o} about the [100] axis (Figure 3.17c). For rotation about the global [010] axis (Figure 3.17b), the crystals in both halves revolve equally of approximately 19^{o} in the same direction. It can readily be concluded that the maximum magnitude of the rotation of crystals around the three global axes are not much different in regions around the (010)[101] notch tip. For a notch tip in the (001)[100] direction (Figure 3.18), the magnitudes of component rotations are lower than those in Figure 3.17. However, the rotations are qualitatively similar to those in the other case. Crystals in the upper and lower halves exhibit equal and opposite rotations about the global [001] and [100] axes (Figures 3.18a and 3.18c, respectively), and rotate equally in the same direction about the global [010] axis (Figure 3.18b). The rotation of crystal in this case is mainly about the global [001] axis with the maximum angle being twice as large as those for the other two axes.

3.3 Conclusions

This chapter has successfully validated the CPFEM formulation and the parameters presented in Chapter 2. The CPFEM simulations of experimental tensile tests of an SEN single crystal have been carried out based on only one single set of parameters. To the best of the author's knowledge, this CPFEM model is among the very few, if not the first, that provide results well matched with various experimental observations of two cases of notch tip orientation widely found in the literature. Also,

by plotting slip traces on the sample surface, this chapter presents direct comparisons (qualitatively) of numerical results with experimental observations, which generally are not available from other studies.

In the first case, the notch tip is in the $(010)[101]$ orientation. The CPFEM model adopt identical conditions to the experimental sample used by Patil et al. [65], in terms of the sample geometry, the boundary conditions, the applied strain load, and the initial crystal orientation. By comparing the slip traces on the sample surface and the inhomogeneity of crystal orientations around the notch tip, the analyses have shown that the simulation results agree very well with the experimental observations [65].

In the second simulation, only the initial crystal orientation is changed so that the notch tip is directed in the $(001)[100]$ orientation. The results of slip traces on the sample surface in this case also match the experimental observations [64] very well.

The difference between Figures 3.12 and 3.13 (also Figures 3.7 and 3.8), i.e. between results on a free surface and on an interior plane, may be due to the different deformation on the two planes. The material on the free surface could deform in a plane stress manner, while that on an interior plane deformed under plane strain condition. Two dimensional plane stress and plane strain simulations need to be carried out and compared with the current 3D results to confirm and fully explain these observations.

4. Microstructure Evolution in SEN Single Crystals Prior to Crack Initiation

Theoretical analyses, particularly those done by Rice [50] and Flouriot et al. [59], have shown that the material's behaviours, in both macro-scale and micro-scale, in a small region around a notch tip significantly affect how crack would nucleate in this region. This chapter numerically examines the deformation and the microstructure evolution in the proximity of a notch tip in Cube and Brass oriented single crystals prior to the initiation of cracks in these samples. The simulations are based on the CPFEM formulation incorporating Bassani-Wu hardening law that was validated in Chapter 3. The results and analyses carried out in this chapter are the first steps toward the modelling of cracking to be carried out in chapter 6.

4.1 CPFEM model

Figure 4.1 schematically shows the geometry of the SEN single crystal to be modelled. All dimensions are in millimeters. The sample is 0.5 mm thick. The rectangular notch locates at the middle of the right edge of the sample. The width and length of the notch are 0.8 mm and 1 mm, respectively. During the simulation, the bottom surface of the sample is fixed in Y direction, while the left wall of the sample is fixed in X direction. The constant strain rate of $0.01s^{-1}$ is applied to the top surface along the positive Y direction to simulate the tensile load. The single crystal model is meshed by 53,030 C3D8 elements (8-node linear brick) in the FEM software Abaqus/Standard. The mesh around the notch is shown in Figure 4.2. There are five layers of element along the sample thickness.

Figure 4.1 shows the Cube oriented sample where the [100] and [010] lattice orientations are aligned with the X and Y axes, respectively. The lattice orientations

along the X and Y axes for the Brass oriented sample are [110] and [$\bar{1}$11], respectively. In Cube oriented sample, the strain is applied in the positive Y direction until it reaches 4.5% while in the Brass oriented sample, the applied strain reaches the maximum of 3%. As will be shown in Chapter 6, cracks initiate in the Cube and Brass oriented samples at these strains. Thus in the following sections, for Cube oriented sample, the results at 1%, 3% and 4.5% nominal strains will be shown. For Brass oriented sample, the results at 1%, 2% and 3% nominal strains will be shown.

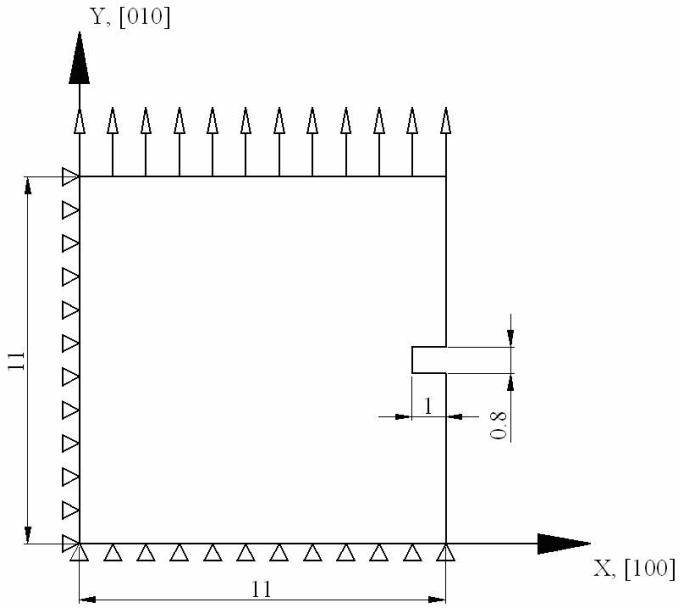

Figure 4.1 Geometry of the single crystal SEN sample and the boundary conditions.

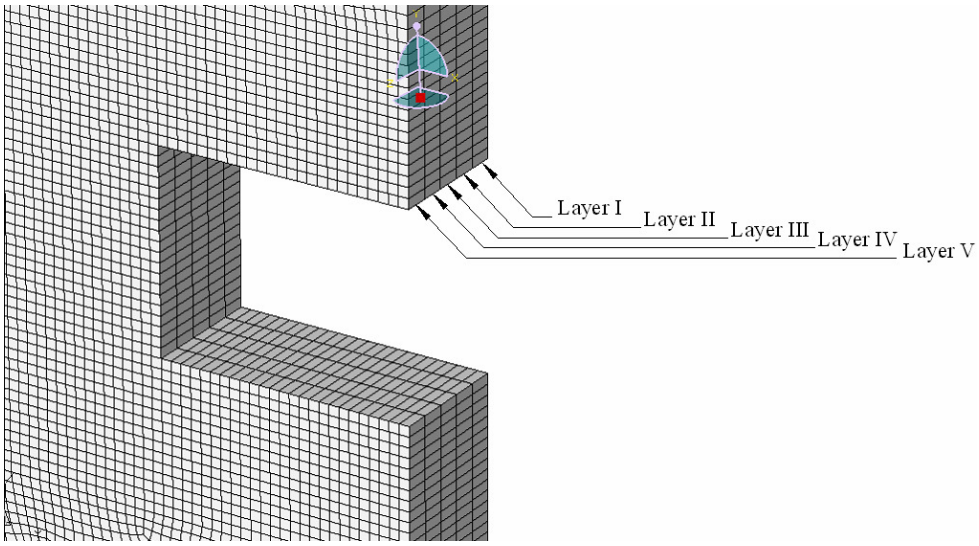

Figure 4.2 Mesh around the notch.

Also, a small the region around the notch is divided into three sub-regions, namely, region I, region II and region III, as shown in Figure 4.3 in order to demonstrate clearly the effects of distance to the notch boundary upon the deformation (e.g. stress, strains) of the samples. Area of sub-regions thus must be large enough so that differences of deformation between them can be well captured, and yet small enough to save calculation time of analyses for those sub-regions (e.g. to determine misorientations or the change of surface roughness). The total simulation times are approximately 45 hours and 89 hours for Cube and Brass oriented samples, respectively, on a cluster computer of 96 CPUs.

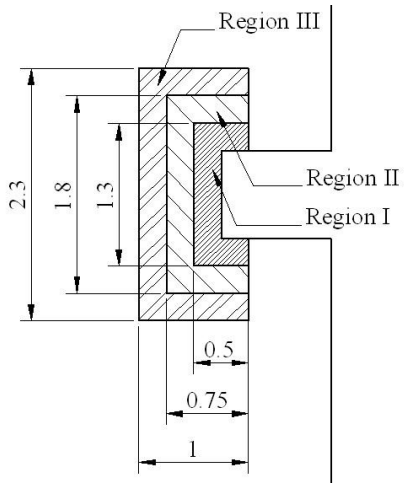

Figure 4.3 Three regions around notch.

4.2 Analyses and discussions of CPFEM results

4.2.1 Stress strain curve

The stress versus nominal strain is plotted for both cases in Figure 4.4. The nominal strain is defined as the extension divided by the original length. The stress is determined as the average of vertical stresses on all nodes on the top surface of the sample. It can be seen that both cases exhibit similar curves to the normal tensile test. The stress increases rapidly at low strains, indicated by the steep slope of the stress strain curves. The slope becomes less steep at higher strains, until the ultimate tensile stress is reached. The corresponding ultimate tensile stresses are approximately 50 MPa and 57 MPa for Cube oriented and Brass oriented samples, respectively. After

reaching this point of ultimate stress, the stress decreases with strain, which corresponds to the necking. The nominal strains where the ultimate tensile stress occurs in Cube oriented and Brass oriented samples are 3% and 2%, respectively. These values are much smaller than those seen in a normal tensile test. This is due to the existence of the notch. The Brass oriented sample shows higher stress than the Cube oriented sample. The Young's modulus of the two samples are approximately 8.5 GPa and 14 GPa, respectively. This is consistent with the nature of anisotropy of Young's modulus in metals [123].

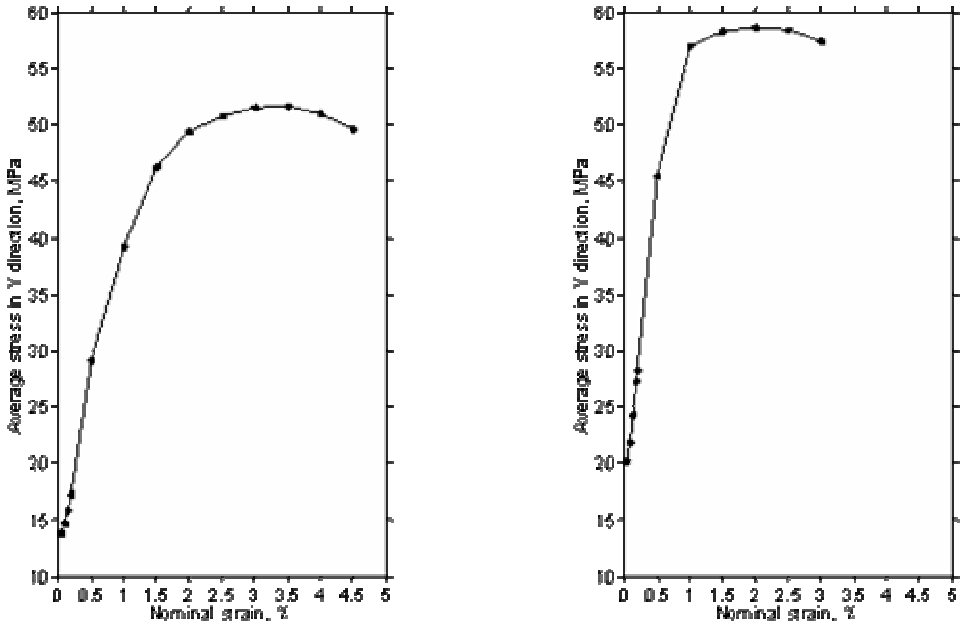

(a) Cube oriented sample (b) Brass oriented sample

Figure 4.4 Stress strain curve from modelling results.

4.2.2 Change of surface roughness

In order to satisfy the compatible condition during deformation, the lattices in two small adjacent regions may rotate in opposite directions, which causes the surface roughness. A higher surface roughness indicates a higher lattice rotation. The change of average surface roughness over various regions around notch is another measure of sample deformation in macro-scale. It is assumed in this work that the initial surface roughness is zero. The average surface roughness is calculated as the sum of distances from all nodes (in the finite element mesh) within the region to a reference

plane divided by the number of nodes, as schematically demonstrated in Figure 4.5. The reference plane represents the sample surface at a particular loading step, and is approximated by three points with the original X, Y coordinates of (0,0), (11,0) and (0,11).

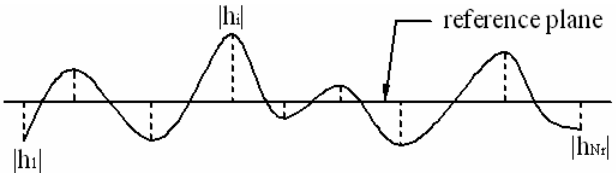

Figure 4.5 Sketch of the calculation of the average surface roughness.

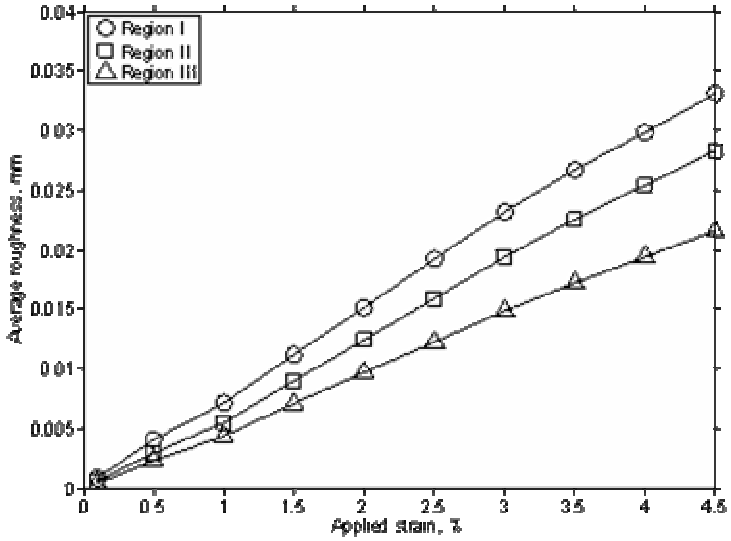

(a) Cube oriented sample

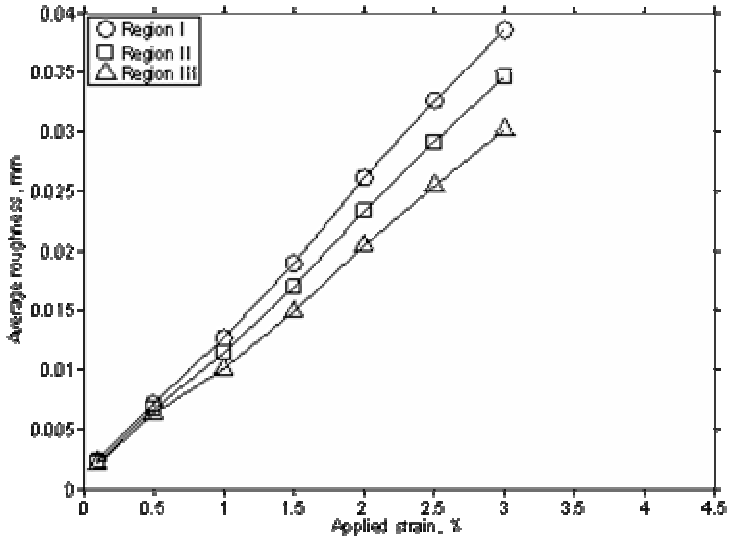

(b) Brass oriented sample

Figure 4.6 Average surface roughness of four regions versus nominal strain (refer to Figure 4.3 for Regions I, II and III).

During the calculation it was seen that roughness values are similar on the front and back surfaces of both samples. Therefore, only roughness values on the top surface are given. The plots of the surface roughness of the three regions versus nominal strain for two samples, Cube oriented and Brass oriented, are shown in Figure 4.6. Both figures reveal the values of roughness gradually increase with strain indicating that the lattices gradually rotate during deformation. Also, these figures show that the roughness is highest in Region I and lowest in Region III at every loading stage. Comparing Figures 4.6a and 4.6b shows that at the same nominal strain the Brass oriented sample (lattice plane $(1\,\bar{1}\,2)$ on the surface) has a higher roughness than the Cube oriented sample (lattice plane (001) on the surface). This agrees qualitatively with various studies that crystal orientation significantly affects the surface roughness, either in a chemical [128] or a mechanical process [129-134]. Yamasaki et al. [131] studied the effects of initial orientation on the surface roughness of Fe–30%Cr alloy single crystals under cyclic loads. Their results indicated that a sample surface on a higher Miller index lattice plane tends to have higher roughness than a surface on a lower Miller index plane. Lee et al. [134] investigated the influence of surface texture on orange peel in a rolled polycrystalline aluminum sample. They observed that grains in Brass orientation tended to be located in the peaks of the surface of the deformed sample.

Figures 4.7 and 4.8 show the deformed mesh at various stages of loading of the Cube and Brass oriented samples, respectively. Figures 4.9 and 4.10 show contour plots of distance to the reference plane at each stage of loading for the Cube and Brass oriented sample, respectively. A close observation of these figures of both samples disclose that such large average roughness in Region I are mainly due to large deformation of elements very close to the notch boundary (best observed in Figures 4.7c and 4.8c), indicated by the dimples around the upper and lower corners of the notches. As will be presented in Section 4.2.3, deformation concentration exists in these areas. Figures 4.9c and 4.10c show that in both samples the upper half of the region around the notch appears more deformed than the lower half. The unsymmetry occurs in the Brass oriented sample at a smaller strain (1%) than in the Cube oriented sample (4.5%). This unsymmetry may be due to the unsymmetric boundary conditions as shown in Figure 4.1. Various studies have also applied same

boundary conditions to simulate tensile tests in single crystals with a notch and reported unsymmetric deformation around the notch tip [70, 135, 136].

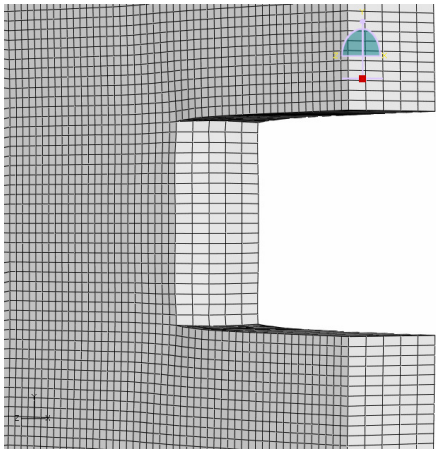

(a) 1% nominal strain

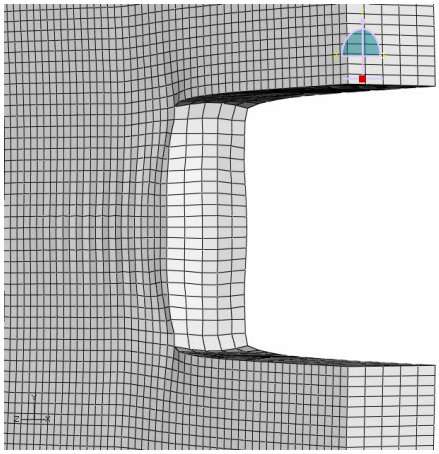

(b) 3% nominal strain

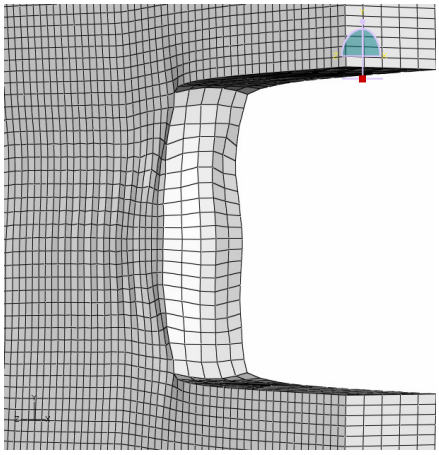

(c) 4.5% nominal strain

Figure 4.7 Deformed mesh around the notch tip, Cube oriented sample.

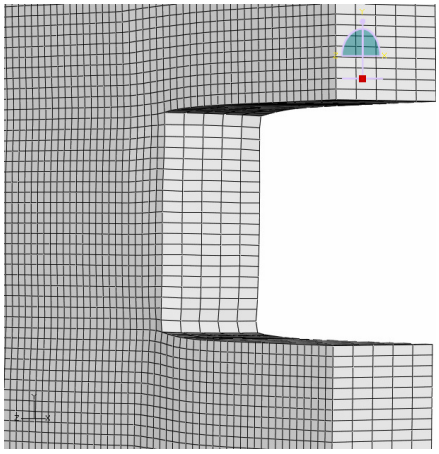

(a) 1% nominal strain

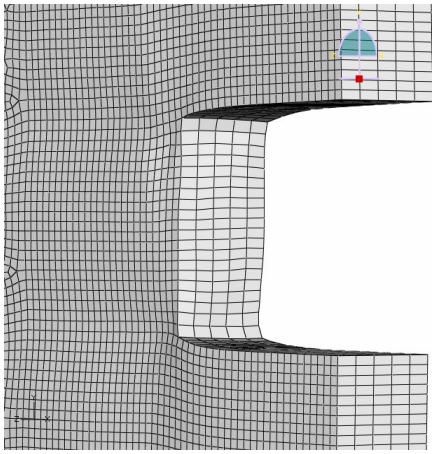

(b) 2% nominal strain

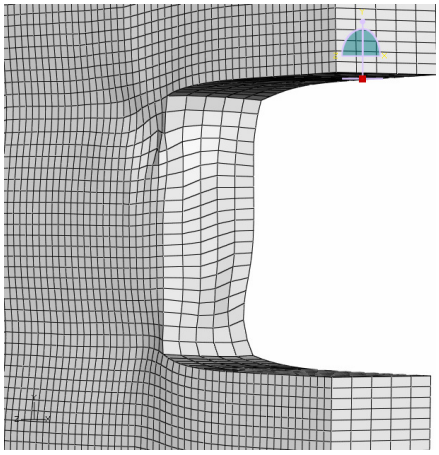

(c) 3% nominal strain

Figure 4.8 Deformed mesh around the notch tip, Brass oriented sample.

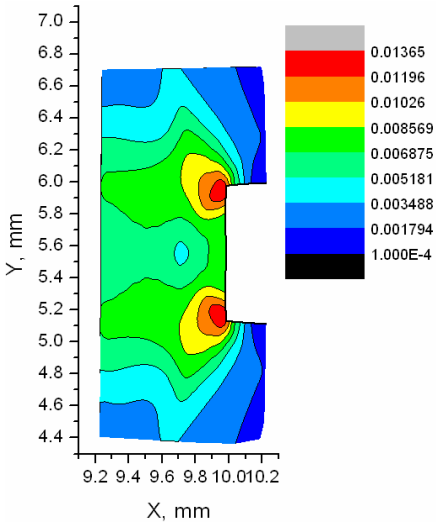

(a) 1% nominal strain

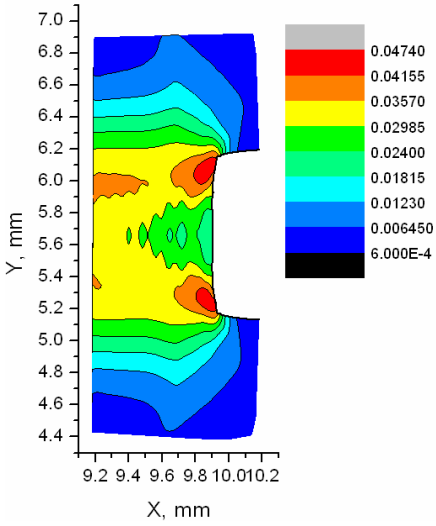

(b) 3% nominal strain

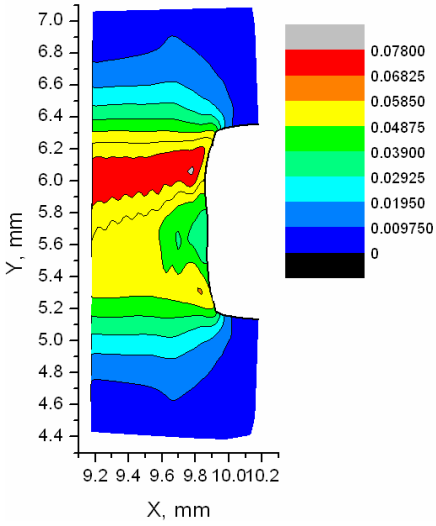

(c) 4.5% nominal strain

Figure 4.9 Contour plots of surface roughness (mm), Cube oriented sample.

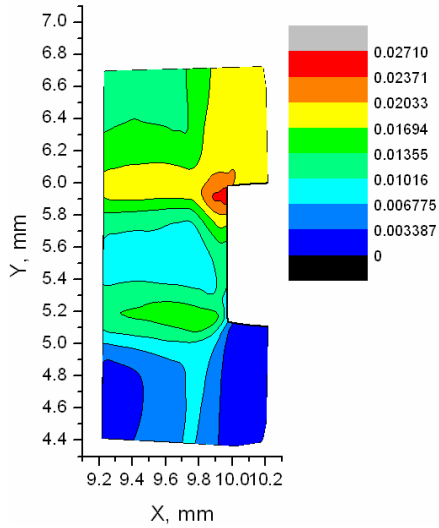

(a) 1% nominal strain

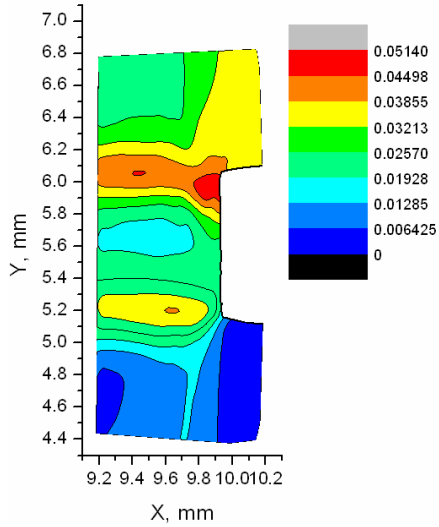

(b) 2% nominal strain

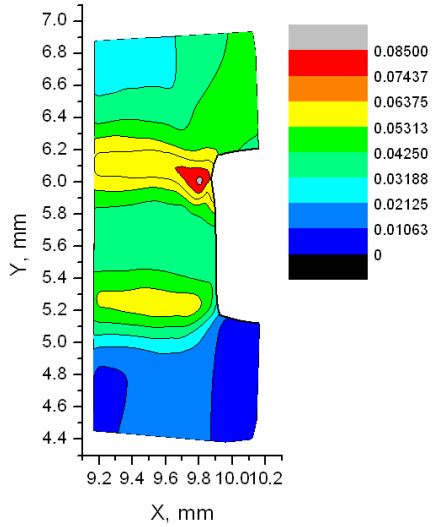

(c) 3% nominal strain

Figure 4.10 Contour plots of surface roughness (mm), Brass oriented sample.

The unsymmetric deformation of the mesh shown in Figures 4.9c and 4.10c directly relates to the unsymmetric distribution of plastic slip and crystal rotation presented in later sections.

4.2.3 Slip traces

The approach adopted in Section 3.2.1 is applied to plot traces of slip on the free surface of the two samples. The plots as shown in Figures 4.11 and 4.12, respectively, are produced at nominal strains of 1%, 3%, and 4.5% for the Cube oriented sample, and at nominal strains of 1%, 2%, and 3% for the Brass oriented sample. It is noted that slip traces appear on the surface of both samples at a very early stage of loading (1% nominal strain). As with the analysis in Section 3.2.1, the majority of slip traces that appear on the surface of the Cube oriented sample also incline at ± 45^{o} to the notch tip, with maximum variations of about ± 2^{o}, as shown in insets (a) and (b) of Figure 4.11c. The variations are lowest at 1% nominal strain, and highest at 4.5% nominal strain. This is because the larger the material deforms, the larger the crystals rotate from their original orientations.

The orientations of the local lattice along the global X and Y axes for the Brass oriented sample are [110] and $[\bar{1}11]$, respectively. And therefore the surface is parallel to the $(1\,\bar{1}\,2)$ lattice plane. The potential slip traces on the sample surface are intersections of slip planes $\{111\}$ with plane $(1\,\bar{1}\,2)$. The orientation of these traces are cross products of normal to slip planes and the normal to sample surface, as described in Equations (4.1a) to (4.1d).

$$\begin{bmatrix}1 & 1 & 1\end{bmatrix}^T \otimes \begin{bmatrix}1 & -1 & 2\end{bmatrix}^T = \begin{bmatrix}3 & -1 & -2\end{bmatrix}^T \tag{4.1a}$$

$$\begin{bmatrix}-1 & 1 & 1\end{bmatrix}^T \otimes \begin{bmatrix}1 & -1 & 2\end{bmatrix}^T = \begin{bmatrix}3 & 3 & 0\end{bmatrix}^T \tag{4.1b}$$

$$\begin{bmatrix}1 & -1 & 1\end{bmatrix}^T \otimes \begin{bmatrix}1 & -1 & 2\end{bmatrix}^T = \begin{bmatrix}-1 & -1 & 0\end{bmatrix}^T \tag{4.1c}$$

$$\begin{bmatrix}1 & 1 & -1\end{bmatrix}^T \otimes \begin{bmatrix}1 & -1 & 2\end{bmatrix}^T = \begin{bmatrix}1 & -3 & -2\end{bmatrix}^T \tag{4.1d}$$

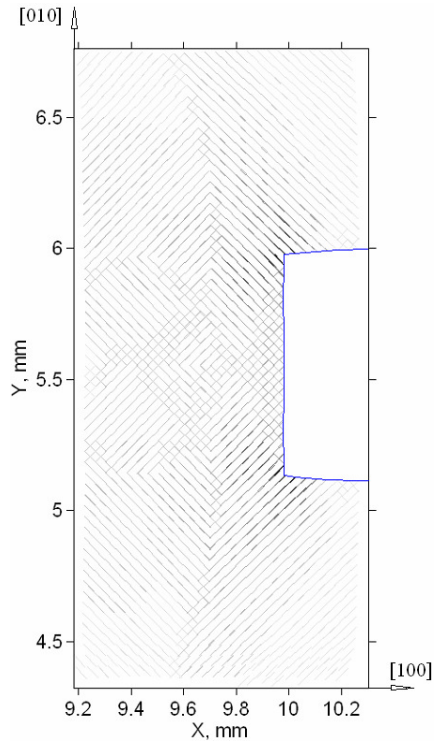

(a) 1% nominal strain

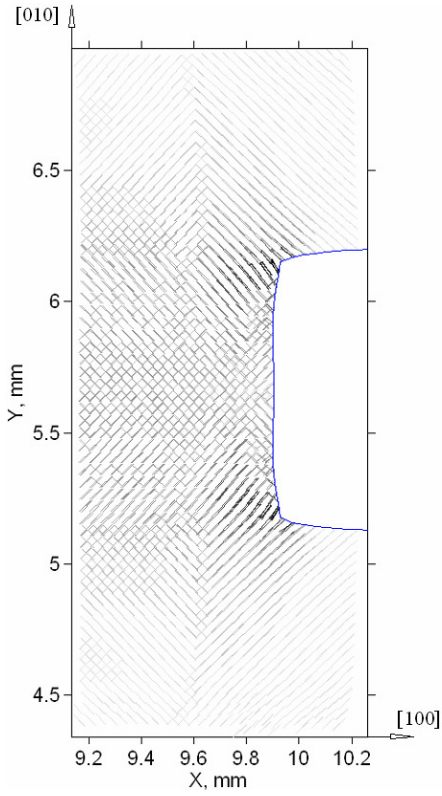

(b) 3% nominal strain

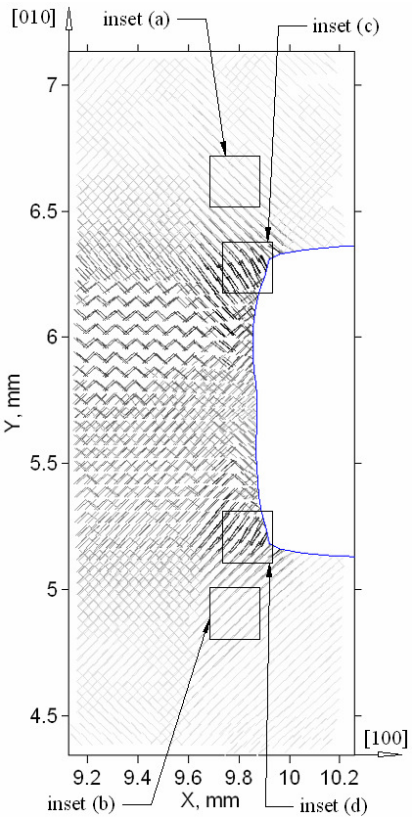

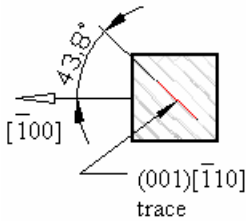

inset (a)

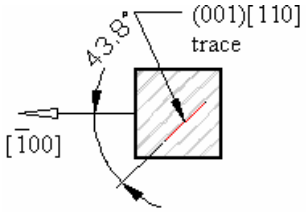

inset (b)

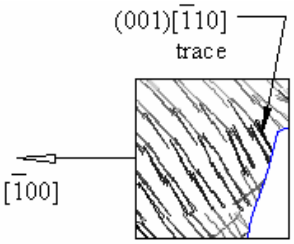

inset (c)

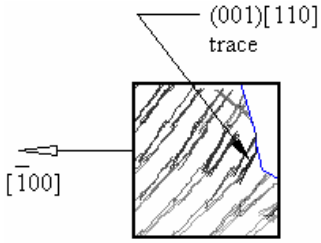

inset (d)

(c) 4.5% nominal strain

Figure 4.11 Slip traces on the surface of the Cube oriented sample.

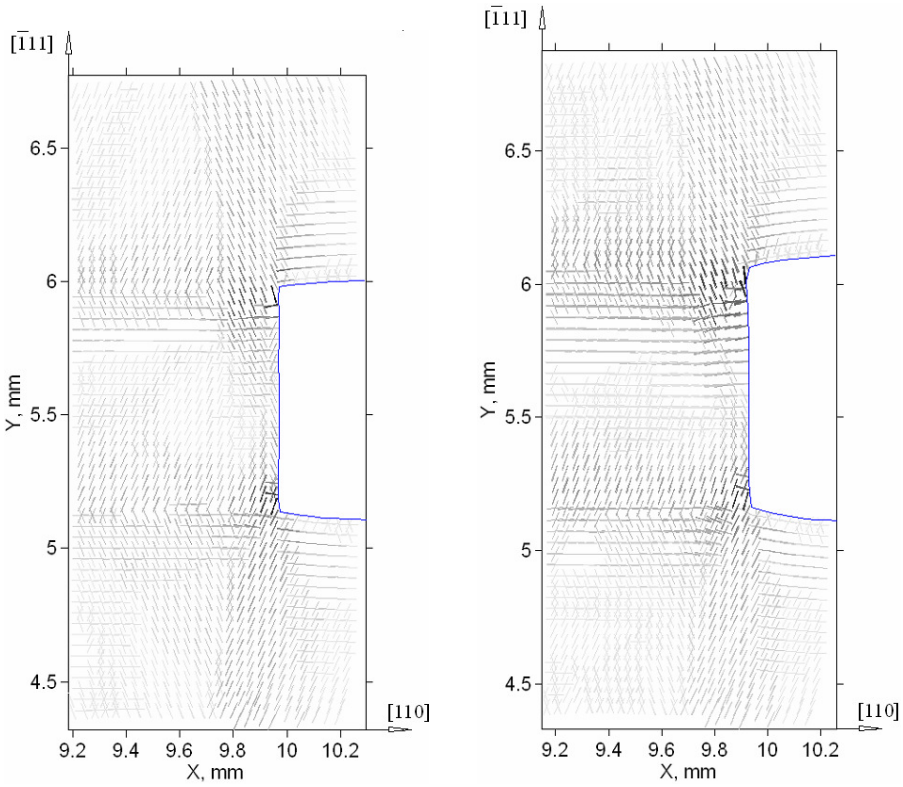

(a) 1% nominal strain (b) 2% nominal strain

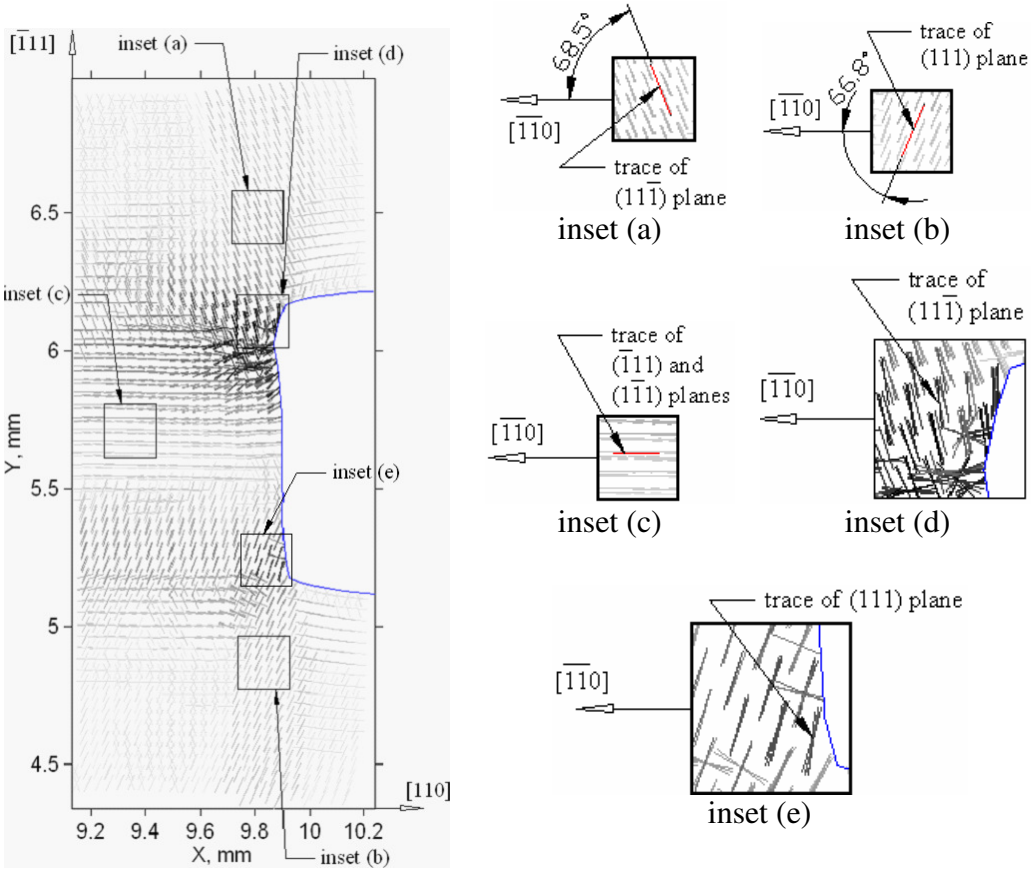

(c) at 3% nominal strain

Figure 4.12 Slip traces on the surface of the Brass oriented sample.

In the Brass oriented sample, the angles between slip traces presented by Equations (4.1a) to (4.1d) and the direction of the notch directed in $[\bar{1}\,\bar{1}\,0]$ lattice orientation are 112.21^{o}, 180^{o}, 0^{o}, and 67.79^{o}, respectively. These approximate theoretical angles are captured very well in the simulation results. They are shown in insets (a), (b), and (c) in Figure 4.12c, where a maximum variation of about $\pm 2^{o}$ occurs at the highest nominal strain because of larger crystal rotations. At points very close to the corners of the notch, the trace orientations deviate more severely, as shown in insets (c) and (d) of Figure 4.11c and insets (d) and (e) of Figure 4.12c. This is due to large rotations of crystals in these points, which also indicates a stress concentration around the boundary of the notch. At these points the assumption of moderate deformation stated in Section 3.2.1 is not met. The analysis of slip trace based on the initial crystal orientation is no longer correct, and must be carried out numerically.

The total of cumulative shear strain on all slip systems at each integration point are collected from CPFEM modelling and plotted in Figures 4.13 and 4.14. SDV121 is the 121^{st} state dependent variable defined in UMAT as the total of cumulative shear strain on all slip systems at an integration point. In other words, it represents the total plastic deformation at that point. The plots indicate that plastic deformation in Brass oriented samples are about two times higher than that in the Cube oriented sample, e.g. at 3% nominal strain, the maximum value of SDV121 in Brass sample is 2.539 (Figure 4.14c), while only 1.331 in Cube sample (Figure 4.13b). Comparing Figures 4.13 and 4.9 (for Cube oriented sample) shows that points having high plastic deformation (in Figure 4.13) correspond to those having high surface roughness (in Figure 4.9). Also, the unsymmetrical deformation in the upper half and lower half of the notch is observed in both figures. The same features can be observed in Brass oriented sample (Figures 4.14 and 4.10). These features are best observed at 4.5% nominal strain (for Cube oriented sample), and 3% nominal strain (for Brass oriented sample).

As the samples are stretched out further the slip activities around the tip of the notch become more severe. This is indicated by the higher number of slip traces appearing (see Figures 4.11 and 4.12), and the magnitude of cumulative plastic shear (Figures 4.13 and 4.14). Such an evolution of slip activities is better described in Figure 4.15.

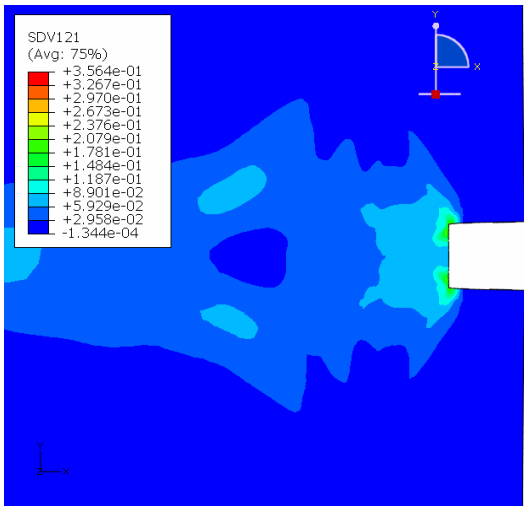

(a) at 1% nominal strain

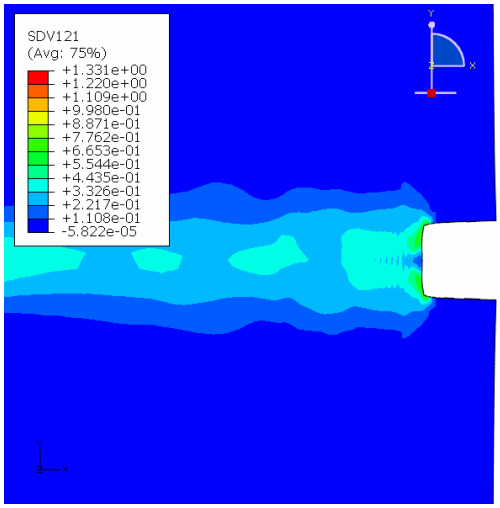

(b) at 3% nominal strain

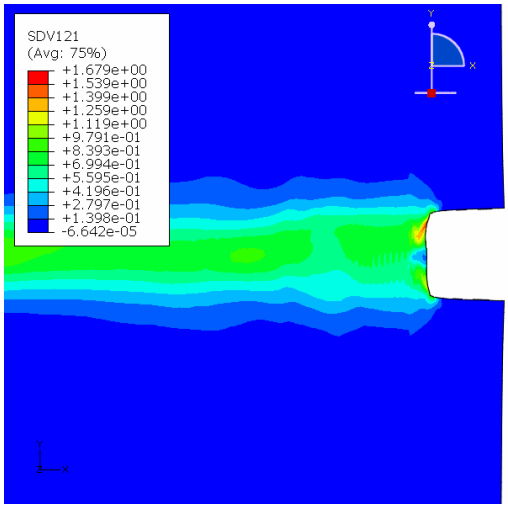

(c) at 4.5% nominal strain

Figure 4.13 Total cumulative shear strain around notch on the Cube oriented sample surface.

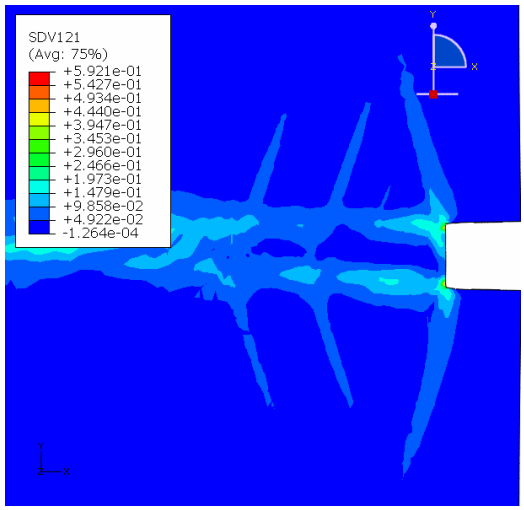

(a) at 1% nominal strain

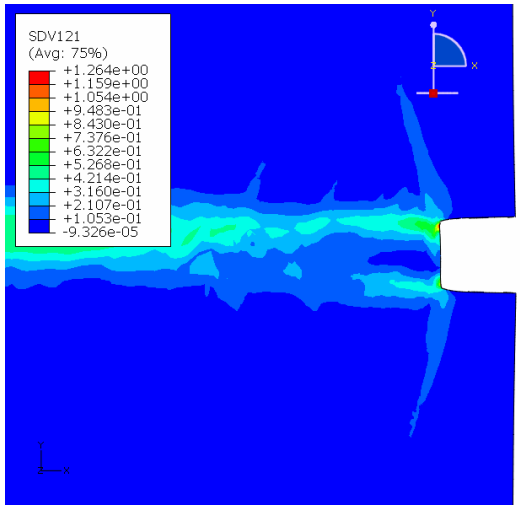

(b) at 2% nominal strain

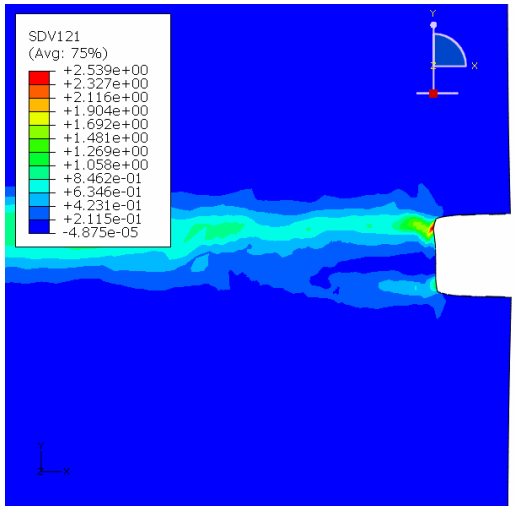

(c) at 3% nominal strain

Figure 4.14 Total cumulative shear strain around notch on the Brass oriented sample surface.

Figure 4.15 presents plots of the maximum of total cumulative shear strain that occurs in each region around the notch (regions I, II, and III) versus nominal (applied) strain. The trend seen in Figure 4.6 exists in Figure 4.15. The maximum of total cumulative shear strain in Region I is higher than those in regions II and III at every stage of loading for both Cube and Brass oriented samples. At the same applied strain, the maximum total cumulative shear strain in any region in the Brass oriented sample is always higher than that in the Cube oriented sample.

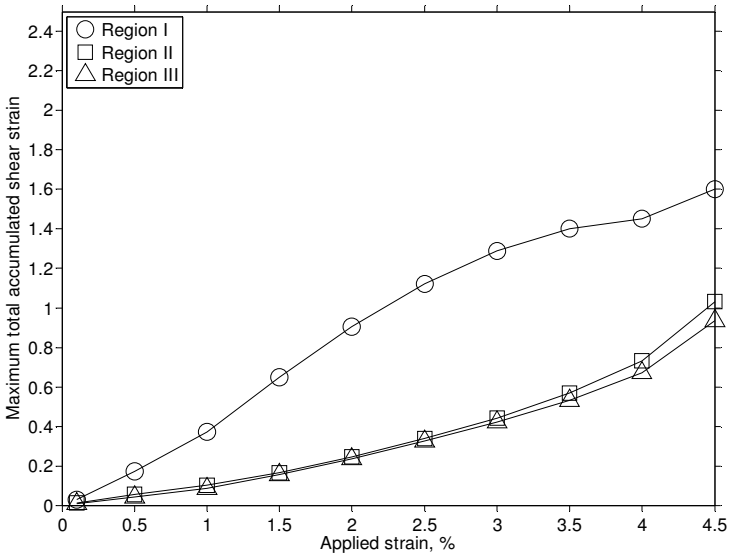

(a) Cube oriented sample

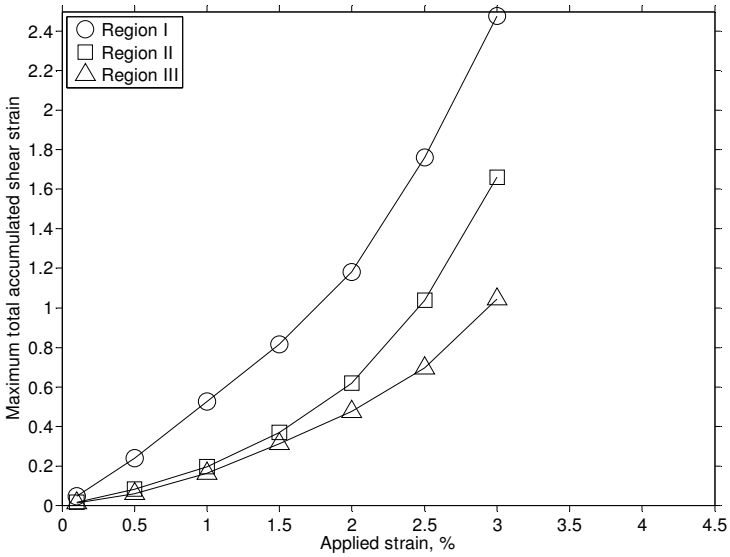

(b) Brass oriented sample

Figure 4.15 Plots of maximum of total cumulative shear strain versus nominal strain.

4.2.4 Crystal rotations

The total rotation angles of crystals with respect to their original orientation are determined following the discussions in Section 3.2.2, and are plotted in Figures 4.16 and 4.17 for limited regions around the notch in the Cube and Brass oriented samples, respectively. The results on the free surface (left plots) and the mid-thickness plane (right plots) are shown to demonstrate the effects of sample thickness on the crystal evolution. The unit in these plots is degrees.

For both Cube and Brass oriented samples, the distributions of total rotation angle on the sample surface and on the midthickness plane have similar shapes. The magnitude of total rotation angles on the midthickness plane is generally smaller than that on the sample surface. This difference appears to be greater when the nominal strain increases. This supports the observations made in Section 3.2.1 that tensile deformation of crystals is larger on the free surface than on the interior plane.

The distribution of total rotation angles follow to some extent the distribution of total cummulative shear strain in Figures 4.13 and 4.14. On the free surface of the Cube oriented sample, two regions of concentrated strain around the corners of the notch at 1% nominal strain (Figure 4.13a) correspond to the darker regions at upper and lower notch corners in Figure 4.16a. At 3% nominal strain (Figure 4.13b) the distribution of large cumulative shear strain at the two corners extend in the direction parallel to the notch and slightly towards each other, which indicates that the region at the middle of the notch deforms less. This corresponds to the formation of two dark bands (large rotation angles) aligned in the direction of notch tip in Figure 4.16b. At 4.5% nominal strain, both plots of the total cumulative shear strain (Figure 4.13c) and the total rotation angle (Figure 4.16c) possess large bands spanning from one corner of the notch to the other and are aligned in the direction of the notch. Finally, both figures 4.13c and 4.16c show that the upper corner of the notch has a wider band of concentrated shear strain and crystal rotation compared to the lower corner. Such unsymmetric distributions directly relate to the unsymmetric deformation of the mesh at the corners of the notch (see Figure 4.9c).

On the free surface

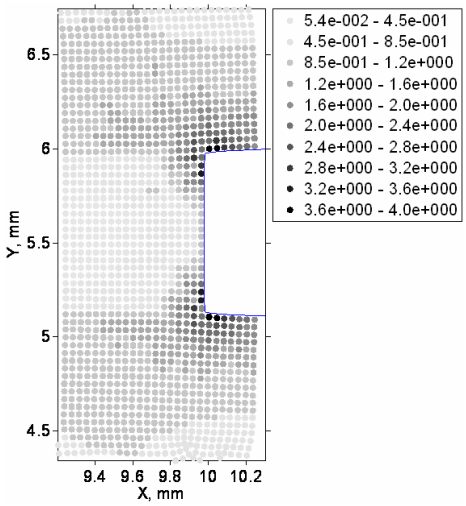

On the mid-thickness plane

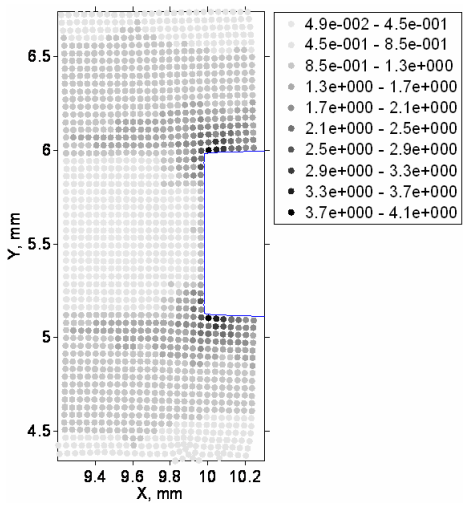

(a) 1% nominal strain

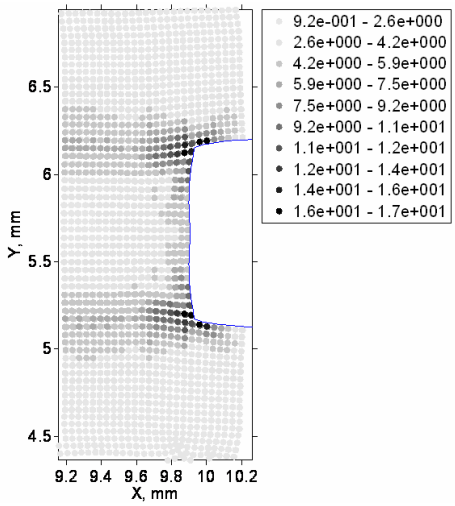

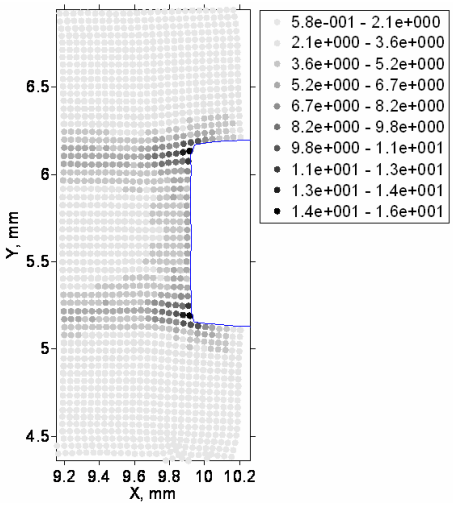

(b) 3% nominal strain

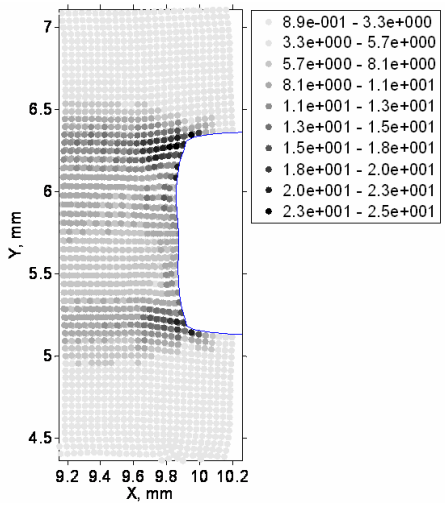

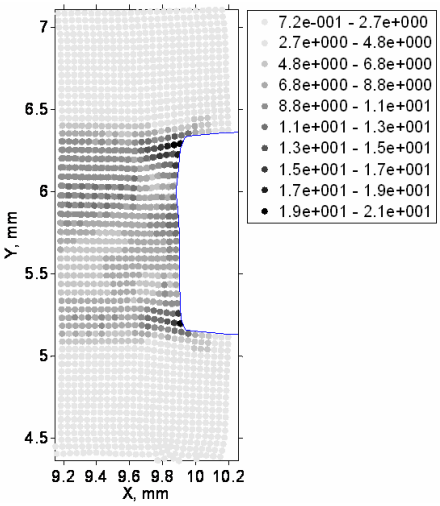

(c) 4.5% nominal strain

Figure 4.16 Contour plots of the total rotation (in degrees) of crystal in the Cube oriented sample.

On the free surface

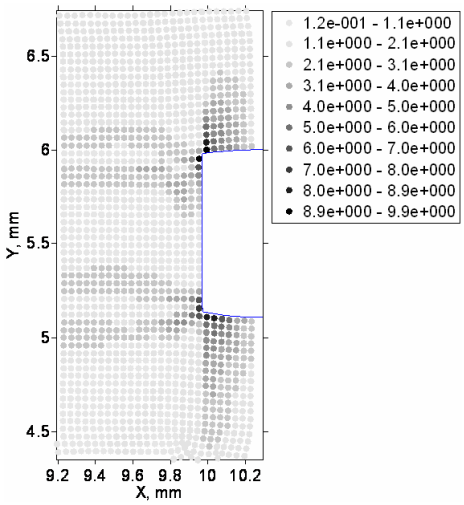

On the mid-thickness plane

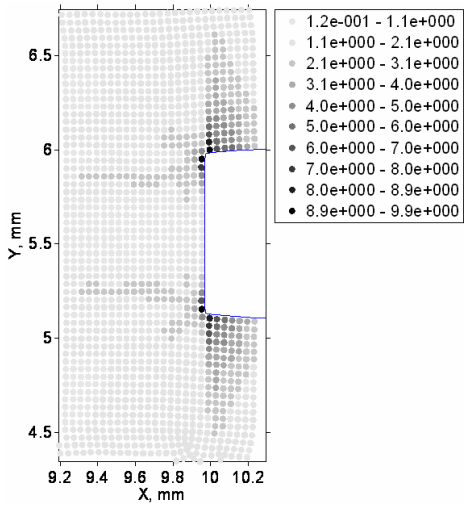

(a) 1% nominal strain

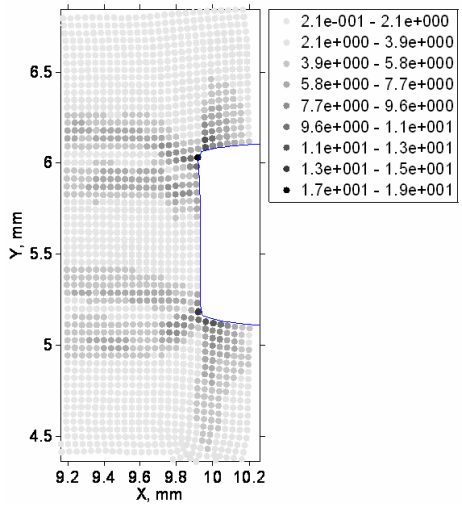

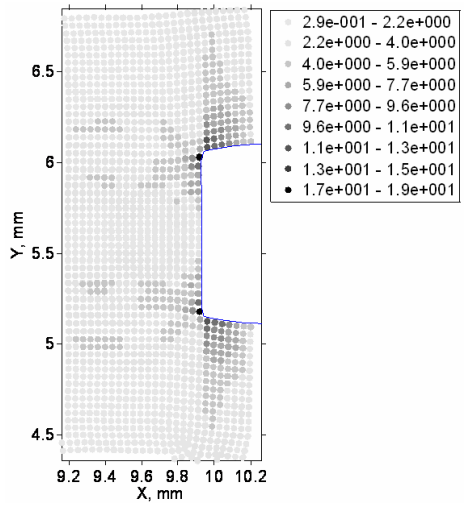

(b) 2% nominal strain

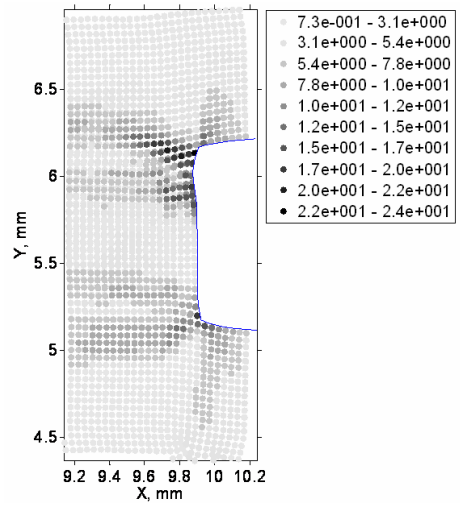

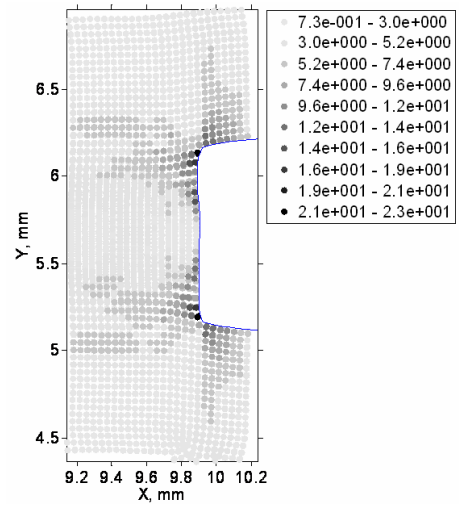

(c) 3% nominal strain

Figure 4.17 Contour plots of the total rotation (in degrees) of crystals in the Brass oriented sample.

The concentration of total cumulative shear strain of the Brass oriented sample distributes in four bands, two are parallel to the notch tip direction, and two are symmetrically inclined at large angle to the notch tip (at 1% nominal strain, Figure 4.14a). The corresponding plot of the total rotation angle reveals two bands parallel to the notch tip direction, while the other two bands are vertical (Figure 4.17a). The resemblance is better at higher nominal strains, where the inclined bands in Figures 4.14b and 4.14c and the vertical bands Figures 4.17b and 4.17c become shorter, and bands parallel to notch tip direction eventually dominate. As with the Cube oriented sample, the Brass oriented sample possesses higher concentrations of shear strain and crystal rotation at the upper part of the notch. Again, this unsymmetry is relating to the unsymmetric deformation of the mesh around the corners of the notch (Figure 4.10c). It is also noted that the crystal rotations in the Brass oriented sample are generally higher than those in the Cube oriented sample, both on the free surface and the mid-thickness plane. For example at 3% nominal strain, while the maximum rotations on the free surface and the mid-thickness plane in Cube oriented sample are 17^{o} and 16^{o} (Figure 4.16b), respectively, the corresponding values in the Brass oriented sample are 24^{o} and 23^{o} (Figure 4.17c), respectively.

In most experimental procedures studying crystal behaviour, the measurement of plastic slip is performed indirectly, by observing the slip traces on the sample surfaces by microscopic Moiré interferometry [52-54]. The direct measurement of local plastic deformation is not normally available. Determining crystal orientations is a fairly basic task using EBSD. Hence the above observations that the behaviour of the total cumulative shear strain resembles the rotation angle can provide an insight into plastic slip happening within a sample based on the observations of its current texture. This is at least applicable for samples undergoing tensile loading.

The decomposition of the total angle of rotation into three components about the X, Y, and Z sample axes ([100], [010], and [001] axes in the global coordinate system) is carried out by following the descriptions in Section 3.2.2. The contour plots of these component rotation angles are presented in Figures 4.18 to 4.20 for the Cube oriented sample at 1%, 3% and 4.5% nominal strains respectively, and in Figures 4.21 to 4.23 for the Brass oriented sample at 1%, 2% and 3% nominal strains,

respectively. The results on the free surface and mid-thickness layer are included in each figure. The unit in these figures is degrees.

The characteristic of the component rotation angles for the Cube oriented sample are generally similar to those observed in Section 3.2.2 for notch tip in the (010)[100] orientation. It can be seen in Figures 4.18 and 4.19 (1% and 3% nominal strains, respectively) that the shape of the contour plots is fairly symmetrical. This implies that crystals in the upper and lower halves of the region around the notch rotate fairly equally in opposite directions around the global [100] and [001] axes (X and Z sample axes), and in the same direction around the global [010] axis (Y sample axis). This symmetry can also be observed in the contour plots of total rotation angle at 1% and 3% nominal strains (Figures 4.16a and 4.16b, respectively). In Figure 4.20, the distributions are not quite symmetric. The magnitude of component rotations tends to be higher in the upper half of the notch. This matches with the unsymmetry in the contour plot of total rotation angle in Figure 4.16c.

As seen in Figures 4.18 to 4.20, within upper half and lower half of the notch, there are equal rotations in opposite directions at the corner of the notch. Such equal and opposite rotations at the corner are apparent around the [100] and [001] global axes at 1% and 3% nominal strains, but become less obvious at 4.5% applied strain. These features exist on both the free surface and the interior plane. The rotations increase dramatically in magnitude with the strain load, e.g. the magnitude of rotation angles around the X, Y, and Z axes on the sample surface, which always appear very close to the notch, increase by factors of 8.27, 8.34 and 4.8 respectively from 1% to 4.5% nominal strain. The crystal rotations in the Cube oriented sample are mainly around the [001] global axis for low loading as was concluded in Section 3.2.2. However at nominal strains larger than 1%, the three rotations become more comparable, e.g. maximum angle around the X, Y, Z axes on the sample surface at 4.5% strain are 20.5^{o}, 22.1^{o}, and 16.7^{o}, respectively. The rotations on the sample surface are larger than those on the mid-thickness plane by various factors, depending on the axis of rotation and magnitude of nominal strain. The average factor is approximately 1.5.

On the free surface | On the mid-thickness plane

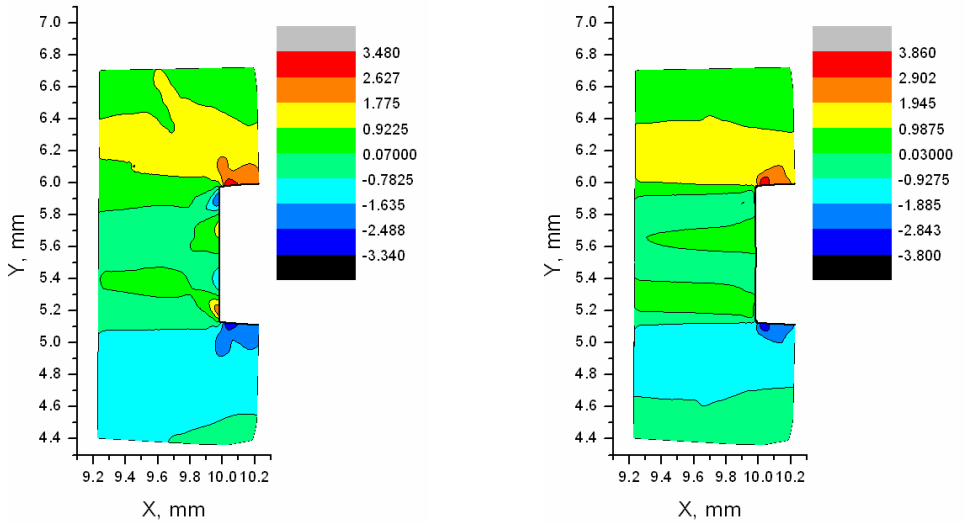

(a) Rotations around the global [001] axis (in degrees)

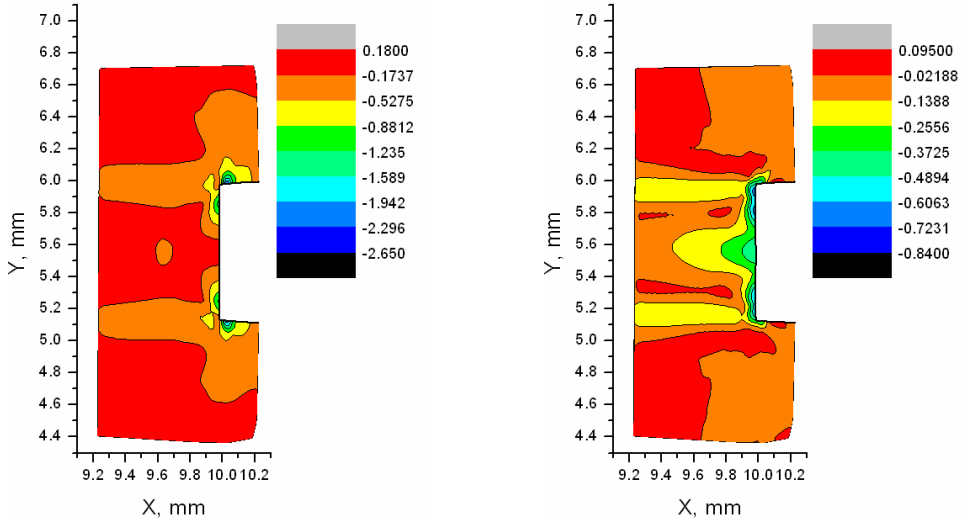

(b) Rotations around the global [010] axis (in degrees)

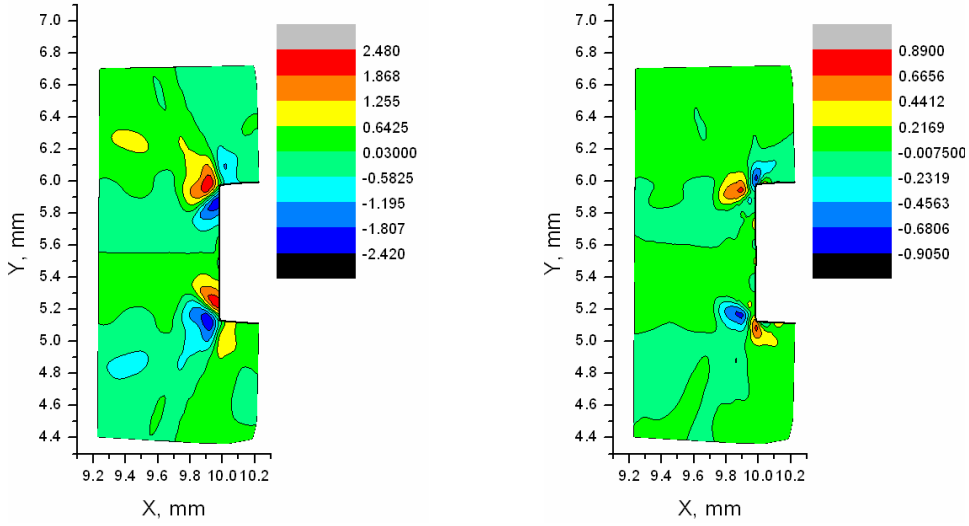

(c) Rotations around the global [100] axis (in degrees)

Figure 4.18 Component rotation angles in Cube oriented sample, 1% nominal strain.

On the free surface

On the mid-thickness plane

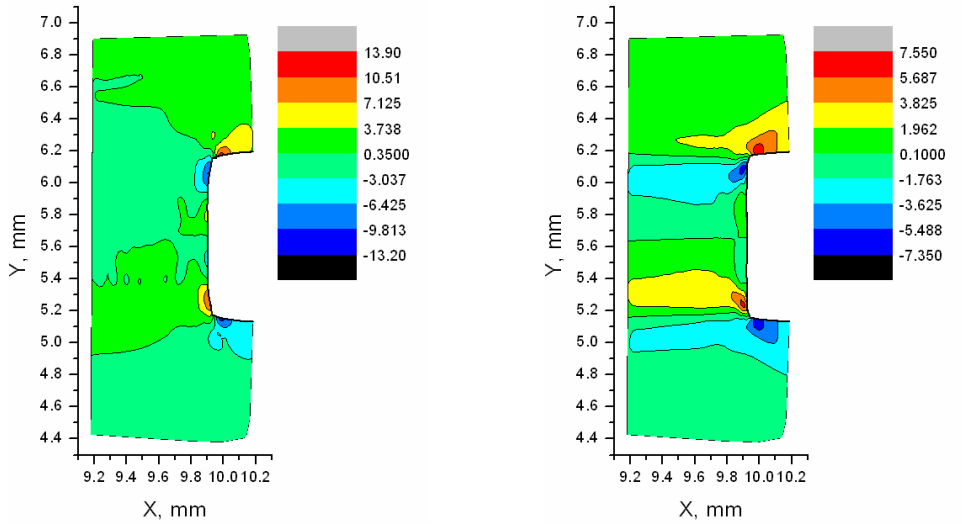

(a) Rotations around the global [001] axis (in degrees)

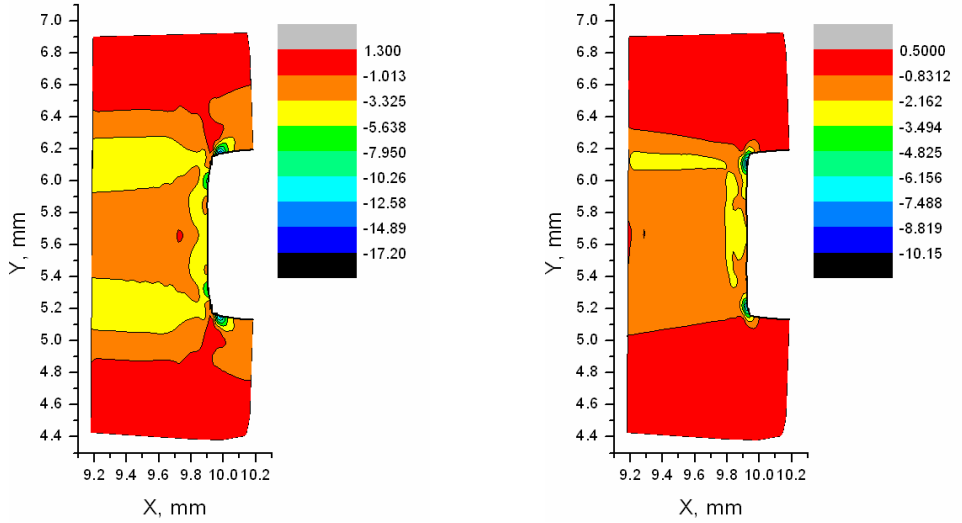

(b) Rotations around the global [010] axis (in degrees)

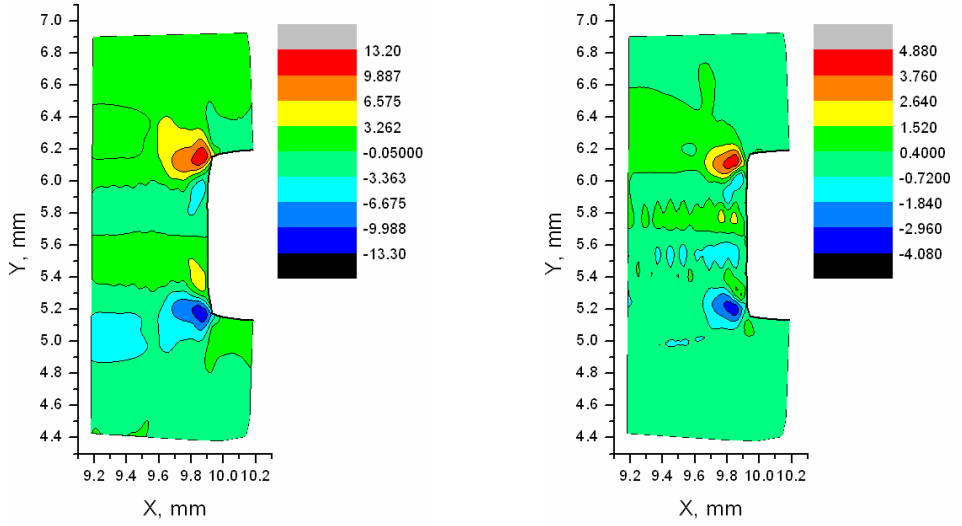

(c) Rotations around the global [100] axis (in degrees)

Figure 4.19 Component rotation angles in Cube oriented sample, 3% nominal strain.

On the free surface | On the mid-thickness plane

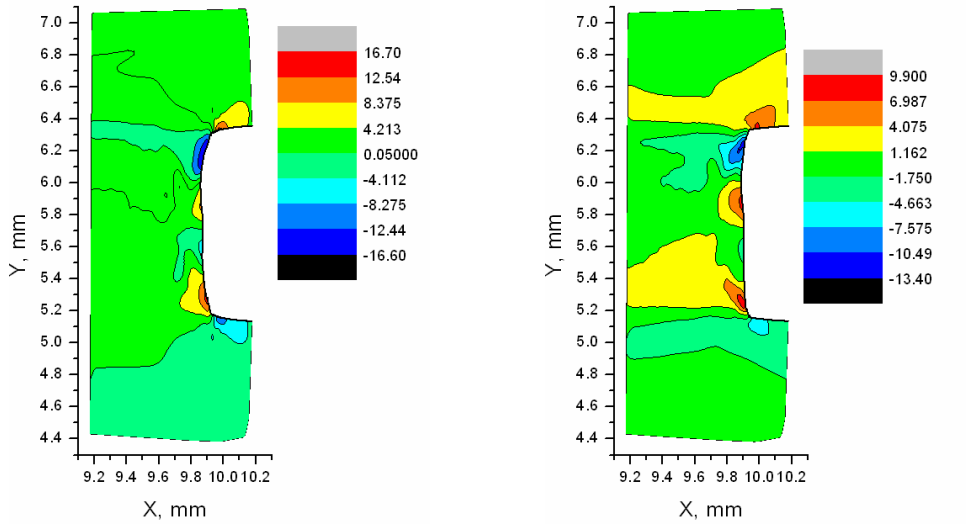

(a) Rotations around the global [001] axis (in degrees)

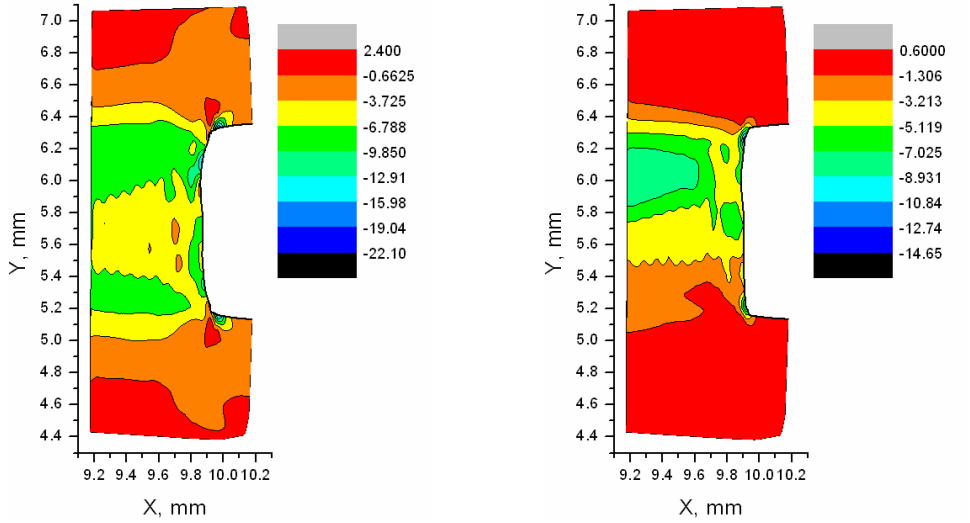

(b) Rotations around the global [010] axis (in degrees)

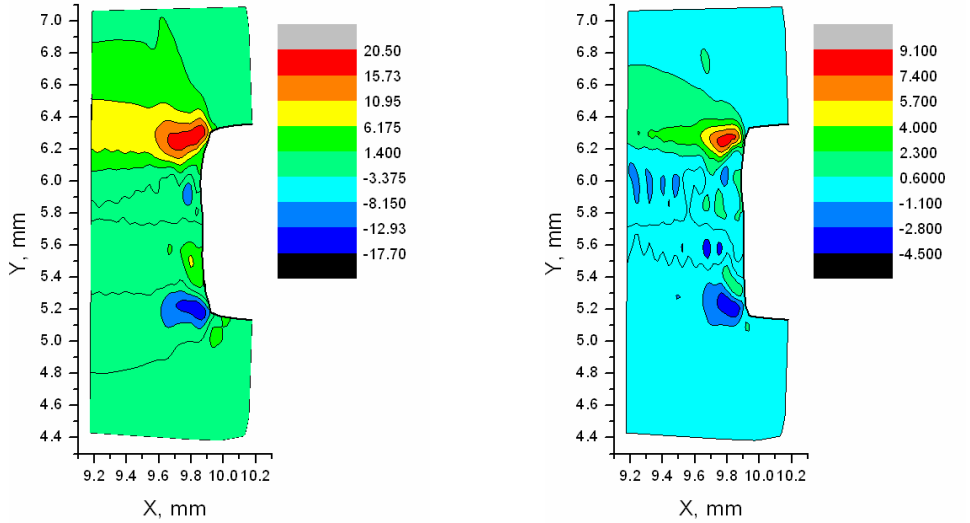

(c) Rotations around the global [100] axis (in degrees)

Figure 4.20 Component rotation angles in Cube oriented sample, 4.5% nominal strain.

On the free surface

On the mid-thickness plane

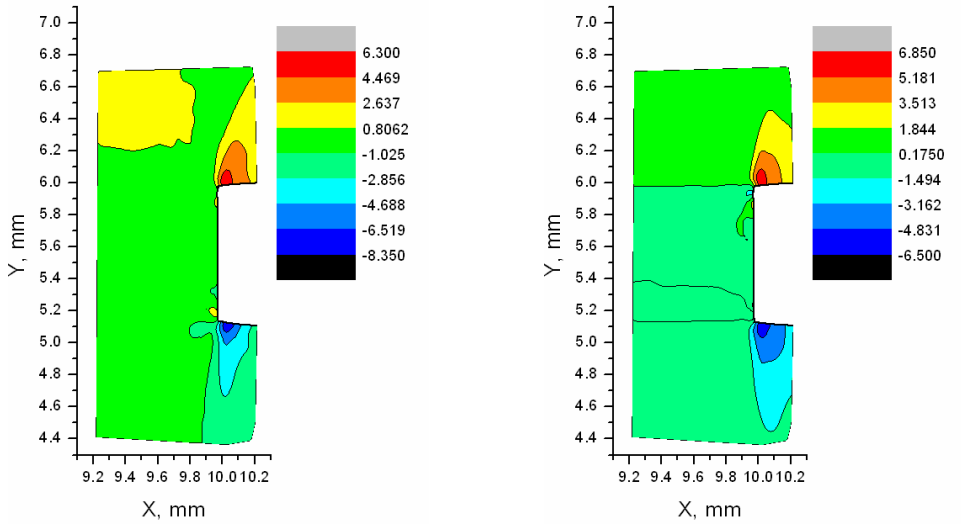

(a) Rotations around the global [001] axis (in degrees)

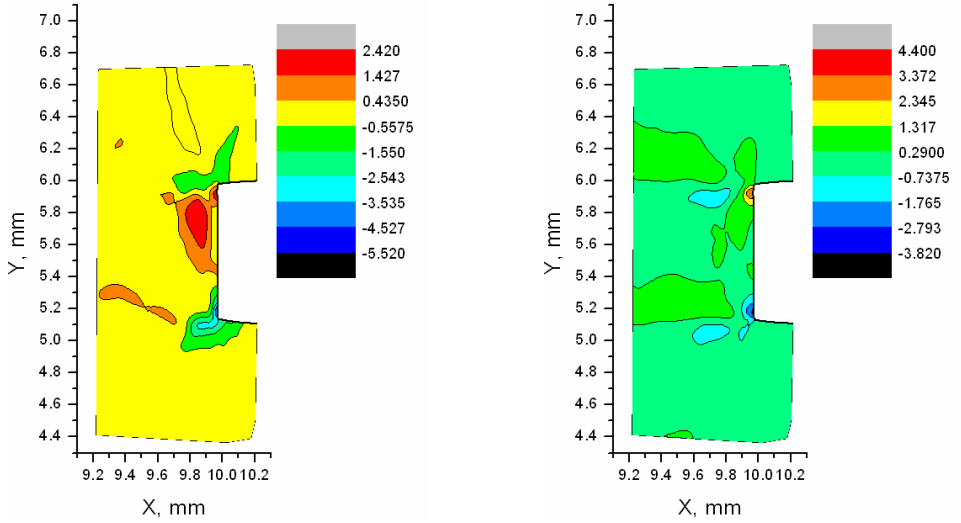

(b) Rotations around the global [010] axis (in degrees)

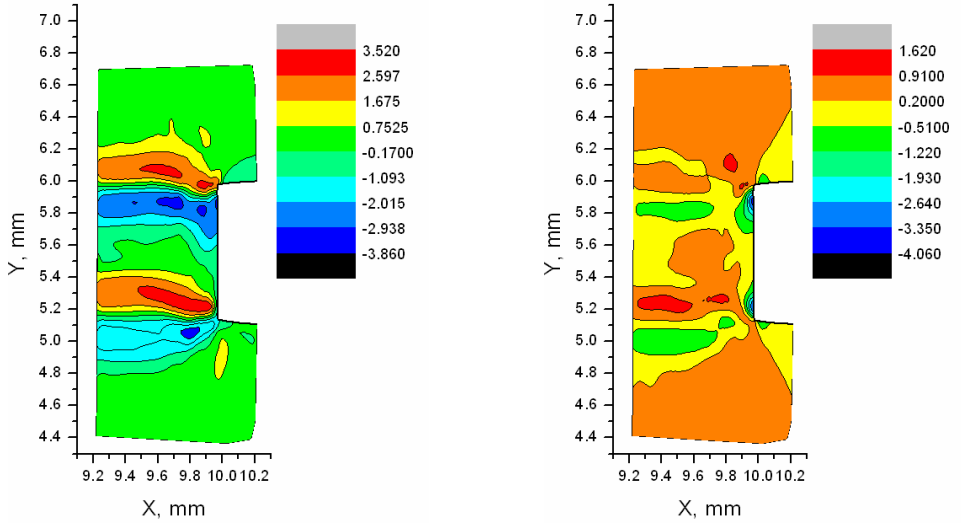

(c) Rotations around the global [100] axis (in degrees)

Figure 4.21 Component rotation angles in Brass oriented sample, 1% nominal strain.

On the free surface

On the mid-thickness plane

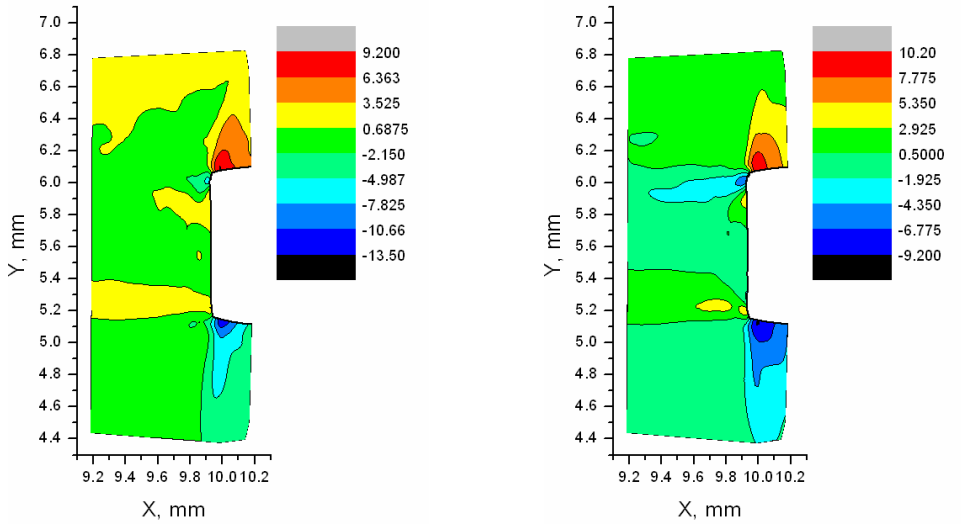

(a) Rotations around the global [001] axis (in degrees)

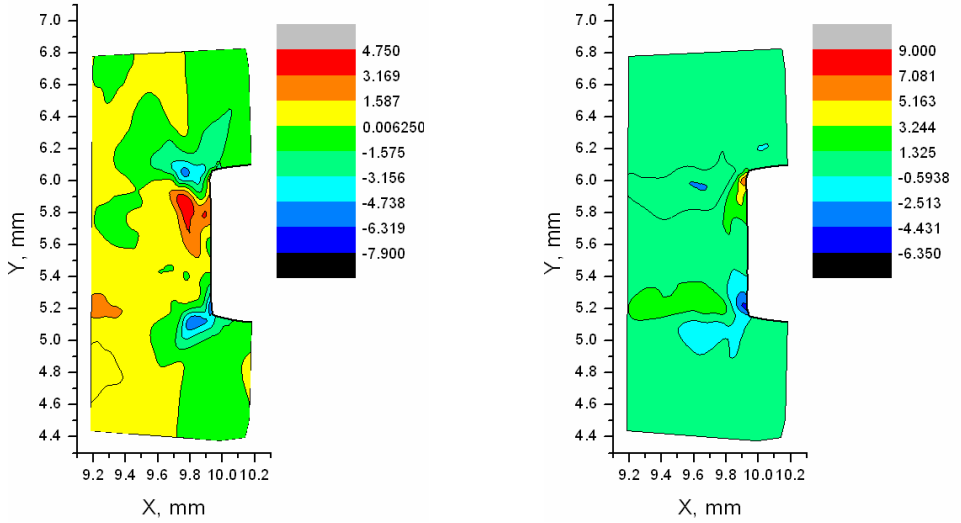

(b) Rotations around the global [010] axis (in degrees)

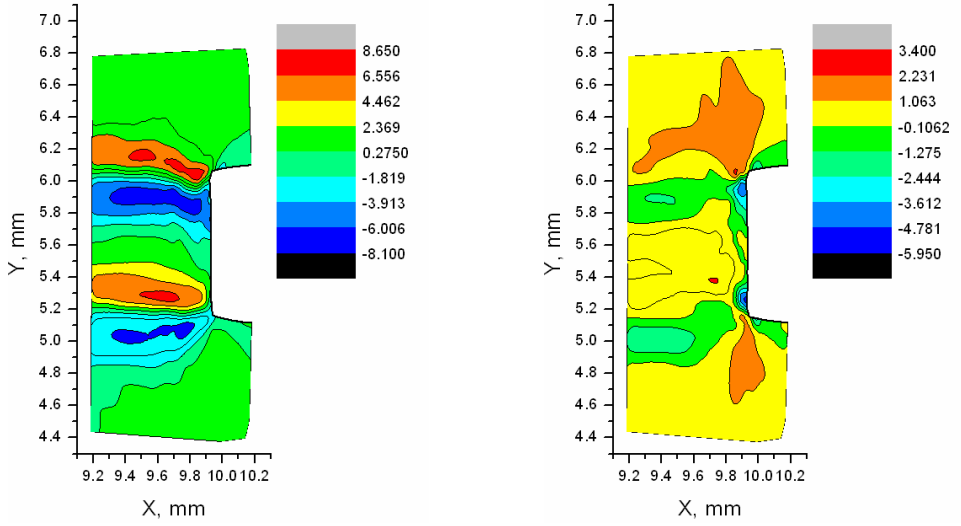

(c) Rotations around the global [100] axis (in degrees)

Figure 4.22 Component rotation angles in Brass oriented sample, 2% nominal strain.

On the free surface

On the mid-thickness plane

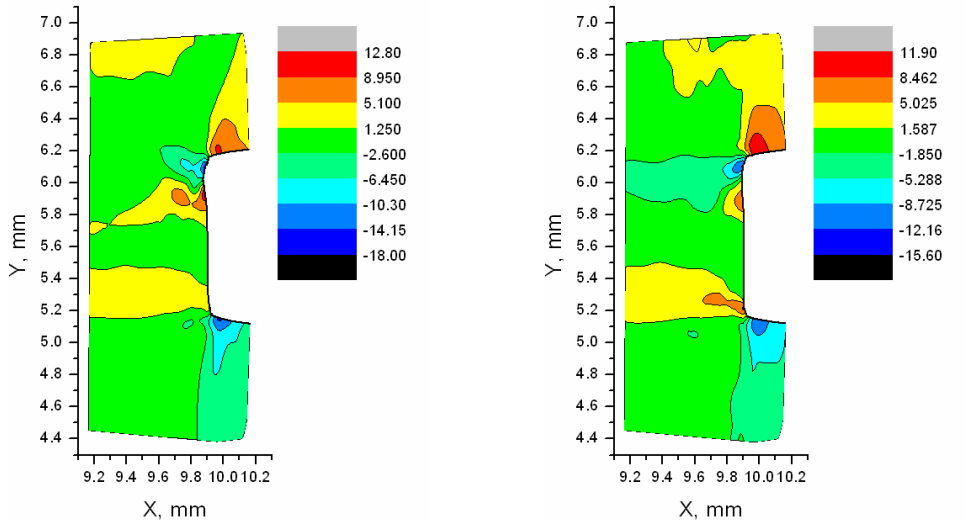

(a) Rotations around the global [001] axis (in degrees)

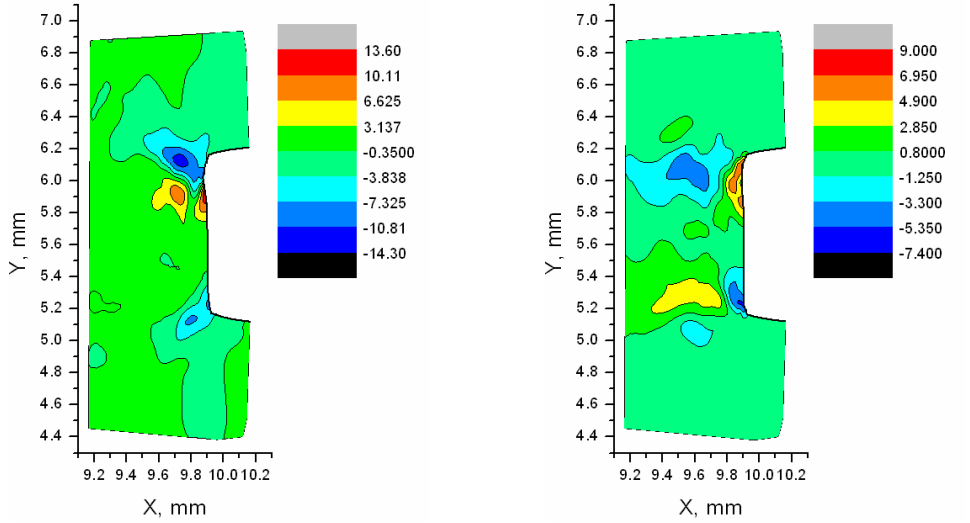

(b) Rotations around the global [010] axis (in degrees)

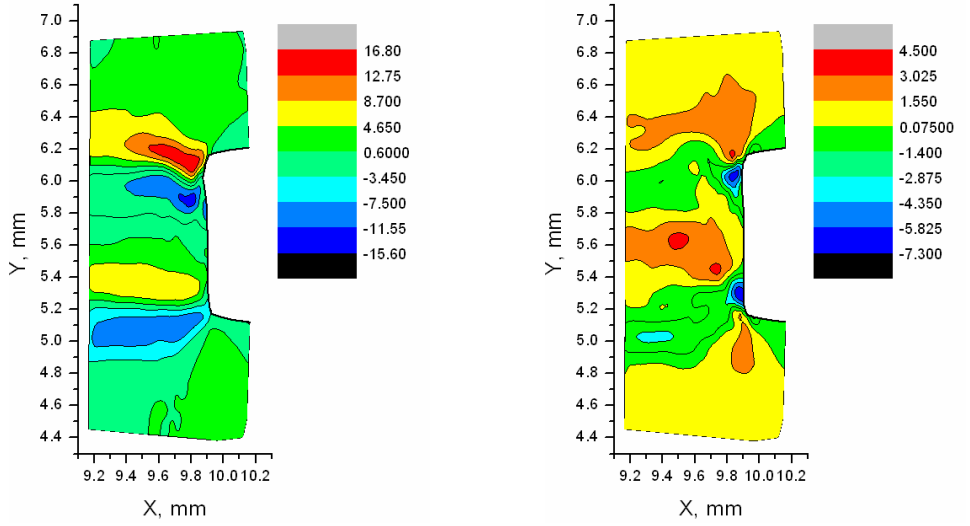

(c) Rotations around the global [100] axis (in degrees)

Figure 4.23 Component rotation angles in Brass oriented sample, 3% nominal strain.

The contour plots throughout Figures 4.21 to 4.23 for the Brass oriented sample are generally not as symmetrical as the Cube oriented sample, except for the rotation around the global [001] axis. Compared to the Cube oriented sample, the magnitude of three component rotations of crystals in the Brass oriented sample are larger. For example, at 1% nominal strain on the interior plane, magnitudes reach 4.1^o, 4.4^o, 6.9^o for rotations about the global [100], [010], and [001] axes respectively. The magnitudes of crystal rotations on the interior plane and on the free surface at 1% nominal strain are of the same order, but the difference between magnitudes increases with an applied load. At 3% nominal strain the difference between magnitudes of rotations on the sample surface and those on the mid-thickness plane is greatest. At this loading the magnitudes of rotation around the global [100], [010], and [001] axes on the sample surface are 16.8^o, 14.3^o, and 18^o respectively. The corresponding values on the midthickness plane are only 7.3^o, 9^o, and 15.6^o, respectively. Fairly equal and opposite rotations around [100] and [001] also occur near the corners of the notch at every stage of loading, which are similar to the Cube oriented sample.

The characteristics of crystal rotation discussed above can also be presented qualitatively by pole figures of normal vectors of slip planes for Cube and Brass oriented samples, respectively, as shown in Figures 4.24 and 4.25. The pole figures include data of crystals throughout the sample thickness within each of the three regions defined in Figure 4.3. The directions [100] and [010] in Figures 4.24 and 4.25 are in the global coordinate system, and correspond to the sample X and Y axes, respectively. Observations similar to those in the disscussions regarding component rotation can be made from the above pole figures. For example the amplitude of crystal evolution for the Cube oriented sample increases with strain load and decreases with distance from the notch, i.e. crystals in region I at 4.5% strain rotate most severely, while those in region III at 1% strain mostly remain in the initial cube orientation. Crystals rotating in regions II and III with up to 3% strain are still not noteworthy while considerable rotation in region I occurs. The distribution of poles in this region is symmetrical around the [100] axis, which implies that crystals rotate about this axis an equal amount in the opposite direction. It is also symmetrical around [010] which denotes symmetrical rotation about the [010] direction. As a

result, we have a pole figure that is symmetrical around the centre point. Crystals rotating in equal and opposite directions about the [100] axis in regions II and III become more obvious at 4.5% strain, evidenced by the stretching of pole distribution along the [010] while remaining symmetrical around the centre point. Furthermore, the pole distribution thickens and splits into two bands that are aligned in the [100] direction in the pole figures of regions II and III, which denotes a larger rotation about [010].

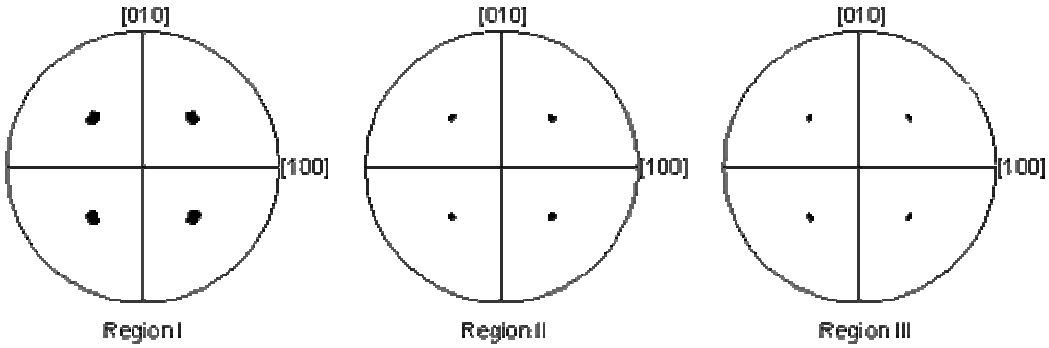

(a) 1% nominal strain

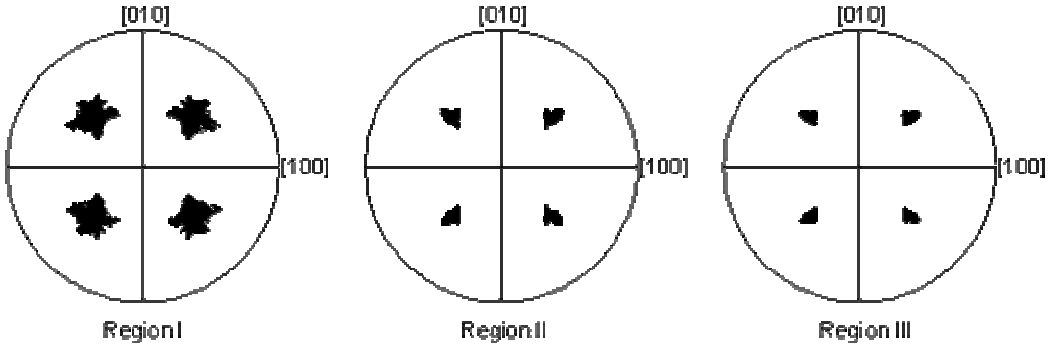

(b) 3% nominal strain

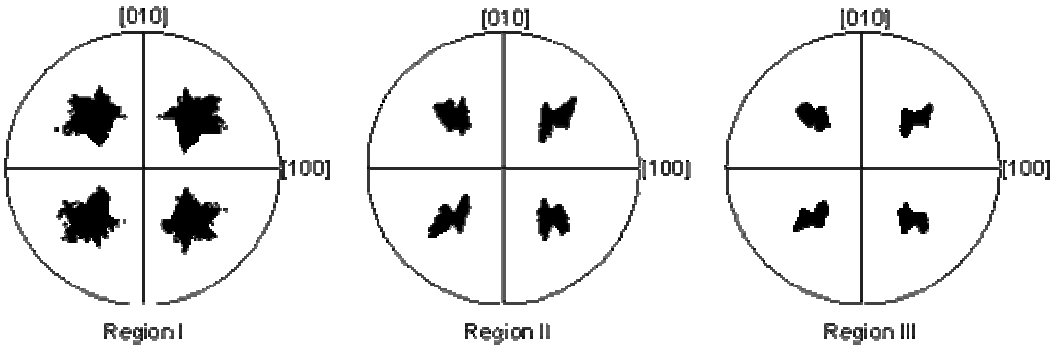

(c) 4.5% nominal strain

Figure 4.24 <111> pole figures of crystals around notch in Cube oriented sample.

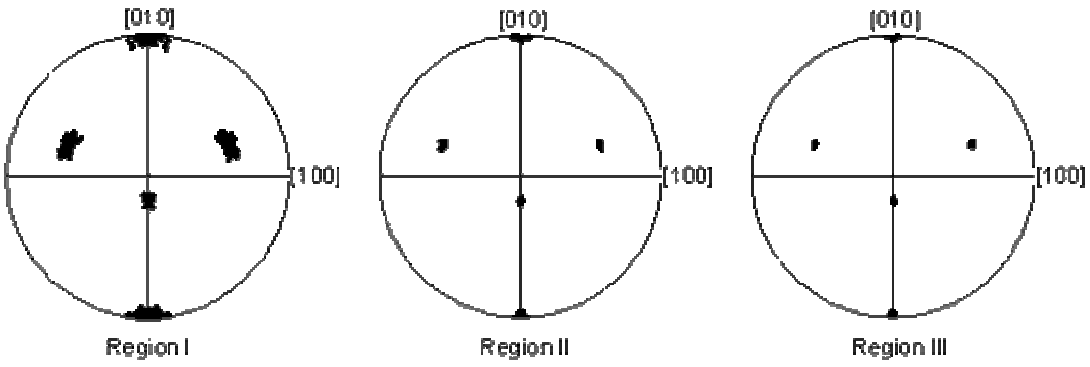

(a) 1% nominal strain

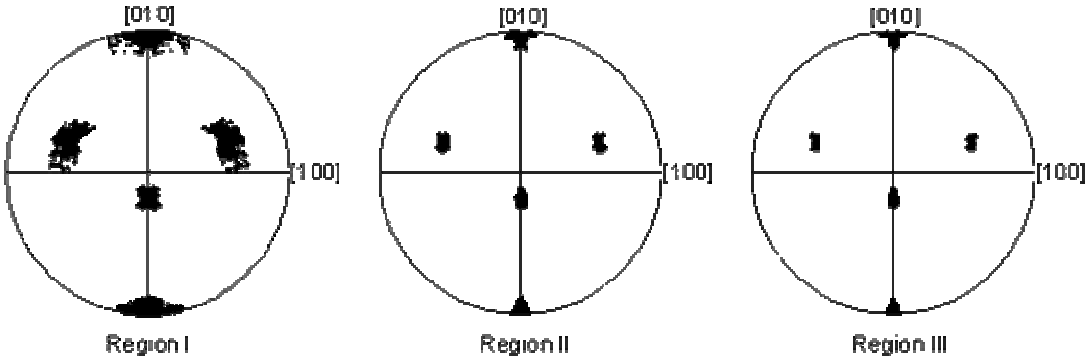

(b) 2% nominal strain

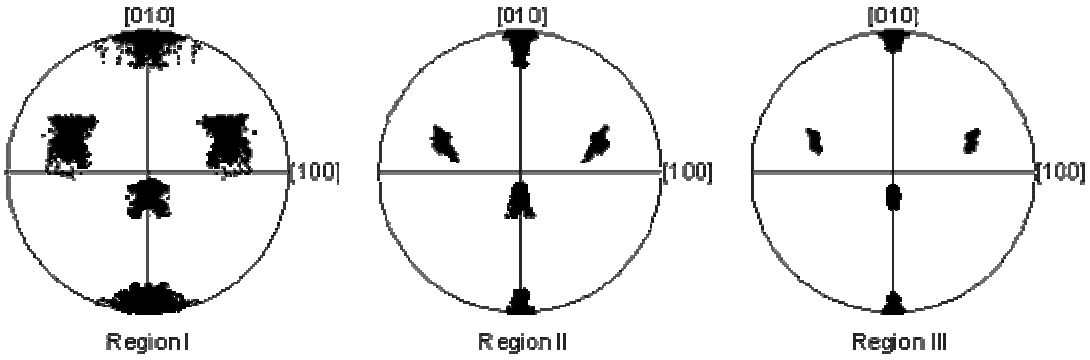

(c) 3% nominal strain

Figure 4.25 <111> pole figures of crystals around notch in Brass oriented sample.

4.3 Conclusions

This chapter has numerically examined the material behaviours around the notch tip in an SEN single crystal aluminum under tensile load. The CPFEM model incorporating Bassani-Wu hardening law, which was validated in Chapter 3, has been used. The deformation has been examined in both macroscale (via the change

of surface roughness and slip traces on the sample surface) and microscale (via the plastic slip and crystal rotation). Deformation in both scales appeared to be most severe in the region very close to notch (region I) than outer regions (regions II and III). Simulation results (e.g. evolution of lattice orientation, stress/strain/displacement fields) obtained from this chapter form a basis for analyses of crack opening carried out in Chapter 6.

The current simulation results show that the change of surface roughness in the Brass oriented sample (lattice plane $(1\,\bar{1}\,2)$ on the surface) is higher than the Cube oriented sample (lattice plane (001) on the surface). This qualitatively agrees with other experimental and numerical studies [128-134] which indicated that a sample surface on a high Miller index lattice plane tends to have higher roughness than a surface on a low Miller index plane [131].

Plots of slip traces on the free surface of Cube and Brass oriented samples match very well with analytical predictions based on the initial crystal orientation (Figures 4.11 and 4.12). At high loads and at locations very close to the boundary of the notch, crystals rotate severely from the initial orientation. Thus the orientation of slip traces in these cases must be determined numerically.

In both Cube and Brass oriented samples, the current simulation results show that magnitudes of the total plastic slip and crystal rotation are higher on the sample surface than on the mid-thickness plane. This may be due to different deformation conditions on the two planes, i.e. the free surface deforms under plane stress condition, while the mid-thickness plane deforms under plane strain condition. Two dimensional plane stress and plane strain simulations need to be done and compared with the current 3D results to properly explain these observations.

For both Cube and Brass oriented samples, the distribution of surface roughness (Figures 4.9 and 4.10) generally has the same patterns with those of total plastic deformation (Figures 4.13 and 4.14) and total crystal rotation (Figures 4.16 and 4.17). At every stage of loading, points having the highest values of surface roughness appear to have the highest crystal rotation and highest plastic deformation.

These features are best observed at 4.5% nominal strain for the Cube oriented sample, and at 3% nominal strain for the Brass oriented sample.

5. Microstructure Evolution in SEN Polycrystalline Aggregates(*)

Chapter 4 used the CPFEM model incorporating the Bassani-Wu hardening law developed in Chapter 2 to study the deformation around the notch tip in an SEN single crystal. This chapter extends the study to simulate plastic deformation and evolution of microstructure at the notch tip in an SEN polycrystalline sample having same dimensions with samples considered in Chapter 4. Section 5.1 briefly presents the properties of the Voronoi diagram, which will then be used to construct the polycrystalline aggregate. Two sets of initial orientations will be assigned to the aggregate to study the influence of initial material textures. For geometrical effects, notch of different shapes will be considered.

5.1 Voronoi diagram and the construction of polycrystalline aggregates

5.1.1 Basic theory of the Voronoi diagram

Let S^V denote a set of n coplanar points (or seeds). For any two different seeds p^V and q^V that belong to S^V, the dominance of p^V over q^V is defined as the part of the plane that is at least as close to p^V as to q^V, and is expressed mathematically as [137]

$$dom\left(p^V, q^V\right) = \left\{x \in R^2 \mid dist(x, p^V) \le dist(x, q^V)\right\} \tag{5.1}$$

dist() denotes a function of distance. Obviously dom(p^V, q^V) specifies the half plane that contains the seed p^V, and is bounded by the perpendicular bisector of p^V and q^V. This perpendicular bisector will be referred to as the separator of p^V and q^V. The region of the seed p^V is defined as the portion of the plane closer to p^V as to the rest of S^V, and is mathematically expressed as

(*) The results in this chapter have been published in reference [138]

$$reg(p^V) = \bigcap_{q^V \in S^V - \{p^V\}} dom(p^V, q^V) \tag{5.2}$$

A region cannot be empty, because at least it contains the seed that forms it. Since the regions of n seeds are made from intersecting n-1 half planes, they are convex polygons. Also, the boundary of each region comprises of at most n-1 segments of straight line and n-1 vertices. Points along the boundary of a region are equidistant from exactly two seeds. Each vertex is equidistant from at least three seeds, i.e. it is the centre of a circle going through at least three seeds but not containing any seed. In other words, regions of n seeds form a polygonal division of the plane, which is called the Voronoi diagram $V(S^V)$ of the set S^V. Because S^V contains n seeds, $V(S^V)$ comprises of n regions. A sample of a planar Voronoi diagram with eight seeds is shown in Figure 5.1.

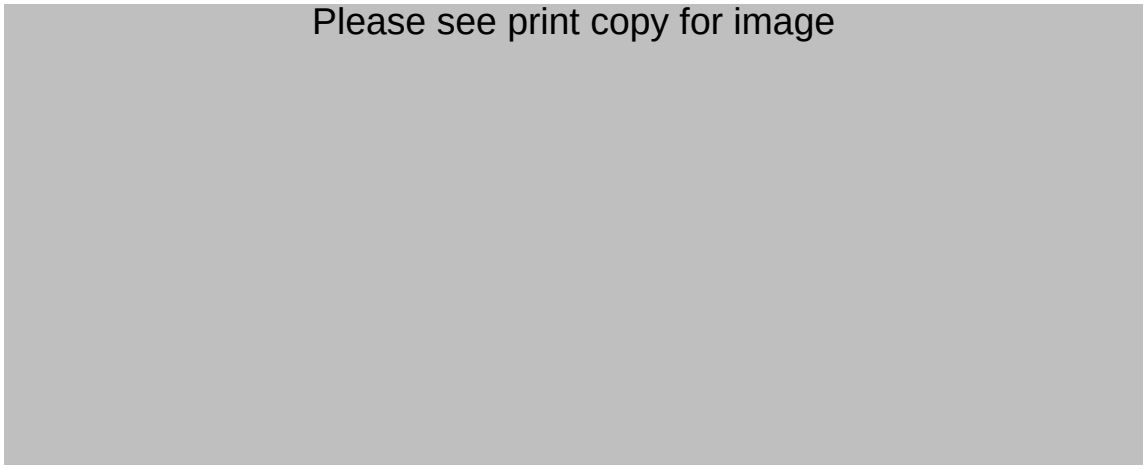

Figure 5.1 Sample of a planar Voronoi diagram with eight seeds. [137]

Figure 5.2 Dual relationship between a Voronoi diagram and the Delaunay triangulation. [137]

From the mathematical viewpoint, the Delaunay triangulation is very closely related to the Voronoi diagram. A planar Delaunay triangulation comprises of triangles connecting seeds of a planar Voronoi diagram so that no seed is contained within any triangle. A sample that demonstrates the relationship between a Voronoi diagram and the Delaunay triangulation is shown in Figure 5.2. A Delaunay edge (solid line) is perpendicular to the corresponding edge in the Voronoi diagram (dashed line), but they do not necessarily intersect each other.

5.1.2 Construction of the polycrystalline structure

In this study, the polygons in a planar Voronoi diagram will be used to represent 2D grains. Because each polygon in the Voronoi diagram contains only one seed, if the total planar area is fixed, the number of seeds will determine the average size of the polygons. The distribution of the distances between seeds will determine the distribution of the size of the polygons. Therefore the average value and distribution of the grain size is controlled by adjusting the number and relative position of the seeds. An algorithm to control the grain size distribution is proposed as follows.

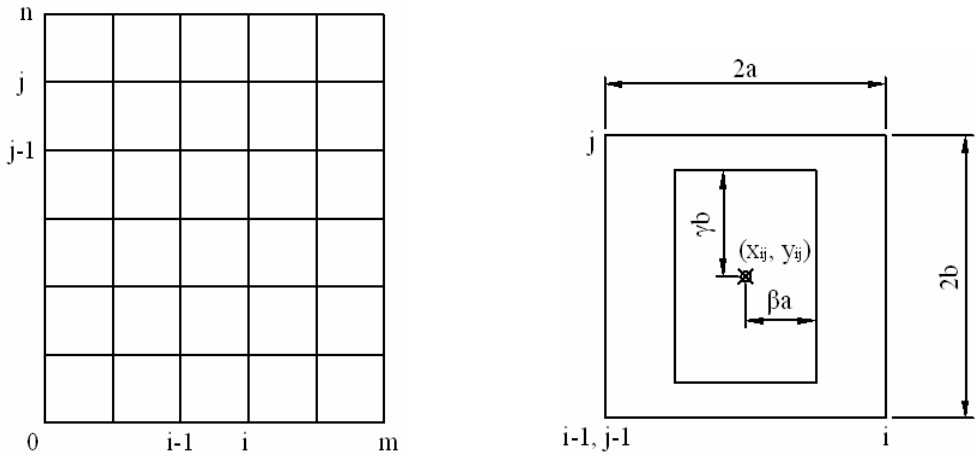

(a) sub-region (b) control sub-region

Figure 5.3 Demonstration of the algorithm to control the grain size distribution.

- Assuming a total number of (m x n) grains are to be generated. The whole planar region is equally divided into m rows and n columns of rectangular sub-regions, as shown in Figure 5.3a. The width and height of each sub-region are 2a and 2b, respectively. Coordinates of the centre of the sub-region (i, j) are denoted by (x_{ij}, y_{ij}).
- Within each sub-region, a rectangle which measures $2\beta a$ wide and $2\gamma b$ high is created ($0 < \beta, \gamma \leq 1$). This rectangle is called the control sub-region, and shares the same centre with the outer sub-region.
- A seed is assigned randomly within a control sub-region. Increasing the values of β or γ increases the size of the control sub-region, which changes the distribution of distances between seeds, which in turn, changes the distribution of grain size.

Based on the given set of seeds S^V, the Voronoi diagram can be constructed based on the Delaunay triangulation. Each Delaunay edge belongs to two triangles, except those connecting seeds on the boundary of the convex hull of S^V (Delaunay boundary edges). Each of these Delaunay boundary edges belongs to only one triangle. For each Delaunay edge belonging to two triangles, the centres of the circumcircles of the triangles are connected by a straight line. For each Delaunay boundary edge, a line is drawn from the centre of the circumcircle of the corresponding triangle perpendicular to the Delaunay edge. The resulting set of straight lines forms the Voronoi diagram.

Implementing the above procedure via Matlab codes, a list of Voronoi edges together with the coordinates of the corresponding vertices is created. From this list of Voronoi edges and vertices, Python codes (an object oriented programming language accompanied Abaqus software) is used to create an FEM model of a polycrystalline aggregate directly in Abaqus/Standard. Figure 5.4 shows the flow chart of the Python program that generates the geometry of the polycrystalline aggregate.

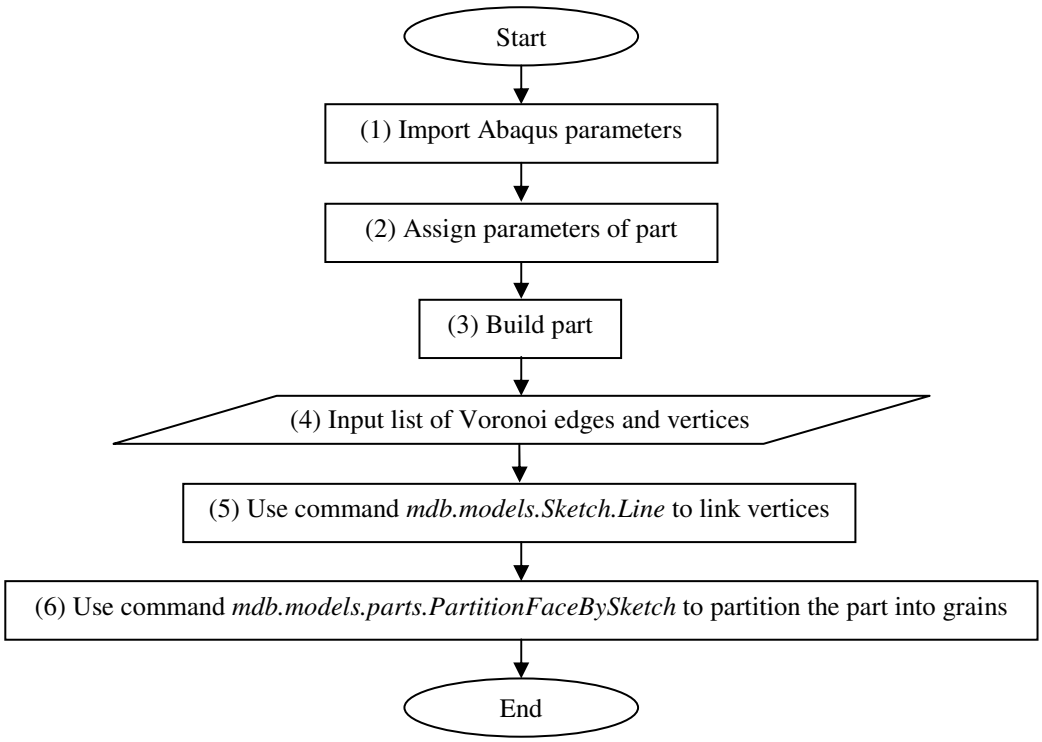

Figure 5.4 Flow chart of the Python code generating the polycrystalline aggregate.

Details of each step in Figure 5.4 are described as follows.

- Step (1) makes objects in Abaqus available to the Python script. Some of these objects include Abaqus basic objects, 'Symbolic Constants' defined by Abaqus, and objects related to Python modules 'sketch', 'part', 'material', 'section', etc.
- Step (2) assigns parameters related to the part (e.g. the outer boundary of the sample (11mm x 11mm), two dimensional deformable body), and plot the outer boundary of the part.
- Step (3) creates (builds) the part from the parameters defined in step (2).
- Step (4) reads in the data file of Voronoi edges and vertices which was generated from Matlab codes.
- Step (5) uses the Python command *mdb.models.Sketch.Line* to draw lines (edges) between vertices as specified in the data file read in step (4).
- Step (6) uses the Python command *mdb.models.parts.PartitionFaceBySketch* to partition the part into grains based on lines (edges) drawn in step (5).

Figure 5.5 presents the flow chart of the Python code that assigns the initial orientation into each grain. Details of each step in the flow chart are described as follows.

- Step (1) makes objects in Abaqus available to the Python script, as described in step (1) of Figure 5.4.
- Step (2) reads in the data file specifying initial orientation and location of the seed of each grain. The location of seeds is determined following the procedure described earlier. Initial orientations can be randomly generated as discussed in Section 5.2.
- Step (3) creates a set of material properties P that are unchanged from grain to grain, e.g. the elastic moduli, parameters for the Bassani-Wu hardening law, constants related to the lattice structure. Indeed, the only material properties that are different between grains are the initial orientations.
- Step (4) extracts the initial orientation of grain i^{th}, which is determined by the location of its seed, and assigns this initial orientation to the set of unchanged material properties P. The newly created set is saved as $A[i]$.

- Step (5) uses the Python command *mdb.models.Material* to create the material section for grain ith.
- Step (6) uses the Python command *mdb.models.materials.UserMaterial* to assign $A[i]$ to the material section of grain ith.
- Step (7) uses the Python command *mdb.models.materials.Depvar* to set the number of state dependent variables for grain ith. These state dependent variables are results from the CPFEM model, e.g. resolved shear stress, direction of slip systems, coordinates of calculation points.
- Steps (4) to (7) are repeated for each grain until the number of grains is reached.

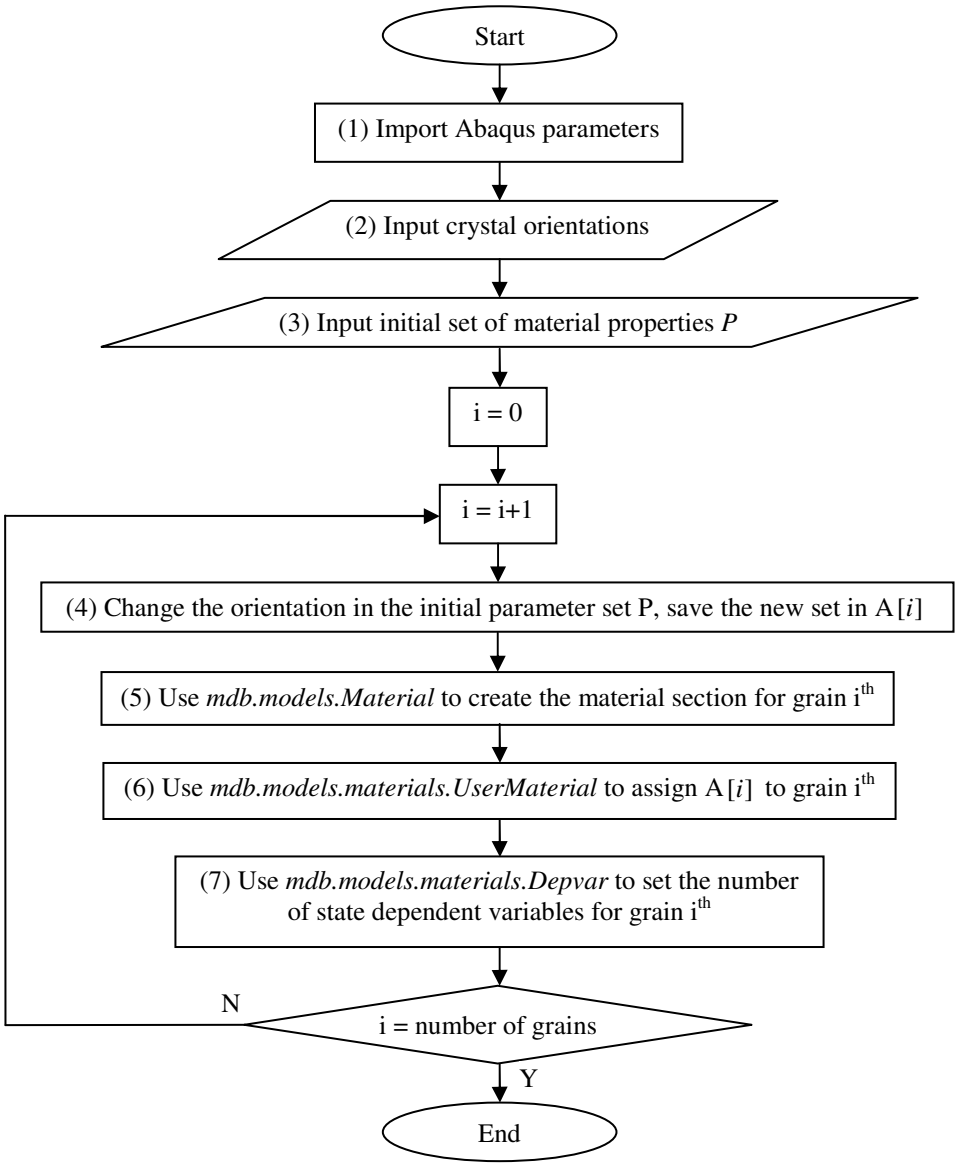

Figure 5.5 Flow chart of the Python code assigning initial orientations into grains.

5.2 CPFEM model [138]

The geometry of the polycrystalline aggregate is shown in Figure 5.6. The dimensions are based on the microscope observation of an annealed high-purity aluminum sample of dimensions 11 mm x 11 mm. These dimensions are similar to those of the single crystal sample used in Chapter 4. Three notch types, namely triangular notch, rectangular notch and circular notch are considered. The three notches are slightly smaller than those used in Chapter 4 so that they are completely contained within two grains A and B as shown in Figure 5.6. The notches have the same 1 mm wide by 0.5 mm deep opening.

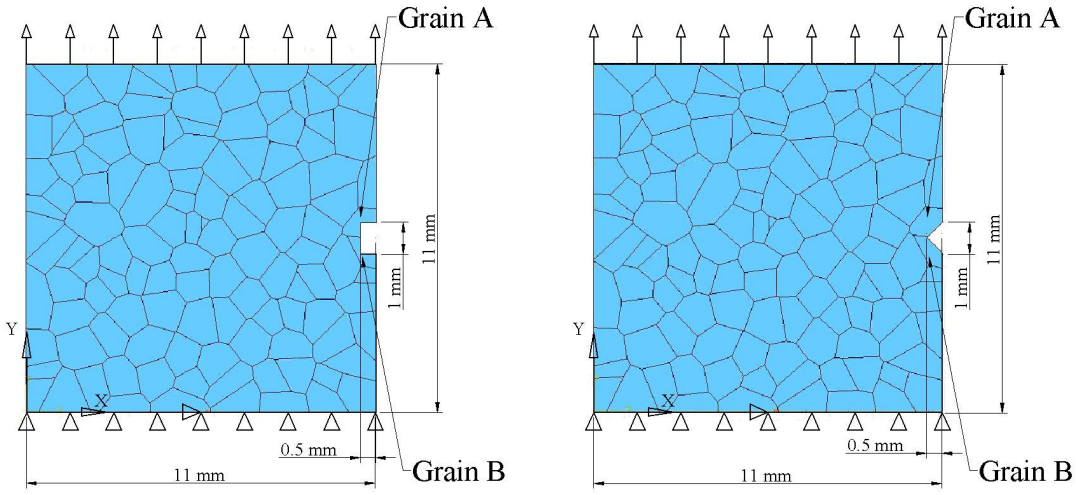

(a) Rectangle-notched sample (b) Triangle-notched sample

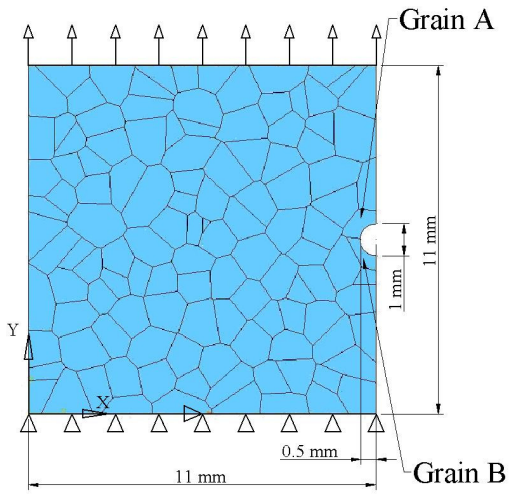

(c) Circle-notched sample

Figure 5.6 Model of polycrystalline aggregate with three notch types

It is assumed in this study that there is only one grain across the thickness of the tensile test sample. Therefore, a two-dimensional (2D) FEM model has been used. Other concerns are the use of a 2D FEM model reduces the computing time and avoids the complexity of building three-dimensional (3D) grain microstructure. The Voronoi diagram approach is used to generate a number of 2D cells where each cell represents a virtual grain. The average grain size is 1.13 mm. An image of the observed sample is shown in Figure 5.7a and a sample of the Voronoi diagram having the same average grain size is shown in Figure 5.7b.

(a) Annealed high-purity polycrystalline aluminum.

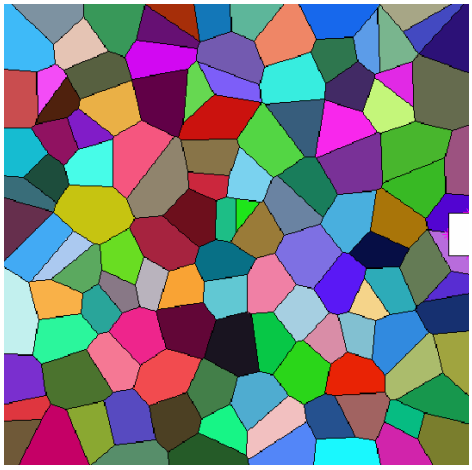

(b) Voronoi diagram approximating the annealed polycrystalline aluminum.

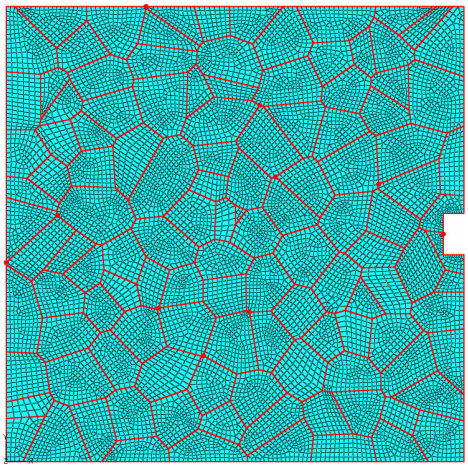

(c) FEM mesh of the Voronoi diagram.

Figure 5.7 Geometry of polycrystalline aluminum samples.

It is assumed that the orientation distribution function is uniformly distributed in Euler space. Using this assumption a randomly generated orientation is assigned to each grain of the polycrystalline aggregate. The misorientation between any two

grains is greater than 15°. Two sets of this randomly generated orientation are used to demonstrate the effect of initial orientation on plastic deformation at the notch tip in a polycrystalline aggregate. This effect will be analyzed by using two grains surrounding the notch, denoted as grains A and B in Figure 5.6. The Euler angles for grains A and B in two sets of orientation are shown in Table 5.1. Pole figures of crystals in these grains are shown in Figure 5.8.

Table 5.1 Euler angles for Grain A and Grain B

	Orientation set	φ_1	Φ	φ_2
Grain A	I	29.26°	1.48°	73.89°
	II	77.25°	85.84°	50.85°
Grain B	I	65.08°	38.15°	77.66°
	II	18.01°	24.33°	22.72°

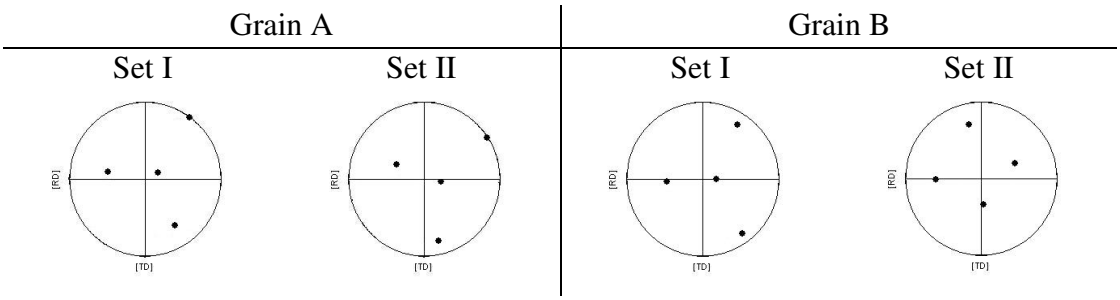

Figure 5.8 Pole figures of sets of initial orientation of grains A and B.

Each grain is meshed by a number of plane stress four-node bilinear elements. A sample of the finite element mesh with a rectangular notch is shown in Figure 5.7c. The total number of elements is approximately 12,000. During the simulation a constant velocity of 1 mm/s is applied upward to the top edge until a total nominal strain of 10% is reached. The bottom edge is fixed in the vertical direction, and the middle point of the bottom edge is fixed in the horizontal direction to avoid rigid body displacement. Left and right sides of the samples are set free (see Figure 5.6).

5.3 Analyses and discussions of CPFEM results [138]

Figures 5.9 and 5.10 illustrate the deformed grains around notches with set I initial orientation and set II initial orientation, respectively. It is obvious that the initial

orientation has a significant influence on the deformed shapes of the notches. The deformation with set II initial orientation is more severe than that with set I, for all notches. This is indicated the greater change of roughness of the edge of notches in Figure 5.10 (set II initial orientation) compared to notches in Figure 5.9. The initial roughness of the edges is assumed zero. In Figure 5.10, roughness of the edge of notches changes from the initial state by approximately 0.0394 mm, 0.0570 mm, and 0.7166 mm for the rectangular, triangular, and circular notches, respectively. The combined effect of notch shape and crystal orientation is also observable in Figure 5.10. The lower half of the edge of rectangular notch (Figure 5.10a), which belongs to grain B, is more deformed than the upper half. On the other hand, the upper half of the edge of triangular notch, which belongs to grain A, is rougher than the lower half which belongs to grain B (Figure 5.10b). Meanwhile, both halves of the circular notch appear to undergo equivalent deformations (Figure 5.10c).

Table 5.2 Values of maximum shear stress plotted in Figures 5.9 and 5.10

	Rectangular notch	Triangular notch	Circular notch
Set I	19.08 MPa	21.48 MPa	19.46 MPa
Set II	27.86 MPa	46.84 MPa	39.34 MPa

The position and orientation of maximum shear stress that occurs in grains A and B are also shown in Figures 5.9 and 5.10. The dotted lines represent grain boundaries. The black dot at one end of the bold solid straight line segments represents the location of maximum shear stress. The direction of the bold solid straight line segments represents the slip directions and their length indicates the relative magnitude of maximum shear stress. In other words, these straight line segments are traces on the sample surface of slip systems that have maximum shear stress. Values of maximum shear stress are listed in Table 5.2. It is clear from Figure 5.9 that the maximum shear stress does not always occur on the boundaries or corners of a notch. The shear stress on a slip system α can be calculated by Equation (5.3), which is another form of the Equation (2.49).

$$\boldsymbol{\tau}^{(\alpha)} = \mathbf{m}^{(\alpha)} \frac{\rho_0}{\rho} \boldsymbol{\sigma} \mathbf{s}^{(\alpha)} \tag{5.3}$$

(a) rectangular notch

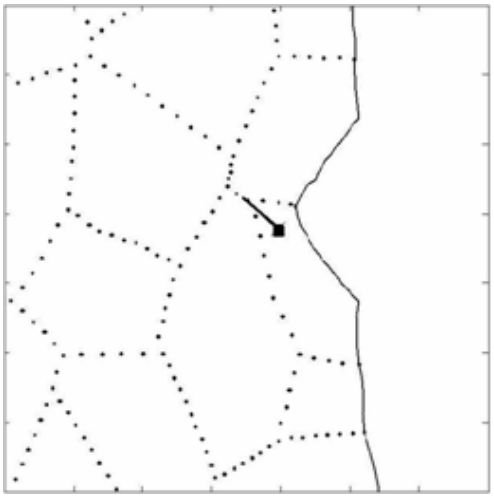

(b) triangular notch

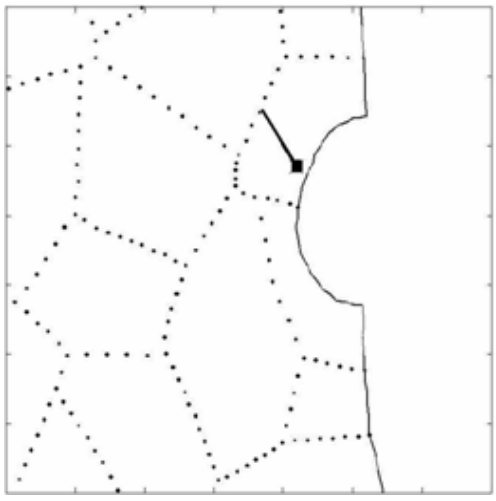

(c) circular notch

Figure 5.9 Deformed samples with Set I initial orientation, 10% nominal strain.

(a) rectangular notch

(b) triangular notch

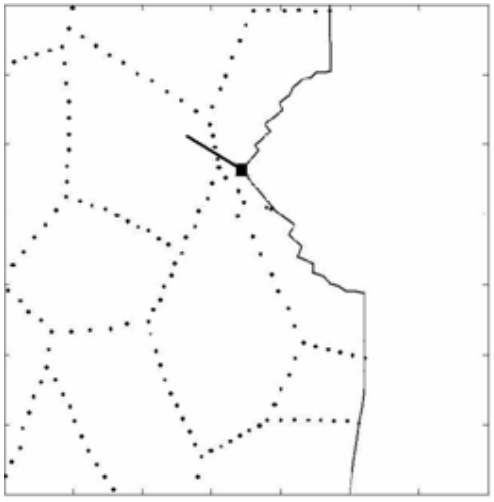

(c) circular notch

Figure 5.10 Deformed samples with Set II initial orientation, 10% nominal strain.

ρ_0 and ρ are the mass density of in the reference and the current states. Because the time increments used in the simulations are small (in the order of 1e-4) these mass densities can be considered identical which makes $\rho_0 / \rho = 1$. Thus the resolved shear stress on slip system α is influenced by Cauchy stress $\boldsymbol{\sigma}$ and the geometry of that system, i.e. the slip direction $\mathbf{s}^{(\alpha)}$ and normal to slip plane $\mathbf{m}^{(\alpha)}$. The orientation of crystals changes significantly after deformation, as depicted later in the <111> pole figures of grains adjacent to notches. Hence the points at which the rotated orientation ($\mathbf{s}^{(\alpha)}$,$\mathbf{m}^{(\alpha)}$) would maximize the shear stresses are not necessarily on the boundary of the notch. On the contrary, the Cauchy stress $\boldsymbol{\sigma}$ around the notch is still much larger than in other areas because of stress concentration. This explains why maximum shear stress might not be exactly on the boundary, but would be somewhere around the notch.

It can be found from Figures 5.9 and 5.10 that the shape of the notches significantly affects the location of maximum shear stress for both sets of initial orientations. Different types of notches lead to different locations of maximum shear stress. These maximum shear stresses vary irregularly with notch geometries. However, the values of maximum shear stress of set I initial orientation are larger than those of set II, which again proves that the initial orientation plays an important role in the local plastic deformation around the notches.

Figure 5.11 shows the contour plots of cumulative shear strain on all the slip systems at each integration point for the initial orientation of set I. The general tendency is area with higher equivalent plastic strain aligns at 45^o to the loading axis, while the plastic behaviour of each grain is highly influenced by its initial orientation. Figure 5.12 presents the same results for the initial orientation of set II. The general tendency of the equivalent plastic strain mentioned before is much more obvious in this case. Besides, for all notch shapes with set I initial orientation (Figure 5.11), the maximum cumulative shear strain seems to occur at an inner site of the sample rather than on the boundary of the notches. However for set II initial orientation (Figure 5.12) it seems that the maximum cumulative shear strain occurs at a point on the notch boundary for all notch shapes. This observation supports the above conclusions regarding the location of maximum resolved shear stresses.

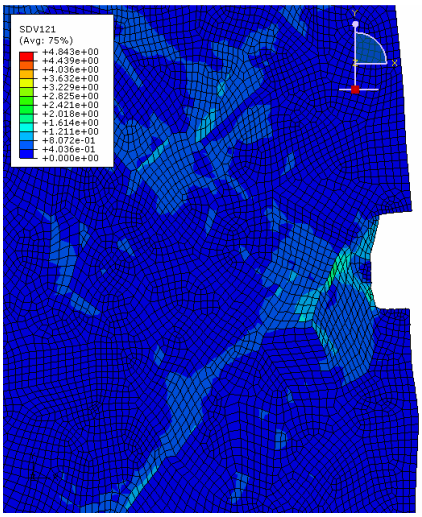

(a) rectangular notch

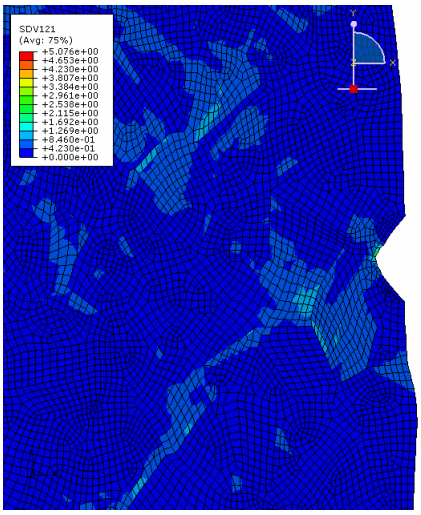

(b) triangular notch

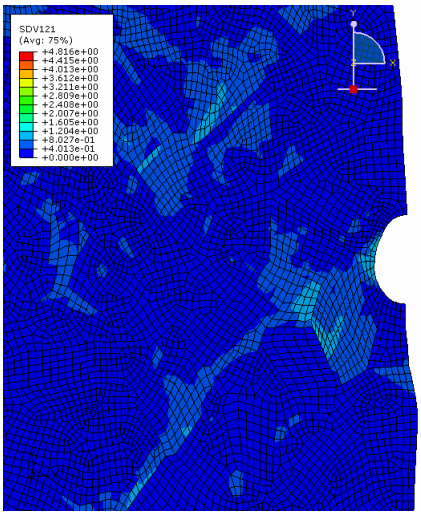

(c) circular notch

Figure 5.11 Cumulative shear strains around the notches, set I initial orientation, 10% nominal strain.

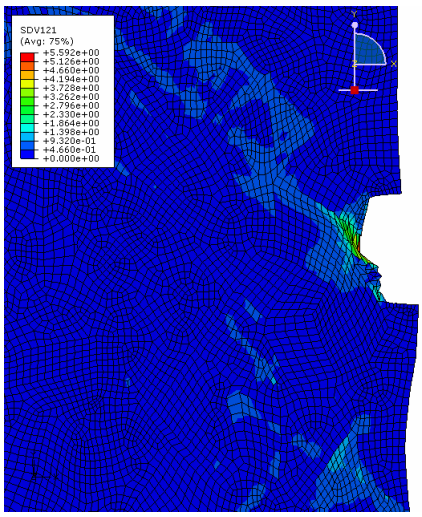

(a) rectangular notch

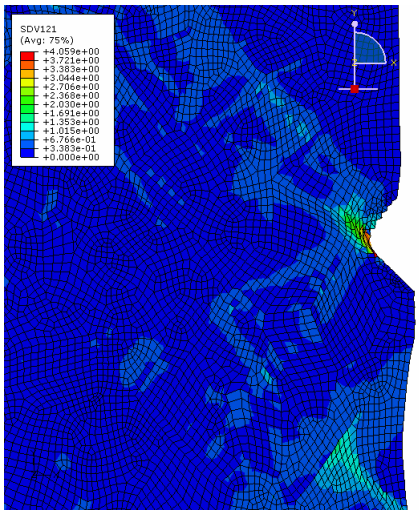

(b) triangular notch

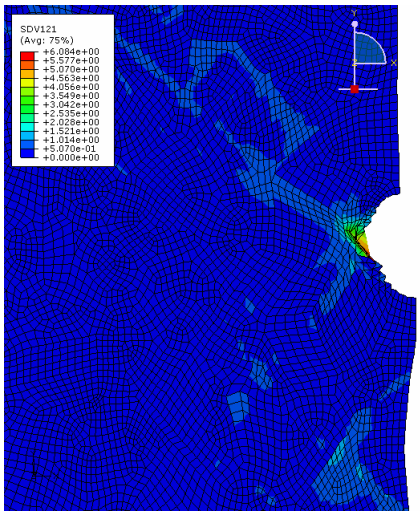

(c) circular notch

Figure 5.12 Cumulative shear strains around the notches, set II initial orientation, 10% nominal strain.

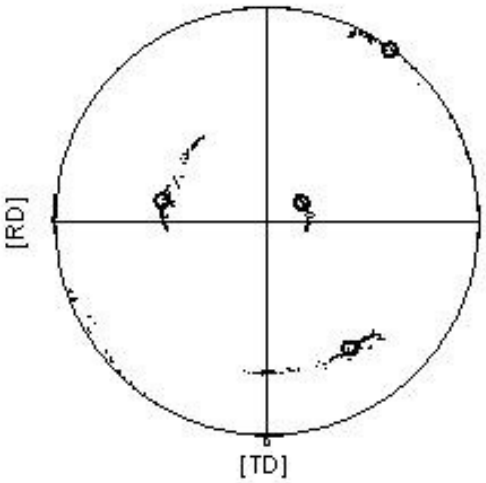

(a) rectangular notch

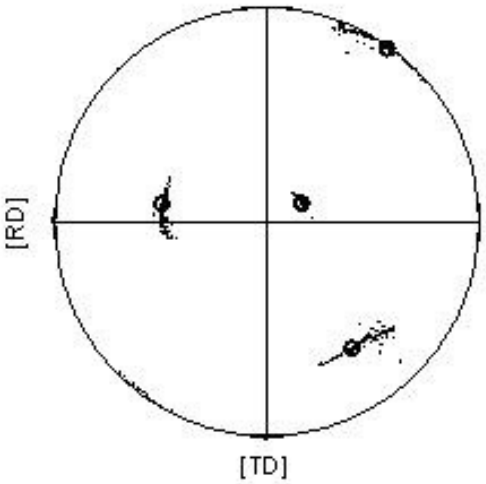

(b) triangular notch

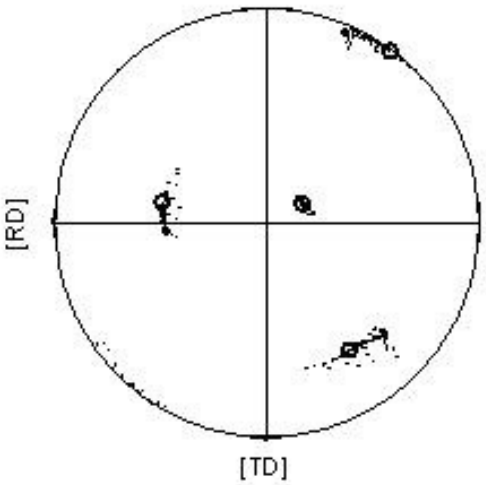

(c) circular notch

Figure 5.13 <111> pole figures for Set I initial orientation in grain A, 10% nominal strain.

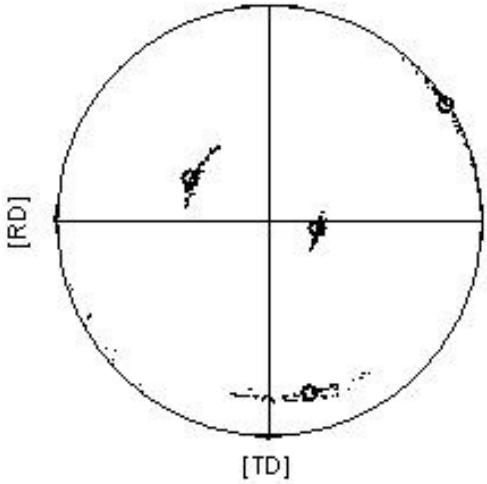

(a) rectangular notch

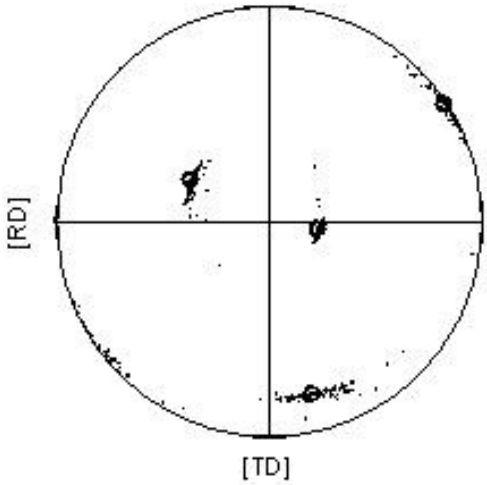

(b) triangular notch

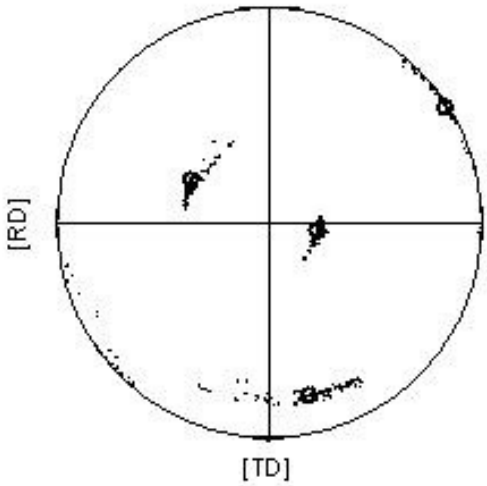

(c) circular notch

Figure 5.14 <111> pole figures for Set II initial orientation in grain A, 10% nominal strain.

The orientation distributions in grain A after deformation are shown by using the <111> pole figures in Figures 5.13 and 5.14, which correspond to set I and set II initial orientation, respectively. The conventional rolling terms, RD, TD, and ND are used to denote the elongation, transverse, and thickness directions, respectively. The hollow circle symbols represent the initial orientations. It is clear that the crystal orientations profoundly rotate around ND, namely the thickness direction of the samples, for all the notches and all the initial orientations. The crystal orientations after deformation are scattered fairly widely, but generally centred on the original orientation. Comparing the results of three notches indicates that the spread of the orientation of the rectangular notch is greater than the other two notches. The pole figures for grain B are not displayed as the same phenomena as those in grain A are observed.

The method proposed by Wert et al. [127] was used to quantitatively analyze the microstructure evolution around the notches during deformation in grain A by determining the rotation angles of the crystal orientation around RD, TD, and ND. Figures 5.15 and 5.16 depict the rotation angles against the nominal strain, which is determined from the displacement of the top edge (u) divided by the initial height of the sample (L), at the point of maximum shear stress for the initial orientations of Set I and Set II, respectively.

Figures 5.15 and 5.16 show that rotation angles increase with increasing strain except for some decreases in Figures 5.16b and 5.16c. For all types of notch geometry and both sets of initial orientations, crystal rotations about three axes appear to evolve in three stages. The rotation around ND (axis normal to the sample surface) is larger than those around the other two directions. For all types of notch geometry, rotations of crystals in Set II initial orientations appear to be greater than those in Set I. This observation reinforces the results mentioned at the beginning of this section that the samples with an initial orientations of set II deform more severely than the samples oriented in set I. Figures 5.15 and 5.16 reinforce the effects of notch shape to the evolution of microstructures around the notch tip, which were observed earlier in this section. Having same initial orientations, crystals around the rectangular notch, triangle notch and circular notch evolve quite differently, which are best observed in Figures 5.16a, 5.16b and 5.16c, respectively.

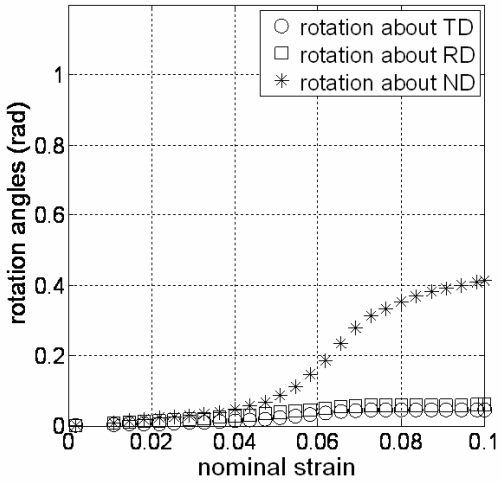

(a) rectangular notch

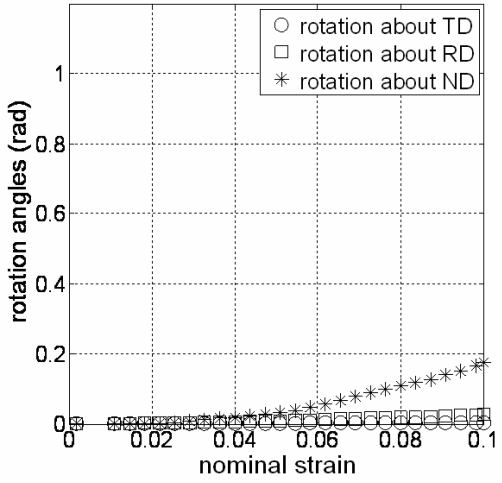

(b) triangular notch

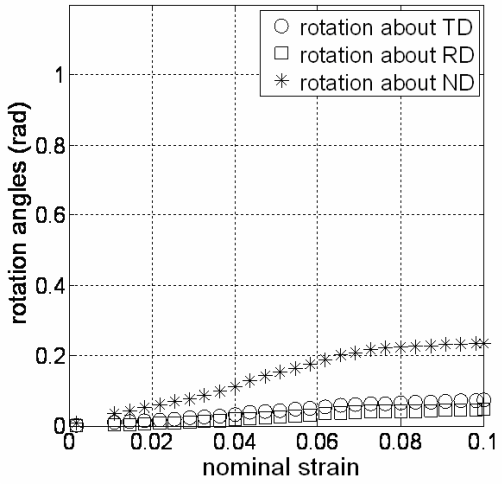

(c) circular notch

Figure 5.15 Rotation angles about three global axes versus the nominal strain for Set I initial orientation, 10% nominal strain.

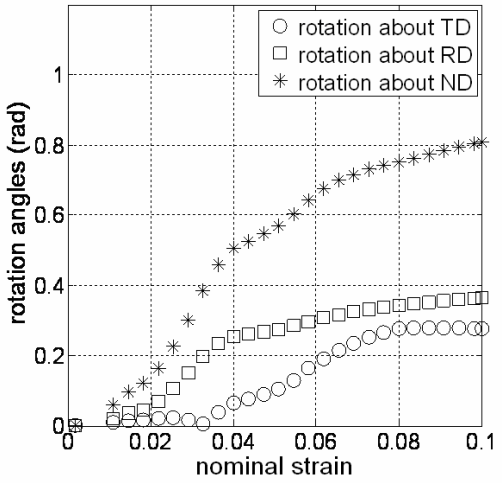

(a) rectangular notch

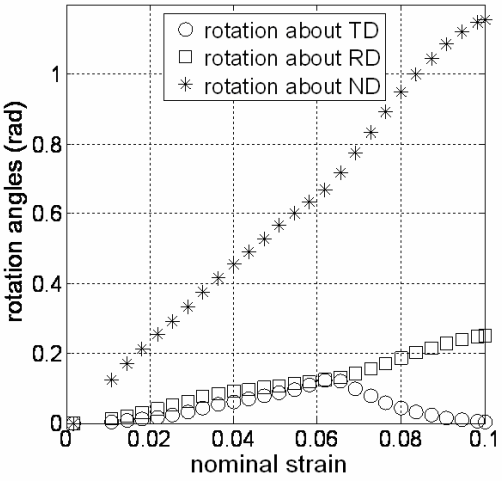

(b) triangular notch

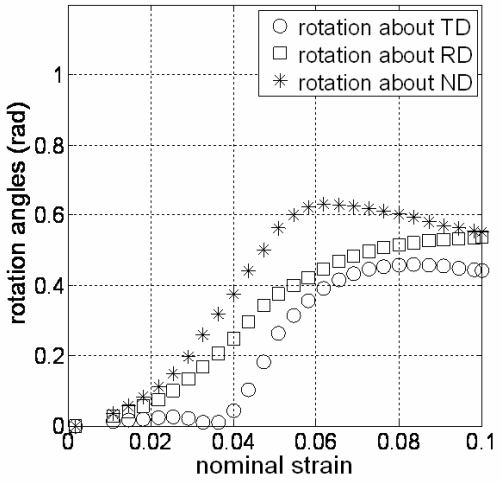

(c) circular notch

Figure 5.16 Rotation angles about three global axes versus the nominal strain for Set II initial orientation, 10% nominal strain.

Figure 5.15a shows that crystals in the rectangular notched sample with set I initial orientation rotate slowly around ND for strains up to 0.05, more rapidly for strains up to 0.08, then slowly again for strains larger than 0.08. The same behaviour is observed for the rectangular notch with set II initial orientation. The crystal rotation about ND in the triangular notched samples for both sets of initial orientation comprises of two stages (Figures 5.15b and 5.16b). The first stage is for nominal strains up to 0.04 and 0.07, for orientation set I and set II, respectively, and then a slightly faster rotation (stage 2). Rotations of crystals in the triangle-notched samples probably has not reached stage 3, because a closer look at the end of the ND rotation curve in Figure 5.15b shows that the slope slightly decreases. This indicates that stage 3 would take place if higher strains were applied. The circular notched samples also show a clear three-stage rotation about ND for both sets of initial orientations. For initial orientation of set I, Figure 5.15c shows that stage 1 occurs at strains smaller than 0.04, stage 2 for strains between 0.04 and 0.08, and stage 3 for strains larger than 0.08. For set II initial orientation, as shown in Figure 5.16c, limits of each stage are nominal strain lower than 0.02 for stage 1, from 0.02 to 0.07 for stage 2, and larger than 0.07 for stage 3.

5.4 Conclusions

Section 1.6 showed that numerous simulations using CPFEM model have been done to investigate the behaviour of an fcc polycrystalline aggregate under tensile load, in both 2D and 3D space. However, a study that uses a CPFEM model incorporating the Bassani-Wu hardening law to examine the combined effects of notch shape and initial orientation on the tensile deformation around a notch tip in a polycrystalline aggregate is still lacking. This chapter presents some preliminary results of such a study. The CPFEM model incorporating the Bassani-Wu hardening law was validated in Chapter 3. Besides, this chapter can also be regarded as an extension of simulations and analyses carried out in Chapter 4 for the case of a polycrystalline aggregate.

The polycrystalline aggregate has been approximated by a 2D Voronoi diagram. The analyses carried out in this chapter have shown that the deformation of a

polycrystalline aggregate with an existing notch is influenced by not only the notch geometry, but also by the initial crystal orientation. In particular, initial orientation greatly influences the location and values of maximum shear stress and cumulative shear strain, and the deformation of the edge of the notch.

The rotation of crystals close to notch tip appears to comprise of three stages. This behviour is more obvious for rotations around ND axis, for all types of notch shape and initial orientation considered. This may be directly attributed to the Bassani-Wu hardening law, which describes the evolution of shear stress in a single slip system as a three stage process.

Review of other studies (Section 1.6) showed that other factors, such as grain size (or the number of grains), sample thickness, type of Voronoi diagram (2D, quasi-3D, full 3D) also influence the behaviours of a polycrystalline aggregate under tensile load. Further works need to be done to examine how these factors affect the conclusions made above regarding crystal rotations and plastic deformation around the notch tip.

6. Misorientation-Dependent Cracking Criterion

In this chapter, the data of orientation evolution obtained from Chapter 4 is further exploited to investigate misorientation, defined as the difference in orientation of two adjacent crystals in the proximity of the notch tip. Misorientation provides us with a new interpretation for lattice rotation of regions around the crack tip. With regards to the fact that crystalline structures along the interfaces (e.g. grain boundaries, phase boundaries) are not as strong as the bulk material, this information serves as a first step toward a new approach to modelling crack initiation and propagation. A methodology for modelling crack opening based on the energy of two misoriented lattices is proposed. This methodology is original and, to the best of the author's knowledge, has not been reported in the literature. The resulting modelling capability allows explicit prediction of crack growth without presuming a crack path, which is essential in the studying of cleavage in ductile materials.

Section 6.1 presents the development and verification of an atomic interaction model which is the core for estimating of the misorientation dependent crack opening criterion. Sections 6.2 to 6.4 present further analyses and discussions of FEM modelling results to determine the nucleation of voids and subsequent crack growth around a notch.

6.1 Atomic interaction model estimating interface fracture energy

6.1.1 Atomic interaction model

An interface between two tilted lattices is uniquely determined in 3D space by five degrees of freedom: two represent the tilt axis orientation, one represents the tilt angle,

and two represent the orientation of interface normal. The tilt axis and interface normal are unit vectors and are perpendicular to each other.

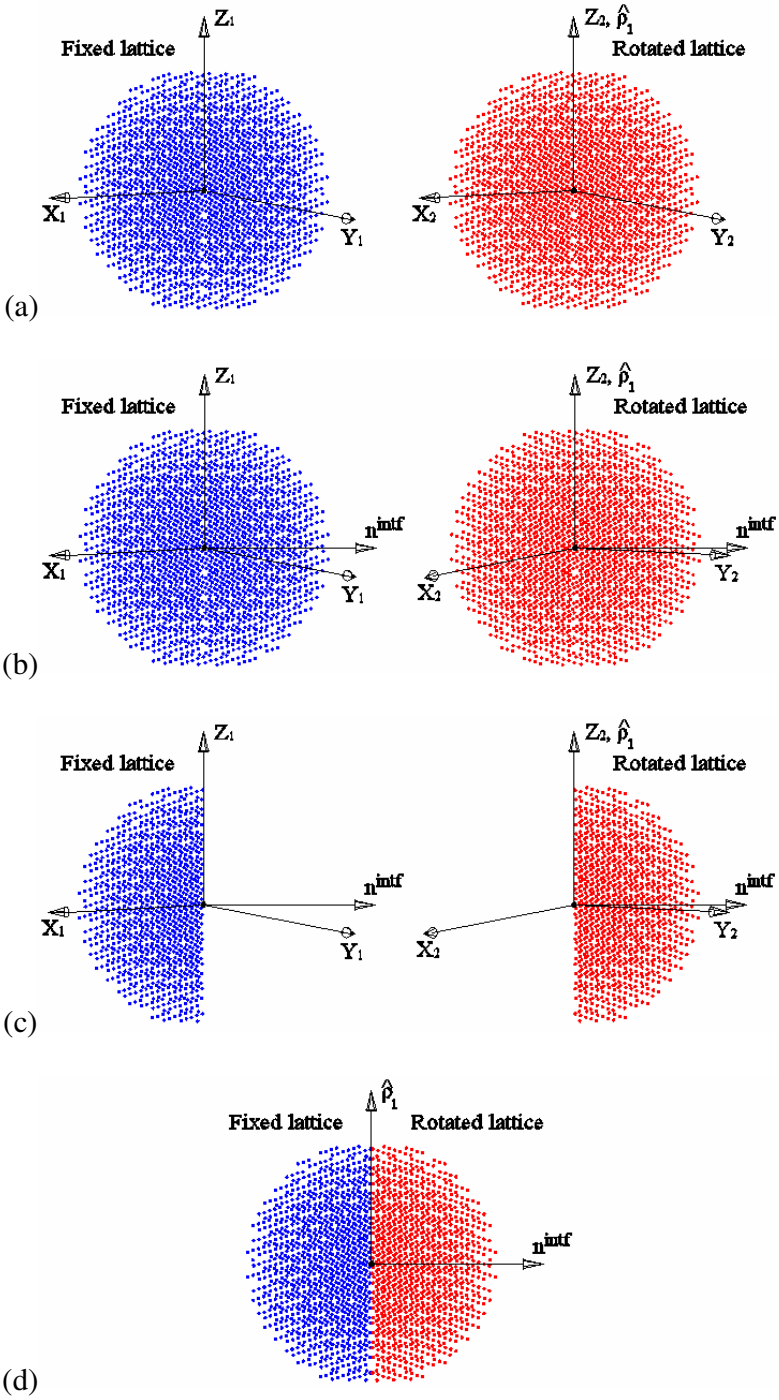

Figure 6.1 Schematic presentation of a sphere made of two tilted lattices.

The geometry of a system of two tilted lattices in the current model is similar to that used by Lee et al. [114]. The generation of a sphere comprising two tilted lattices is schematically shown in Figure 6.1.

- Two concentric spherical samples of fcc lattice are built, the diameter of each is 40.5 Angstroms (10 times of lattice constant of fcc crystal). Figure 6.1a shows these two concentric spheres separately. Each sphere has its own local coordinate system located at the centre of the spheres. Two coordinate systems, denoted by (X_1,Y_1,Z_1) and (X_2,Y_2,Z_2) for the fixed lattice and rotated lattice respectively, are originally coincident.
- The left sphere is fixed, while the right sphere is tilted around a tilt axis by a predefined tilt angle. Figure 6.1b demonstrates the rotation of the right sphere around the axis Z_1 (which is coincident with axis Z_2). $\hat{\boldsymbol{\rho}}_l$ denotes the tilt axis with respect to the coordinate system of the fixed lattice. The resulting interface is represented by an arbitrary unit vector $\mathbf{n}^{intf}$ which is normal to the tilt axis $\hat{\boldsymbol{\rho}}_l$ and is rooted at the centre of the spheres.
- In Figure 6.1c, half the fixed sphere on the positive side of the interface is removed, and so is half of the rotated sphere on the negative side of the interface.
- We finally obtain a sphere halved by two misoriented lattices with an interface that is on the equatorial plane (Figure 6.1d).

The orientation of the interface normal is determined as follows.

- The interface is swept around the tilt axis starting from the mirror plane of X axis of two local coordinate systems (i.e. a sweeping angle of 0^o) to 180^o with a 1^o interval. This arrangement results in symmetric tilt boundaries at sweeping angles of 0^o and 180^o.
- At each sweeping angle, the sphere halved by two misoriented lattices as described above is generated.
- In other works modelling crystal interfaces using MD or MS [111, 113, 114, 139], the lattices do not normally undergo external loading, relaxation is mainly

affected and determined from the equilibrium conditions of the atomic interactions around the interface. In the context of the current work, misorientations are derived from the CPFEM results, so the lattices are assumed to be subjected to external loadings. Therefore relaxation at the interface is approximately obtained by separating two lattices until the total potential energy reaches a minimum.

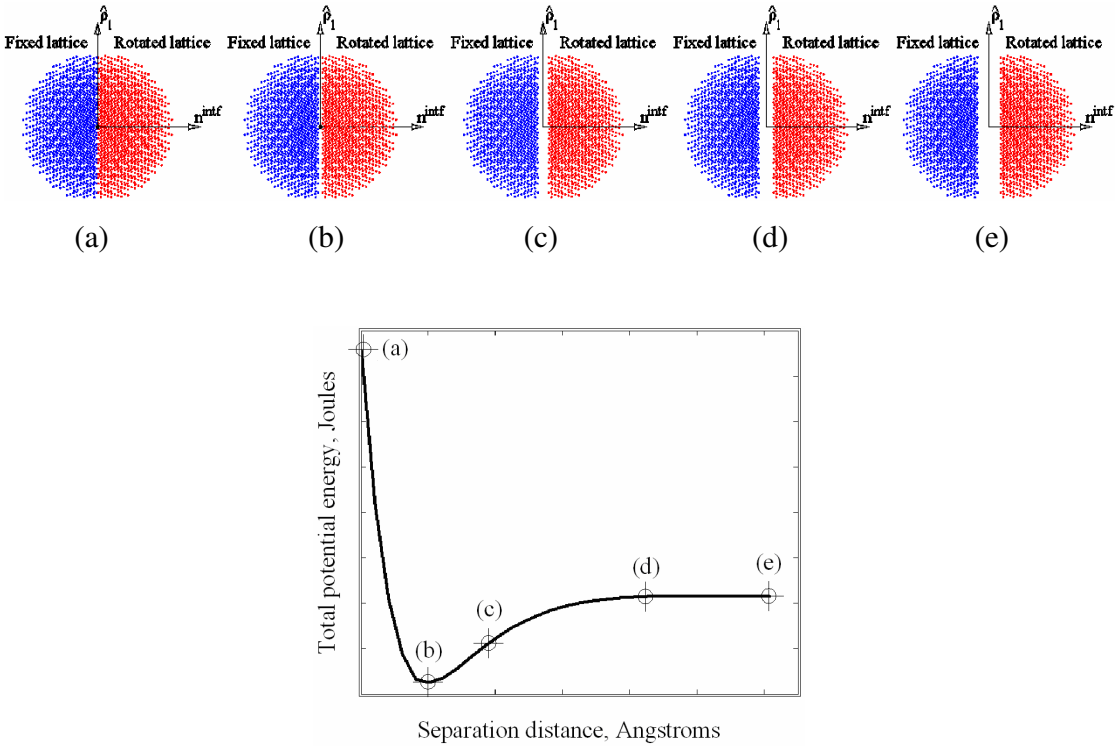

Figure 6.2 Schematic presentation of the determination of relaxation at the interface.

A schematic presentation of the determination of relaxation at the interface is shown in Figure 6.2, together with a sample of the curve of total potential energy of two hemispheres versus the separation distance between them. The shape of the curve was observed during the calculation in this work. Points (a) to (e) on the curve are demonstrated by the corresponding figures of the position of the hemispheres. The two hemispheres are pulled apart along the direction of the interface normal vector. At each position of separation, the integrated EAM

potential function for Al [101] is used to calculate the total potential energy of the system of two hemispheres. The resulting plot of total potential energy versus separation distance has the shape as shown in Figure 6.2.

Point (a) on the curve in Figure 6.2 corresponds to the state in which two misoriented hemispheres are at their original positions (no separation). As the two hemispheres move apart, the total potential energy of the whole system decreases until it reaches a minimum value at point (b). The energy at this point is called total potential energy at relaxation. Further separation of the two hemispheres results in increasing the total potential energy of the system (point (c) on the curve), toward a negative asymptote (points (d) and (e) on the curve). The energy at this asymptote is the sum of free energy of two hemispheres. During the calculation in this thesis, it was observed that system energy reaches a minimum value (point (b)) when the two hemispheres are about 1 Angstroms apart, and reaches 99% of the asymptotic value when the two hemispheres are about 5 Angstroms to 6 Angstroms apart, which is approximately the cut-off distance in various EAM potential functions for aluminum [98-102].

- For the given tilt axis and tilt angle, the true interface of two misoriented lattices is determined as the results in the lowest total potential energy at relaxation, i.e. this interface orientation provides the most stable geometry of the system of the two lattices being considered.

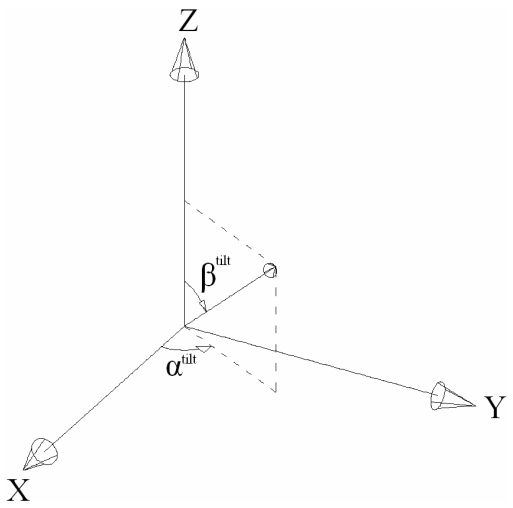

Figure 6.3 Angles defining tilt axis with respect to the reference coordinate system.

In this thesis we define misorientation energy as the energy required to create the stable misoriented structure of two lattices from a single crystal. It is calculated as the difference between the total potential energy of the original single crystal sphere (i.e. at a tilt angle of 0^o) and the lowest total potential energy at relaxation, as determined above. This definition is similar to the definition of grain boundary energy used in MD or MS simulations [114]. However, grain boundary is defined as the interface of two lattices misoriented greater than 15^o. For misorientations smaller than 15^o, the interface is commonly called subgrain boundary. Thus the definition of misorientation energy in this thesis generally refers to the energy of both grain and subgrain boundaries.

The difference between the lowest total potential energy at relaxation (point (b) on the curve in Figure 6.2) and the total free energy of two hemispheres (point (e) on the curve in Figure 6.2) is the energy required to break the atomic bonds and bring the system of two lattices from a stable structure to two halves fully apart. In this thesis it is called the interface fracture energy and plays a vital role in developing an explicit microstructure-based and computationally inexpensive criterion for crack opening. Such a criterion is still lacking in simulations of crack growth and/or crack initiation to date.

6.1.2 Verifications of the atomic interaction model

The model described above is applied to the calculation of the grain boundary energy of <100> and <110> tilt boundaries in fcc aluminum. The results are compared with those from MD simulations found in the literature [111, 139], as shown in Figure 6.4.

The curves from the model developed in this work and the MD models are generally in good agreement with both cases of tilt boundaries. The current model can predict small cusps in boundary energy curve of <100> tilt boundary even though there are some deviations in absolute values (Figure 6.4a). The agreement is even better for <110> tilt boundary (Figure 6.4b), where large cusps at about 70^o and 129^o tilt angles are captured quite accurately. Cusps occur on boundary energy curves because of uniformly spaced dislocations created on the tilt boundaries at particular tilt angles. The two large cusps in

<110> tilt boundary energy plots are due to low-energy {111} and {113} twin boundaries that result from tilting two lattices around <110> axis angles of 70° and 129°, respectively. [95]

Deviations between the results may come from different relaxation conditions as well as the potential functions employed. As mentioned above, relaxation in the current model is obtained by pulling the two lattices apart until they reach a minimum total energy, rather than from equilibrium conditions in MD or MS simulations.

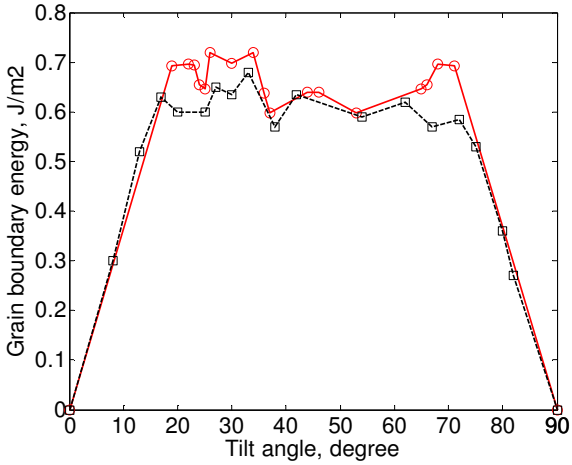

(a) <100> tilt boundary

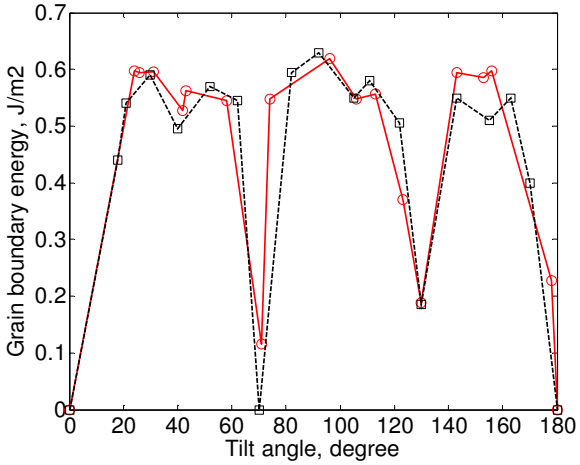

(b) <110> tilt boundary

Figure 6.4 Computed grain boundary energy using the current atomic interaction model (solid lines) and from the literature using MD [111, 139] (dashed lines).

Simpler assumptions of relaxation in the current model compared with other MD or MS models result in considerably less expensive computational time. This advantage allows us to construct a database of misorientation energy, interface fracture energy and interface normal vector of an aluminum tilted bicrystal (dependent variables) with tilt axis and tilt angle as independent variables. The tilt axis orientation is represented by a unit vector, which can be fully described in the 3D space by two angles, as shown in Figure 6.3, where $0 \leq \alpha^{tilt}, \beta^{tilt} \leq 180$. We assume that the fixed lattice described in Section 6.1.1 to be the reference, the local coordinate system of which coincides with the global XYZ system (Figure 6.3), and so becomes the reference system. Tilt axis orientation is expressed with respect to coordinate system of the fixed lattice as

$$\hat{\boldsymbol{\rho}}_1 = \begin{bmatrix} \hat{\rho}_x & \hat{\rho}_y & \hat{\rho}_z \end{bmatrix}^T = \begin{bmatrix} \sin\beta^{tilt}\cos\alpha^{tilt} & \sin\beta^{tilt}\sin\alpha^{tilt} & \cos\beta^{tilt} \end{bmatrix}^T \tag{6.1}$$

Let θ be the total tilt angle. The total rotation matrix transforming the tilted lattice from the fixed (reference) lattice is

$$\mathbf{R}^{\hat{\rho},\theta} = \begin{bmatrix} \hat{\rho}_x^2(1-\cos\theta)+\cos\theta & \hat{\rho}_x\hat{\rho}_y(1-\cos\theta)-\hat{\rho}_z\sin\theta & \hat{\rho}_x\hat{\rho}_z(1-\cos\theta)+\hat{\rho}_y\sin\theta \\ \hat{\rho}_x\hat{\rho}_y(1-\cos\theta)+\hat{\rho}_z\sin\theta & \hat{\rho}_y^2(1-\cos\theta)+\cos\theta & \hat{\rho}_y\hat{\rho}_z(1-\cos\theta)-\hat{\rho}_x\sin\theta \\ \hat{\rho}_x\hat{\rho}_z(1-\cos\theta)-\hat{\rho}_y\sin\theta & \hat{\rho}_y\hat{\rho}_z(1-\cos\theta)+\hat{\rho}_x\sin\theta & \hat{\rho}_z^2(1-\cos\theta)+\cos\theta \end{bmatrix} \tag{6.2}$$

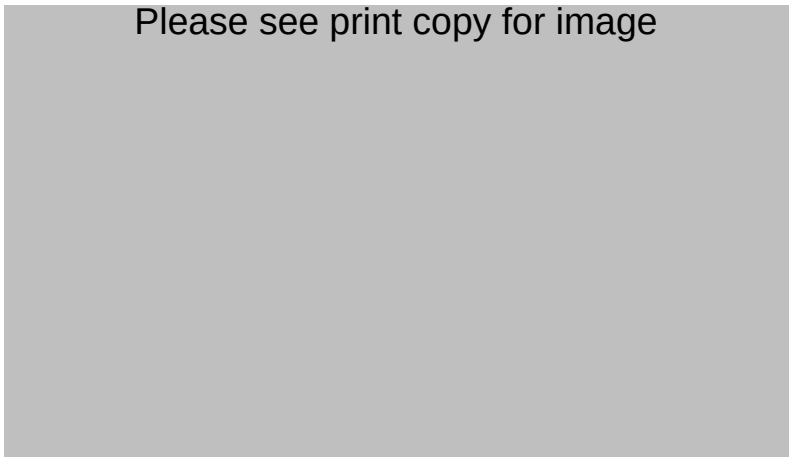

Figure 6.5 Euler angles of rotations of the reference lattice toward the tilted lattice. [140]

The misorientation described by tilt axis/angle pair as above can also be described by Euler angles φ_1, Φ, φ_2, following Bunge notation [140], as shown in Figure 6.5. The XYZ system in Figure 6.5 is the reference system identical to that shown in Figure 6.3; <100> orientations represent the coordinate system of the tilted lattice. φ_1, Φ, φ_2, in that order, are rotations transforming the reference lattice toward the tilted lattice. In the matrix form, the total rotation transforming reference lattice to tilted lattice is

$$\mathbf{R}^{Euler} = \begin{bmatrix} \cos\varphi_1 & \sin\varphi_1 & 0 \\ -\sin\varphi_1 & \cos\varphi_1 & 0 \\ 0 & 0 & 1 \end{bmatrix} \begin{bmatrix} 1 & 0 & 0 \\ 0 & \cos\Phi & \sin\Phi \\ 0 & -\sin\Phi & \cos\Phi \end{bmatrix} \begin{bmatrix} \cos\varphi_2 & \sin\varphi_2 & 0 \\ -\sin\varphi_2 & \cos\varphi_2 & 0 \\ 0 & 0 & 1 \end{bmatrix}$$

$$= \begin{bmatrix} \cos\varphi_1\cos\varphi_2 - \sin\varphi_1\sin\varphi_2\cos\Phi & \sin\varphi_1\cos\varphi_2 + \cos\varphi_1\sin\varphi_2\cos\Phi & \sin\varphi_2\sin\Phi \\ -\cos\varphi_1\sin\varphi_2 - \sin\varphi_1\cos\varphi_2\cos\Phi & -\sin\varphi_1\sin\varphi_2 + \cos\varphi_1\cos\varphi_2\cos\Phi & \cos\varphi_2\sin\Phi \\ \sin\varphi_1\sin\Phi & -\cos\varphi_1\sin\Phi & \cos\Phi \end{bmatrix} \quad (6.3)$$

Equating Equation (6.2) to Equation (6.3) allows us convert the three angles representing axis/angle pair to Euler angles, and vice versa.

In the constructed database the angles α^{tilt} and β^{tilt} sweep from 0^o to 180^o with 5^o intervals, tilt angle θ sweeps from 0^o to 180^o with 2^o intervals. The contour plots of misorientation energy and interface fracture energy versus angles α^{tilt} and β^{tilt} (Figure 6.3) for tilt angles 5^o, 10^o, and 15^o are shown in Figures 6.6, 6.7 and 6.8, respectively. The contours are symmetric around <100> orientations of tilt axes, hence only data corresponding to α and β within 0^o to 90^o is presented. At these moderate misorientation angles the interfaces between the two lattices are considered in the literature as sub-grain boundaries.

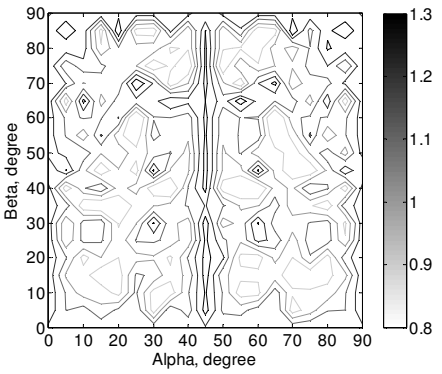

(a) Interface fracture energy, J/m^2

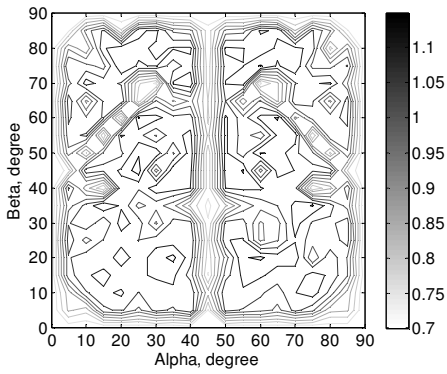

(b) Misorientation energy, J/m^2

Figure 6.6 (a) Interface fracture energy and (b) Misorientation energy at tilt angle 5^o.

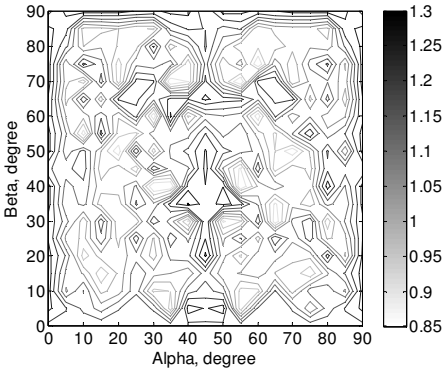

(a) Interface fracture energy, J/m^2

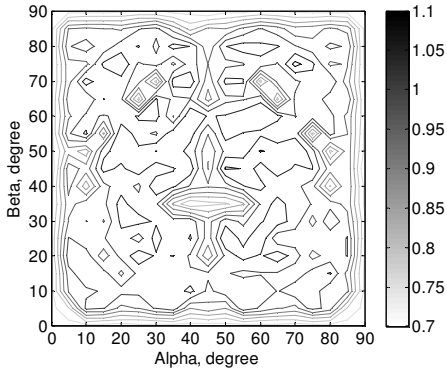

(b) Misorientation energy, J/m^2

Figure 6.7 (a) Interface fracture energy and (b) Misorientation energy at tilt angle 10^o.

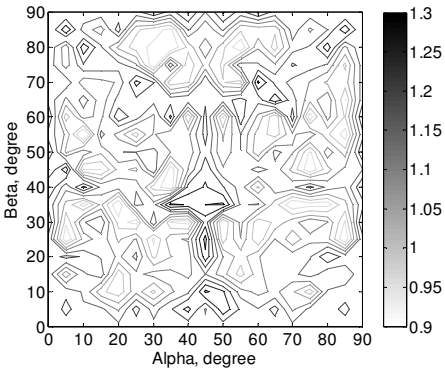

(a) Interface fracture energy, J/m^2

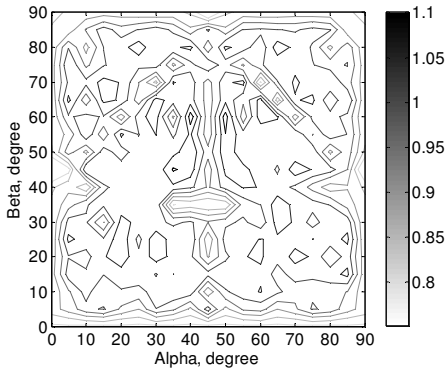

(b) Misorientation energy, J/m^2

Figure 6.8 (a) Interface fracture energy and (b) Misorientation energy at tilt angle 15^o.

As predicted in the results from previous MD simulations as well as from the theory of dislocations for sub-grain boundaries [95], the current results show that misorientation energy increases with the increment of tilt angle. This trend applies to every orientation of the tilt axis. Interface fracture energy, on the contrary, decreases when the tilt angle increases. As defined in Section 6.1.1, the interface fracture energy in this work is the energy required to break atomic bonds at the interface and bring two lattices completely apart. At lower tilt angles the lattices require less energy to create a new interface from the original single crystal. The geometry of the system is also closer to single crystal structure which makes it harder (more energy required) to break the whole structure into two independent parts.

6.2 Misorientation angle and misorientation energy

6.2.1 Misorientation angle

Any two adjacent points *i* and *j* in CPFEM model initially having the same orientation could become significantly misoriented after some loading. This misorientation matrix $\mathbf{R}_{\mathbf{ij}}^{\mathbf{k}}$ between point *i* and point *j* can be defined as

$$\mathbf{R}_{\mathbf{ij}}^{\mathbf{k}} = \mathbf{R}_{\mathbf{j}}^{\mathbf{k}} \bullet \left(\mathbf{R}_{\mathbf{i}}^{\mathbf{k}}\right)^{-1} \tag{6.4}$$

where $\mathbf{R}_{\mathbf{i}}^{\mathbf{k}}$ and $\mathbf{R}_{\mathbf{j}}^{\mathbf{k}}$ are the orientation matrices of crystals at point *i* and *j*, respectively. As both $\mathbf{R}_{\mathbf{i}}^{\mathbf{k}}$ and $\mathbf{R}_{\mathbf{j}}^{\mathbf{k}}$ are orthogonal and normalized, so is $\mathbf{R}_{\mathbf{ij}}^{\mathbf{k}}$. If we assume the rotation to crystal *j* from crystal *i* pure tilt, the axis $\hat{\boldsymbol{\rho}}_{\mathbf{g}}$ (in the global coordinate system) and the angle θ_{ij} (misorientation angle) of tilt can then be determined from $\mathbf{R}_{\mathbf{ij}}^{\mathbf{k}}$ by

$$\hat{\boldsymbol{\rho}}_{\mathbf{g}} = \left[\left(\mathbf{R}_{\mathbf{ij}}^{\mathbf{k}}\right)_{32} - \left(\mathbf{R}_{\mathbf{ij}}^{\mathbf{k}}\right)_{23} \quad \left(\mathbf{R}_{\mathbf{ij}}^{\mathbf{k}}\right)_{13} - \left(\mathbf{R}_{\mathbf{ij}}^{\mathbf{k}}\right)_{31} \quad \left(\mathbf{R}_{\mathbf{ij}}^{\mathbf{k}}\right)_{21} - \left(\mathbf{R}_{\mathbf{ij}}^{\mathbf{k}}\right)_{12}\right]^{T} \tag{6.5}$$

$$2\cos\theta_{ij} + 1 = \left(\mathbf{R}_{\mathbf{ij}}^{\mathbf{k}}\right)_{11} + \left(\mathbf{R}_{\mathbf{ij}}^{\mathbf{k}}\right)_{22} + \left(\mathbf{R}_{\mathbf{ij}}^{\mathbf{k}}\right)_{33} \tag{6.6}$$

In the CPFEM modelling full integration 8-node linear brick elements are used. Each element contains eight integration points. The misorientation angle between any two integration points will be considered. The total number of misorientation to be examined in an element is 28. Results of distribution of misorientation angles for Cube and Brass oriented samples, which have been modelled in Chapter 4 with 53,030 elements, are shown in Figures 6.9 and 6.10, respectively.

On the Cube oriented sample, at 1% nominal strain, almost 95% of misorientation angles in regions II and nearly 100% of those in region III are between 0^o-0.2^o (misorientation angles distribute around 0.1^o with $\pm 0.1^o$ deviation). While the maximum misorientation angle in region I is up to 4^o, less than 2% of the misorientation angles in region I are larger than 2^o. The same trends occur for misorientations in all three regions at 3% strain. At this stage of loading, even though the maximum tilt angles in regions I increases up to 15^o, and that in regions II, III up to about 3^o, more than 95% of misorientations appearing in region II and III and almost 90% of those in region I are still lower than 2^o. As the sample is stretched further the crystals in all three regions become more misoriented, and the regions closer to the notch have higher increments of maximum misorientation. In particular, the maximum misorientation angle in region I reaches 21^o at 4.5% strains while the corresponding values for regions II and III are only 9^o, and 7^o, respectively.

The same tendency is observed for misorientations around the notch in the Brass oriented sample, i.e. the maximum magnitude of misorientation angles increases with load, and decreases with distance away from the notch. The maximum misorientation angle in region I at 3% nominal strain (where voids nucleate) is about 18^o, which is less than that in the Cube oriented sample which is 21^o at void nucleation. However in the Brass oriented sample the maximum misorientation angles at 1% strain in three regions are approximately 8^o, 3^o and 2^o, respectively, which are larger than those in the Cube oriented sample (about 4^o, 1^o and 1^o, respectively).

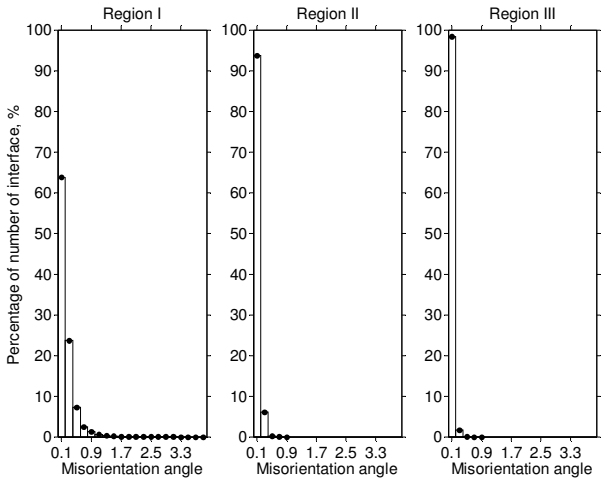

(a) 1% nominal strain

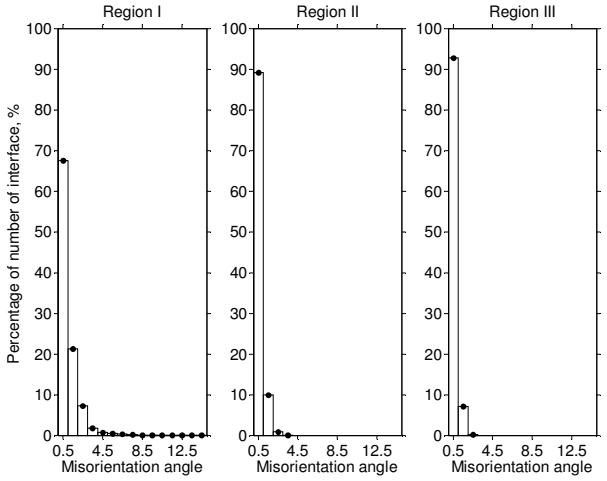

(b) 3% nominal strain

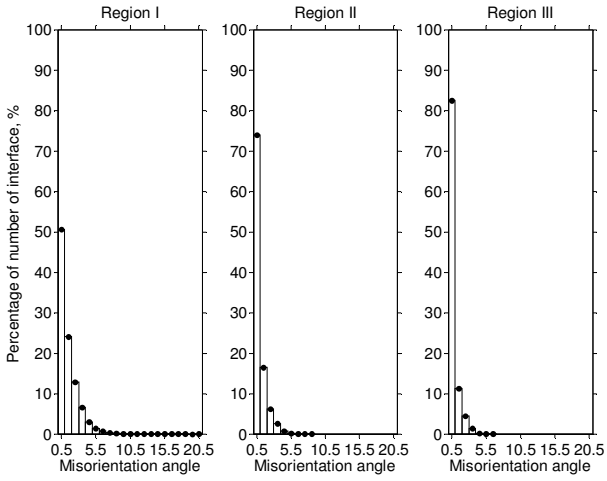

(c) 4.5% nominal strain

Figure 6.9 Distribution of misorientation angle (in degrees) in regions around the notch tip in the Cube oriented sample.

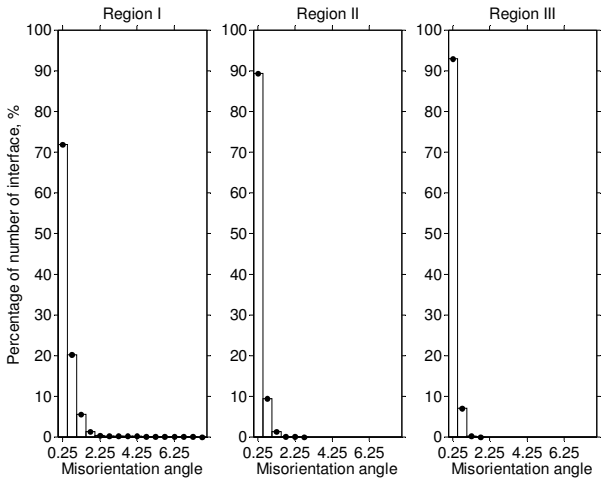

(a) 1% nominal strain

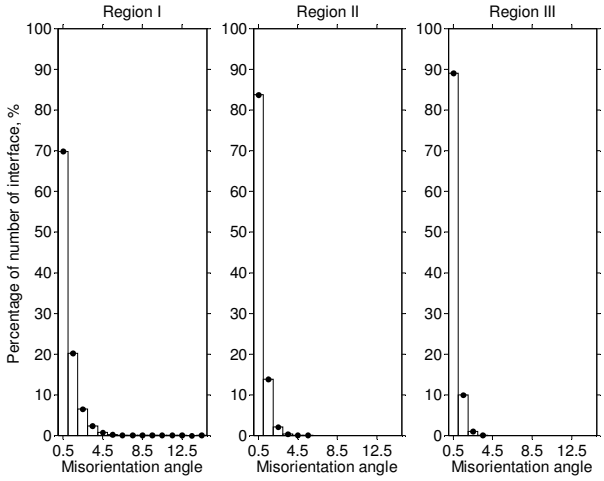

(b) 2% nominal strain

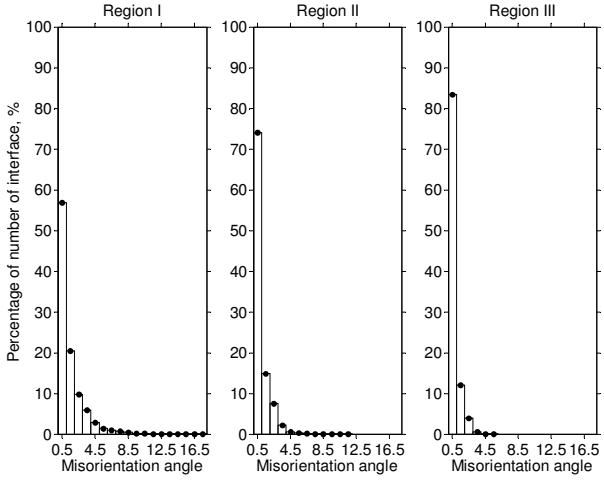

(c) 3% nominal strain

Figure 6.10 Distribution of misorientation angle (in degrees) in regions around the notch tip in the Brass oriented sample.

It is noteworthy that in both Cube and Brass oriented samples, more than 90% of all misorientations are lower than 15^{o} at every loading stage, i.e. the majority of new interfaces created in the region around the notch tip are sub-grain boundaries.

The distribution of misorientation between crystals in regions around the notch in the two samples is better observed in Figures 6.11 and 6.12 where the contour plots of misorientation angles on the sample surface (left plots) and on the mid-thickness layer (right plots), are shown. The unit in these contour plots is degrees.

The characteristics of the distribution of misorientation angles in the Cube and Brass oriented samples are different in a couple of ways. The contour plots of misorientations in the Cube sample take the general shape of the distribution of Mises stress at the corresponding nominal strain. Figure 6.13 shows the contour plots of Mises stress on the surface of this sample at three stages of loading. Both large Mises stress and large misorientation angle spread along three bands parallel to the notch tip direction, which are best observed at 4.5% nominal strain. Meanwhile the distribution of large misorientation in the Brass oriented sample is similar in shape to the cumulative shear strain (Figure 4.14) and particularly with the distribution of the total rotation of crystals from the initial orientation (Figure 4.17), i.e. two parallel bands originating from notch corners with values of misorientation in the upper band are generally larger than those in the lower band. These similarities are most obvious at 3% nominal strain (see Figures 4.14c, 4.17c and 6.12c).

Finally, the misorientations on the free surface of the Cube oriented sample are larger than those on the mid-thickness plane (Figures 6.11b and 6.11c), except at 1% nominal strain where they are approximately equal (Figure 6.11a). Also, the difference between misorientation angles on the two planes appears to increase with a higher load. On the other hand, in the Brass oriented sample (Figure 6.12) the maximum misorientation angles that occur on sample surface and on the interior plane seem to be equal at every stage of loading.

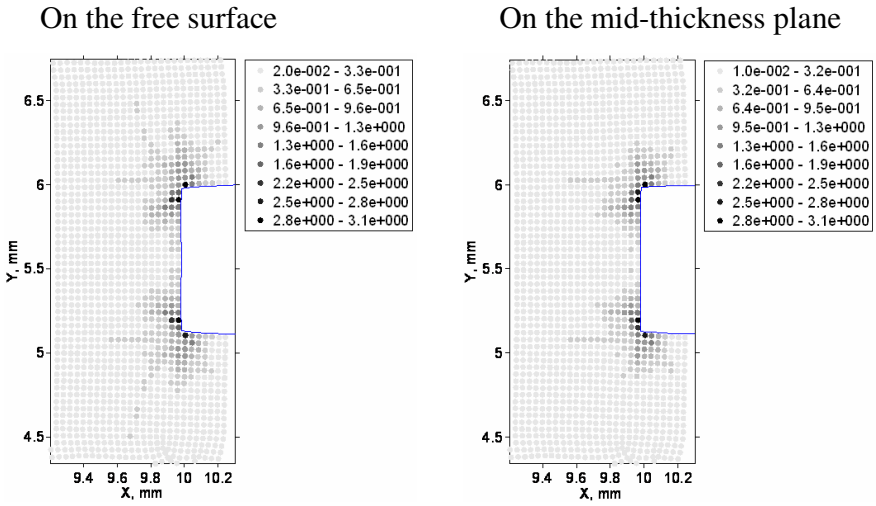

(a) 1% nominal strain

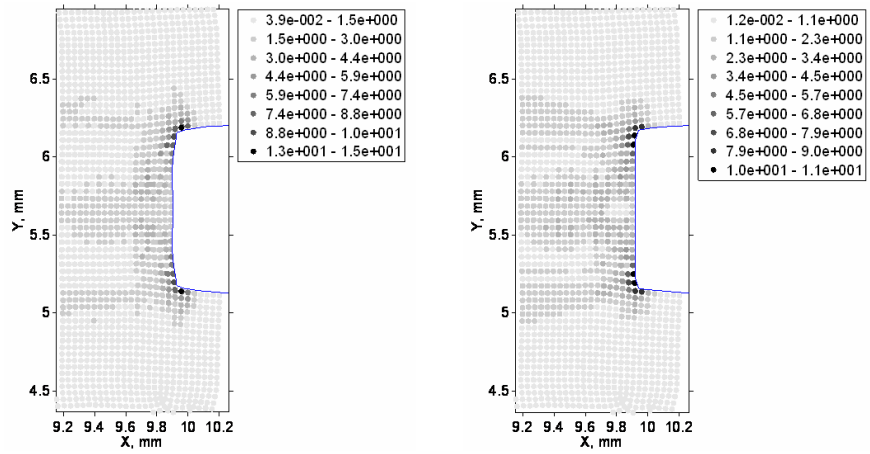

(b) 3% nominal strain

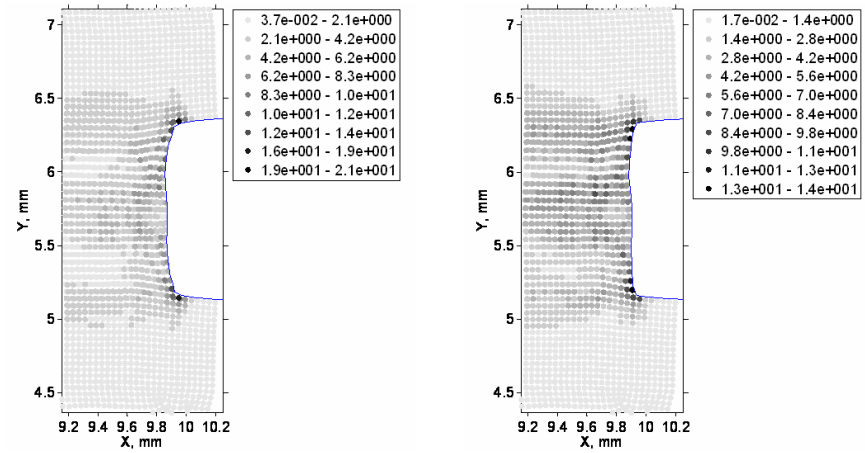

(c) 4.5% nominal strain

Figure 6.11 Contour plots of misorientation angle (in degrees) between two adjacent crystals in the Cube oriented sample.

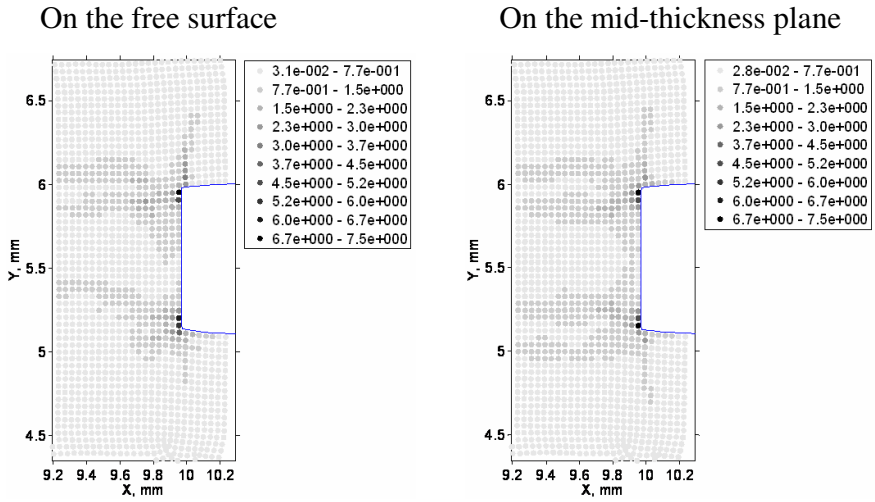

(a) 1% nominal strain

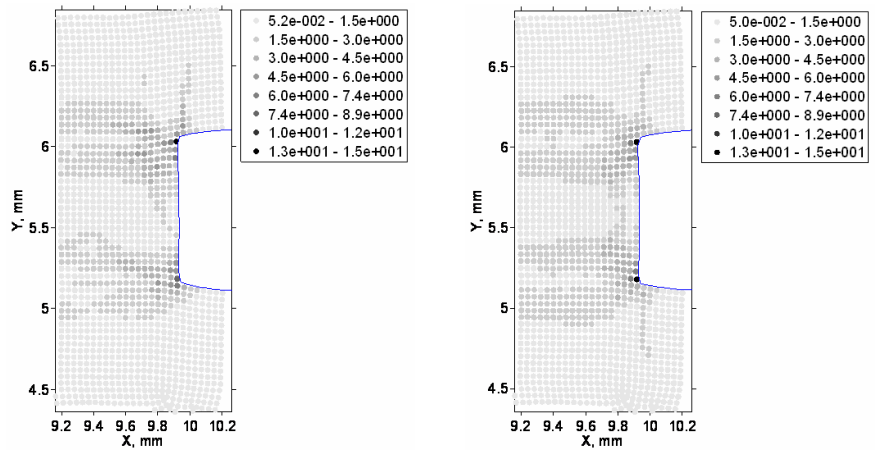

(b) 2% nominal strain

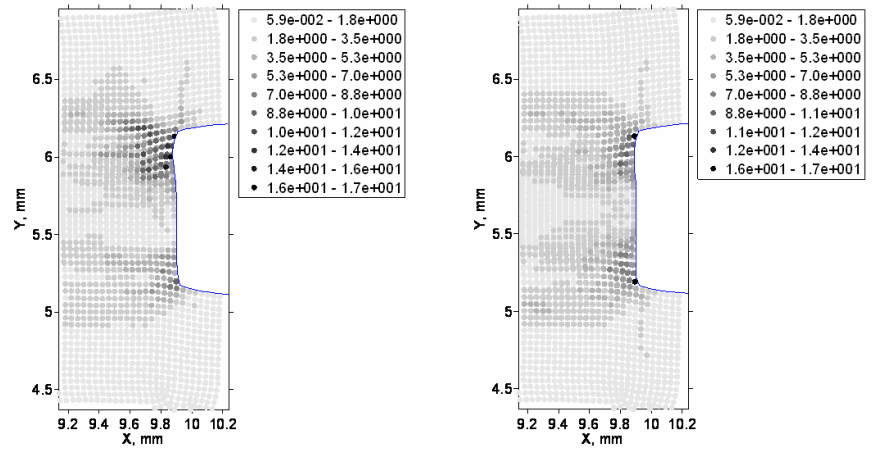

(c) 3% nominal strain

Figure 6.12 Contour plots of misorientation angle (in degrees) between two adjacent crystals in the Brass oriented sample.

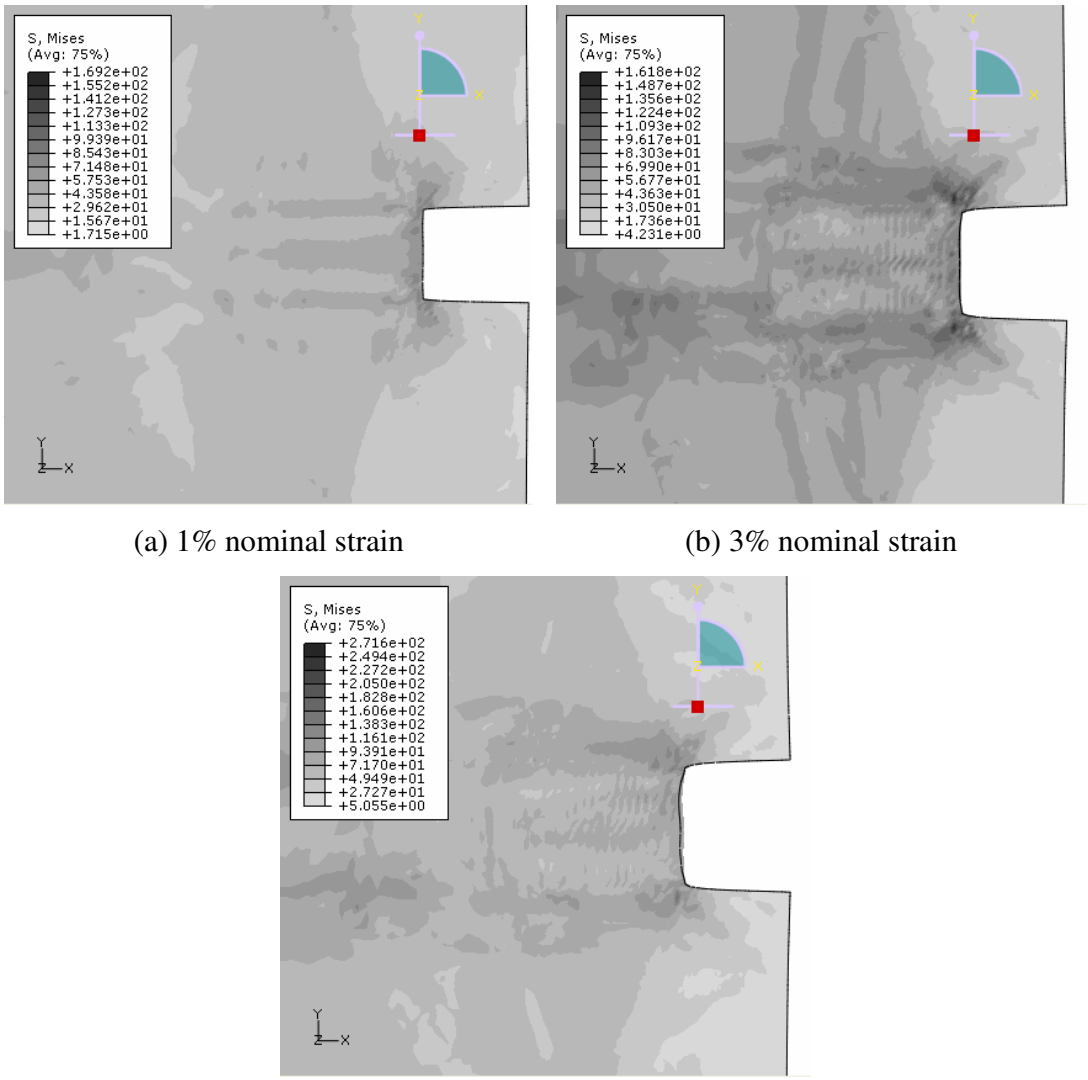

(a) 1% nominal strain (b) 3% nominal strain

(c) 4.5% nominal strain

Figure 6.13 Mises stress (MPa) on the surface of the Cube oriented sample.

6.2.2 Misorientation energy

Misorientation energy could be estimated from the atomic interaction model described in Section 6.1.1. As mentioned in Section 6.1.2, from the atomic interaction model developed in this work a database of interface fracture energy and misorientation energy was constructed with either tilt axis (characterized by two angles α^{tilt} and β^{tilt}) and tilt angle θ or three Euler angles φ_1, Φ, φ_2 as independent variables. This allows us to

calculate the boundary energy of the newly created interfaces around the notch from the tilt axis and angles determined by Equations (6.5) and (6.6). While constructing the database, one lattice was assumed to rotate while the other which was fixed and used as the reference. Tilt axis orientation and Euler angles in the database, therefore, are expressed according to the coordinate system of the fixed lattice. The orientation of a tilt axis obtained from Equation (6.5) is in the global coordinate system attached to the modelling sample, and needs to be transformed into the coordinate system of crystal *i* so that it is compatible with the database, as follows [141]

$$\begin{bmatrix} \hat{\rho}_i \\ \hat{\rho}_j \\ \hat{\rho}_k \end{bmatrix}_l = \begin{bmatrix} \mathbf{i_l}\cdot\mathbf{i_g} & \mathbf{i_l}\cdot\mathbf{j_g} & \mathbf{i_l}\cdot\mathbf{k_g} \\ \mathbf{j_l}\cdot\mathbf{i_g} & \mathbf{j_l}\cdot\mathbf{j_g} & \mathbf{j_l}\cdot\mathbf{k_g} \\ \mathbf{k_l}\cdot\mathbf{i_g} & \mathbf{k_l}\cdot\mathbf{j_g} & \mathbf{k_l}\cdot\mathbf{k_g} \end{bmatrix} \begin{bmatrix} \hat{\rho}_i \\ \hat{\rho}_j \\ \hat{\rho}_k \end{bmatrix}_g = \mathbf{D_{gi}} \begin{bmatrix} \hat{\rho}_i \\ \hat{\rho}_j \\ \hat{\rho}_k \end{bmatrix}_g \tag{6.7}$$

Matrix $\mathbf{D_{gi}}$ transforms coordinates of a tilt axis in the global coordinate system, $\hat{\boldsymbol{\rho}}_g = \begin{bmatrix} \hat{\rho}_i & \hat{\rho}_j & \hat{\rho}_k \end{bmatrix}_g^T$, to those in the local coordinate system of crystal *i*, $\hat{\boldsymbol{\rho}}_\mathbf{l} = \begin{bmatrix} \hat{\rho}_i & \hat{\rho}_j & \hat{\rho}_k \end{bmatrix}_l^T$. $\begin{pmatrix} \mathbf{i_l} & \mathbf{j_l} & \mathbf{k_l} \end{pmatrix}^T$ is the set of unit vectors along the coordinate axes of the local coordinate system of crystal *i*, which are identical to the three columns of matrix $\mathbf{R_i^k}$. $\begin{pmatrix} \mathbf{i}_g & \mathbf{j}_g & \mathbf{k}_g \end{pmatrix}^T$ is the set of unit vectors along coordinate axes the global coordinate system, which are $[1\ 0\ 0]^T$, $[0\ 1\ 0]^T$, $[0\ 0\ 1]^T$.

Angles α^{tilt} and β^{tilt} are determined from $\hat{\boldsymbol{\rho}}_\mathbf{l} = \begin{bmatrix} \hat{\rho}_i & \hat{\rho}_j & \hat{\rho}_k \end{bmatrix}_l^T$ by Equation (6.1). Each set of (α^{tilt}, β^{tilt}, θ) corresponds to three pairs $[\alpha_{\min}^{tilt} \quad \alpha_{\max}^{tilt}]$, $[\beta_{\min}^{tilt} \quad \beta_{\max}^{tilt}]$ and $[\theta_{\min} \quad \theta_{\max}]$ in the database that define an eight-node element surrounding the data point (α^{tilt}, β^{tilt}, θ). Dependent variables, e.g. misorientation energy, interface fracture energy, and interface normal, at this data point are determined by isoparametric interpolation, similar to that applied in Abaqus for first-order brick elements [122]. Isoparametric element coordinates g^{iso}, h^{iso}, r^{iso} of the data point are defined by

$$g^{iso} = \frac{2}{\alpha_{\max}^{tilt} - \alpha_{\min}^{tilt}}\left(\alpha - \alpha_{\min}^{tilt}\right) - 1 \tag{6.8a}$$

$$h^{iso} = \frac{2}{\beta_{\max}^{tilt} - \beta_{\min}^{tilt}}\left(\beta - \beta_{\min}^{tilt}\right) - 1 \tag{6.8b}$$

$$r^{iso} = \frac{2}{\theta_{\max} - \theta_{\min}}\left(\theta - \theta_{\min}\right) - 1 \tag{6.8c}$$

The trilinear interpolation for value of a dependent variable u^{var} is carried out based on g^{iso}, h^{iso}, r^{iso} by Equation (6.9). g_i^{iso}, h_i^{iso}, r_i^{iso} and u_i^{var}, respectively are isoparametric coordinates and value of the dependent variable at node *i* of the data element.

$$u^{\text{var}} = \frac{1}{8}\sum_{i=1}^{8}\left(1 + g_i^{iso} g^{iso}\right)\left(1 + h_i^{iso} h^{iso}\right)\left(1 + r_i^{iso} r^{iso}\right)u_i^{\text{var}} \tag{6.9}$$

Misorientation energy in the Cube and Brass oriented samples prior to crack initiations can be interpolated from the database using Equation (6.9). Calculation results showed that on both samples, the distribution and magnitude of misorientation energy on the free surface and on the mid-thickness plane are similar at every stage of loading. Thus only the contour plots of misorientation energy on the sample surface will be presented. Figure 6.14 shows results at nominal strains of 1%, 3%, and 4.5% for the Cube oriented sample. Figure 6.15 shows results at nominal strains of 1%, 2%, and 3% for the Brass oriented sample. The plots show that the maximum of the required energy to create new interfaces from the original single crystal is approximately 1.2 J/m^2, which is reached at a very early stage of loading (1% nominal strain) for both samples (Figures 6.14a and 6.15a). Even though the maximum misorientation angles increase with higher loads (see Figures 6.11b-c and 6.12b-c), the maximum misorientation energy remains mostly unchanged (Figures 6.14b-c and 6.15b-c). As a higher load is applied, the amount of strain energy from the external load spent to create new interfaces increases, indicated by the wider distribution of maximum interface energy around the notch tip.

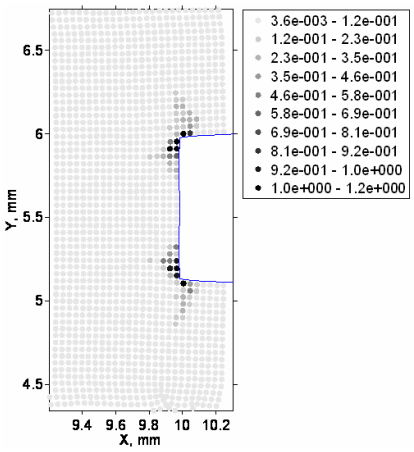

(a) 1% nominal strain

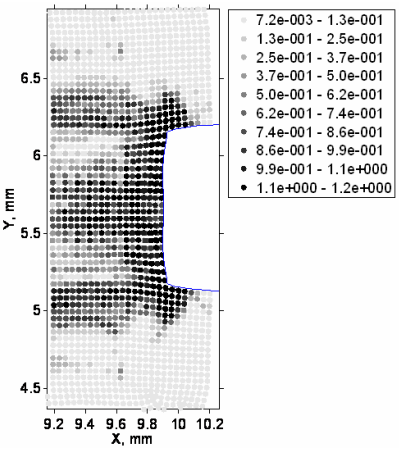

(b) 3% nominal strain

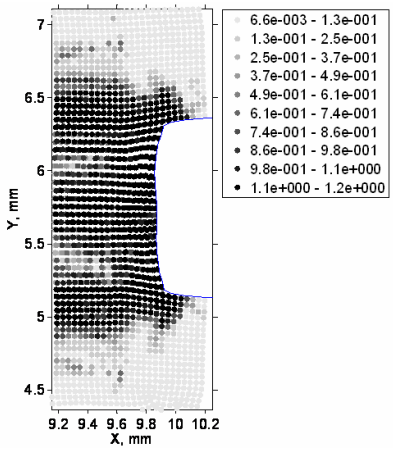

(c) 4.5% nominal strain

Figure 6.14 Misorientation energy (J/m^2) on the free surface of the Cube oriented sample.

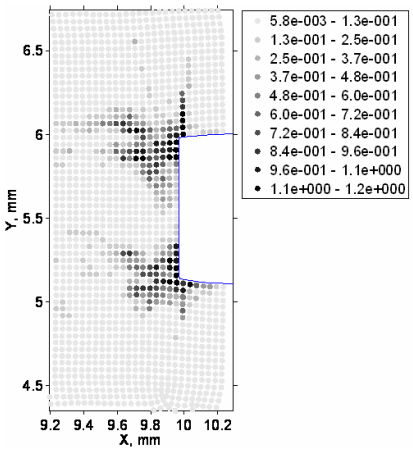

(a) 1% nominal strain

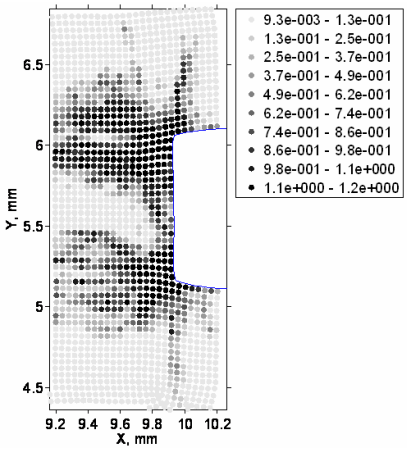

(b) 2% nominal strain

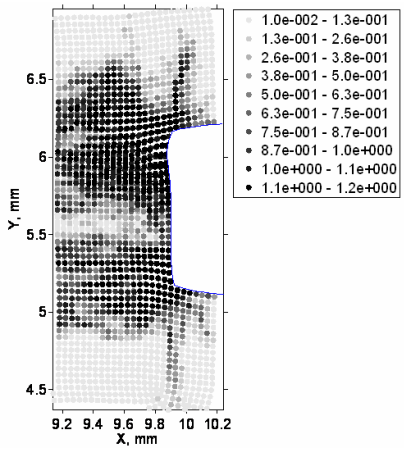

(c) 3% nominal strain

Figure 6.15 Misorientation energy (J/m^2) on the free surface of the Brass oriented sample.

The maximum misorientation energy of 1.2 J/m^2 in Figures 6.14 and 6.15 is in the same order of magnitude with values of grain boundary energy of various crystal structures that are summarized in [95]. The seemingly opposite trends of misorientation angle and energy can be explained qualitatively by looking at plots of misorientation energy versus tilt angle of the <100> and <110> tilt boundaries (Figure 6.4) as examples. These plots reveal that misorientation energy evolves with tilt angles in three stages. The first and the third stages occur within a small range of tilt angle (around 15^o and 20^o in Figures 6.4a and 6.4b, respectively) in which the misorientation energy increases (in the first stage) or decreases (in the third stage) linearly with the tilt angle. The second stage occurs within a wider range of misorientation angles in which the misorientation energy varies around an average value of approximately 0.6 J/m^2 and 0.5 J/m^2 in Figures 6.4a and 6.4b, respectively, except for a few particular tilt angles (e.g. 70^o and 129^o in Figure 6.4b) where the tilted lattices create low energy crystal structures. It should be noticed that the <100> and <110> tilt boundaries are special cases in terms of the resulting lattice structures being periodic and closely related to the single crystal structure. For misorientations that result from experiments or numerical modelling, the lattices rotate relative to each other around arbitrary axes. The chances that the newly formed lattice structures have such special geometry are miniscule. Hence, the wide range of misorientation angles in stage 1, as well as the special tilt angles forming low energy crystal structures in stage 2 (as in Figure 6.4b), are less likely to happen. Maximum misorientations in the current simulation results (Figures 6.11-6.12) could be considered to occur in the second stage, which explains why maximum misorientation energy does not change with maximum misorientation angle.

6.3 Misorientation-dependent cracking criterion

The interface fracture energy is defined in Section 6.1.1 as the energy required to pull two points away from each other along the direction normal to their interface until they are fully apart. A strain energy having the same nature must be estimated for pairs of points in the CPFEM modelling samples so that it is comparable to the interface fracture

energy, in order to determine whether a crack occurs along the interface of a particular point pair. The estimation of such strain energy is schematically described in Figure 6.16.

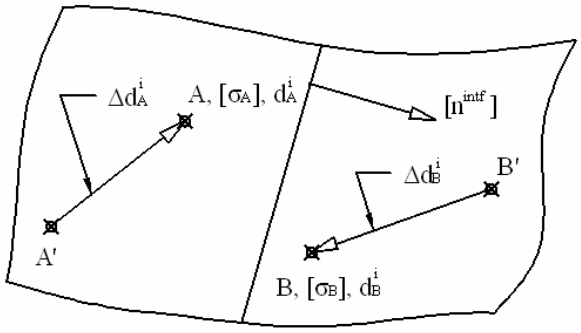

Figure 6.16 Sketch of the estimation of strain energy on the interface of two lattices.

The lattices are represented by two integration points A and B at the current time step *i*. $\boldsymbol{\sigma}_A$ and $\boldsymbol{\sigma}_B$ are Cauchy stress at integration points A and B, as obtained directly from Abaqus simulations. Points A' and B' represent the positions of points A and B at time step *i-1*, respectively. The displacement vectors A'A and B'B are represented by $\boldsymbol{\Delta}\mathbf{d}_A^i = \left[\mathbf{d}_A^i - \mathbf{d}_A^{i-1}\right]$ and $\boldsymbol{\Delta}\mathbf{d}_B^i = \left[\mathbf{d}_B^i - \mathbf{d}_B^{i-1}\right]$, respectively. $\mathbf{d}_A^i$ and $\mathbf{d}_B^i$ denote the coordinates of points A and B. The user-defined subroutine UMAT was modified to provide $\boldsymbol{\Delta}\mathbf{d}_A^i$ and $\boldsymbol{\Delta}\mathbf{d}_B^i$ at each increment step as state dependant variables. The interface normal vector is denoted by $\mathbf{n}^{\text{intf}}$, which was tabulated in the database determined from the atom interaction model in Section 6.1.1. The values of a specific $\mathbf{n}^{\text{intf}}$ could be interpolated from the database following Equations (6.8) and (6.9).

The net displacement of the two lattices in the direction normal to the interface is $\left(\boldsymbol{\Delta}\mathbf{d}_A^i - \boldsymbol{\Delta}\mathbf{d}_B^i\right)\mathbf{n}^{\text{intf}}$. The net stress acting on the interface in the interface normal direction is $\left(\mathbf{n}^{\text{intf}}\right)^T \boldsymbol{\sigma}_A \mathbf{n}^{\text{intf}} - \left(\mathbf{n}^{\text{intf}}\right)^T \boldsymbol{\sigma}_B \mathbf{n}^{\text{intf}}$, where $\left(\mathbf{n}^{\text{intf}}\right)^T \boldsymbol{\sigma}_A \mathbf{n}^{\text{intf}}$ is the Cauchy stress at integration point A projected on the interface normal direction. The net strain energy on the interface under the effects of external loading is

$$W_{\text{intf}} = \left|\left(\mathbf{n}^{\text{intf}}\right)^T \boldsymbol{\sigma}_A \mathbf{n}^{\text{intf}} - \left(\mathbf{n}^{\text{intf}}\right)^T \boldsymbol{\sigma}_B \mathbf{n}^{\text{intf}}\right| \left(\Delta\mathbf{d}_A^i - \Delta\mathbf{d}_B^i\right)\mathbf{n}^{\text{intf}} \tag{6.10}$$

Positive W_{intf} implies two lattices being pulled apart while negative W_{intf} means them being pushed against each other. Let E_{crit} denote the interface fracture energy or the critical energy of crack opening, which could be interpolated from the database constructed in Section 6.1.2 for the given interface orientation. It is noted that the value of E_{crit} is positive. Then, $\left(W_{\text{intf}} - E_{crit}\right)$ readily becomes a direct indication of crack opening. The energy criterion of crack opening is

$$\left(W_{\text{intf}} - E_{crit}\right) \geq 0 \tag{6.11}$$

Prior to crack opening, $\left(W_{\text{intf}} - E_{crit}\right)$ is negative and regions having higher $\left(W_{\text{intf}} - E_{crit}\right)$ (i.e. smaller in magnitude) are more likely to have cracks nucleated. Plots of maximum $\left(W_{\text{intf}} - E_{crit}\right)$ and average $\left(W_{\text{intf}} - E_{crit}\right)$ that occurs in regions around the notch tip in the Cube and Brass oriented samples versus nominal strain are shown in Figure 6.17. These plots show results prior to crack initiations in both samples, thus the nominal strain is up to 4.5% for the Cube oriented sample, and 3% for the Brass oriented sample.

Figure 6.17 reveals that the maximum and the average values of $\left(W_{\text{intf}} - E_{crit}\right)$ of interfaces in region I are higher than or at least equal to those of interfaces in regions II and III in both samples at all stages of loading. This observation combined with the conclusion made in Chapter 4 that deformation is most severe in regions very close to notch tip makes it reasonable to limit the analysis of crack opening in a small region around the notch tip, at least at early stages of crack opening. In both samples, while values of the maximum $\left(W_{\text{intf}} - E_{crit}\right)$ in regions II and III increase gradually and reasonably closely with each other, the increments of the maximum $\left(W_{\text{intf}} - E_{crit}\right)$ in region I appear to be in three stages. Stage 1 for the Cube oriented sample is from the beginning of loading to 1.5% nominal strain. In stage 2, nominal strains from 1.5% to 4%, the values of maximum $\left(W_{\text{intf}} - E_{crit}\right)$ vibrate around -0.2 J/m^2. At 4.5% nominal

strain, maximum $(W_{\text{intf}} - E_{crit})$ jumps to 1.3 J/m^2 when cracking occurs (stage 3). For the Brass oriented sample stage 1 ends earlier at 0.5%. Stage 2 is between 0.5% and 2.5% nominal strains, with the average value is at -0.6 J/m^2, lower than that in Cube oriented sample. Stage 3 is also a large jump at 3% strain to 0.8 J/m^2 when cracks initiate.

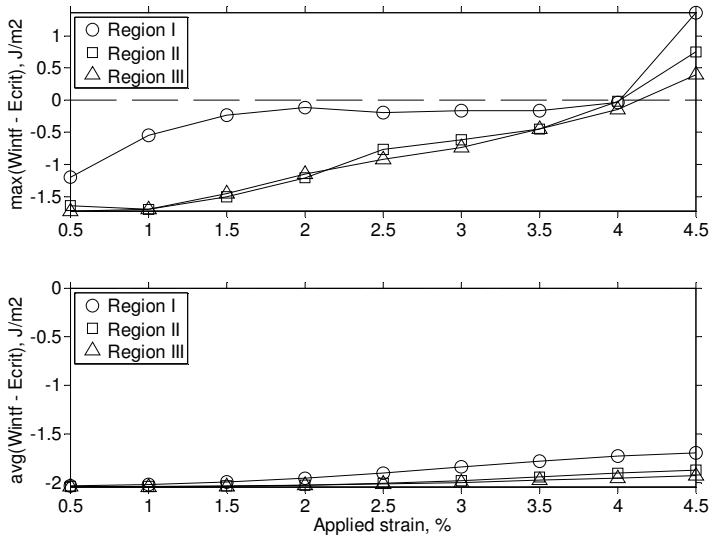

(a) Cube oriented sample

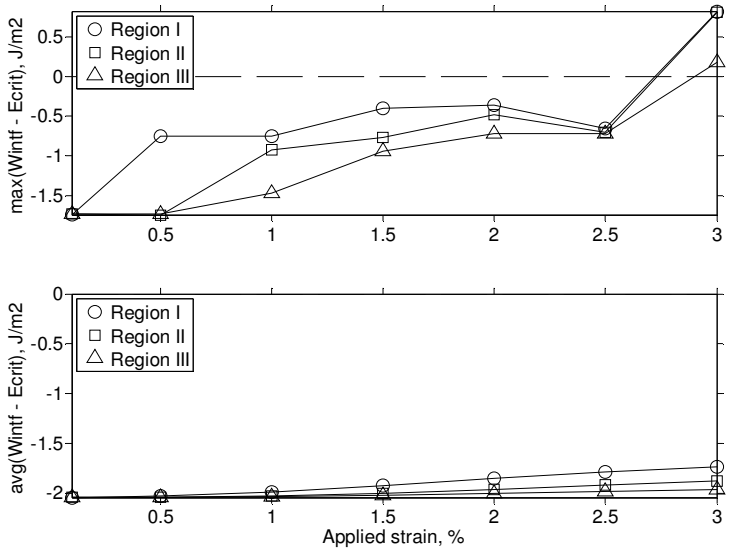

(b) Brass oriented sample

Figure 6.17 Plots of the maximum and average $(W_{\text{intf}} - E_{crit})$ versus applied strain prior to crack nucleation.

6.4 Applying the misorientation-dependent cracking criterion into CPFEM

To model crack opening at initiation and the subsequent growth, the element removal technique in Abaqus/Standard is employed. The procedure to implement this technique is summarized as follows.

- The total strain load is divided into a series of small loading step. Each small loading step is applied in an analysis (loading analysis), which is saved when finished so that it could be continued (restarted) in the subsequent loading analysis. The Abaqus keywords `*Model change, activate` is included in the loading step in the current Abaqus input file to specify that elements may need to be removed in the subsequent loading analysis.
- At the end of each loading analysis, a misorientation-dependent crack opening analysis is carried out to determine if any element reaches the crack opening criteria (dead element).
- Dead elements, if any, are removed in the next loading analysis. In the input file of this loading analysis, two steps need to be specified. The first step removes dead elements by means of keywords `*Model change, remove`, followed by the labels of dead elements. Forces exerted by the removed elements on the remaining part of the mesh are ramped down to zero gradually, so that the effect of these elements on the whole model is completely absent at the end of the removing step. The second step is the loading step, which also includes *Model change, activate as mentioned above. The calculations for this loading step are performed on the newly formed mesh.

As mentioned in Section 6.2.1, there are 28 lattice pairs in an 8-node element being used in the current simulations. It is approximated in this study that if at least one pair of integrations points satisfy the energy criterion described above, the corresponding element is marked as “dead” and removed from the mesh by the element removal technique in Abaqus/Standard, as outlined above. The missing space at the position of the removed element effectively acts as a void in the material. The images of the front

view of all voids nucleated throughout the thickness of the sample relative to the notch boundary in the Cube oriented sample (at 4.5% nominal strain) and Brass oriented sample (at 3% nominal strain) are shown in Figures 6.18a and 6.19. A larger number of removed elements that are side by side with each other form a larger void than that results from a single removed element. Figures 6.18 and 6.19 show that voids nucleate in the Cube and Brass oriented samples with various sizes at separate positions. While they appear only in the upper part of notch in the Cube oriented sample (Figure 6.18a), voids spread all over the place around notch in the Brass oriented sample (Figure 6.19). Even so, it is noteworthy that both samples have voids that nucleate on the notch boundary, even though such nucleation could be at separate locations (Figures 6.18a and 6.19).

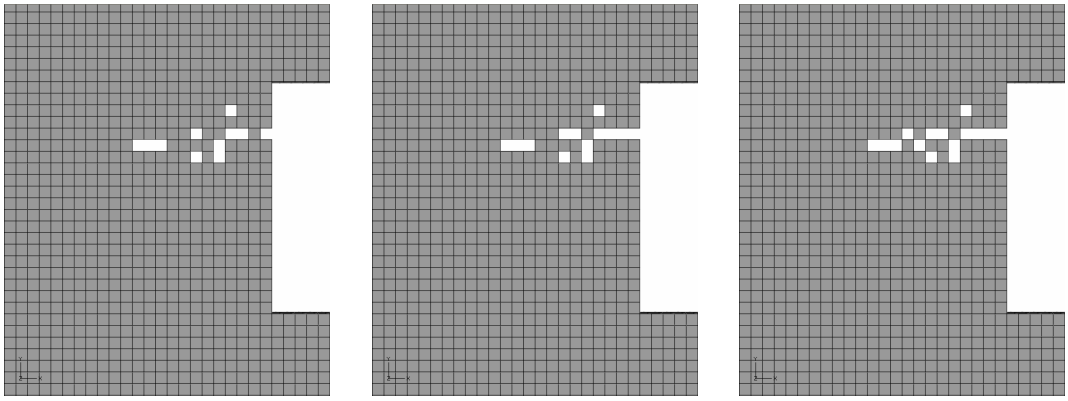

(a) 4.5% nominal strain (b) 5.3% nominal strain (c) 5.8% nominal strain

Figure 6.18 Voids nucleated around the notch tip in the Cube oriented sample.

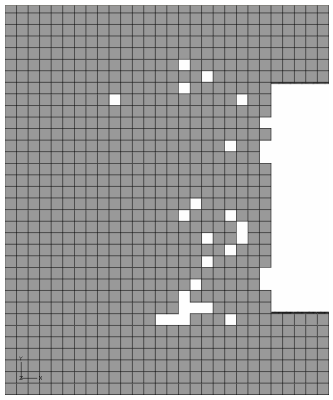

Figure 6.19 Voids nucleated around the notch tip in the Brass oriented sample (at 3% nominal strain).

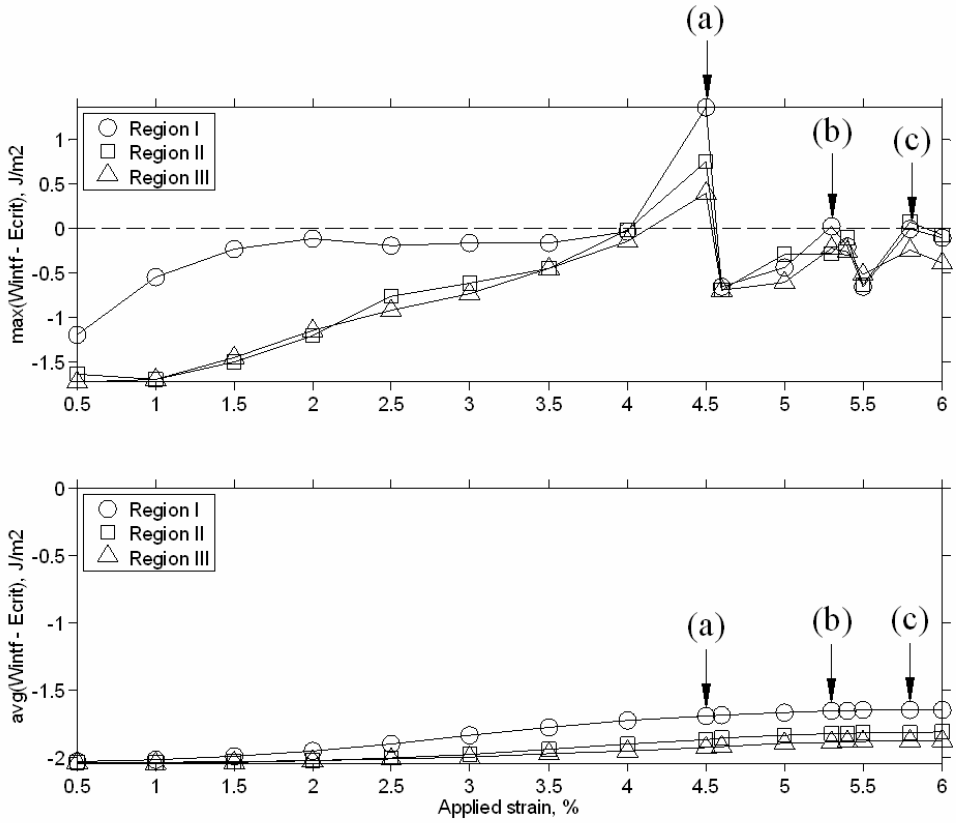

Figure 6.20 Evolution of the maximum and average $(W_{\text{intf}} - E_{crit})$ with nominal strain.

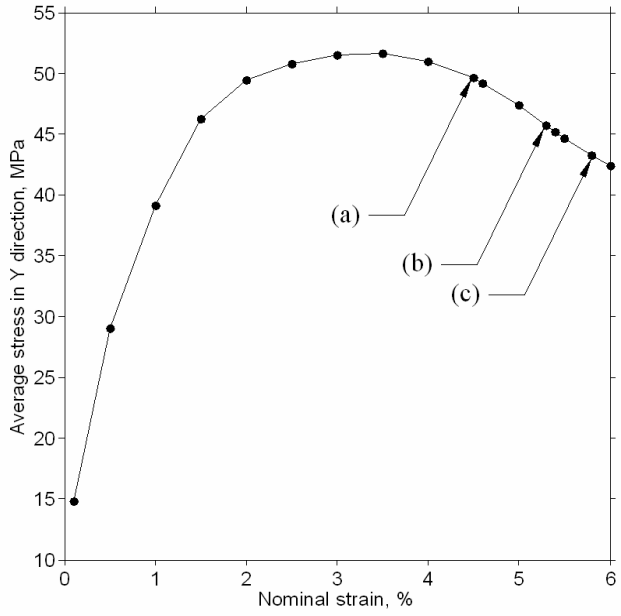

Figure 6.21 Stress strain curve of Cube oriented sample up to 6% nominal strain.

Under higher loads, the evolution of maximum and average values of $(W_{\text{intf}} - E_{crit})$ in the Cube oriented sample is shown in Figure 6.20 up to 6% nominal strain. The stress strain curve of the Cube oriented sample prior to cracking, as shown in Figure 4.4a is continued by a section that corresponds to strains applied after void nucleation (higher than 4.5%), as shown in Figure 6.21. Points on $(W_{\text{intf}} - E_{crit})$ curves that exceed the dash line (on which $(W_{\text{intf}} - E_{crit})$ equals zero) indicate the nucleation of new voids. These points are marked as (a), (b) and (c) on Figures 6.20 and 6.21 at 4.5%, 5.3% and 5.8% nominal strains, respectively. The locations of newly created voids at these nominal strains are shown respectively in Figure 6.18, where the connections of new voids to the existing ones essentially describe the nature of the growth or expansion of a crack in materials. As more voids appear, the stress strain curve in Figure 6.21 shows a continued decrease of stress (i.e. the sample ability to withstand external load) with respect to the strain applied.

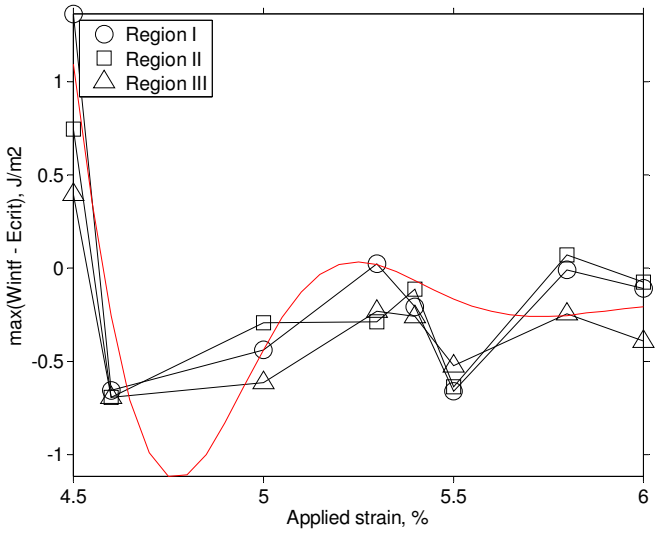

Figure 6.22 Section of maximum $(W_{\text{intf}} - E_{crit})$ curves versus applied strains after crack nucleation.

A closer look at Figure 6.20 in the section corresponding to strains higher than 4.5% shows that the maximum $(W_{\text{intf}} - E_{crit})$ curve in three regions behaves similar to an

under-damped sinusoidal oscillator. This section is redrawn in Figure 6.22, together with a sample of the general shape of the response of an under-damped sinusoidal oscillator. The overshoots occur at 4.5% nominal strain where crack openings are first detected. The highest overshoot belongs to the maximum $\left(W_{\text{intf}} - E_{crit}\right)$ curve of region I. The second highest and lowest overshoots occur on curves of region II and region III, respectively. The curves then oscillate with their amplitudes gradually decrease to zero. After reaching critical points at 4.5%, 5.3% and 5.8% nominal strains where voids nucleate, the curves slope downward until they reach a minimum value, then start going upward. At this stage, this observation is explained in this work that the sample undergoes energy restoration after each time new voids nucleate. In other words, the crystal lattice in the sample, particularly around the notch tip, is 'restructured' (for example via rotation of crystals) to make it more stable (lower energy). As further voids nucleate, the energy restorations become shorter, indicated by smaller amplitudes of the curve below the dashed line. Further simulations need to be done to justify this observation, and further analyses are required to fully explain the phenomenon.

The nature of cracking initiating from a void, which might not be on a free surface, and the subsequent propagation by connections of voids, as being considered in the current work has been observed in various MD simulations [69-72]. Shimomura et al. [69] reported MD simulation of a tensile test on a single crystal Cu thin film. The X, Y, and Z sample axes initially were in $[0\bar{1}1]$, $[2\bar{1}\bar{1}]$, and [111] lattice orientations. The film was elongated up to 8% along [111] direction. The so-called (111) islands were observed as atoms moved along the stretching direction <111> on two adjacent (111) planes. These migrations of atoms resulted in vacancies which accumulated and merged with each other to form small voids. These small voids if reaching a critical dimension would initiate crack. Shimomura et al. claimed that the same mechanism could also occur in bulk materials if dislocations in the deformed metals cannot move fast enough, which leads to the appearance of voids, i.e. crack initiation.

Figures 6.18a and 6.19 show that voids nucleate in the Cube oriented sample in a different manner compared to voids in the Brass oriented sample, which indicates the

effect of initial orientation. Numerous studies have reported the same conclusions [70-72]. Gao et al. [71] and Lu et al. [72] conducted MD simulations of propagation of Mode I crack in bcc single crystal iron samples. Various lattice orientations were considered. For all orientations, voids resulted from the inhomogeneous displacement of atoms appeared both inside the bulk material (i.e. away from the crack tip) and close to the crack tip. Gao et al. concluded that the initial lattice orientation significantly affects the behaviours of the crack growth. Also, their results showed that <111>{1-10} are favourable directions along which cracks in a bcc single crystal iron sample propagate more readily.

Particularly, Farrisey et al. [70] reported MD simulations of void growth from an existing notch in fcc single crystal copper samples under tensile load. Two cases of initial orientation were considered. In the first orientation, the loading axis was along the [010] lattice direction and the sample surface was along the (001) lattice plane (Cube orientation). In the second orientation, the loading axis was along the [110] lattice direction and the sample surface was along the $(\bar{1}\,1\bar{2})$ lattice plane (Brass orientation). These two cases are similar to the two orientations of SEN single crystal aluminum samples being considered in this work. Thus the behaviours of crack opening from simulation results of Farrisey el al. [70] can be qualitatively compared with results in this chapter.

These MD results are shown in Figures 6.23 and 6.25 for the Cube orientation and Brass orientation, respectively. The initial circular notch was located in the middle of the sample in both cases to stimulate crack growth. There were six atoms along the thickness of the samples. The tensile load was applied in the vertical direction up to 30% nominal strain (frame (8) in Figure 6.23 and frame (6) in Figure 6.25). The corresponding stress strain curves are shown in Figures 6.24 and 6.26. Points (1) to (8) on the curve in Figure 6.24 correspond to frames (1) to (8) in Figure 6.23. The same numbering order was applied for the Brass orientation (Figures 6.25 and 6.26).

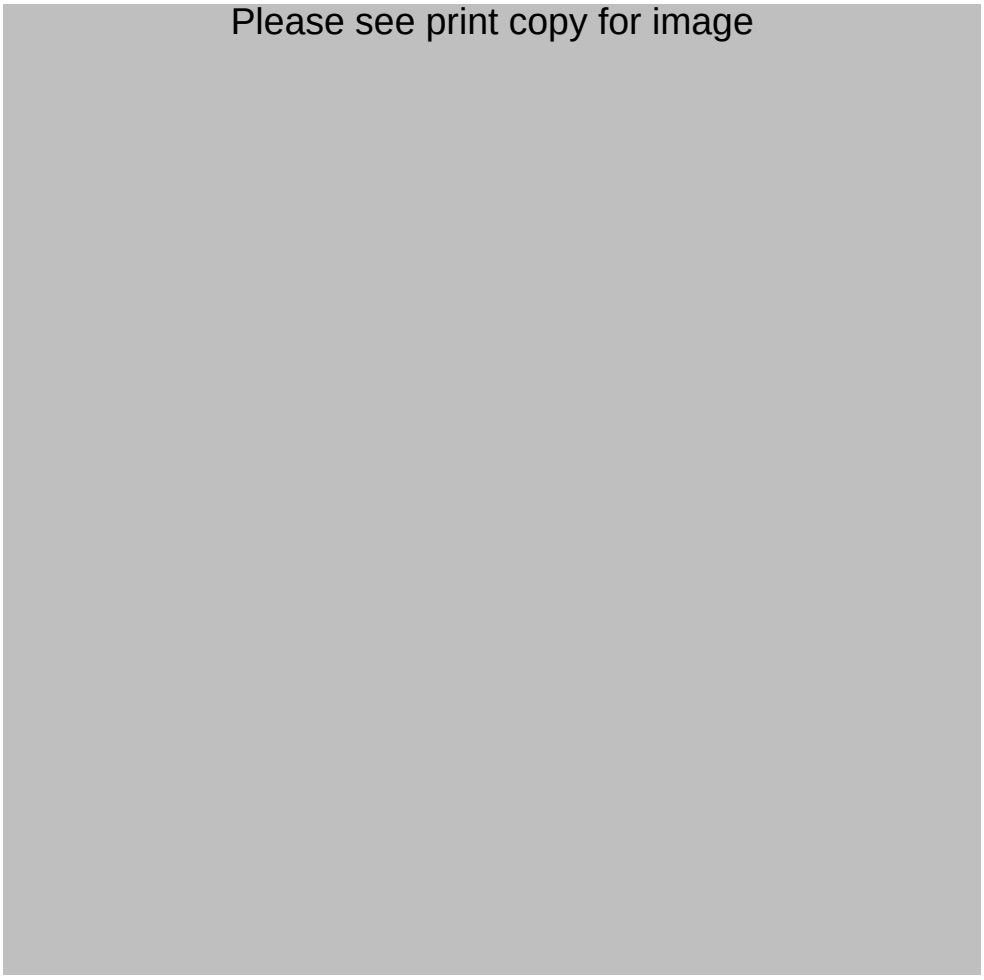

Figure 6.23 Void growth in an fcc single crystal (copper) with Cube orientation from MD simulations [70].

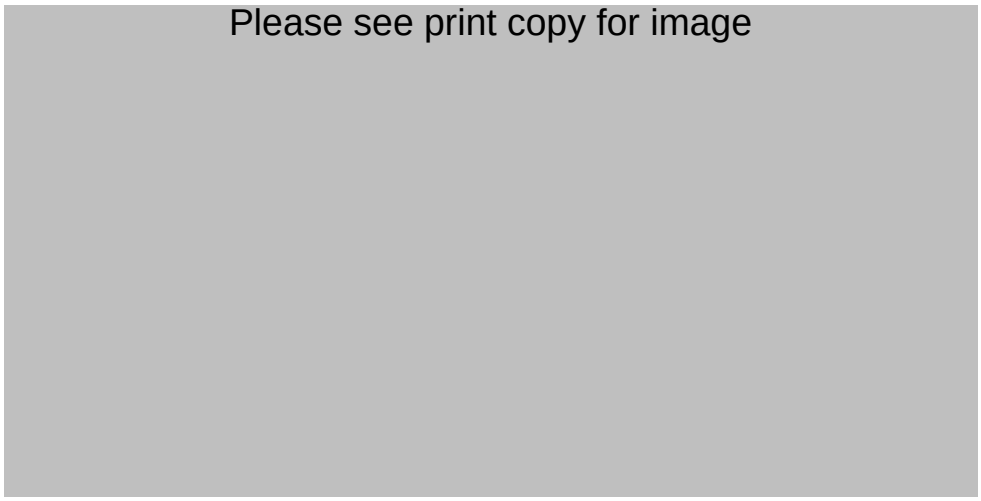

Figure 6.24 Tensile stress-strain curve from MD simulations of void growth in an fcc single crystal (copper) with Cube orientation [70].

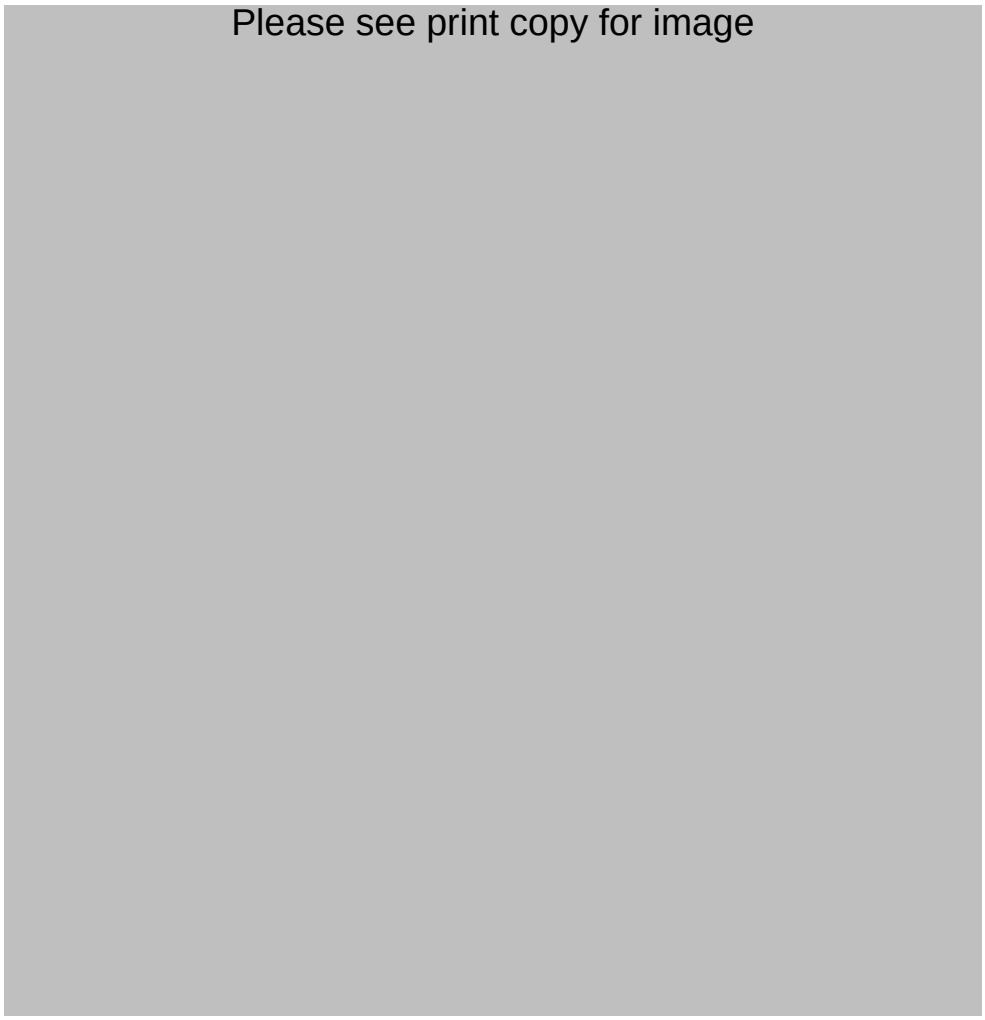

Figure 6.25 Void growth in an fcc single crystal (copper) with Brass orientation from MD simulations [70].

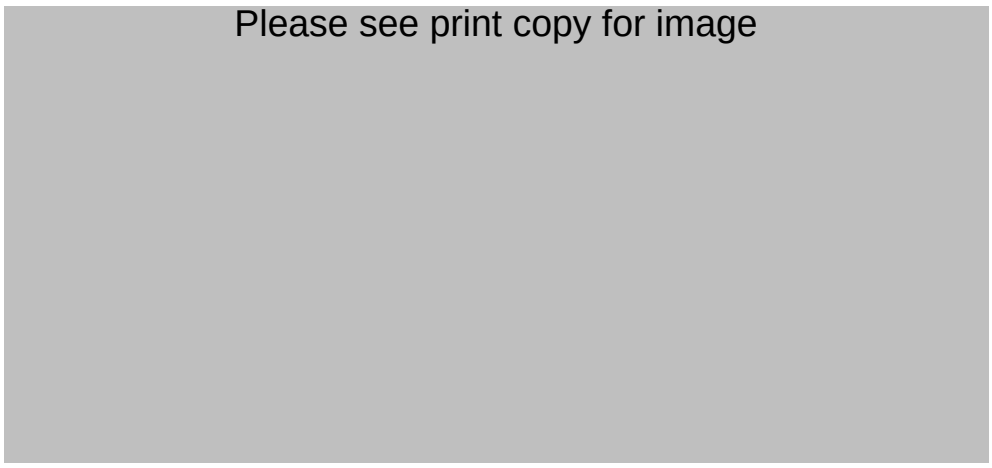

Figure 6.26 Tensile stress-strain curve from MD simulations of void growth in an fcc single crystal (copper) with Brass orientation [70].

MD simulations predicted that voids in an fcc single crystal with Cube orientation (Figure 6.23) start growing from the four corners of the notch, then steadily propagate in the direction normal to the loading direction. This trend is captured reasonably well in the preliminary results of crack growth using CPFEM modelling in this work, as shown in Figure 6.18. This figure shows that the propagation of voids in the Cube oriented sample appears to align in the horizontal direction (i.e. normal to the direction of tensile load).

In Figure 6.25, MD simulations predicted that the growth of voids in an fcc single crystal with Brass orientation does not follow any particular direction. The notch in Figure 6.25 appears to expend approximately the same amount in all directions, and thus keeps a fairly rounded shape throughout the deformation. This behaviour of void growth is captured to some extent by the current CPFEM modelling, as shown in Figure 6.19. In this figure, the nucleation of voids in the Brass oriented sample occurs at various locations around the notch tip.

The corresponding stress-strain curves from MD simulations (Figures 6.24 and 6.26) do not match curves obtained from the current CPFEM modelling. Values of maximum tensile stress for Cube and Brass orientations from MD simulations were 8000MPa and 11000 MPa, respectively. The corresponding values from the current CPFEM model are only approximately 55 MPa. The deviations are from different materials (copper versus aluminum) and the nature of the two modelling techniques (MD versus CPFEM). Another possible source of deviation is the rate of the applied tensile load. Farrisey et al. [70] also concluded that stress levels predicted from their MD simulations were an order of magnitude higher than those from a crystal plasticity model.

6.5 Conclusions

This chapter has proposed a criterion for crack opening based on the data of lattice evolution. The chapter has also successfully demonstrated the implementation of this

newly developed criterion into a CPFEM model to predict crack initiation (in terms of the nucleation of voids) and crack growth (in terms of coalescence of new voids and existing voids). The effect of the newly formed voids on the FEM mesh is captured by using the element removal technique in Abaqus/Standard. This combined approach enables the modelling of explicit crack growth without presuming a crack path. Also, because the crack opening criterion is evaluated based on the lattice evolution during the loading period, a predefined energy criterion for crack opening, which could be erroneous, is avoided. The development of the methodology to model crack opening in this chapter is original and is presented here for the first time.

The core of the new crack opening criterion is a model of atomic interaction for a pair of lattices with a simplified relaxation at their interface. The results of interface energy obtained from this model for symmetrical <100> and <110> tilt boundaries match very well with results from MD simulations found in the literature. This atomic interaction model is used to construct a database of fracture energy and normal vector of the interface of pure aluminum bicrystals. The tilt axis/angle pair of the interface is used as independent variables for the database.

As part of the new methodology to model crack opening, misorientation angle which is defined as the angle between two misoriented (tilted) adjacent crystals is determined from the data of lattice evolution from CPFEM modelling. Analyses show that over 90% of misorientation angles around the notch tip in Cube and Brass oriented fcc single crystals are lower than 15^{o}, i.e. the majority of newly formed interfaces are sub-grain boundaries. These analyses for misorientation provide new insights into the lattice evolution within a single crystal. To the best of the author's knowledge, these analyses of CPFEM modelling results have not been reported in the literature.

Each tilt axis/angle pair from the misorientation data defines an interface, the energy of which is a minimum. Fracture energy and normal vector of the corresponding interface are interpolated from the above database. Strain energy on this interface is calculated from the stress and displacement fields from CPFEM simulation. The strain energy is

then compared with the fracture energy to determine whether the fracture occurs on the interface. This is the crack opening criterion used in this work. Elements containing interface(s) satisfying this criterion are removed from the FEM mesh by using the element removal technique.

Preliminary results of void nucleation and void growth around the notch tip in Cube and Brass oriented samples using CPFEM modelling appear to agree with MD simulations of void growth in fcc single crystals [70]. However, further simulations need to be done to justify and fully explain the observations of crack path and energy restoration.

7. Conclusions and Suggestions for Further Developments

7.1 Conclusions

This thesis numerically investigates the deformation of single crystals aluminum as well as aluminum polycrystalline aggregates in regions around a notch tip of an SEN tensile sample. The notch, of various shapes and sizes, can effectively be considered as an existing crack in materials where large deformation and cleavage are likely to occur even at a fairly early stage of loading. To account for the effects of crystal orientations, a CPFEM formulation incorporating the Bassani-Wu hardening law has been developed in Chapter 2. Even though this hardening law [115] requires more parameters in its formulation compared with other laws [117, 118-121], it enables a CPFEM model to capture more accurately the three-stage hardening within slip systems. This capability is not available if other hardening laws are used.

The theory of crystal plasticity has been implemented into the user-defined subroutine UMAT in Abaqus/Standard. The element removal technique in Abaqus/Standard is also used to model void nucleation and the subsequent crack growth based on a newly developed misorientation-dependent energy criterion for crack opening. The results are summarized as follows.

7.1.1 Verification of the CPFEM formulation

A CPFEM simulation model that has same dimensions, boundary conditions, and the applied load with the experiments done by Patil et al. [65] has been used. Two cases of

the orientation of the notch are considered in Chapter 3 to validate the CPFEM formulation incorporating the Bassani-Wu hardening law developed in Chapter 2.

- For notch tip in the $(010)[101]$ orientation, the analyses of simulation results from the current study reveal sets of slip traces on the sample surface inclining 54.5^o and 0^o to the notch tip direction. These results agree very well with the analytical solution by Rice [50] and experimental observations by Patil et al. [65]. Analyses of rotation of crystals from initial orientations show bands of concentrated rotations that are aligned at 49.1^o and 86.6^o to the notch tip direction, which also matches with EBSD results reported by Patil et al. [65].

- For notch tip in $(010)[100]$, analyses of FEM results show that slip traces on sample surface inclining $\pm 45^o$ to the notch tip direction, which agree very well with the analytical solution by Flouriot et al. [59] and experimental results [64].

Rice's asymptotic solutions for a notch tip in the $(010)[101]$ orientation have attracted verifications by various experimental and numerical works. Meanwhile, no simulation works has been found so far attempting to model and successfully verifying the analytical solutions and experimental observations of Flouriot and co-workers [59, 64] for a crack tip in the $(010)[100]$ direction. The simulations and analyses carried out in Chapter 3 are among a very few, if not the first, attempts that accurately predict experimental observations of both cases of notch tip orientation by a single model (one set of material parameters).

7.1.2 Deformation around a notch tip in single crystals prior to cracking

Chapter 4 examines the tensile deformation, in both macro-scale and micro-scale, in a small region around a notch tip in Cube and Brass oriented samples prior to crack initiations. The simulations are based on the CPFEM model incorporating Bassani-Wu hardening law that was validated in Chapter 3. Results from these simulations form a basis for further analyses for crack opening to be carried out in Chapter 6.

Tensile deformation in both macro-scale (e.g. change of the average roughness and slip traces on the sample surface) and micro-scale (e.g. lattice rotations and plastic slip) appears to be more severe in the region right around the notch boundary than outer regions. In three regions around the notch and at every stage of loading, plastic slip and the change of average surface roughness in the Brass oriented sample are approximately 1.5 times higher than those in the Cube oriented sample.

Following the analyses described in Chapter 3, slip traces on a sample surface can be predicted based on the initial crystal orientation. Using results of lattice orientation from CPFEM modelling, slip traces are plot on the surface of Cube and Brass oriented samples which agree well with analytical predictions. However at a higher load (e.g. 4.5% nominal strain for Cube sample and 3% nominal strain for Brass sample) and at locations where stress concentration occurs (e.g. around corners of the notch), crystals rotate severely from their original direction. Analytical predictions are no longer correct and thus slip traces in these cases must be determined numerically.

For both Cube and Brass oriented samples, results of crystal rotation and plastic slip appear to be higher on the free surface than on the mid-thickness plane. Also in both samples, the distribution of surface roughness generally has the same patterns with those of the total plastic deformation and the total crystal rotation. This is best observed at 4.5% nominal strain for the Cube oriented sample, and at 3% nominal strain for the Brass oriented sample.

7.1.3 Deformation around a notch tip in a polycrystalline aggregate

Chapter 5 extends the study in Chapter 4 to investigate the plastic deformation and microstructure evolution at the notch tip in an SEN polycrystalline aluminum. The polycrystalline sample has same dimensions with single crystal samples considered in Chapter 4 and is approximated by a 2D Voronoi diagram. While numerous works have numerically examined the behaviours of polycrystalline aggregates, a study that

investigates the combined effects of notch geometry and initial orientation using the CPFEM incorporating Bassani-Wu hardening law similar to that presented in Chapter 5 is still lacking.

The deformation of an fcc polycrystalline aggregate with an existing notch appear to be influenced by not only the notch geometry, but also by the initial orientations. Particularly, the initial orientation greatly influences the location and magnitudes of the maximum shear stress and cumulative shear strain around the notch. Crystals around the notch tip evolve from the initial orientation in three stages, most obviously for the component of rotation about the axis normal to the sample surface. This may be directly attributed to the Bassani-Wu hardening law, which describes the evolution of shear stress in a single slip system as a three stage process.

7.1.4 Simulations of crack initiation and crack growth

Chapter 6 further exploits the data of lattice rotation obtained from Chapter 4 to develop a crack opening criterion that depends on the evolution of lattice structure. The core of the criterion is a model estimating atomic interactions between two fcc lattices, with simplified relaxation conditions at the interface. The results of misorientation energy for <100> and <110> tilt boundaries obtained from the model match with those from MD simulations very well.

Misorientation, defined as the difference in orientation of two adjacent lattices, has been estimated. The analysis has shown that around the notch tip in both Cube and Brass oriented samples, over 90% of misorientation angles are less than 15^{o} at every stage of loading. That said, for nominal strains up 4.5% and 3% for Cube and Brass oriented samples respectively, the majority of deformation induced interfaces in the region around the notch tip are sub-grain boundaries. This analysis for misorientation together with the obtained results provides new insights into the evolution of crystals.

Based on the newly developed atomic interaction model and the data of misorientation obtained from the CPFEM modelling, the interface fracture energy E_{crit}, which is defined as the energy required to bring two misoriented lattices to complete separation, is calculated. The net strain energy in the direction normal to the interface W_{intf} is estimated based on Cauchy stress and displacement fields of the pair of lattices forming the interface. The energy criterion for crack opening employed in this study is stated as $(W_{\text{intf}} - E_{crit}) \geq 0$.

Chapter 6 has also successfully demonstrated the implementation of the new crack opening criterion into the CPFEM model that was developed in Chapter 2. Elements in the finite element mesh satisfying this criterion are removed from the mesh using the element removal technique available in Abaqus/Standard. While missing elements effectively act as voids in the material, crack opening (in terms of void nucleation) and the subsequent crack growth (in terms of coalescence of new and existing voids) are captured naturally without presuming a crack path. This capability to explicitly model crack path is essential in the studying of cleavage in ductile materials.

The initial results in Chapter 6 qualitatively agree with conclusions made from MD simulations regarding behaviours of crack growth in Cube and Brass oriented fcc single crystals [70]. Also, the response of the maximum $(W_{\text{intf}} - E_{crit})$ with strain applied after voids nucleate closely resembles that of an under-damped sinusoidal oscillator.

The development of the methodology to model crack opening presented in Chapter 6 is original. To the best of the author's knowledge, (i) the simplified relaxation at the interface of a bicrystal (in the atomic interaction model), (ii) the estimation of misorientation, and (iii) the misorientation-dependent energy criterion combined with element removal technique in Abaqus/Standard are presented in this thesis for the first time.

7.2 Suggestions for further developments

- Results of plastic slip and crystal rotation on the free surface of a single crystal sample are generally higher than those on an interior plane (see Chapter 4). This may be attributed to different deforming conditions on the two planes, i.e. plane stress versus plane strain conditions. This difference could be properly explained by carrying out 2D plane stress and plane strain simulations of the same models and comparing 2D results with the current 3D results.

- Reviewing other studies (Section 1.6) showed that various factors (e.g. grain size, type of Voronoi diagram, sample thickness) affect simulation results of tensile deformation of a polycrystalline aggregate. Thus a parametric study should be done to examine how above factors influence the results of crystal deformation obtained in Chapter 5.

- Longer simulations (higher applied tensile loads) on samples having various initial orientations would fully characterize the behaviour of mode I crack growth in SEN single crystals. Also, these simulations would justify and fully explain the observations made in Chapter 6 regarding the response of the maximum $\left(W_{\text{intf}} - E_{crit}\right)$ versus nominal strain after cracks/voids initiate.

- Currently the misorientation based energy criterion for crack opening is carried out after each loading step. Meanwhile, there might be elements satisfying the criterion somewhere in the middle of a loading step. As the crystals evolve under the continuing loading, input parameters of the criterion at these elements (e.g. interface normal vector and interface fracture energy) also change. Hence at the end of the analysis, those elements might no longer satisfy the criterion, and are missed out, i.e. not removed from the mesh.

  The prediction of crack opening would be improved if the atom interaction model is implemented directly into Abaqus/Standard, so that the crack opening criterion is

judged at the end of each time increment. This results in a “real-time” modelling of void nucleation. From the technical viewpoint, such modification is possible by using Python codes accompanied the Abaqus model to call an external program, which is the atom interaction model, at the end of each time increment. The computational time would be longer, but it is still much shorter than a full MD simulation or a multi-scale simulation incorporating MD.

- Regarding the analysis of slip traces presented in Chapter 3, it can be inversely implemented to predict the crystal orientation from the observation of slip traces on a sample surface. If combined with an SEM facility that can capture images of a sample surface during a tensile test, the slip trace analysis in this work can be used to determine the evolutions of crystal during the test. This saves time re-preparing samples and running EBSD scanning for crystal orientation.

- The methodology to model crack opening proposed in Chapter 6 can be readily applied to model fracture in various problems where the evolution of the crystal lattice is provided. Minor modifications need to be made in UMAT (for the crystal plasticity theory) and the atomic interaction model (for the misorientation-dependent fracture energy) if crystal structures other than fcc are used.

- The analysis for misorientation (Section 6.2) also provides orientation of the interface of a bicrystal. Using this information, a methodology can potentially be developed to numerically determine the formation of grain boundaries from an original single crystal (single grain) under mechanical deformations.

References

[1] D. Roylance, 2001, *Introduction to Fracture Mechanics*, weblog, accessed 25/06/2009, http://ocw.mit.edu/NR/rdonlyres/Materials-Science-and-Engineering/3-11Mechanics-of-MaterialsFall1999/F34792CC-7AA5-47F0-81AD-13664B5F856C/0/frac.pdf

[2] K. Hellan, *Introduction to Fracture Mechanics*, McGraw-Hill Book Company, United States of America, 1984.

[3] A.A. Griffith, "The phenomena of rupture and flow in solids", *Philosophical Transactions of the Royal Society of London, Series A*, vol. 221, pp. 163-198, 1920.

[4] G.R. Irwin, "Fracture Dynamics", in: *Proceedings of the ASM Symposium on Fracturing of Metals*, Cleveland, 1948.

[5] E. Orowan, "Fracture and Strength of Solids", *Reports on Progress in Physics*, vol. 12, pp. 185-232, 1949.

[6] A. Needleman, "A continuum model for void nucleation by inclusion debonding", *Journal of Applied Mechanics*, vol. 54, pp. 525–531, 1987.

[7] H. Tang, Y.S. Choi, A. Acharya, S. Saigal, "Effects of lattice incompatibility-induced hardening on the fracture behavior of ductile single crystals", *Journal of the Mechanics and Physics of Solids*, vol. 52, pp. 2841-2867, 2004.

[8] J.D. Clayton, D.L. McDowell, "Homogenized finite elastoplasticity and damage: theory and computations", *Mechanics of Materials*, vol. 36, pp. 799-824, 2004

[9] N. Bonfoh, P. Lipinski, A. Carmasol, S. Tiem, "Micromechanical modeling of ductile damage of polycrystalline materials with heterogenous particles", *International Journal of* Plasticity, vol. 20, pp. 85-106, 2004

[10] G. Wang, S.F. Li, "A penny-shaped cohesive crack model for material damage", *Theoretical and Applied Fracture Mechanics*, vol. 42, pp. 303-316, 2004

[11] D. Columbus, M. Grujicic, "A comparable discrete-dislocation/nonlocal crystal-plasticity analysis of plane-strain mode I fracture", *Materials Science and Engineering A*, vol. 323, pp 386-402, 2002.

[12] M.P. O'Day, W.A. Curtin, "Bimaterial interface fracture: A discrete dislocation model", *Journal of the Mechanics and Physics of Solids*, vol. 53, pp. 359-382, 2005.

[13] H.H.M. Cleveringa, E. Van der Giessen, A. Needleman, "A discrete dislocation analysis of mode I crack growth", *Journal of the Mechanics and Physics of Solids*, vol. 48, pp. 1133-1157, 2000.

[14] J.H. Rose, J. Ferrante, J.R. Smith, "Universal binding energy curves for metals and bimetallic interfaces", *Physical Review Letters*, vol. 47, pp. 675–678, 1981.

[15] J.H. Rose, J.R. Smith, J. Ferrante, "Universal features of bonding in metals", *Physical Review B*, vol. 28, pp. 1835–1845, 1983.

[16] M. Grujicic, Y. Zhang, "Crystal plasticity analysis of the effect of dispersed β-phase on deformation and fracture of lamellar $\gamma+\alpha_2$ titanium aluminide", *Materials Science and Engineering A*, vol. 265, pp. 285-300, 1999

[17] M. Grujicic, S.G. Lai, "Effect of martensitic transformation in Ti–15 at.%V beta phase particles on lamellar boundary decohesion in gamma TiAl—Part I: derivation of interface decohesion potentials", *Journal of Materials Science*, vol. 33, pp. 4389-4400, 1998.

[18] M. Grujicic, S.G. Lai, "Effect of martensitic transformation in Ti–15 at.%V beta phase particles on lamellar boundary decohesion in gamma TiAl—Part II: finite element analysis of crack bridging phenomenon", *Journal of Materials Science*, vol. 33, pp. 4401-4415, 1998.

[19] M. Grujicic, Y. Zhang, "Combine atomistic:crystal plasticity analysis of the effect of beta phase precipitates on deformation and fracture of lamellar $\gamma+\alpha_2$ titanium aluminide", *Journal of Materials Science*, vol. 34, pp. 1419-1437, 1999.

[20] X.-P. Xu, A. Needleman, "Void nucleation by inclusion debonding n a crystal matrix", *Modeling and Simulation in Materials Science and Engineering*, vol. 1, pp. 111–132, 1993.

[21] V. Tvergaard, J.W. Hutchinson, "The influence of plasticity on mixed mode interface toughness", *Journal of the Mechanics and Physics of Solids*, vol. 41, pp. 1119–1135, 1993.

[22] P.D. Zavattieri, H.D. Espinosa, "Grain level analysis of crack initiation and propagation in brittle materials", *Acta Materialia*, vol. 49, pp. 4291-4311, 2001

[23] K. Tanaka, T. Mura, "A dislocation model for fatigue crack initiation", *Journal of Applied Mechanics*, vol. 48, pp. 97-103, 1981.

[24] K. Tanaka and T. Mura, "A theory of fatigue crack initiation at inclusions", *Metallurgical Transactions A*, vol. 13A, pp. 117-123, 1982.

[25] T. Mura, Y. Nakasone, "A theory of fatigue crack initiation in solids", *Journal of Applied Mechanics*, vol. 57, pp. 1-6, 1990.

[26] G. Venkataraman, Y-W. Chung, Y. Naokasone, T. Mura, "Free energy formulation of fatigue crack initiation along persistent slip bands: calculation of S-N curves and crack depths", *Acta Metallurgica et Materialia*, vol. 38, pp. 31-40, 1990.

[27] H. Fan, L.M. Keer, T. Mura, "The effect of plastic deformation on crack initiation in fatigue", *International Journal of Solids and Structures*, vol. 28, pp. 1095-1104, 1991.

[28] T. Mura, "A theory of fatigue crack initiation", *Materials Science and Engineering*, vol. A176, pp. 61-70, 1994.

[29] A. Bruckner-Foit, X. Huang, "Numerical simulation of micro-crack initiation of martensitic steel under fatigue loading", *International Journal of Fatigue*, vol. 28, pp. 963-971, 2006.

[30] S. Meyer, A. Bruckner-Foit, A. Moslang, "A stochastic simulation model for microcrack initiation in a martensitic steel", *Computational Materials Science*, vol. 26, pp. 102-110, 2003.

[31] R.G. Tryon, T.A. Cruse, "A reliability-based model to predict scatter in fatigue crack nucleation life", *Fatigue and Fracture of Engineering Materials and Structures*, vol. 21, pp. 257-267, 1998.

[32] R.G. Tryon, T.A. Cruse, "Probabilistic mesomechanical fatigue crack nucleation model", *ASME Journal of Engineering Materials and Technology*, vol. 19, pp. 65-70, 1996.

[33] J. Andersson, "The influence of grain size variation on metal fatigue", *International Journal of Fatigue*, vol. 27, pp. 847-852, 2005.

[34] T. Hoshide, K. Kusuura, "Life prediction by simulation of crack growth in notched components with different microstructures and under multiaxial fatigue", *Fatigue & Fracture of Engineering Materials & Structures*, vol. 21, pp. 201-213, 1998.

[35] C. Déprés, C.F. Robertson, M.C. Fivel, "Crack initiation in fatigue: experiments and three-dimensional dislocation simulations", *Materials Science and Engineering A*, vol. 387-389, pp. 288-291, 2004.

[36] L.M. Kachanov, "Time of the rupture process under creep conditions", *Izv. Akad. Nauk*, S.S.R. Otd Tech Nauk, vol. 8, pp. 26-31, 1958.

[37] J. Lemaitre, "A continuous damage mechanics model for ductile fracture", *Journal of Engineering Materials and Technology*, vol. 107, pp. 83-89, 1985.

[38] J. Lemaitre, *A course on damage mechanics*, Sprinder-Verlag.

[39] J. Lemaitre, R. Desmorat, M. Sauzay, "Anisotropic damage law of evolution", *European Journal of Mechanics – A. Solids*, vol. 19, pp. 187-208, 2000.

[40] C.L. Chow, J. Wang, "An anisotropic theory of continuum damage mechanics for ductile fracture", *Engineering fracture mechanics*, vol. 27, pp. 547-558, 1987.

[41] Y. Wei, C.L. Chow, "A damage-coupled TMF constitutive model for solder alloy", *International Journal of damage mechanics*, vol. 10, pp. 133-152, 2000.

[42] A.H. Zhao, C.L. Chow, "An efficient explicit algorithm for damage-coupled viscoplastic fatigue model", *Finite elements in analysis and design*, vol. 43, pp. 681-690, 2007.

[43] C.L. Chow, Y. Wei, "Constitutive modeling of material damage for fatigue failure prediction", *International Journal of Damage Mechanics*, vol. 8, pp. 355-375, 1999.

[44] Y. Wei, C.L. Chow, M.K. Neilson, H.E. Fang, "Constitutive model for Sn-Pb solder under fatigue loading", *International Journal of Damage Mechanics*, vol. 13, pp. 147-161, 2004.

[45] Y. Wei, C.L. Chow, P. Vianco, E. Fang, "Isothermal fatigue damage model for lead-free solder", *International Journal of Damage Mechanics*, vol. 15, pp. 109-119, 2006.

[46] Y. Jiang, H. Sehitoglu, "A model for rolling contact failure", *Wear*, vol. 224, pp. 38-49, 1999.

[47] Y. Jiang, M. Feng, "Modeling of fatigue crack propagation", *Journal of Engineering Materials and Technology*, vol. 126, pp. 77-86, 2004.

[48] L. Feng, K. Zhang, G. Zhang, H. Yu, "Anisotropic damage model under continuum slip crystal plasticity theory for single crystals", *International Journal of Solids and Structures*, vol. 39, pp. 5279-5293, 2002.

[49] L. Xue, "Damage accumulation and fracture initiation in uncracked ductile solids subject to triaxial loading", *International journal of solids and structures*, vol. 44, pp. 5163-5181, 2007.

[50] J.R. Rice, "Tensile crack tip fields in elastic-ideally plastic crystals", *Mechanics of Materials*, vol. 6, pp. 317-335, 1987.

[51] M. Saeedvafa, J.R. Rice, "Crack tip singular fields in ductile crystals with Taylor power-law hardening. II: Plane strain", *Journal of the Mechanics and Physics of Solids*, vol. 37, pp. 673-691, 1989.

[52] T.W. Shield, K.S. Kim, "Experimental measurement of the near tip strain field in an iron-silicon single crystal", *Journal of the Mechanics and Physics of Solids*, vol. 42, pp. 845-873, 1994.

[53] T.W. Shield, "An experimental study of the plastic strain fields near a notch tip in a copper single crystal during loading", *Acta Materialia*, vol. 44, pp. 1547-1561, 1996.

[54] W.C. Crone, T.W. Shield, “Experimental study of the deformation near a notch tip in copper and copper-beryllium single crystals”, *Journal of the Mechanics and Physics of Solids*, vol.49, pp. 2819-2838, 2001.

[55] A.M. Cuitino, M. Ortiz, “Computational modeling of single crystals”, *Modeling and Simulation in Materials Science and Engineering*, vol. 1, pp. 225-263, 1992.

[56] A.M. Cuitino, M. Ortiz, “Three-dimensional crack-tip fields in four-point-bending copper single crystal specimens”, *Journal of the Mechanics and Physics of Solids*, vol. 44, pp. 863-904, 1996.

[57] W.J. Drugan, “Asymptotic solutions for tensile crack tip fields without kink-type shear bands in elastic-ideally plastic single crystals”, *Journal of the Mechanics and Physics of Solids*, vol. 49, pp. 2155-2176, 2001.

[58] R. Mohan, M. Ortiz, C.F. Shih, “An analysis of cracks in ductile single crystals – II: Mode I loading”, *Journal of the Mechanics and Physics of Solids*, vol. 40, pp. 315-337, 1992.

[59] S. Flouriot, S. Forest, L. Remy, “Strain localization phenomena under cyclic loading: application to fatigue of single crystals”, *Computational Materials Science*, vol. 26, pp. 61-70, 2003.

[60] J.R. Rice, D.E. Hawk, R.J. Asaro, “Crack tip fields in ductile crystals”, *International Journal of Fracture*, vol. 42, pp. 301-321, 1990.

[61] R. Narasimhan, A.J. Rosakis, “Three-dimensional effects near a crack tip in a ductile three-point bend specimen: Part I – A numerical investigation”, *Journal of Applied Mechanics*, vol. 57, pp. 607-617, 1990.

[62] H.Y. Subramanya, S. Viswanath, R. Narasimhan, “A three-dimensional numerical study of mixed mode (I and II) crack tip fields in elastic-plastic solids”, *International Journal of Fracture*, vol. 136, pp. 167-185, 2005.

[63] J.W. Kysar, C.L. Briant, “Crack tip deformation fields in ductile single crystals”, *Acta Materialia*, vol. 50, pp. 2367-2380, 2002.

[64] S. Flouriot, S. Forest, G. Cailletaud, A. Koster, L. Remy, B. Burgardt, V. Gros, S. Mosset, J. Delautre, “Strain localization at the crack tip in single crystal CT specimens under monotonous loading: 3D finite element analyses and application to nickel-base superalloys”, *International Journal of Fracture*, vol. 124, pp. 43-77, 2003.

[65] S.D. Patil, R. Narasimhan, P. Biswas, R.K. Mishra, “Crack tip fields in a single edge notched aluminum single crystal specimen”, *Journal of Engineering Materials and Technology*, vol. 130, pp. 021013-1 – 021013-11, 2008.

[66] E. Smith, “Cleavage crack formation and the effect of the structure of the nucleating deformation process”, *Acta Metallurgica*, vol. 16, pp. 313-320, 1968.

[67] T.H. Lin, Y.M. Ito, “Mechanics of a fatigue crack nucleation mechanism”, *Journal of the Mechanics and Physics of Solids*, vol. 17, pp. 511-523, 1969.

[68] M. Maki-Jaskari, K. Kaski, A. Kuronen, “Simulations of crack initiation in silicon”, C*omputational Materials Science*, vol. 17, pp. 336-342, 2000

[69] Y. Shimomura, M. Kiritani, I. Mukouda, “Computer simulation study of the atomistic mechanism of deformation and fracture initiation in thin fcc metal films”, *Materials Science and Engineering A*, vol. 350, pp. 238-244, 2003.

[70] L. Farrissey, M. Ludwig, P.E. McHugh, S. Schmauder, “An atomistic study of void growth in single crystalline copper”, *Computational Materials Science*, vol. 18, pp. 102-117, 2000.

[71] Y. Gao, C. Lu, G. Michal, A.K. Tieu, “A study of crack propagation in bcc iron by molecular dynamics method”, *Key Engineering Materials*, vol. 395-397, pp. 453-456, 2008.

[72] C. Lu, Y. Gao, H. Zhu, A.K. Tieu, “Atomic simulation of effect of stacking fault and dislocation on fracture behaviour in Fe crystal”, *Key Engineering Materials*, vol. 395-397, pp. 457-460, 2008.

[73] H. Rafii-Tabar, L. Hua, M. Cross, “A multi-scale atomistic-continuum modeling of crack propagation in a two-dimensional macroscopic plate”, *Journal of Physics: Condensed Matter*, vol. 10, pp. 2375-2387, 1998

[74] B. Wang, V. Karuppiah, H. Lu, S. Roy, R. Komanduri, “Two-dimensional mixed mode crack simulation using the material point method”, *Mechanics of Advanced Materials and Structures*, vol. 12, pp. 471-484, 2005.

[75] H. Tan, J.A. Nairn, “Hierarchical, Adaptive, Material Point Method for Dynamic Energy Release Rate Calculations”, Comput Methods in Appl. Mech. and Engng., vol. 191, pp. 2095–2109, 2002.

[76] P.F. Thomason, G. Rauchs, P.J. Withers, “Multi-scale finite element modeling of fatigue crack growth in TiAl intermetallic matrix TiNb and Nb platelet composites”, *Acta Materialia*, vol. 50, pp. 1453-1466, 2002.

[77] H. Tan, W. Yang, “Atomistic/continuum simulation of interfacial fracture – Part II: Atomistic/dislocation/continuum simulation”, *Acta Mechanica Sinica*, vol. 10, pp. 237-249, 1994.

[78] S. Hao, W.K. Liu, C.T. Chang, “Computer implementation of damage models by finite element and meshfree methods”, *Computer methods in applied mechanics and engineering*, vol. 187, pp. 401-440, 2000.

[79] L. Xia, C.F. Shih, “Ductile crack growth – I. A numerical study using computational cells with microstructureally-based length scales”, *Journal of the Mechanics and Physics of Solids*, vol. 43, pp. 233-259, 1995.

[80] L. Xia, C.F. Shih, "Ductile crack growth – II.Void nucleation and geometry effects on macroscopic fracture behaviour", *Journal of the Mechanics and Physics of Solids*, vol. 43, pp. 1953-1981, 1995.

[81] N. Sukumar, J.-H. Prevost, "Modeling quasi-static crack growth with the extended finite element method – Part I: Computer implementation", *International Journal of Solids and Structures*, vol. 40, pp. 7513-7537, 2003.

[82] R. Huang, N. Sukumar, J.-H. Prevost, "Modeling quasi-static crack growth with the extended finite element method – Part II: Numerical application", *International Journal of Solids and Structures*, vol. 40, pp. 7539-7552, 2003.

[83] N. Sukumar, D.J. Srolovitz, "Finite element-based model for crack propagation in polycrystalline materials", *Journal Computational and Applied Mathematics*, vol. 23, pp. 363-380, 2004.

[84] O. Watanabe, Y. Yamamoto, "Application of crystal plasticity to plastic behaviour at notched plate and crack propagation", *International Journal of Mechanical Sciences*, vol. 42, pp. 2191-2208, 2000.

[85] Z.W. Guan, E.C. Zhu, "Nonlinear finite element modeling of crack behaviour in oriented strand board webbed wood I-beams with openings", *Journal of Structural Engineering-ASCE*, vol. 130, pp. 1562-1569, 2004.

[86] E.C. Zhu, Z.W. Guan, D.J. Pope, P.D. Rodd, "Effects of openings on oriented strand board webbed wood I-joists", *Journal of Structural Engineering-ASCE*, vol. 133, pp. 145-149, 2007.

[87] Z.W. Guan, E.C. Zhu, "Finite element modeling of anisotropic elasto-plastic timber composite beams with openings", *Engineering Structures*, vol. 31, pp. 394-403, 2009.

[88] X. You, T. Connolley, P.E. McHugh, H. Cuddy, C. Motz, "A combined experimental and computational study of deformation in grains of biomedical grade 316LVM stainless steel", *Acta Materialia*, vol. 54, pp. 4825-4840, 2006.

[89] T. Fulop, W.A.M. Brekelmans and M.G.D. Geers, "Size effects from grain statistics in ultra-thin metal sheets", *Journal of Materials Processing Technology*, vol. 174, pp. 233-238, 2006.

[90] Y.J. Wei, L. Anand, "Grain-boundary sliding and separation in polycrystalline metals: application to nanocrystalline fcc metals", *Journal of the Mechanics and Physics of Solids*, vol. 52, pp. 2587-2616, 2004.

[91] E. Nakamichi, K. Hiraiwa, H. Morimoto, M. Harimoto, "Elastic/crystalline viscoplastic finite element analyses of single- and poly-crystal sheet deformations and their experimental verification", *International Journal of Plasticity*, vol. 16, pp. 1419-1441, 2000.

[92] K. Haldrup, R.D. McGinty, D.L. McDowell, “Effects of constraints on lattice re-orientation and strain in polycrystallline simulations”, *Computational Materials Science*, vol. 44, pp. 1198-1207, 2009.

[93] J.J. Gilman, “Direct measurements of the surface energies of crystals”, *Journal of Applied Physics*, vol. 31, pp. 2208-2218, 1960.

[94] V.K. Kumikov, K.B. Khokonov, “On the measurement of the surface free energy and surface tension of solid metals”, *Journal of Applied Physics*, vol. 54, pp. 1346-1350, 1983.

[95] J.M. Howe, *Interfaces in Materials – Atomic Structure, Thermodynamics and Kinetics of Solid-Vapor, Solid-Liquid and Solid-Solid Interfaces*, John Wiley & Sons, Inc., United States of America, 1997.

[96] R.C. Lincoln, K.M. Koliwad, P.B. Ghate, “Morse potential evaluation of second- and third- order elastic constants of some cubic metals”, *Physical Review*, vol. 157, pp. 463-466, 1967.

[97] Voter, AF 1994, ‘The embedded-atom method’, in JH Westbrook and RL Fleischer (ed.), *Intermetallic Compounds: Vol. 1, Principles*, John Wiley & Sons Ltd, pp 77-89.

[98] R.R. Zope, Y. Mishin, “Interatomic potentials for atomistic simulations of the Ti-Al system”, *Physical Review B*, vol. 68, pp. 024102-1 - 024102-14, 2003.

[99] Y. Mishin, M.J. Mehl, D.A. Papaconstantopoulos, “Embedded-atom potential for B2-NiAl”, *Physical Review B*, vol. 65, pp. 224114-1 - 224114-14, 2002.

[100] Y. Mishin, D. Farkas, M.J. Mehl, D.A. Papaconstantopoulos, “Interatomic potentials for monoatomic metals from experimental data and ab initio calculations”, *Physical Review B*, vol. 59, pp. 3393-3407, 1999.

[101] H.N.G. Wadley, X. Zhou, R.A. Johnson, M. Neurock, “Mechanisms, models and methods of vapor deposition”, *Progress in Materials Science*, vol. 46, pp. 329-377, 2001.

[102] B-J. Lee, J-H. Shim, M.I. Baskes, “Semiempirical atomic potentials for the fcc metals Cu, Ag, Au, Ni, Pd, Pt, Al, and Pb based on first and second nearest-neighbor modified embedded atom method”, *Physical Review B*, vol. 68, pp. 144112-1 – 144112-11, 2003.

[103] J. Mackenzie, A.J.W. Moore, J.F. Nicholas, “Bonds broken at atomically flat crystal surfaces – I. Face-centred and body-centred cubic crystals”, *Journal of Physics and Chemistry of Solids*, vol. 23, pp. 185-196, 1962.

[104] J. Mackenzie, J.F. Nicholas, “Bonds broken at atomically flat crystal surfaces – II. Crystals containing many atoms in a primitive unit cell”, *Journal of Physics and Chemistry of Solids*, vol. 23, pp. 197-205, 1962.

[105] M. Alden, H.L. Skriver, S. Mirbt, B. Johansson, “Surface energy and magnetism of the 3d metals”, *Surface Science*, vol. 315, pp. 157-172, 1994.

[106] H Erschbaumer, A.J Freeman, C.L Fu, R Podloucky, “Surface states, electronic structures and surface energy of the Ag(001) surface”, *Surface Science*, vol. 243, pp. 317-322, 1991.

[107] H. Bross, M. Kauzmann, “Electronic structure, surface states, surface energy, and work function of the Cu(100) surface”, *Physical Review B (Condensed Matter)*, vol. 51, pp. 17135-17150, 1995.

[108] K. Kokko, P.T. Salo, R. Laihia, K. Mansikka, “Work function and surface energy of optimized lithium slabs”, *Physical Review B (Condensed Matter)*, vol. 52, pp. 1536-1539, 1995.

[109] M. Methfessel, D. Hennig, M. Scheffler, “Trends of the surface relaxations, surface energies, and work functions, of the 4d transition metals”, *Physical Review B (Condensed Matter)*, vol. 46, pp. 4816-4829, 1992.

[110] S.G. Wang, E.K. Tian, C.W. Lung, “Surface energy of arbitrary crystal plane of bcc and fcc metals”, *Journal of Physics and Chemistry of Solids*, vol. 61, pp. 1295-1300, 2000.

[111] G.C. Hasson, C. Goux, “Interfacial energies of tilt boundaries in aluminum, experimental and theoretical determination”, *Scripta Metallurgica*, vol. 5, pp. 889-894, 1971.

[112] D. Wolf, “Structure-energy correlation for grain boundaries in FCC metals – III. Symmetrical tilt boundaries”, *Acta Metallurgica*, vol. 38**,** pp. 781-790, 1990.

[113] S.R. Nishitani, S. Ohgushi, Y. Inoue, H. Adachi, “Grain boundary energies of Al simulated by environment-dependent embeded atom method”, *Materials Science and Engineering A*, vol. 309-310, pp. 490-494, 2001.

[114] B.-J. Lee, S.-H. Choi, “Computation of grain boundary energies”, *Modeling and Simulation in Materials Science and Engineering*, vol. 12, pp. 621-632, 2004.

[115] J.L. Bassani, T.Y. Wu, “Latent hardening in single crystals II. Analytical characterization and predictions”, *Proceedings of the Royal Society of London A,* vol. 435, pp. 21-41, 1991.

[116] T.Y. Wu, J.L. Bassani, C. Laird, “Latent hardening in single crystals I. Theory and experiments”, *Proceedings of the Royal Society of London A,* vol. 435, pp. 1-20, 1991.

[117] R.J. Asaro, “Micromechanics of crystals and polycrystals”, *Advances in Applied Mechanics*, vol. 23, pp. 1-115, 1983.

[118] G.I. Taylor, “Analysis of plastic strain in a cubic crystal”, *Journals of Institutional Metals*, vol. 62, pp. 307-324, 1938.

[119] B. Budiansky, T.T. Wu, "Theoretical prediction of plastic strains of polycrystals", *Proceedings of the 4th US National Congress of Applied Mechanics (ASME)*, pp. 1175-1185, 1962.

[120] J.W. Hutchinson, "Elastic–plastic behavior of polycrystalline metals and composites", *Proceedings of Royal Society of London*, vol. A319, pp. 247-272, 1970

[121] K.S. Havner, A.H. Shalaby, "A simple mathematical theory of finite distortional latent hardening in single crystals", *Proceedings of Royal Society of London*, vol. A358, pp. 47-70, 1977.

[122] *ABAQUS Theory manual*, version 6.6, 2006, ABAQUS Inc.

[123] Y.G. Huang, "A user-material subroutine incorporating single crystal plasticity in the ABAQUS finite element program", *Mech Report 178*, Division of Engineering and Applied Sciences, Harvard University, Cambridge, Massachusetts, 1991.

[124] N. Stanford, *Effect of microstructural stability on the annealing bahaviour of deformed aluminum single crystals*, PhD Thesis, University of Wollongong, Australia, 2002.

[125] Q. Liu, C. Maurice, J. Driver, N. Hansen, "Heterogeneous microstructures and microtextures in cube-oriented Al crystals after channel die compression", *Metallurgical and Materials Transactions A*, vol. 29A, pp. 2333–2344, 1998.

[126] A. Akef, J.H. Driver, "Orientation splitting of cubeoriented face-centred cubic crystals in plane strain compression", *Materials Science and Engineering A*, vol. A132, pp. 245–255, 1991.

[127] J.A. Wert, Q. Liu, N. Hansen, "Dislocation boundary formation in a cold-rolled cube-oriented Al single crystal", *Acta Materialia*, vol. 45, pp. 2565-2576, 1997.

[128] M. Shikida, T. Masuda, D. Uchikawa, K. Sato, "Surface roughness of single crystal silicon etched by TMAH solution", *Sensors and Actuators A: Physical*, vol. 90, pp. 223-231, 2001.

[129] T.J. Turner, M.P. Miller, "Modeling of the influence of material structure on deformation induced surface roughening in AA7050 thick plate", *Journal of Engineering Materials and Technology*, vol. 129, pp. 367-380, 2007.

[130] G. Parry, A.G. Evans, J.W. Hutchinson, "Initiation of geometric roughening in polycrystalline metal films", *Comptes Rendus Mecanique*, vol. 336, pp. 224-231, 2008.

[131] T. Yamasaki, Y. Kaneko, H. Miyamoto, S. Hashimoto, T. Mimaki, "Tensile orientation dependence of surface-roughness evolution in cyclically deformed Fe-30%Cr alloy single crystals", *Materials Science and Engineering A*, vol. 319-321, pp. 569-573, 2001.

[132] Z. Zhao, R. Radovitzky, and A. Cuitino, "A study of surface roughening in fcc metals using direct numerical simulation", Acta Materialia, vol. 52, pp. 5791-5804, 2004.

[133] S.G. Long, Y.C. Zhou, Y. Pan, "Computation of deformation-induced textures in electro-deposited nickel coating", *Transactions of Nonferrous Metals Society of China*, vol. 16, pp. s232-s238, 2006.

[134] P.S. Lee, H.R. Piehler, B.L. Adams, G. Jarvis, H. Hampel, A.D. Rollett, "Influence of surface texture on orange peel in aluminum", *Journal of Materials Processing Technology*, vol. 80-81, pp. 315-319, 1998.

[135] L. Wang, S.R. Daniewicz, M.F. Horstemeyer, S. Sintay, A.D. Rollett, "Three-dimensional finite element analysis using crystal plasticity for a parameter study of microstructurally small fatigue crack growth in a AA7075 aluminum alloy", *International Journal of Fatigue*, vol. 31, pp. 651-658, 2009.

[136] A.G. Thakare, R. Narasimhan, R.K. Mishra, "Numerical simulations of void growth near a notch tip in ductile single crystals", *Mechanics of Materials*, vol. 41, pp. 506-519, 2009.

[137] F. Aurenhammer, "Voronoi diagrams- a survey of a fundamental geometric data structure", *ACM Computing Surveys*, vol. 23, pp. 345-405, 1991.

[138] N.N. Huynh, C. Lu, L. Si, K. Tieu, "A study of microstructural evolution around crack tip using crystal plasticity finite-element method", *Proceedings of the Institution of Mechanical Engineers Part J Journal of Engineering Tribology*, vol. 222, pp. 183-192, 2008.

[139] G. Hasson, J.-Y. Boos, I. Herbeuval, M. Biscondi, C. Goux, "Theoretical and experimental determinations of grain boundary structures and energies: correlation with various experimental results", *Surface Science*, vol. 31, pp. 115-137, 1972.

[140] V. Randle, O. Engler, *Introduction to Texture Analysis – Macrotexture, Microtexture & Orientation Mapping*, CRC Press, United States of America, 2000.

[141] K.S. Fu, R.C. Gonzalez, C.S.G. Lee, *Robotics – Controls, Sensing, Vision, and Intellligence*, McGraw-Hill Book Company, United States of America, 1987.

[142] H.W. Li, H. Yang, Z.C. Sun, "A robust integration algorithm for implementing rate dependent crystal plasticity into explicit finite element method", *International Journal of Plasticity*, vol. 24, pp. 267-288, 2008.

[143] R.D. McGinty, D.L. McDowell, "A semi-implicit integration scheme for rate independent finite crystal plasticity", *International Journal of Plasticity*, vol. 22, pp. 996-1025, 2006.

[144] A. Zamiri, F. Pourboghrat, F. Barlat, "An effective computational algorithm for rate-independent crystal plasticity based on a single crystal yield surface with an

application to tube hydroforming", *International Journal of Plasticity*, vol. 23, pp. 1126-1147, 2007.

[145] H. Takahashi, H. Motohashi, M. Tokuda, T. Abe, "Elastic–plastic finite element polycrystal model", *International Journal of Plasticity,* vol. 10, pp. 63–80, 1994.

[146] S. Nemat-Nasser, T. Okinaka, L. Ni, "A physically-based constitutive model for bcc crystal with application to polycrystal tantalum", *Journal of the Mechanics and Physics of Solids*, vol. 46, pp. 1009–1038, 1996.

[147] R. Knockaert, Y. Chastel, E. Massoni, "Rate-independent crystalline and polycrystalline plasticity, application to fcc materials", *International Journal of Plasticity*, vol.19, pp. 1245–1270, 2000.

[148] L. Anand, M. Kothari, "A computational procedure for rate-independent crystal plasticity", *Journal of the Mechanics and Physics of Solids*, vol. 44, pp. 525–558, 1996.

[149] S.R. Kalidindi, C.A. Bronkhorst, L. Anand, "Crystallographic texture evolution in bulk deformation process of fcc metals", *Journal of the Mechanics and Physics of Solids*, vol. 40, pp. 537-569, 1992.

[150] L. Delannay, P.J. Jacque, S.R. Kalidindi, "Finite element modeling of crystal plasticity with grains shaped as truncated octahedrons", *International Journal of Plasticity*, vol. 22, pp. 1879–1898, 2006.

[151] R.D. McGinty, *Crystallographic multiscale representation of polycrystalline inelasticity*, PhD Thesis, Georgia Institute of Technology, USA, 2001.

[152] D. Pierce, R.J. Asaro, A. Needleman, "Material rate dependence and localized deformation in crystalline solids", *Acta Metallurgica*, vol. 31, pp. 1951–1976, 1983.

[153] A. Needleman, R.J. Asaro, J. Lemonds, D. Peirce, "Finite element analysis of crystalline solids", *Computer Method in Applied Mechanics and Engineering*, vol. 52, pp. 689–708, 1985.

[154] J.L. Raphanel, G. Ravichandran, Y.M. Leroy, "Three-dimensional rate-dependent crystal plasticity based on Runge–Kutta algorithms for update and consistent linearization", *International Journal of Solids and Structures*, vol. 41, pp. 5995–6021, 2004.

[155] E. Busso, G. Cailletaud, "On the selection of active slip systems in crystal plasticity", *International Journal of Plasticity*, vol. 21, pp. 2212–2231, 2005.

[156] X. Ling, M.F. Horstemeyer, G.P. Potirniche, "On the numerical implementation of 3D rate-dependent single crystal plasticity formulations", *International Journal for Numerical Methods in Engineering*, vol. 63, pp. 548–568, 2005.

[157] G. Rousselier, S. Leclercq, “A simplified polycrystalline model for viscoplastic and damage finite element analyses”, *International Journal of Plasticity*, vol. 22**,** pp. 685–712, 2006.